CITY UNIVERSITY
LONDON

CHARACTERISATION OF ACOUSTIC WAVES IN OPTICAL WAVEGUIDES

BY

Suchara SRIRATANAVAREE

A THESIS SUBMITTED FOR THE
DEGREE OF DOCTOR OF PHILOSOPHY
AT

CITY UNIVERSITY LONDON

PHOTONICS MODELLING GROUP
SCHOOL OF ENGINEERING AND MATHEMATICAL SCIENCES
NORTHAMPTON SQUARE, LONDON EC1V 0HB
UNITED KINGDOM

JANUARY 2014

TABLE OF CONTENTS

LIST OF TABLES

Chapter 2

Chapter 3

Chapter 4

Chapter 5

Chapter 6

LIST OF FIGURES

Chapter 1

Chapter 2

Chapter 3

Chapter 4

Chapter 5

Chapter 6

LIST OF SYMBOLS AND ABBREVIATIONS

B	Bending mode
B1	*y* dominant of the Bending mode
B2	*x* dominant of the Bending mode
BPM	Beam Propagation Method
BS	Brillouin Scattering
CMOS	Complementary Metal Oxide Semiconductor
CW	Continuous Wave
FDM	Finite Different Method
FEM	Finite Element Method
GAWBS	Guided Acoustic Wave Brillouin Scattering
Ge	Germanium
H	Full vectorial magnetic field
H	Waveguide height
Hb_x	U_x Dominant displacement vector
Hb_y	U_y Dominant displacement vector
Hb_z	U_z Dominant displacement vector
IC	Integrated Circuit
KET	Key Enabling Technologies
MMM	Mode matching method
PCF	Photonic crystal fibre
PIC	Photonics Integraed Circuit
PS	Porous Silicon
R	Radial mode
SBS	Stimulated Brilluoin Scattering
Si	Silicon
SiO_2	Silica
SOI	Silicon-On-Insulator
T	Torsional mode
TE	Transverse Electric
TM	Transverse Magnetic

TR	Torsional-Radial mode
U_{x_max}	Maximum values of the displacement vectors along *x* direction
U_{y_max}	Maximum values of the displacement vectors along *y* direction
U_{z_max}	Maximum values of the displacement vectors along *z* direction
VLSI	Very Large Scale Integration
W	Waveguide width
W_s	Slot waveguide width
k_A	Momentum vectors of acoustic
k_P	Momentum vectors of pump
k_S	Momentum vectors of Stokes wave
ω_B	Stokes shift
ω_P	Angular frequencies of pump
ω_S	Stokes wave
f_B	Maximum backward frequency shift
n_{eff}	Effective index
β_o	Optical propagation constant
k_o	Free space wavenumber
ω	Angular frequency
ε_o	Free space permittity
μ_o	Free space permeability
A_{eff}	Effective area
Γ_{ij}	Overlap between optical and acoustic modes
V	Volume
ρ	Density
a	Acceration
u	Displacement
$\mathbf{E_t}$	Transverse electric field
T	Stress
S	Strain
t	Time
F	Force
m	Mass
c_{IJ}	Elastic stiffness constant

L	Stiffness matrix
M	Mass matrix
N	Shape function
E	Young's modulus
K	Bulk modulus
σ	Poisson's ratio
λ and μ	Lame constants
ϕ_{li}	Incident longitudinal
ϕ_{lr}	Reflected longitudinal
Ψ_{sr}	Reflected shear
k	Acoustic propagation constant
V_R	Rayleigh velocity
V_S	Shear or transverse velocity
V_L	Longitudinal velocity
f_∞	Atkin's extrapolated value
f_a	Normalised frequency
U_t	Vector displacement combination of U_x and U_y
dV	Volume of the solid structure
Γ_{Si}	Power confinement in silicon
Γ_{SiO2}	Power confinement in silica
S_z	Poynting vector
λ	Wavelength
Δ	Area of triangle
!	Factorial

ACKNOWLEDGEMENTS

First and foremost, I would like to express my deepest gratitude to my supervisor, Professor B. M. A. Rahman, for his assistance, guidance, inspiration, encouragement and support throughout my research project and the writing up of this thesis. I would also like to thank Professor K.T.V. Grattan for his valuable advices and influence throughout this research. Additionally, I would like to thank Professor T. Sun for her guidance and support.

Secondly, I am much obliged to my family. I would like to thank my parents for their love, understanding, support, and encouragement to allow me to pursue my dream to finish my PhD.

I would also like to sincerely thank all my colleagues at the Photonics Research Group and my friends at university for maintaining a friendly and joyful work atmosphere.

DECLARATION

I hereby to grant powers of discretion to the University Librarian to allow the thesis to be copied in whole or in part without further reference to the author. The permission covers only single copies made for study purposes, subject to normal conditions of acknowledgement.

ABSTRACT

Photonic active devices exploit the interaction of light with other physical effects such as carrier, fields, power density, stress, temperature, or sound. The Stimulated Brillouin scattering (SBS) in optical waveguide is an important nonlinear effect results from the coherent interactions between optical and acoustic modes. The SBS can be considered as a primary obstacle effect in limiting the power scaling in many high power photonic devices because it normally has a lower threshold than other nonlinear effects.

However, it is also well known that the interaction of light and sound can be exploited in several key applications. The guiding of acoustic wave in of optical waveguides allow interactions of light wave with the related phenomena of Brillouin Scattering (BS), Stimulated Brillouin Scattering (SBS) and Guided Acoustic Wave Brillouin Scattering (GAWBS).

This thesis describes and studies the characteristics of different acoustic modes in optical waveguides by using the finite element method (FEM). A numerical approach based on the versatile FEM has been developed and employed for the analysis of acoustic modes in optical waveguides and also their interactions with optical modes. The high and low index contrast waveguides which can be designed, fabricated and optimized for different applications. The detailed spatial variations of the transverse and longitudinal displacement vectors are shown for longitudinal, bending, torsional, radial and torsional-radial modes in these waveguides.

The vectorial acoustic modes in optical waveguides are shown for both the high and low index contrast silica waveguide along with their dispersion curves, the displacement vectors for transverse and longitudinal movements and the modal hybridness have been determined and shown.

Stimulated Brillouin Scattering (SBS) frequencies are also reported here for sub-wavelength size silica, Ge-doped rectangular and silicon slot optical waveguides. Variation of the displacement vectors, modal hybridness, and modal dispersion are also shown. A finite element based computer code is developed using a full vectorial acoustic model and combining this with another full vectorial optical model, the interaction between acoustic and optical modes are presented here and their overlap integrals have also been calculated.

Chapter 1

Introduction

This chapter commences with a basic introduction of the acoustic wave which describes the propagation of sound in solid and how sound is propagated inside a waveguide. The propagation of sound waves in dielectric waveguides with core and cladding materials can be classified into different varieties of waves types, such as, longitudinal, transverse, bending, torsional, radial and torsional-radial modes. In addition, the propagation of sound in such waveguides are depended on the wavelength, frequency, and velocity of the sound waves. Often for high optical power delivery through an optical waveguide, it is useful to reduce optical-acoustic interactions to avoid reflection of optical power. On the other hand, it would be useful to enhance optical-acoustic interactions for various applications, such as sensing stress and temperature. So, the aim of this thesis is to develop a computer code, so that the optical-acoustic interactions can be accurately calculated in such waveguides. Further, the aim and objectives of this research will be discussed along with the structure of the thesis and finally this chapter concludes with a summary of each chapter in the thesis.

1.1 Introduction to Acoustic Waves

Sound in general is a mechanical wave which is created by vibrating objects. The vibrations of the object set particles in the surrounding medium in periodic motion, thus transporting energy through the medium. Also, acoustic wave is based on time varying deformations or vibrations in materials in which, particles that contain many atoms will move in unison to produce a mechanical wave. Interestingly, when the particles of a medium are displaced from their equilibrium positions, internal restoration forces arise. It is therefore, these elastic restoring forces between particles, combined with inertia of the particles, that leads to the oscillatory motions of the medium.

Acoustic waves propagate due to the periodic displacement of the molecules inside a waveguide and are characterized by the material density, elasticity, Young modulus, and Poisson's ratio [Auld, 1973]. The particle displacement can be either in the longitudinal direction or in the transverse plane. In an acoustic waveguide when the core material is surrounded by a cladding material, the propagation of waves can be classified as being of the torsional, bending or longitudinal type [Thruston, 1978]. Further, modes can be supported, provided at least one of the velocities (the shear or longitudinal velocities) of the cladding exceeds that of the core. In solids, sound waves can propagate in four principle modes such as longitudinal waves, shear waves, surface waves, and in thin materials as plate waves. This will be discussed in Chapter 2 but most importantly, the longitudinal and shear waves are the two modes of propagation most widely used in the study of wave theory and also in this research.

1.1.1 Properties of Acoustic plane wave - *Wavelength, Frequency and Velocity* and their interactions with optical wave

It is important to know that among the properties of waves propagating in isotropic solid materials are wavelength, frequency, and velocity. The wavelength is directly proportional to the velocity of the wave and inversely proportional to the frequency of the wave. In this thesis, propagation properties of acoustic waves in optical

waveguides such as, optical fibres, rectangular dielectric waveguides and slot waveguides will be studied.

To begin with, understanding of light guidance is important. Light is an electromagnetic wave which many theories sought to describe light as a ray. However the simple definition of light can be described in terms of visible light in which it is visible to human eye and that it is also responsible for the sense of sight. Subsequently, the study of light and interaction of light with matter is termed as optics (optical wave) and that light and sound both travel as waves of energy. However, these waves are different and have different properties which affect their behaviour.

Therefore, one of the objectives is to study and exploit [Agrawal, 2007] interactions between acoustic and optical waves. Implicitly, the acoustic properties of optical waveguides allow interactions with the propagation of light through the related phenomena of Brillouin Scattering (BS), Stimulated Brillouin Scattering (SBS) and Guided Acoustic Wave Brillouin Scattering (GAWBS) [Shelby, 1985]. Therefore, it is these properties to allow us to study the interaction between acoustic and optic. Most importantly, by using the SBS effect, the interaction between acoustic and optic is studied by calculating the phase matching and then carried out the overlap integral of the acousto-optic interaction. However, in the fields of engineering with many effects and applications, further investigation have to be carried out for future work.

1.2 Nonlinear Scattering Effects

Nonlinear scattering effects in optical fibres are due to the inelastic scattering of a photon to a lower energy photon. The energy difference is absorbed by the molecular vibrations or phonons in the medium. In other words one can state that the energy of a light wave is transferred to another wave, which is at a higher wavelength (lower energy) such that energy difference appears in the form of phonons. The other wave is known as the Stokes wave. The signal can be considered as pump wave. Of course,

high-energy photon at the so-called anti-Stokes frequency can also be created if phonon of right energy and momentum is available.

There are two nonlinear scattering phenomenon in fibres and both are related to vibrational excitation modes of silica. These phenomenon are known as stimulated Brillouin scattering (SBS) and stimulated Raman scattering (SRS). The fundamental difference is that, the optical phonons participate in SRS while SBS is through acoustic phonons. As a result of this difference, SBS occurs only in one direction i.e., backward while SRS can occur in both the directions, forward and backward.

The nonlinear scattering processes cause disproportionate attenuation at high optical power levels. It also causes the transfer of optical power from one mode to other modes in forward or backward direction at different frequency. In fact the stimulated scattering mechanisms (SBS or SRS) also provide optical gain but with a shift in frequency.

1.3 Stimulated Brillouin Scattering (SBS) and basic theory

Stimulated Brillouin scattering (SBS) is well known inelastic scattering processes resulting from the interaction of light with matter. Inelastic scattering of light by acoustic phonons was first predicted by Léon Brillouin [Brillouin, 1922] in 1922, who theoretically predicted light scattering by acoustic phonon with the related density in a medium, resulted in thermally generated sound waves. Such thermal agitation is capable of scattering incident lightwaves with shifted frequency of an acoustic wave in the medium, in which, contributed to the generation of two new spectral components: the Stokes and anti-Stokes waves with down and up-shifted frequencies. These frequency shifts are proportional to the acoustic mode velocity and have been called the Brillouin frequency. This in turn resulted in the characterisation of acoustic and thermodynamic properties of materials e.g., sound velocity, sound attenuation coefficients, elasticity constants and isothermal compressibility.

1.3.1 Basic Theory

Brillouin scattering is a nonlinear process that can occur in optical fibres at a large intensity. The large intensity produces compression (due to electric field also known as pump field) in fibre core through the process known as electrostriction [Boyd, 1992]. This phenomenon produces density-fluctuations in fibre medium. It increases the material disorder, which in turn modulates the linear refractive index of medium and results in an electrostrictive-nonlinearity [Buckland and Boyd, 1996]. The modulated refractive index behaves as an index grating, which is pump-induced. The scattering of pump light through Bragg diffraction by the pump-induced index grating is called Brillouin scattering. The disorder is time dependent so the scattered light is shifted (Brillouin shift) in frequency by the frequency of sound wave.

Quantum mechanically, the Brillouin shift originates from the photon-phonon interaction and associated Doppler displacement. In this interaction either a phonon is annihilated (Stokes process-positive Brillouin shift) or created (anti-Stokes process negative Brillouin shift).

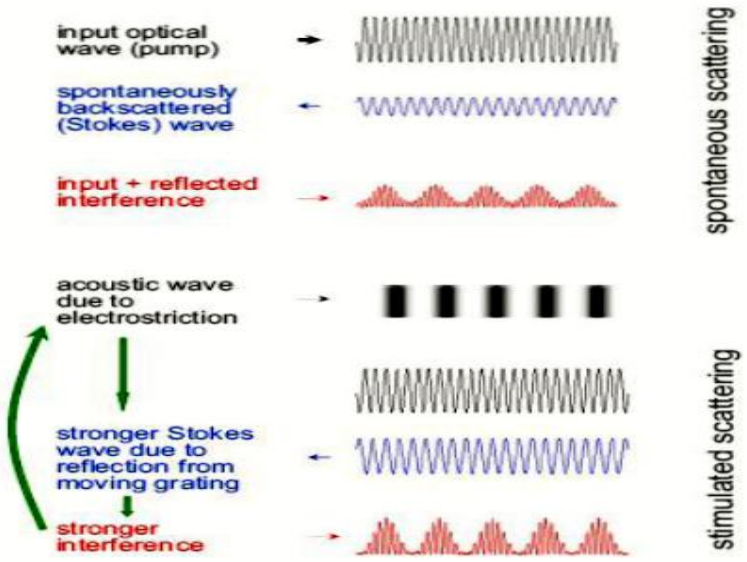

Figure 1.1. Spontaneous Brillouin scattering top and Stimulated Brillouin scattering bottom phenomenon [Kobyakov, 2003].

1.3.2 Physical process

For an oscillating electric field at the pump frequency ω_p, the electrostriction process generates a macroscopic acoustic wave (involved phonons are coherent) at some frequency ω_B. The Brillouin scattering may be spontaneous or stimulated as shown in

Fig.1.1. In spontaneous Brillouin scattering, there is annihilation of a pump photon, which results in creation of Stokes photon and an acoustic phonon simultaneously. The conservation laws for energy and momentum must be followed in such scattering processes.

For energy conservation, the Stokes shift ω_B must be equal to (ω_P-ω_S), where ω_P and ω_S are angular frequencies of pump and Stokes waves. Additionally, the momentum conservation requires k_A=(k_P-k_S), where k_A, k_P and k_S are momentum vectors of acoustic, pump and Stokes waves respectively. If v_A is acoustic velocity then dispersion relation [Agrawal, 2001] can be written as

$$\omega_B = v_A \left|\vec{k}_A\right| = v_A \left|\vec{k}_P - \vec{k}_S\right|$$
$$\textbf{or} \quad \omega_B = v_A \left|\vec{k}_P\right| \sin\frac{\theta}{2} \tag{1.1}$$

where θ is the angle between the pump and Stokes momentum vectors and modulas of k_P and k_S is taken as nearly equal. From above expression, it is clear that the frequency shift depends on angle θ. For θ=0°, shift is zero i.e., there is no frequency shift in forward direction (no Brillouin scattering). The θ=π represents the backward direction and in this situation the shift is maximum. The maximum backward frequency shift (f_B=ω_B/2π) is calculated from Eq. (1.1) and the relationship $\left|\vec{k}_P\right| = 2\pi n / \lambda_P$ as

$$f_B = \frac{2nv_A}{\lambda_P} \tag{1.2}$$

where *n* is the mode index.

In single mode fibres, the spontaneous Brillouin scattering may occur in forward direction also. The reason behind this is that there is relaxation of the wave vector selection rule due to guided nature of acoustic waves. This process is known as guided acoustic wave Brillouin scattering [Agrawal, 2001]. In this case a small amount of extremely weak light is generated.

When scattered wave is produced spontaneously, it interferes with the pump beam. This interference generates spatial modulation in intensity, which results in

amplification of acoustic wave by the electrostriction effect. The amplified acoustic wave in turn raises the spatial modulation of intensity and hence the amplitude of scattered wave. Again there is increment in amplitude of acoustic wave. This positive feedback dynamic is responsible for the stimulated Brillouin scattering, which ultimately, can transfer all power from the pump to the scattered wave.

1.3.3 Applications of SBS Phenomenon

In the early days of research, the propagation of acoustic waves in electromagnetic waveguides was studied [Kino, 1973], [Auld, 1973]. However, following that the interactions between acoustic and optical waves are being exploited [Lagasse, 1972], [Jen, 1986], [Engan, 1988], [Thurston, 1978] and [Safaai-Jazi, 1988]. More recently, the application of optical fibre sensors based on BS has also been explored [Yu, 2003] and studied [Kobyakov, 2009].

Acoustic waves guided in the optical waveguide has been researched extensively, for example, many have examined the propagation of both optical and acoustic waves for sensing applications. Success of these sensors lies in lowering the SBS threshold to achieve low power, short fibre length and multi-Stokes line generation. However, problems arising in communication system in which SBS is a dominant nonlinear penalty. This affects applications in optical transmission systems, such as high power fibre lasers and amplifiers [Limpert, 2007]. Therefore, SBS is not desirable for high power lasers because it limits the amount of output optical power. Recently, SBS effects in optical fibres has resulted in a new optical transmission fibres and laser fibres with increasing SBS thresholds using Al/Ge co-doping in the fibre core [Li, 2007]. Subsequently, SBS process in optical fibre is being extensively investigated both in optical communication and sensor system. For examples, recent applications include hybrid erbium/Brillouin amplifier [Strutz, 2000], lasers [Cowle, 1997], distributed measurement of strain and temperature [Kee, 2000]. Fibre-based sensing is important in several different industries, including temperature and leak monitoring of oil [Bao, 1995], natural gas, and other pipelines [Zou, 2006], distributed temperature and or fire sensing in hazardous environments that include mines and tunnels, power line temperatures, and point pressure sensors [Thévenaz, 1999]. Slowlight and optical delay line [Thevenaz, 2009]. These systems may be

based on either stimulated Brillouin scattering [Culverhouse, 1989] and [Kurashima, 1990] or Spontaneous Brillouin scattering [Kurashima, 1993] and [Shimizu, 1994], depending on the system configuration.

1.4 Numerical methods

The role of computerized modelling and simulation tools is important in reducing the time and costs involved in investigating phenomena for the non experimental study. Simulating tools play a part in optimization of the physical parameters, in characterization and in improving efficiency of the device. Much progress has been made in the field of modelling and simulation techniques in photonics. Numerical methods have been studied, new technique developed, and existing techniques have been improved. Nowadays, there are different types of numerical methods available to study acoustic waveguides, for examples the Finite Different Method (FDM) technique [Alford, 1974], or the numerical analysis on elastic waveguides by using mode-matching method [Lawrie, 2009] or an efficient Green's function [Matsuda, 2007] for acoustic waveguide. In addition, there is also a method for modelling sound propagation in acoustic waveguides by using a Beam propagation numerical method (BPM) [Laude, 2005] and [Mermelstein, 2009].

In Beam propagation method (BPM), is the study of an evolution of an input field as a function of the spatial coordinates, including the propagation direction (taken as z direction). It is described as the marching algorithms that take the same steps of the field in sequence of the input device, propagate it along the length of the *z* direction. The BPM algorithm then propagates the field through the interval in the *z* direction. The field at the end of the propagation step then acts as the input field for the next propagation step and so on. BPM method were first proposed and used in optics in the 1970s by Feit and Fleck.

For Finite Different method (FDM), it involved substituting the partial derivatives in partial differential equation describing the physical process by an algebraic approximation based on simple relations between the values of the function

of the desired system. Due to the small finite distances between consecutive values of the function, this method is known as FDM. The Finite difference theory for general initial value problems and parabolic problems then had an intense period of development during the 1950s and 1960s, when the concept of stability was explored in the Lax equivalence theorem and the Kreiss matrix lemmas, with further major contributions given by Douglas, Lees, Samarskii, Widlund and others.

For the Mode Matching method (MMM), the waveguide structures can be viewed in terms of two basic building blocks. The building blocks are uniform regions of the dielectric waveguide interfaced by the dielectric step discontinuities. Then each block is analysed individually and combined together for the desired structure. Characterising the step discontinuities as transformers and the representation of the uniform dielectric regions as uniform transmission lines leads to a transverse equivalent network of the waveguide structure. In 1986, Dagli and Fonstad presented a modification where the continuous spectra are discretised by converting integrals into summations using suitable basis functin expansions rather than artificially bounding the structure to discretise the continuous model spectrum.

Green's function (GF) is a fundamental solution to a linear differential equation, a building block that can be used to construct many useful solutions. The exact form of the GF depends on the differential equation, the body shape, and the type of boundary conditions present. Green's functions are named in honour of English mathematician and physicist George Green (1793-1841). The GF method can be viewed as a restatement of a boundary value problem into integral form. The GF method is useful if the GF is known (or can be found), and if the integral expressions can be evaluated.

In this thesis use of the Finite Element Method (FEM), which is a versatile and powerful numerical technique for obtaining approximate solutions to a wide variety of engineering problems is considered. Most importantly, FEM is widely used in different fields of science and technology where many engineering problems can be defined in terms of governing equations.

1.5 Photonics

Photonics is one of the key enabling technologies (KET) playing an important role in the shaping of tomorrow's world in many areas such as in communications, energy, sensing, entertainment, and health and safety. Photonic active devices exploit the interaction of lights with other physical effects such as carrier, fields, power density, stress, temperature, or sound. The SBS in optical waveguides is an important nonlinear effect results from the coherent interactions between optical and acoustic modes. However, the analyses of such interactions are not trivial, especially with the increased complexity of modern optical waveguide structures, exemplified in photonic crystal fibres and sub-wavelength waveguides, such as nanowires [Dainese, 2006]. In a way that is similar to the hybrid modes in high-index contrast optical waveguides, the acoustic modes in optical waveguides are also complex. In these cases, a rigorous full vectorial analysis [Rahman, 1984] is required for the accurate characterization of optical wave propagation. In this thesis, a numerical approach based on the versatile FEM has been developed and applied for the analysis of arbitrarily shaped acoustic waveguides and subsequently both weakly and strongly guiding acoustic waveguides have been studied.

1.6 Aims and Objectives

The main objective of this research is to develop a computer code based on the FEM to study acoustic wave guiding. In doing so, optical waveguides and acoustic waveguides will need to be evaluated first. Subsequently, focus will be on the more interesting optical wave and acoustic wave interaction in a waveguide. As SBS is an important parameter in acoustic waveguide, careful considerations and design procedures will be studied in order to design a waveguide for the optimization of the interaction between optical and acoustic waves. Therefore the main aims of this thesis are as followed:

1. To study the background literatures of acoustic wave in solid, in particular its physical quantities such as particle displacement, particle velocity, stress,

strain and elasticity. To discuss various types of waveguide modes that can exist in bounded media, particularly in longitudinal and shear wave.

2. To develop a computer model based on the FEM, suitable to use for acoustic waveguide structure. Specifically, how the Hooke's Law equation is incorporated into the computer model will be discussed and in particular, more attention will be on the stress and strain relation. The develop computer code will need to be benchmarked to ensure the efficiency of the program by comparing the results with other published papers.

3. To study the characteristic of the displacement vector profiles of the acoustic waves by using the FEM for both weakly and strongly guiding acoustic waveguides.

4. To analyze the characteristics of the longitudinal, transverse, bending, torsional, radial and torsional-radial modes by investigating on different types of waveguides. Such as, the study on a low index contrast acoustic waveguide form by a Germanium-doped silica (Ge doped SiO_2) core with pure silica (SiO_2) cladding, or a strongly guided rectangular silica waveguide, or a strip waveguide made of Porous silicon on silica buffer layer which is then surrounded by polymer.

5. To study the propagation of the wave and classify different acoustic modes by analysing the slot waveguide where light is guided in the low optical index slot region. The structure is made of using silica slot with two silicon cores on the side and silica nitride buffer layer at the bottom.

6. To investigate the interactions between the acoustic and the optical modes in various types of waveguides such as fibre, rectangular, strip and slot waveguides. The effects of SBS and the associated frequency shift due to the interaction of these hybrid acoustic modes with the fully hybrid optical mode needs also to be studied. The overlap between the fundamental H^y_{11} optical

mode with the dominant acoustic longitudinal and transverse modes needs to be calculated.

1.7 Structure of the thesis

The structure of this thesis aims to cover the development of the full vectorial finite element computer code based model by using acoustic waves. The finite element based computer model is allowed to study the different types of the acoustic wave of optical waveguide structures and to characterise the propagation of different wave types through various waveguide structures, such as longitudinal waves, transverse waves or the propagation of waves in which they can classified as being the bending (B), torsional (T), radial (R) or torsional-radial (TR) types. The interaction between acoustic and optic by using the SBS effect is also studied by calculating the phase matching and the overlap integral of acousto-optic interaction.

Chapter 1 begins by giving an introduction to the research and presents the aims and objectives along with the structure of the thesis. It will briefly show that the propagation of the acoustic waves is due to the particle displacement, material density and elasticity of the molecule inside the waveguide. It will also show that different types of waves exist in solid in which, most importantly, the longitudinal and shear wave in particular will only be considered in this thesis.

Chapter 2 commences to show the fundamental and background information on acoustic theory. The propagation of sound wave and other physical quantities that are related with the acoustic waves are to be discussed here in greater detail with examples from published literatures. The theory behind the interaction of acoustic wave and optical wave in waveguides will be discussed. Different wave modes according to their propagation nature such as pure longitudinal mode, pure transverse mode, torsional mode, radial mode, torsional-radial mode, quasi-Longitudinal mode and quasi-transverse mode are presented here.

Chapter 3 describes the theory of the finite element method. Furthermore, the incorporation of FEM formulation with the acoustic wave theory is presented in this chapter. Most importantly, the validity of the developed code will be benchmarked with a steel rod and compares with published results [H-Hennion, 1996].

Chapter 4 reports the analysis of silica fibre with low and high index contrast. The low-index contrast silica (SiO_2) acoustic waveguide is studied with the SiO_2 core doped with 7% TiO_2 with pure SiO_2 cladding. Although similar studies have been reported previously [Safaai-Jazi, 1988], in those cases the shear and transverse modes were decoupled. In the present study, the co-existence of both the shear and the longitudinal modes is going to be considered and subsequently acoustic waves in a strongly guiding SiO_2 nanowire waveguide will be discussed, including their contribution to the SBS.

Chapter 5 shows detail analysis of rectangular waveguides, the analysis of the high index and low-index contrast SiO_2 waveguide and a strip waveguide with detail spatial variation of the transverse and longitudinal displacement vector will be carried out for the bending (B), torsional (T), radial (R) and torsional-radial (TR) modes. Furthermore, the weakly guiding of Ge-doped SiO_2 core with SiO_2 pure cladding along with the strongly guided of SiO_2 core surrounded by Xe gas cladding will be studied for varieties of transverse modes such as B, T, R and TR modes. Additionally, the strip waveguide of PS core with SiO_2 substrate layer and surrounded by polymer will be presented with the longitudinal and transverse mode. Furthermore, the variation of the displacement vectors, modal dispersion will be shown with the interaction between acoustic and optical mode calculates in the overlap integral form along with the SBS frequency shift.

Chapter 6 studies the unique feature of a slot waveguide, where light is guided in a low index region (which can also be air). The study will be shown that dimension of such waveguide can be as low as 100 nm. As the high index contrast is needed to enhance the power in the slot region, the optical modes are hybrid in nature in which, acoustic wave velocities with the acoustic frequencies for different width and height will be carried out. The acousto-optic interaction in the slot

waveguide will be carried out and reported in the form of overlap integral calculation between acoustic and optic waves.

Chapter 7 concludes with the thought that modelling a waveguide with acoustic wave by a newly developed acoustic FEM code can be realised. Further, the acoustic FEM model corroborates with the full vectorial optical waveguide model. This Chapter gives summary to all the Chapters concerns and will conclude that the computer based acoustic wave in the optical waveguide will accurately and efficiently find all the acoustic wave propagation in waveguides and their characteristic of propagation such as longitudinal, transverse, bending, torsional, radial and torsional-radial modes. In addition, the analysis of acousto-optic interaction will be reported from the overlap integral calculation.

1.8 Summary

This chapter contains the basic introduction to the research in the field of acoustic wave propagation in optical waveguide, in particular to emphasize the industrial needs for fibre designs for high power laser with narrow linewidth and good beam quality to reduce the nonlinear effect such as SBS and achieve simultaneously single mode operation. The aim and objectives are also focused in terms of the acousto-optic interaction to suppress the SBS threshold that are associated from the frequency shift due to the interaction by calculating the overlap integral ratio between acoustic and optic. The structure of the thesis is also presented with a brief description on each chapter.

Chapter 2

Acoustic Theory

2.1 Introduction

The propagation of acoustic wave must be expressed in terms of tensor quantities and the relation between them; in general acoustic wave propagation in solids is complicated by the fact that solids are not always isotropic. One may simply assume that the waves of interest are either pure longitudinal or pure shear waves, and that all physical quantities (particle displacement, particle velocity, stress, strain, elasticity) can be expressed in one dimensional form. However, the equation of motion, Hooke's law, and the elastic parameters must be stated first, and then reduced them to one-dimensional terms. Further the tensor notation will be introduced and the reduced subscript notation will be used later on with some of the detailed discussions are given in Appendix A.

Later, various type of waves that can exist in isotropic media will be discussed, and the commonly used notation for the elastic constant in isotropic media will also be mentioned. The discussion of the basic concepts of reflection and refraction at the boundary between two media will be stated with further description of different types of waveguide modes that can exist in bounded media. Finally the

important topic of surface acoustic waves in an isotropic media will be considered here.

In this thesis, we have been considered acoustic wave propagation in 2 dimension waveguide problems. We will restrict our studies to the straight waveguides of uniform cross sectional shape: guided wave solutions are assumed to have propagation dependence as $e^{(-jkz)}$, where the waveguide is aligned along the *z* axis and *k* is called the propagation constant of the acoustic wave.

2.2 Sound Wave in Nonpiezoelectric Materials: One Dimensional Theory

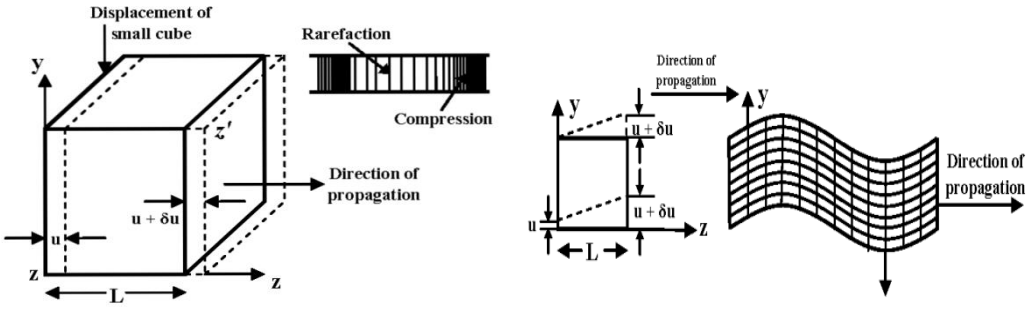

(a) (b)

Figure 2.1. (a) Longitudinal wave propagation; (b) shear wave propagation (full cube not shown) [Auld and Kino, 1971].

There are two basic types of waves that are important in acoustic wave propagation. The first is the longitudinal wave, in which the motion of the particle in the acoustic medium is only in the direction of propagation. Thus when a force is applied to the acoustic medium, the medium expands or contracts in the *z* direction, as shown in Fig. 2.1(a). The second type of wave is a shear wave, which is described as, the motion of a particle in the medium is transverse to the direction of propagation, as illustrated in Fig. 2.1(b). Shear waves are associated with the flexing or bending of a material (e.g. twisting a rod). Therefore, there may not be any change in volume or density of the material in a shear wave mode, as shown in Fig. 2.1(b).

In general, the acoustic waves that can propagate through a solid medium may combine both the shear and longitudinal motions. However, in a crystalline medium with anisotropic elastic properties, the direction of propagation can be chosen to be along one of the principle axes of the crystal; in this case the basic modes can be purely longitudinal or purely shear wave. The basic wave equation for acoustic propagation can be defined in the longitudinal case. The results obtained are identical in the form of those as shear wave propagation.

2.2.1 Stress

A force, applied to a solid stretches or compresses it and the force per unit area applied to a solid is called the stress. In the one-dimensional case, we shall denote it by symbol *T*. First considering a slab of material of infinitesimal length *L*, as shown in Fig. 2.2. Figure 2.2(a) illustrates the application of longitudinal stress, and Fig. 2.2(b) illustrates the application of shear stress. The stress T*(z)* is defined as the force per unit area on particles to the left of the plane *z*. The longitudinal stress is defined as positive if the external stress applied to the right hand side of the slab is in the +*z* direction, while the external stress applied to the left hand side of the slab is -*T* in the -*z* direction. If the stress is taken to be positive in the transverse +*x* or +*y* directions, then these definition also apply to shear stress. The net difference between the external stresses applied to each side of the slab is $L\left(\frac{\partial T}{\partial z}\right)$. Thus the net force applied to move the unit volume of the material relative to its centre of mass is $\frac{\partial T}{\partial z}$.

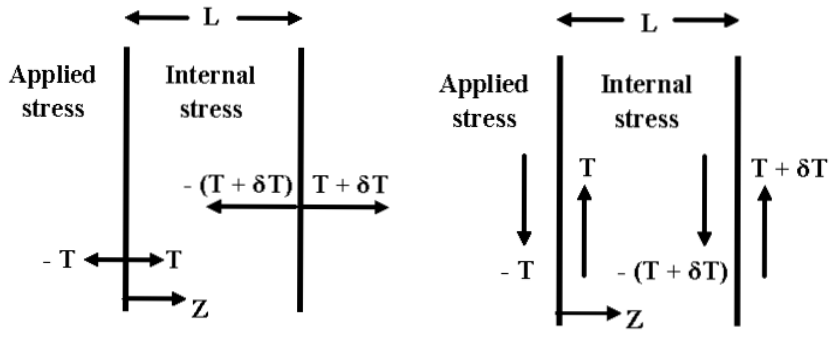

(a) (b)

Figure 2.2. (a) Stress in the longitudinal direction for a slab of length *l*, (b) stress in the shear direction [Auld and Kino, 1971].

2.2.2 Displacement and Strain in One Dimensional

Suppose that in the one-dimensional case, the plane z in the material is displaced in the z direction by longitudinal stress to a plane $z'=z+u$, as shown in Fig. 2.1(a). The parameter u is called the displacement of the material and in general, it is a function of z. At some other point in the material $z+L$, the displacement u changes to $u+\delta u$. If the displacement u is constant throughout the entire material, then the material has simply undergone a bulk translation. Such gross movements are of no interest to us here. However, we are only interested in the variation of particle displacement as a function of z.

By using a Taylor expansion, the change in u in a unit length L in the first order is δu, where,

$$\delta u = \frac{\partial u}{\partial z} L = SL \tag{2.1}$$

The fractional extension of the material is defined as:

$$S = \frac{\partial u}{\partial z} \tag{2.2}$$

and the parameters S is called the strain.

The same treatment used for the longitudinal motion can also be used in the case of the shear wave. We can define a shear strain as $S = \frac{\delta u}{L} = \frac{\delta u}{\delta z}$. Here the difference is that the displacement u is in the x or y direction, perpendicular to the propagation direction.

The diagram in Fig. 2.1(b) shows that there is no change in the area of the rectangle as shear motion distorts it. Longitudinal motion, however, changes the cube volume by δuA, in which A is the area of x, y face. Thus the relative change in the volume is $\frac{\delta V}{V} = \frac{\delta uA}{A \cdot L} = \frac{\delta u}{L} = S.$

Hooke's law and elasticity states that for all small stresses applied to a one-dimensional system, the stress is proportional to the strain, or,

$$T = cS \tag{2.3}$$

where c is the elastic constant of the material. The parameters T and c would be tensors in the general system, but can be represented by one component for one-dimensional longitudinal or shear wave propagation. This is because it is easier to bend a solid than to stretch it, the shear elastic constant is normally smaller than the longitudinal elastic constant.

2.2.3 Equation of Motion

The equation of motion is described as a point in material when a small time-variable stress is applied to it. From this Newton's second law, the force per unit area applied to the material is $L\left(\frac{\partial T}{\partial z}\right)$, so the equation of motion will be,

$$\begin{aligned} F &= ma = \rho \boldsymbol{V} a = \rho \boldsymbol{V} \dot{v} \\ \frac{F}{\boldsymbol{V}} &= \rho \dot{v} \\ \frac{F}{\partial x.\partial y.\partial z} &= \rho \dot{v} \\ as\ T &= \frac{F}{\partial x \partial y},\ so \\ \frac{T}{\partial z} &= \rho \dot{v} \\ \frac{\partial T}{\partial z} &= \rho \dot{v} = \rho \ddot{u} \end{aligned} \tag{2.4}$$

where $\boldsymbol{V}$ is the volume, m is mass, u is the displacement, v is the velocity, a is the acceleration, ρ is its mass density and dot on the top identifies its time derivative.

2.3 Tensor Notation and Constitutive Relations Materials

In all the cases, when referring to shear or longitudinal waves, we will describe wave interactions in a one dimensional form: provided that the propagation of the wave of

interest is along an axis of symmetry of a crystal. However, to carry out quantitative calculations, we must first state the equation of motion, Hooke's law, and the elastic parameters of the crystal, and then reduce them to one dimensional term. Tensor notation will be introduced; to simplify the resulting equations, we also introduce reduced subscript notation. Some of the notations used are given in Appendix A.

2.3.1 Displacement and Strain

In general, the displacement is a vector u with three Cartesian components u_x, u_y and u_z, each of which can be a function of the three Cartesian components x, y, and z of the position R. Thus, in general, $\boldsymbol{S}$ will be a tensor with nine components with the variation of U_i with j as the Cartesian coordinate, as example.

$$S_{xx} = \frac{\partial u_x}{\partial x} \tag{2.5}$$

and

$$S_{xy} = \frac{1}{2}\left(\frac{\partial u_x}{\partial y} + \frac{\partial u_y}{\partial x} \right) \tag{2.6}$$

where by using symmetry notation of the crystal form, $S_{xy}=S_{yx}$ with S_{xx}, S_{xy}, S_{xz}, S_{yx}, S_{yy}, S_{yz}, S_{zx}, S_{zy} and S_{zz} defined similarly. For pure one-dimensional motion, however, we can represent $\boldsymbol{S}$ by only one component (e.g., S_{xx} or S_{zz} for one dimensional longitudinal strain and S_{xy} for one dimensional shear strain). The symmetry of Eq. 2.6 shows that $S_{xy}=S_{yx}$.

2.3.2 Stress in a Rectangular Cube

Next the stress on a cube of volume $\delta x\, \delta y\, \delta z$ is considered and illustrated in Fig. 2.3.

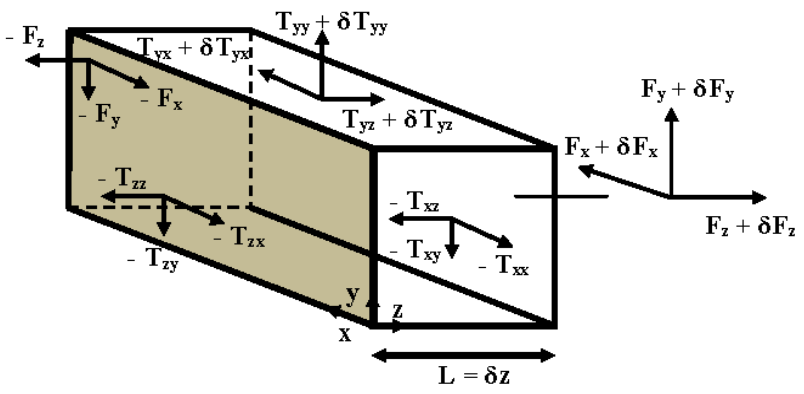

Figure 2.3. Application of general stress components [Auld, 1973].

The force applied to the left-hand surface $\delta x\ \delta y$ given by a shaded area, is called the traction F, where the stress on a cube of volume is given as *δx, δy, and δz.* The force applied to this surface has three components: $-F_x$ and $-F_y$ both parallel to the surface, and $-F_z$, perpendicular to the surface. The opposite traction force applied to the surface has components $F_x+\delta F_x$, $F_y+\delta F_y$, and $F_z+\delta F_z$.

In Section 2.2, the parameter L is equivalent to δz and by carrying out a Taylor expansion to first order in δz, this traction force has components of $F_x+((\partial F_x)/\partial z)$, $F_y+((\partial F_y)/\partial z)$, and $F_z+((\partial F_z)/\partial z)$, in the z direction. The stresses on a surface perpendicular to the z axis can be defined as follows:

$$\textbf{Shear stress: } T_{zx} = \frac{F_x}{\delta x \delta y} \tag{2.7}$$

$$\textbf{Shear stress: } T_{zy} = \frac{F_y}{\delta x \delta y} \tag{2.8}$$

$$\textbf{Longitudinal stress: } T_{zz} = \frac{F_z}{\delta x \delta y} \tag{2.9}$$

The first subscript of the tensor T denotes the coordinate axis normal to a given plane; the second subscript denotes the axis to which the traction is parallel. There are nine possible stress components: in which the terms T_{xx}, T_{yy} and T_{zz} are longitudinal stress components, while the terms $T_{xy}=T_{yx}$, $T_{xz}=T_{zx}$, and $T_{yz}=T_{zy}$ are shear stress components and they are equal in pairs, because internal stresses can give no net rotation of the body. So the initial 9 elements reduce to 6 independent values.

$$T = \begin{bmatrix} T_{xx} & T_{xy} & T_{xz} \\ T_{yx} & T_{yy} & T_{yz} \\ T_{zx} & T_{zy} & T_{zz} \end{bmatrix} = \begin{bmatrix} T_1 & T_6 & T_5 \\ T_6 & T_2 & T_4 \\ T_5 & T_4 & T_3 \end{bmatrix} = \begin{bmatrix} T_1 \\ T_2 \\ T_3 \\ T_4 \\ T_5 \\ T_6 \end{bmatrix} \tag{2.10}$$

The force per unit volume in the *z* direction is the net resultant of the force per unit volume applied to an infinitesimal cube, that is,

$$f_z = \frac{\partial T_{zx}}{\partial x} + \frac{\partial T_{zy}}{\partial y} + \frac{\partial T_{zz}}{\partial z} \tag{2.11}$$

It follows from Eq. 2.11 that the equation of motion in the *z* direction is,

$$\rho \ddot{u}_z = \rho \dot{v}_z = \frac{\partial T_{zx}}{\partial x} + \frac{\partial T_{zy}}{\partial y} + \frac{\partial T_{zz}}{\partial z} \tag{2.12}$$

with corresponding equations for the other components of *u* and *v*. This is discussed more in depth in Appendix A**.**

By adding all the forces terms, the equation of motion in the *z* direction in full tensor form is,

$$\rho \frac{\partial^2 u_z}{\partial t^2} = \frac{\partial T_{zx}}{\partial x} + \frac{\partial T_{zy}}{\partial y} + \frac{\partial T_{zz}}{\partial z} \tag{2.13}$$

In reduced notation, Eq. 2.13 may be written in the form of,

$$\rho \frac{\partial^2 u_z}{\partial t^2} = \frac{\partial T_5}{\partial x} + \frac{\partial T_4}{\partial y} + \frac{\partial T_3}{\partial z} \tag{2.14}$$

Similar relations for the equations of motion in the *y* and *x* directions can also be obtained.

It is often convenient to use the symbolic notation [Auld, 1969], which is discussed more fully in Appendix A, and written as,

$$\nabla \cdot T = \hat{x}\left(\frac{\partial T_{xx}}{\partial x} + \frac{\partial T_{xy}}{\partial y} + \frac{\partial T_{xz}}{\partial z}\right) + \hat{y}\left(\frac{\partial T_{yx}}{\partial x} + \frac{\partial T_{yy}}{\partial y} + \frac{\partial T_{yz}}{\partial z}\right) + \hat{z}\left(\frac{\partial T_{zx}}{\partial x} + \frac{\partial T_{zy}}{\partial y} + \frac{\partial T_{zz}}{\partial z}\right) \tag{2.15}$$

This may be written compactly as:

$$(\nabla \cdot T)_i = \sum_j \frac{\partial}{\partial u_j} T_{ij} \tag{2.16}$$

where $i, j=x, y, z$.

The translation equational of motion in rectangular Cartesian coordinates is:

$$\frac{\partial T_{ij}}{\partial u_j} = \rho \frac{\partial^2 u_i}{\partial t^2} - F_i \tag{2.17}$$

where F_i is the external force and in this case it is taken as zero.

2.3.3 Hooke's Law and Elasticity

In its simplest form Hooke's law states that for small elongation of an elastic system the stress is proportional to the strain. In general the term of components with respect to an orthonormal basis, the generalized form of Hooke's law is written as:

$$T_{ij} = c_{ijkl} S_{kl} \tag{2.18}$$

in which the tensor c (c_{ijkl}) containing 81 9×9 elastic coefficient must be defined to link the stress tensor T (T_{ij}) and the strain tensor S (S_{kl}) both with 9 components. The tensor c is called the stiffness tensor. However, the symmetry condition reduces 9 components of T and S to only 6 components and allow us to write the stress-strain relations in a more compact from as [T] = [c][S]:

$$T = \begin{bmatrix} T_1 \\ T_2 \\ T_3 \\ T_4 \\ T_5 \\ T_6 \end{bmatrix}, c = \begin{bmatrix} c_{11} & c_{12} & c_{13} & c_{14} & c_{15} & c_{16} \\ c_{21} & c_{22} & c_{23} & c_{24} & c_{25} & c_{26} \\ c_{31} & c_{32} & c_{33} & c_{34} & c_{35} & c_{36} \\ c_{41} & c_{42} & c_{43} & c_{44} & c_{45} & c_{46} \\ c_{51} & c_{52} & c_{53} & c_{54} & c_{55} & c_{56} \\ c_{61} & c_{62} & c_{63} & c_{64} & c_{65} & c_{66} \end{bmatrix}, S = \begin{bmatrix} S_1 \\ S_2 \\ S_3 \\ 2S_4 \\ 2S_5 \\ 2S_6 \end{bmatrix} \tag{2.19}$$

The relation between T_{xx} and the applied strains S_{xx} and S_{yy} is given as:

$$T_{xx} = c_{xxxx}S_{xx} + c_{xxyy}S_{yy} \tag{2.20}$$

The relation between T_{xz} and the applied strain S_{xz} is,

$$\begin{aligned} T_{xz} &= c_{xzxz}S_{xz} + c_{xzzx}S_{zx} \\ &= 2c_{xzxz}S_{xz} \end{aligned} \tag{2.21}$$

where $S_{xz}=S_{zx}$ and $c_{xzxz}=c_{xzzx}$, due to symmetry. In each of these cases, the first two subscripts of the elastic tensor correspond to the subscripts for the stress tensor, and the last two subscripts correspond to those for the strain tensor.

2.3.4 Tensor Notation

A simpler notation, described more fully in Appendix A, can be used to denote the components of the vectors and tensors involved. This thesis has used the subscripts *i*, *j*, and *k* to denote any one of the *x*, *y*, and *z* axes of the interest tensor components. Similarly, the tensors denote stress and strain are T_{ij} and S_{ij}, respectively. Hooke's law in Eq 2.18 shown that *k* and *l* are floating subscripts indicating summation over *k* and *l*, where *i* and *j* indicate the stress components required. Since both T_{ij} and S_{kl} are symmetric, this symmetry is reflected in c_{ijkl}, which is also symmetric, in which:

$$c_{ijkl} = c_{jilk} = c_{ijlk} = c_{jilk} \tag{2.22}$$

and,

$$c_{ijkl} = c_{klij} \tag{2.23}$$

These symmetry operations reduce the number of independent constants from 81 to 36 to 21 for crystals of different symmetries. For isotropic solids it has already been demonstrated that there are only two independent elastic constants. In fact it is well known that for an isotropic solid the reduced notation of the stiffness matrix will be used. Although, there can be 81 terms for [c], but given in Eq. 2.19, in reality these [T] and [S] had only 6 independent terms. Due to the symmetry of the stress tensor, strain tensor, and stiffness tensor, only 21 elastic coefficients of [c] are

independent. As stress is measured in unit of pressure and strain is dimensionless, the entries of c_{ijkl} are also in the unit of pressure.

2.3.5 Reduced Subscript Notation

As $T_{ij}=T_{ji}$ and $S_{ij}=S_{ji}$, there are actually only six independent tensor quantities. The subscripts *i*, *j*, and *k* will be used to denote the tensor components of interest in what is called *the reduced form*. Hence T_I is a component of the stress tensor, which replaces the longer unreduced notation T_{ij}, and S_I is a component of a strain tensor, which replaces the longer reduced notation S_{ij}. Table 2.1 summarizes how this notation is used, by taking the strain tensor, and the stress tensor as examples. It also gives notation describing the stress and the strain tensors in non reduced form in Table 2.2.

Table 2.1. Tensor and vector components.

Stress or vector component	***Example***	***Meaning***
Strain, S_I	S_1 (I=1) = S_{xx}	Longitudinal strain in *x* direction
	S_2 (I=2) = S_{yy}	Longitudinal strain in *y* direction
	S_3 (I=3) = S_{zz}	Longitudinal strain in *z* direction
	S_4 (I=4) = $2S_{yz}$	Shear strain, motion about *x* axis; shear in *y* and *z* directions
	S_5 (I=5) = $2S_{xz}$	Shear strain, motion about *y* axis; shear in *x* and *z* directions
	S_6 (I=6) = $2S_{xy}$	Shear strain, motion about *z* axis; shear in *x* and *y* directions
Stress, T_I	T_1 (I=1) = T_{xx}	Longitudinal stress in the *x* direction
	T_2 (I=2) = T_{yy}	Longitudinal stress in the *y* direction
	T_3 (I=3) = T_{zz}	Longitudinal stress in the *z* direction
	T_4 (I=4) = T_{yz}	Shear stress about *x* axis
	T_5 (I=5) = T_{xz}	Shear stress about *y* axis
	T_6 (I=6) = T_{xy}	Shear stress about *z* axis

Table 2.2. Example of the reduced tensor notation.

Elastic constant		***Meaning***
Reduced notation	***Standard notation***	
c_{IJ}	c_{ijkl}	The ratio of the *I* th stress component to the *J* strain component
c_{11}	c_{1111}	The longitudinal elastic constant relating longitudinal stress and strain components in the *x* direction
c_{44}	c_{2323}	The shear elastic constant relating shear stress and strain components in the 4-direction (motion about *x* axes)
$c_{12} = c_{21}$	$c_{1122} = c_{2211}$	$c_{IJ} = c_{JI}$

When the material is not piezoelectric, we can write,

$$T_I = c_{IJ} S_J \tag{2.24}$$

or, the relations of the stress-strain of the material properties are usually expressed in matrix from, referring stress and strain components to some appropriate basis. The general relationships look like this (ignoring temperature changes and initial stress, for simplicity) and most importantly to remember the factor of 2 in the shear strains.

$$\begin{bmatrix} T_1 \\ T_2 \\ T_3 \\ T_4 \\ T_5 \\ T_6 \end{bmatrix} = \begin{bmatrix} c_{11} & c_{12} & c_{13} & c_{14} & c_{15} & c_{16} \\ c_{21} & c_{22} & c_{23} & c_{24} & c_{25} & c_{26} \\ c_{31} & c_{32} & c_{33} & c_{34} & c_{35} & c_{36} \\ c_{41} & c_{42} & c_{43} & c_{44} & c_{45} & c_{46} \\ c_{51} & c_{52} & c_{53} & c_{54} & c_{55} & c_{56} \\ c_{61} & c_{62} & c_{63} & c_{64} & c_{65} & c_{66} \end{bmatrix} \begin{bmatrix} S_1 \\ S_2 \\ S_3 \\ 2S_4 \\ 2S_5 \\ 2S_6 \end{bmatrix} \tag{2.25}$$

Original 9x9 [c] matrix can be reduced to a 6x6 [c] matrix as shown in Eq. 2.25, by using the reduced notation. However, all of these 36 elements are not independent. Generally, there are 21 independent elastic constants ($c_{IJ}=c_{JI}$), but these reduce to far fewer independent terms in crystals with certain symmetries. In a cubic crystal, for instance: $c_{11}=c_{22}=c_{33}$, $c_{12}=c_{21}=c_{13}=c_{31}=c_{23}=c_{32}$, and $c_{14}=c_{15}=c_{16}=0$, $c_{24}=c_{25}=c_{26}=0$, $c_{34}=c_{35}=c_{36}=0$. Thus there are only three independent constants: c_{11}, c_{44}, and c_{12}. If the material is isotropic, it can be shown that,

$$c_{11} - c_{12} = 2c_{44} \tag{2.26}$$

While for the isotropic case,

$$c_{IJ} = \begin{bmatrix} \lambda+2\mu & \lambda & \lambda & 0 & 0 & 0 \\ \lambda & \lambda+2\mu & \lambda & 0 & 0 & 0 \\ \lambda & \lambda & \lambda+2\mu & 0 & 0 & 0 \\ 0 & 0 & 0 & \mu & 0 & 0 \\ 0 & 0 & 0 & 0 & \mu & 0 \\ 0 & 0 & 0 & 0 & 0 & \mu \end{bmatrix} \tag{2.27}$$

where λ and μ are the Lame coefficients which will be discussed later in Section 2.4.

2.4 Waves in Isotropic Media

2.4.1 Lamé Constants

In Appendix A it is shown that, due to symmetry of the crystal, the number of independent elastic constants in an isotropic medium reduces to two. These two independent constants are called the Lamé constants, λ and μ. These parameters are useful for determining the total stored energy of the system and are related to the elastic constants already defined, as follows: [Royer, 2000]

$$c_{11} = c_{22} = c_{33} = \lambda + 2\mu \tag{2.28}$$

$$c_{12} = c_{13} = c_{23} = c_{21} = c_{31} = c_{32} = \lambda \tag{2.29}$$

and

$$c_{44} = c_{55} = c_{66} = \mu = \frac{c_{11} - c_{12}}{2} \tag{2.30}$$

All other off-diagonal terms are zero. The parameter μ is known as the shear modulus, or the modulus of rigidity.

The general relationship between the speed of sound in a solid and its density and elastic constants is given by the following equation:

$$V = \sqrt{\frac{c_{ij}}{\rho}} \tag{2.31}$$

where V is the speed of sound, c is the elastic constant, and ρ is the material density. This equation may take a number of different forms depending on the type of wave (longitudinal or shear) and the particular elastic constants that are need to be used.

It must also be mentioned that the subscript ij attached to c in the above equation, is used to indicate the directionality of the elastic constants with respect to the wave type and direction of wave travel. In isotropic materials, the elastic constants are the same for all directions within the material. However, most materials are anisotropic and the elastic constants differ with each direction.

2.4.2 Shear and Longitudinal Waves

The shear wave velocity V_s determined from the effective elastic constant for shear waves, is defined as

$$V_s = \sqrt{\frac{c_{44}}{\rho}} \tag{2.32}$$

$$\frac{V_s}{V_l} = \sqrt{\frac{c_{44}}{c_{11}}} = \sqrt{\frac{\mu}{\lambda + 2\mu}} \tag{2.33}$$

then

$$V_l = \sqrt{\frac{c_{11}}{\rho}} \tag{2.34}$$

When calculating the velocity of a longitudinal wave, Young's Modulus and Poisson's Ratio are commonly used. When calculating the velocity of a shear wave, the shear modulus is used. It is often most convenient to make the calculations using Lame's Constants, which are derived from Young's Modulus and Poisson's Ratio.

Table 2.3. Relations between the various elastic constants and Poisson's ratio σ for an isotropic solid.

	***E*, σ**	***E*, μ**	**λ, μ**	**c_{11},c_{12}**
λ	$\frac{E\sigma}{(1+\sigma)(1-2\sigma)}$	$\frac{\mu(E-2\mu)}{3\mu-E}$	λ	c_{12}
μ	$\frac{E}{2(1+\sigma)}$	μ	μ	$\frac{c_{11}-c_{12}}{2}$
E	**E**	**E**	$\frac{\mu(3\lambda+2\mu)}{\lambda+\mu}$	$c_{11}-2\frac{c_{12}^2}{c_{11}+c_{12}}$
K	$\frac{E}{3(1-2\sigma)}$	$\frac{\mu E}{3(3\mu-E)}$	$\lambda+\frac{2}{3}\mu$	$\frac{c_{11}+2c_{12}}{3}$
σ	σ	$\frac{E-2\mu}{2\mu}$	$\frac{\lambda}{2(\lambda+\mu)}$	$\frac{c_{12}}{c_{11}+c_{12}}$

Alternatively, an isotropic solid can also be equally well characterized by an alternative pair of parameters, the Young's modulus, **E**: proportionality constant between uni-axial stress and strain, Bulk modulus, **K**: a measure of the incompressibility of a body subjected to hydrostatic pressure and the Poisson's ratio, σ: the ratio of radial strain to axial strain, instead of the elastic constants c_{11} and c_{12}

or the Lamé constants λ, μ: material constants that are derived from Young's Modulus and Poisson's Ratio. The relation between these coefficients is shown in the Table 2.3.

2.5 Refraction and Snell's Law

When an acoustic wave passes through an interface between two materials at an oblique angle, and the materials have different indices of refraction, both reflected and refracted waves are produced. This effect is similar as for light, which is why objects seen across an interface appear to be shifted relative to where they really are.

Refraction takes place at an interface due to the different velocities of the acoustic waves within the two materials. The velocity of sound in each material is determined by the material properties (elastic modulus and density) for that material. In Fig. 2.4, a series of plane waves are shown travelling in one material and entering a second material that has a higher acoustic velocity. Therefore, when the wave encounters the interface between these two materials, the portion of the wave in the second material is moving faster than the portion of the wave in the first material. It can be seen that this causes the wave to bend.

Snell's law describes the relationship between the angles and the velocities of the waves. Snell's law equates the ratio of material velocities $\mathbf{V_1}$ and $\mathbf{V_2}$ to the ratio of the sine's of incident (θ_1) and refracted (θ_2) angles, as shown in the following equation.

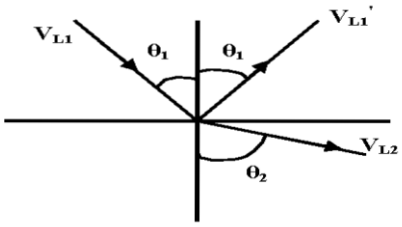

$$\frac{\sin\theta_1}{\mathbf{V}_{\mathbf{L}_1}} = \frac{\sin\theta_2}{\mathbf{V}_{\mathbf{L}_2}}$$

Where:

$\mathbf{V}_{\mathbf{L}_1}$ is the longitudinal wave velocity in material 1.

$\mathbf{V}_{\mathbf{L}_2}$ is the longitudinal wave velocity in material 2.

Figure 2.4. The diagram of reflected and refracted longitudinal (V_L) wave.

Note that in Fig. 2.4, there is a reflected longitudinal wave ($V_{L1'}$) shown. This wave is reflected at the same angle as the incident wave because the two waves are

travelling in the same material, and hence have the same velocities. This reflected wave is unimportant in our explanation of Snell's law, but it should be remembered that some of the wave energy is reflected at the interface.

When a longitudinal wave moves from a slower to a faster material, there is an incident angle that makes the angle of refraction for the wave 90°. This is known as the first critical angle. The first critical angle can be found from Snell's law by putting in an angle of 90° for the angle of the refracted ray. At the critical angle of incidence, much of the acoustic energy is in the form of an inhomogeneous compression wave, which travels along the interface and decays exponentially with depth from the interface. This wave is sometimes referred to as a "creep wave." Because of their inhomogeneous nature and the fact that they decay rapidly, creep waves are not used as extensively as Rayleigh surface waves. However, creep waves are sometimes more useful than Rayleigh waves because they suffer less from surface irregularities and coarse material microstructure due to their longer wavelengths.

2.5.1 Plane Wave Reflection and Refraction

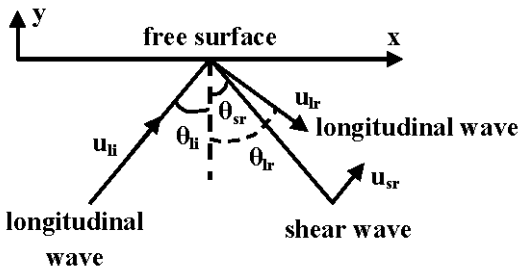

Figure 2.5. Longitudinal wave incident on a free surface. There are two reflected waves: "*longitudinal wave*" and "*shear wave*".

The reflection of an infinite plane wave at a free surface has to be considered. If a plane longitudinal or shear wave is normally incident on a surface, the reflected wave will also be a wave of the same type and of equal amplitude. The boundary condition is that the normal component of stress at the surface is zero. More generally, if a longitudinal wave is incident in the *x-y* plane on a free surface *y=0* at an angle θ_{li} to the normal, as illustrated in Fig. 2.5, it will give rise to a reflected longitudinal wave at an angle θ_{lr} to the normal and a reflected shear wave at an angle θ_{sr} to the normal.

The displacement associated with this shear wave will have a component in the vertical direction, so we call it a *shear vertical* wave.

The longitudinal wave can be represented in terms of a potential ∅, which varies as $\exp^{-jk_l r}$ where the vector r is the direction of wave. The incident longitudinal wave potential $\emptyset_{li}$, in the coordinate system of Fig. 2.5, is defined as,

$$\phi_{li} = A_{li} e^{-jk_l (x \sin\theta_{li} + y \cos\phi_{li})} \tag{2.35}$$

In the same way, there must be a reflected longitudinal wave $\emptyset_{lr}$ of the form,

$$\phi_{lr} = A_{lr} e^{-jk_l (x \sin\theta_{lr} - y \cos\phi_{lr})} \tag{2.36}$$

and, in general, a reflected shear wave Ψ_{sr} of the form

$$\Psi_{sr} = A_{sr} e^{-jk_s (x \sin\theta_{sr} - y \cos\phi_{sr})} \tag{2.37}$$

where the potential Ψ_{sr} is a vector in the z direction. Any other components in Ψ_{sr} would give rise to additional components of T and u, and thus would not satisfy the boundary conditions.

The boundary condition at the surface is that the total normal component of stress must be zero. Therefore, as shown in Section 2.3 and Appendix A, the stress components at the surface are,

$$T_2 = T_{yy} = 0 \tag{2.38}$$

and

$$T_6 = T_{xy} = 0 \tag{2.39}$$

These stress components are derived as sums of the components of the longitudinal and shear waves. Thus, to satisfy the boundary conditions at any point along the surface $y=0$, all components of longitudinal and shear waves must have the same phase variation along the surface.

This implies, from Eqs. 2.35 - 2.37, that,

$$k_l \sin\theta_{li} = k_l \sin\theta_{lr} = k_s \sin\theta_{sr} \tag{2.40}$$

This can be concluded that the angle of incident equals to the angle of reflection for the longitudinal waves, similar to the reflection of electromagnetic (EM) waves, or,

$$\theta_{li} = \theta_{lr} \tag{2.41}$$

This also arrives at the condition that,

$$\frac{\sin\theta_{sr}}{\sin\theta_{li}} = \frac{k_l}{k_s} = \frac{V_s}{V_l} = \sqrt{\frac{\mu}{\lambda + 2\mu}} \tag{2.42}$$

This condition is similar to the Snell's law for the reflection of EM waves and is based on the same considerations. As V_s<V_l in all isotropic solids, the reflected shear wave propagates at an angle closer to the normal than the reflected longitudinal wave.

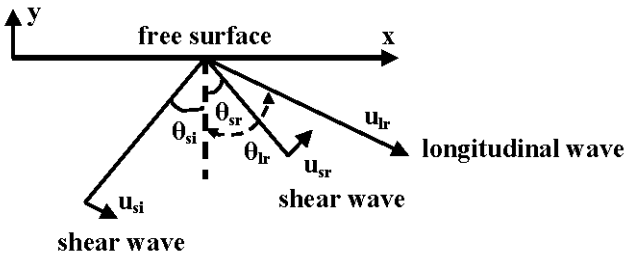

Figure 2.6. Shear wave incident on a free surface.

If we consider the opposite case of excitation by a shear vertical wave, we can conclude that by using the same type of notation as illustrated in Fig. 2.6:

$$\frac{\sin\theta_{lr}}{\sin\theta_{si}} = \frac{k_s}{k_l} = \frac{V_l}{V_s} = \sqrt{\frac{\lambda + 2\mu}{\mu}} \tag{2.43}$$

2.6 Modes of Sound Wave Propagation

In air, sound travels by the compression and rarefaction of air molecules in the direction of travel. However, in solids, molecules can support vibrations in other directions, hence, a number of different types of sound waves are possible. Waves can be characterized in space by oscillatory patterns that are capable of maintaining their shape and propagating in a stable manner. The propagation of waves is often described in terms of what are called "wave modes."

In solids, sound waves can propagate in four principle modes that are based on the way the particles oscillate. Sound can propagate as longitudinal waves, shear waves, surface waves, and in thin materials as plate waves. Longitudinal and shear waves are the two modes of propagation most widely used. The particle movement responsible for the propagation of longitudinal and shear waves is illustrated below.

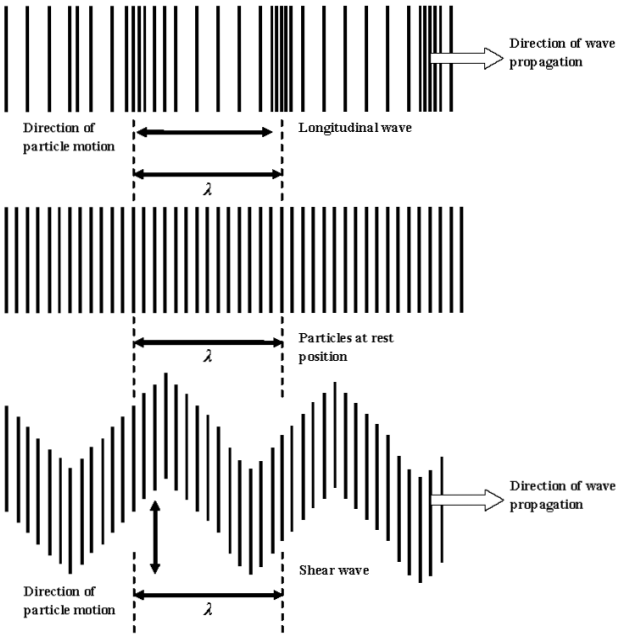

Figure 2.7. Longitudinal and shear wave direction of propagation.

As mentioned previously, longitudinal and transverse (shear) waves are most often used for wave inspection. However, at surfaces and interfaces, various types of elliptical or complex vibrations of particles make other waves possible. Some of these wave modes such as Rayleigh and Lamb waves are also useful for the inspection. Table 2.4 summarizes many, but not all, of the wave modes in solids.

Table 2.4. Summarized possible wave modes in solid.

Wave Types in Solids	*Particle Vibrations*
Longitudinal	Parallel to wave direction
Transverse (Shear)	Perpendicular to wave direction
Surface - Rayleigh	Elliptical orbit - symmetrical mode
Plate Wave - Lamb	Component perpendicular to surface (extensional wave)
Plate Wave - Love	Parallel to plane layer, perpendicular to wave direction
Stoneley (Leaky Rayleigh Waves)	Wave guided along interface
Sezawa	Antisymmetric mode

Longitudinal and transverse waves were discussed earlier, so the surface and plate waves are described in the following sections.

Surface (or Rayleigh) waves travel along the surface of a relatively thick solid material penetrating only to a depth of one wavelength. Surface waves combine both a longitudinal and transverse motions to create an elliptic orbit motion. The major axis of the ellipse is perpendicular to the surface of the solid this is because as the depth of an individual atom from the surface increases the width of its elliptical motion decreases. Surface waves are generated when a longitudinal wave intersects a surface near the second critical angle and they travel at a velocity between 0.87 and 0.95 of a shear wave. Rayleigh waves are useful because they are very sensitive to surface defects (and other surface features) and they follow the surface around curves. Because of this, Rayleigh waves can be used to inspect areas that other waves might have difficulty reaching.

Plate waves are similar to surface waves except they can only be generated in materials a few wavelengths thick. Lamb waves are the most commonly used plate waves. Lamb waves are complex vibrational waves that propagate parallel to the test surface throughout the thickness of the material. Propagation of Lamb waves depends on the density and the elastic material properties of a component. They are also influenced a great deal by the test frequency and material thickness. Lamb waves are generated at an incident angle in which the parallel component of the velocity of the wave in the source is equal to the velocity of the wave in the test material. Lamb waves can travel several meters inside the steel and so are useful to scan metal plate, wire, and tubes.

With Lamb waves, a number of modes of particle vibration are possible, but the two most common modes are symmetrical and asymmetrical. The complex motion of the particles is similar to the elliptical orbits for surface waves. Symmetrical Lamb waves move in a symmetrical fashion about the median plane of the plate. This is sometimes called the extensional mode because the wave is "stretching and compressing" the plate along the direction of the wave motion. Wave motion in the symmetrical mode is most efficiently produced when the exciting force is parallel to the plate. The asymmetrical Lamb wave mode is often called the "flexural mode" because a large portion of the motion moves in a normal direction to the plate, and a little motion occurs in the direction parallel to the plate. In this mode, the body of the plate bends as the two surfaces move in the same direction.

2.7 Surface Waves

Since the different types of waves that can exist in a solid medium of finite width are discussed. In this section, more attentions are devoted to Rayleigh waves. Rayleigh waves exist only near the surface of a semi-infinite medium. For this reason such waves are called *surface waves*. A familiar example of a surface wave is one that propagates along the surface of water. In this case, the wave motion is strong at the surface of the water and falls off very rapidly into its interior. In a water wave, the inertial forces are associated with the mass of the water and the restoring forces are due to gravity, rather than Hooke's law.

When an observer analyzing seismic motions of the earth, three distinct events can occur due to a distant disturbance. The first is a result of longitudinal waves propagating through the interior of the earth. The second due to shear waves, which, because they propagate at a slower velocity than longitudinal waves, they reach the observer at a later time. Finally, a third disturbance, due to a wave propagating along a curve surface of the earth, reaches the observer; this surface wave disturbance is the strongest of the three.

Lord Rayleigh [Rayleigh, 1904] proposed a theory for the surface wave, which shows that it consists of a mixture of shear and longitudinal stress components. This is because there is no restoring force at a surface of a solid medium, any force normal to the surface must be zero. Thus the boundary condition at the surface is that the normal components of stress must be zero. If a wave propagating in the *z* direction exist in a semi-infinite medium, the total energy per unit length in the wave must be finite. This, in turn, implies that the field components associated with the wave will decay exponentially into the interior of the medium. It is possible to obtain a mathematical solution that satisfies the boundary conditions.

Surface acoustic waves are technically important because their energy is concentrated in a relatively small region, approximately one wavelength deep, near the surface. The waves are therefore accessible from the surface. Thus Rayleigh waves produced by seismic disturbances are the one most easily detected by sensors on the surface of the earth.

2.7.1 Rayleigh Wave in an Isotropic Medium

Consider a medium that is semi-infinite in the *-y* direction with a free surface at *y=0* and particle displacement only along the *y* and *z* axes, as illustrated in Fig. 2.8.

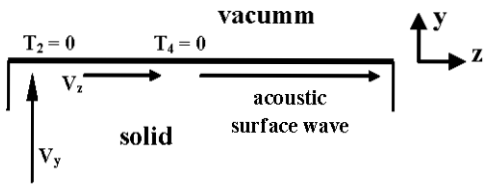

Figure 2.8. Configuration for acoustic surface wave analysis.

The Rayleigh wave dispersion relation can be written as a cubic equation in β^2. Then the dispersion relation can also be written [Lagasse, 1973] in terms of the Rayleigh wave velocity $V_R=\omega/\beta$, in the form of,

$$\left(\frac{V_R}{V_s}\right)^6-\left(\frac{V_R}{V_s}\right)^4+8\left[3-2\left(\frac{V_s}{V_l}\right)^2\right]\left(\frac{V_R}{V_s}\right)^2-16\left(1-\frac{V_s}{V_l}\right)^2=0 \qquad (2.44)$$

where V_s, V_l and V_R are the shear wave velocity, the longitudinal wave velocity and the Rayleigh wave velocity respectively.

This dispersion relation has a real root, the Rayleigh root, which can be stated in the approximate from,

$$\frac{k_s}{\beta} = \frac{V_R}{V_s} \approx \frac{0.87 + 1.12\sigma}{1+\sigma} \tag{2.45}$$

The Rayleigh wave is a non dispersive wave, with V_R varying from $0.87V_s$ to $0.95V_s$ as Poisson's ratio varies from 0 to 0.5. A plot of V_R/V_s as a function of V_s/V_l is compared with approximate solution in Fig. 2.9.

Note that the two other roots of the dispersion relation are neglected. These correspond to waves propagating from y=-∞, which are reflected from the surface.

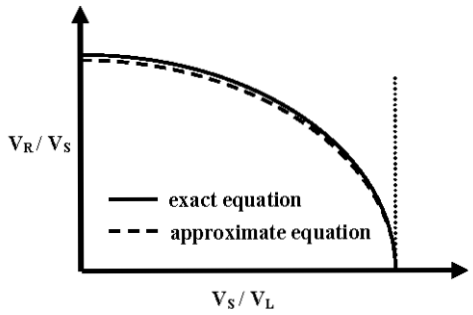

Figure 2.9. Isotropic Rayleigh wave velocity V_R as a function of the bulk shear wave velocity V_s and the bulk longitudinal wave velocity V_L.

The Rayleigh wave velocity V_R is always less than the shear wave velocity V_s or the longitudinal wave velocity V_l. This is necessary for the waves to fall off in amplitude exponentially into the interior of the medium, and hence $k_r > k_l$ and $k_r > k_s$. The shear wave velocity is always less than the longitudinal wave velocity. Consequently, the Rayleigh wave velocity must always be considerably less than the longitudinal wave velocity but only slightly less than the shear wave velocity. This is because the Rayleigh wave velocity is closest to the shear wave velocity, most of the stored energy in the medium is associated with the shear wave components, rather than the longitudinal ones; thus in many respects the Rayleigh wave behaves like a shear wave.

2.8 2D Acoustic Waveguide

Next, we focus on guidance in a 2D waveguide, as our objective is to study the interaction of acoustic wave and optical wave in optical waveguides. Acoustic waves propagate due to the periodic displacement of the molecules inside a waveguide and the wave guidance is more complex and also determined by the material density, elasticity, Young modulus, and Poisson's ratio of the constituent materials. These acoustic modes can be guided, provided at least one of the velocities (the shear or longitudinal velocities) of the cladding exceeds that of the core. The particle displacement can be either in the longitudinal direction or in the transverse plane and propagation of the waves can be classified as longitudinal, torsional, bending or flexural modes.

The 2D acoustic waveguide consisted of core and cladding material, in order to guide the light through the guided core, this material has to have the lower wave velocity. This is analogous to having acoustic index of the clad lower than that of the core. This lower velocity is due to higher acoustic index inside the core hence where the acoustic mode will be guided. In optical waveguide, such as in an optical fibre, core or clad is doped such that refractive index of the core is higher than that of the clad to confine light in the core. The doping material will be considered differently depended on the type of doped, it could cause the acoustic velocity in the core higher or lower. Figure 2.10 illustrates waveguide can be in different shape and form.

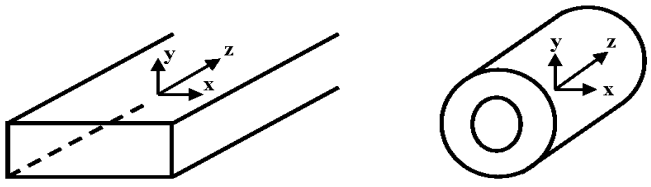

(a) (b)

Figure 2.10. The 2D acoustic waveguide with the propagation direction (a) rectangular and (b) circular.

The propagation direction will be similar to the one directional dimension whereas longitudinal along the *z* axis and the shear wave will be perpendicular to the direction of propagation.

The propagation of an acoustic wave along the *z* direction may be associated with the molecular displacement and for a time harmonic wave, the displacement vectors, $\mathbf{U_i}$, can be written in the following form [Geoffrey, 1973]:

$$\mathbf{U}_\mathbf{i} = u\left(u_x, u_y, ju_z\right)\exp\left\{j\left(\omega t - kz\right)\right\} \tag{2.46}$$

where the angular acoustic frequency, ω, denotes the time dependence; the propagation constant, *k* identifies the axial dependence of the acoustic wave and u_x, u_y and u_z are the particle displacement vectors along the *x*, *y* and *z* directions respectively, seen through the stress-displacement equation (if needed other orthogonal coordinate system can also be considered). For a loss-less system, u_z (the longitudinal component) is 90 degrees out of phase with the two transverse displacements, u_x and u_y, components. In this case, by defining u_z as an imaginary component, as shown in Eq. 2.46, the system equation can be simplified to a real eigenvalue equation. A similar approach has been considered for loss-less optical waveguides to transform an otherwise complex eigenvalue problem to a much simpler real symmetric eigenvalue equation [Rahman, 1984]. The deformation in an acoustically vibrating body can be described by the strain field, *S*, given by:

$$S = \nabla u \tag{2.47}$$

The elastic restoring forces can be defined in terms of the stress field, *T* and the inertial and elastic restoring forces in a freely vibrating medium are related through the translational equation of motion where:

$$\nabla \cdot T = \rho \frac{\partial^2 u}{\partial t^2} \tag{2.48}$$

where ρ is the density of the material.

Hooke's Law states that the strain and stress are linearly proportional to each other and are given by:

$$T_{ij} = c_{ijkl} S_{kl} \;\; ; \;\; i, j, k, l = x, y, z \tag{2.49}$$

Here, the microscopic spring constants, c_{ijkl}, are called the elastic stiffness constants. The compliance and stiffness tensors can be denoted in the matrix form:

$$[T]=[c][S] \tag{2.50}$$

in which c_{ijkl} is the fourth order tensor which obeys the symmetry condition and hence can be represented by using two suffix notations. Furthermore, the elastic stiffness constants are related to the shear and longitudinal velocities.

Classically, in the finite element method for a solid structure, the displacement field, *u*, can be written with the interpolation shape function, [N], and of the vector of the nodal values of the displacement field U where:

$$u=[N]U \tag{2.51}$$

$$u=\begin{Bmatrix}u_x\\u_y\\u_z\end{Bmatrix}=\left[\begin{array}{ccc|ccc|ccc}N_1&0&0&N_2&0&0&N_3&0&0\\0&N_1&0&0&N_2&0&0&N_3&0\\0&0&N_1&0&0&N_2&0&0&N_3\end{array}\right]\begin{Bmatrix}u_x^1\\u_y^1\\u_z^1\\u_x^2\\u_y^2\\u_z^2\\u_x^3\\u_y^3\\u_z^3\end{Bmatrix} \tag{2.52}$$

The general system of equations associated with this problem can be written as detailed derivation will be given in Chapter 3:

$$\left([L]-\omega^2[M]\right)U=F \tag{2.53}$$

where [L] is the stiffness matrix, related to strain energy and [M] is the mass matrix related to the kinetic energy. These matrices are generated for a given acoustic propagation constant, *k*. The column vectors, *F*, contain the nodal values of the applied forces, which in this case are taken to be equal to zero. Solving this generalized eigenvalue equation of the system yields the eigenvalue as ω^2, where ω

is angular frequency and the eigenvector U, the displacement vector. From the given input k and output ω, phase velocity of the acoustic wave, v, can be calculated from:

$$v = \frac{\omega}{k} \tag{2.54}$$

However, if it is required to calculate the propagation constant for a given frequency, a simple iterative approach can be considered. Numerically efficient computer code has been developed by using the sparse matrix solver along with the versatile mesh generation for an arbitrary shaped waveguide and results of an analysis are presented in this thesis for a range of acoustic and optical waveguides.

For two-dimensional analysis, cross-section of the waveguide is meshed by using many first order triangular elements. All three components of the magnetic fields are represented by piece-wise polynomials within the elements. However, this will be discussed more fully in the Chapter 3 for the Finite Element Method.

2.9 Properties of Waves in Waveguide

The acoustic plane waves are of either longitudinal (compressional) or shear nature; in combination, they form specific types of frequency-dependent wave motions, with their own individual propagation properties, for the corresponding structural waveguide. These modes in waveguide have higher order spatial variations which increases with the frequency, and they only exist beyond their cut-off frequencies. The frequency dependence of these wave modes can be calculated with dispersion curves, showing, for example, the phase velocity and group velocity.

In this project the guided wave technique has been used for different optical waveguides. In each of these cases, the wave motion can be categorised into families of wave modes according to their propagation nature. The similar type of waveguides such as fibre, square, rectangular and slot waveguides have given a similar modes result, and thus share the same families of wave modes, whereas the rectangular and

slot waveguide with the unequal width and height have given the non-degenerate modes.

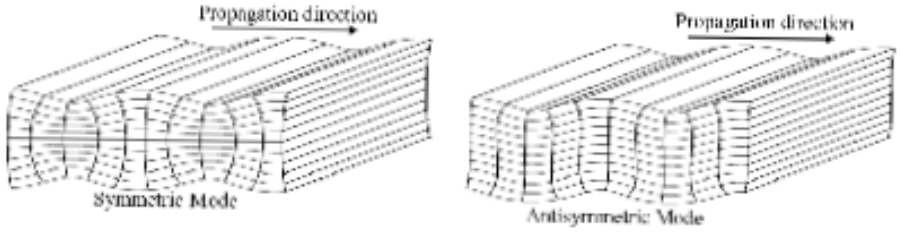

(a) (b)

Figure 2.11. Wave motion of guided waves in plates for (a) symmetric mode and (b) antisymmetric mode [Fong, 2005].

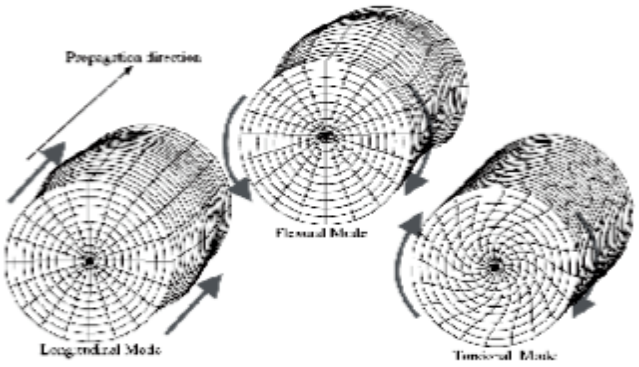

(a) (b) (c)

Figure 2.12. Wave motion of guided waves in bars or pipes for (a) longitudinal mode, (b) flexural mode and (c) torsional mode. [Fong, 2005].

For the wave modes, they are either symmetric or antisymmetric along the mid plane through the thickness as shown in Fig. 2.11, which is the characteristic used to group them into the corresponding families. The wave modes in general are divided into three families, namely the longitudinal modes (a purely axially symmetric wave motion), the flexural modes (an asymmetric mode involving a bending motion along the propagation direction) and the torsional mode (a twisting motion along the centre axis), as shown in Fig. 2.12. The torsional mode can also be of the radial mode (a mode radially outwards or inwards from the center axis), and the torsional-radial (a squeezing motion from the side of the core and spread to the centre).

2.10 Mode Classification

Mode in bulk homogeneous materials are more simple in nature, and these modes can be grouped easily. However, modes in acoustic waveguide, particularly in optical waveguides are more complex. They have all the longitudinal and transverse displacement components. However, initially these are grouped in pure longitudinal modes and pure transverse modes and later on we will discuss about more general hybrid modes. The following sections show the results obtained from the numerical simulations for various waveguides, carried out here.

2.10.1 Pure Longitudinal Mode

In this thesis we have considered *z* as the propagation direction. For the pure longitudinal mode in the general structure of the waveguide only U_z exists, whereas U_x and U_y components are equal to zero. The transverse components can be taken as *r*, and θ axis, to be more suitable to treat circular waveguides. On the other hand, Cartesian *x* and *y* axes can also be considered, which is more suitable for general shapes of acoustic waveguides and adopted here. The acoustic fibre are also similar to the normal waveguide also for the pure longitudinal propagation direction in the *z* direction U_z (r,θ). However, it will be shown later on that often modes are more complex with all the components being present. The fundamental mode, L_{01} has U_z profile Gaussian in shape and is shown in Fig. 2.13.

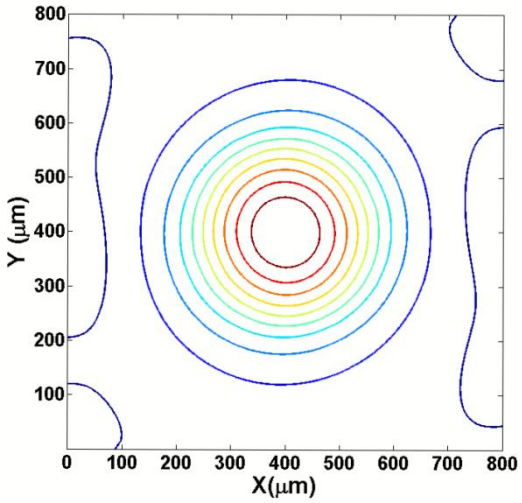

Figure 2.13. U_z profile of the longitudinal L_{01} mode or U_z mode.

The longitudinal L_{01} mode is one of the most important one, which has the dominant U_z mode with the maximum intensity in the *z* direction as shown in Fig. 2.13. Later on in this thesis the studies of acousto-optic interaction by using the acoustic mode of the longitudinal L_{01} mode to calculate the overlap interaction with the optical modes, will also be shown.

For higher order $U_z(r,\theta)$ modes, for the variations in the transverse plane, notation similar as the L_{mn} modes used for optical fibres can be considered. On the other hand for Cartesian coordinate systems, notation used for integrated optics such as H_{mn}^{x} or H_{mn}^{y} can be considered, where H^x or H^y are dominant field component and *m* and *n* are related to their spatial variations.

Beside the fundamental L_{01} mode shown in Fig. 2.13, however, there are also higher order longitudinal mode with more rapid spatial variation, some of them are shown below;

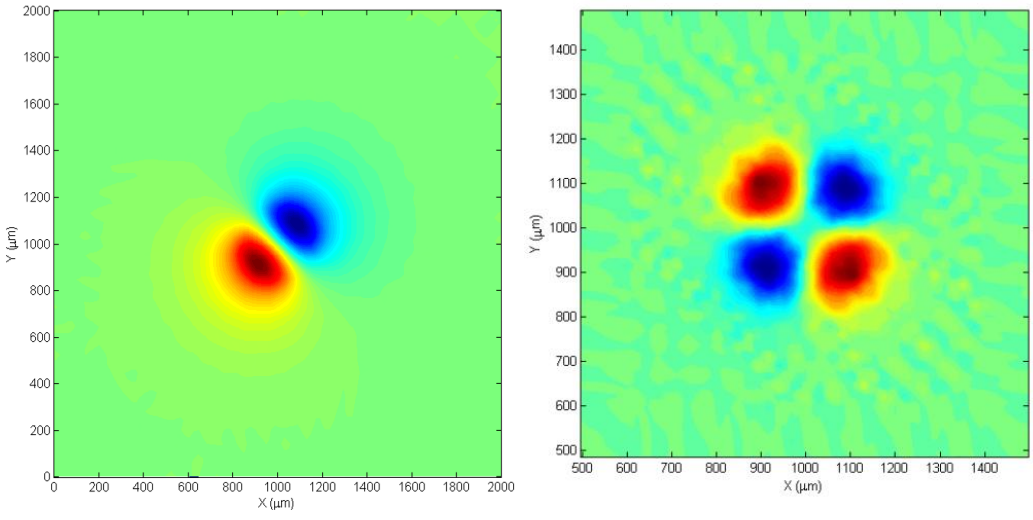

(a) (b)

Figure 2.14. Higher order longitudinal (a) L_{11} (b) L_{21} of the U_z modes.

The higher order U_z variation of the longitudinal mode is shown in Fig. 2.14(a), the longitudinal L_{11} shown the variation of one negative and one positive peak in the U_z direction, whereas the longitudinal L_{21} in Fig. 2.14(b) shown the four spatial variation of two positive and two negative U_z displacement in the opposite direction in the waveguide cross-section.

2.10.2 Pure Transverse Modes

For the transverse wave the displacement is in the transverse plane, perpendicular to *z* direction, and the U_z has zero displacement. There can be many different combinations of U_x and U_y components. In this thesis if $U_x > U_y$ then, this is identified as the U^x mode. In the case when the waveguide has 90 degree rotational symmetry, such as square or circular waveguide, then U^x and U^y modes are degenerate in nature.

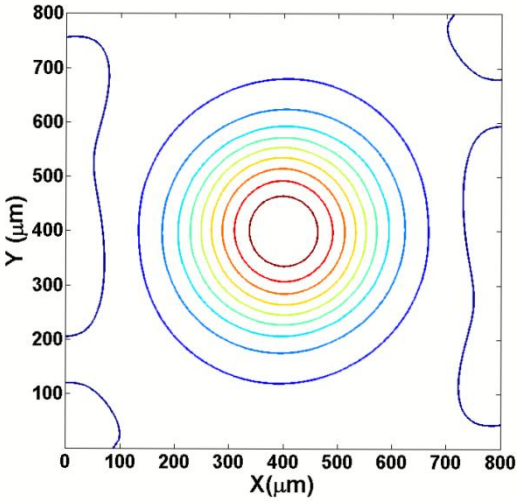

(a)

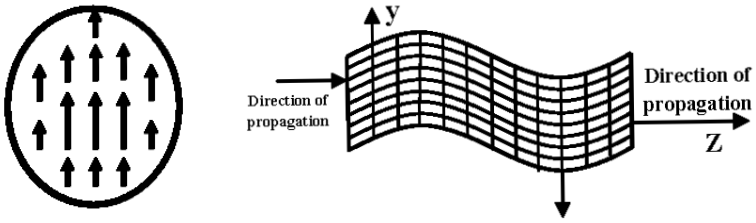

(b) (c)

Figure 2.15. Fundamental shear S_{01} along *y*-axis for the U_y displacement (a) U^y mode (b) U_y displacement (c) propagation in the *y* direction in fibre.

The dominant transverse U^y mode (or can also be called shear S_{01} mode), its U^y displacement profile is shown in Fig. 2.15(a), this shows the U^y contour profile is nearly Guassian in shape. Figure 2.15(b) shows the displacement is only in the *y* directions, so the waveguide bends in the +*y* direction. However, as the time varies, it periodically changes its sign, so the waveguide bends in upper and lower *y*-direction as shown in Fig. 2.15(c) in which volume remains the same.

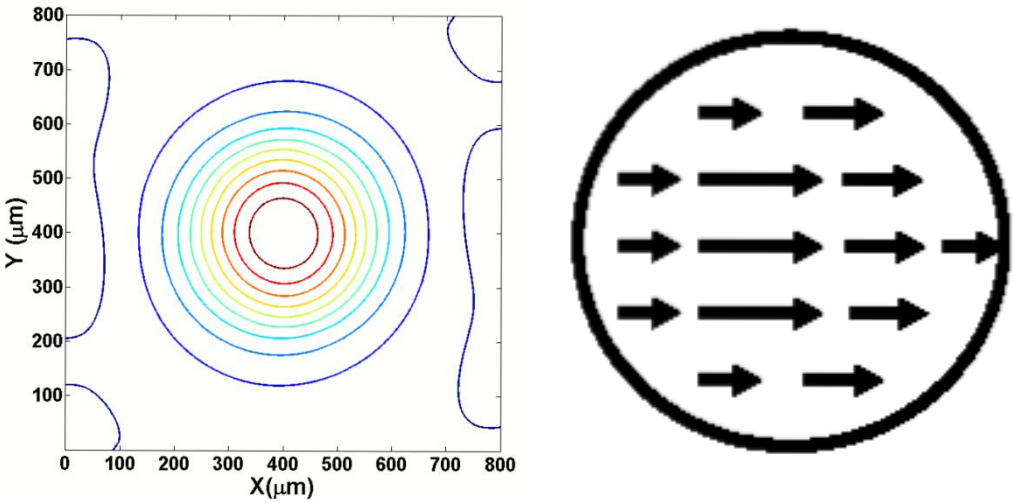

(a) (b)

Figure 2.16. Fundamental shear S_{01} for the U_x displacement (a) U^x mode, (b) the displacement in the *x* direction in fibre along *x*-axis.

On the other hand, a pure U^x mode will have dominant U^x component, and the fundamental mode may have its $U^x(x,y)$ profile similar to the Gaussian profile as shown in Fig. 2.16(a) with the displacement is in the *x* direction as shown in Fig. 2.16(b). However, if a structure has 90^0 rotational symmetry then both $U^x(x,y)$ and $U^y(x,y)$ will be equally present. Their vector combination of S_{01} mode is also shown here which is the summation of the U_x and U_y modes.

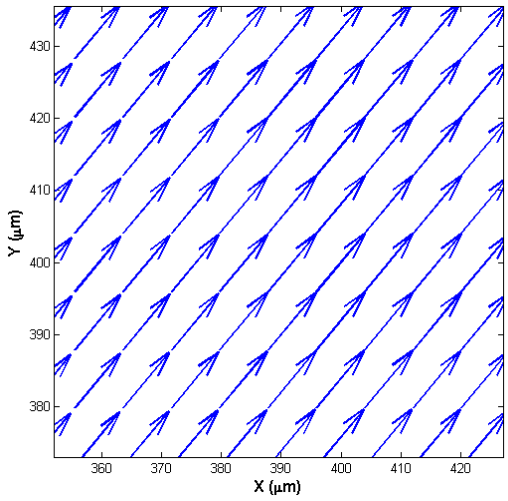

Figure 2.17. Fundamental shear S_{01} for the vector plot $U_t = \vec{U}_x + \vec{U}_y$.

The vector plot of S_{01} is shown in Fig.2.17 which indicates the displacement vector is rotated 45^0 to the axis for the fundamental S_{01} mode. This clearly shows

waveguide bends in the *x-y* plane in the diagonal direction. Similarly these transverse mode can be higher order transverse modes and some spatial variations of the U^x and U^y are shown in Fig. 2.18(a) and (b):

Torsional Mode

For the higher order S_{11} mode, the displacement in the U_x and U_y direction are shown in Fig. 2.18(a) and (b), respectively. The U_x profile shows 2 peaks, one positive and another negative, placed in the upper and lower part of the waveguide as shown in Fig. 2.18(a). On the other hand, U_y profile shows 2 peaks placed on the left and right of the waveguide as shown in Fig. 2.18(b).

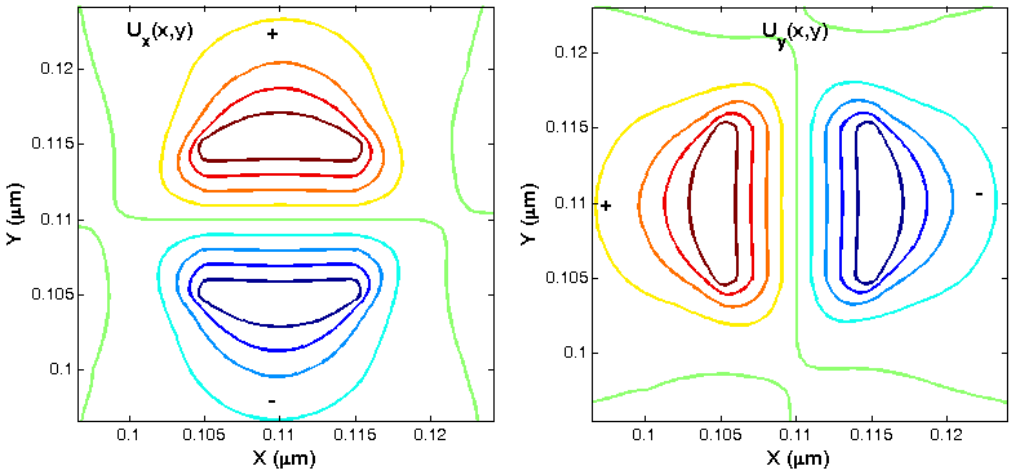

(a) (b)

Figure 2.18. Shear S_{11} for the Torsional mode (T) (a) U_x (b) U_y displacement in fibre.

The combination of these U_x and U_y displacement vectors is shown in Fig. 2.18 for the S_{11} mode which yields the vector plot as anticlockwise rotation as this is shown in Fig. 2.19(a), which can also be identified as a Torsional mode.

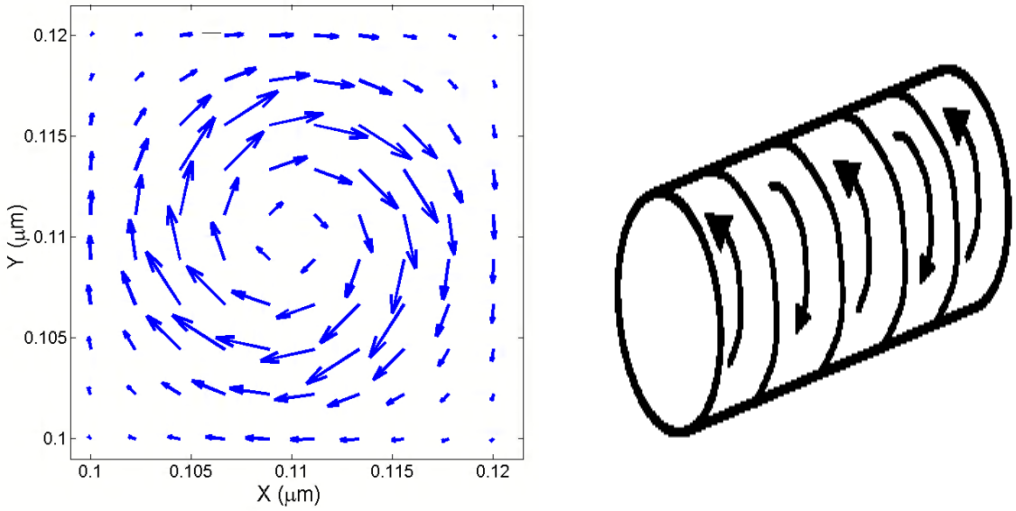

(a) (b)

Figure 2.19. Shear S_{11} for the Torsional mode (T) (a) vector plot $U_t = \vec{U}_x + \vec{U}_y$, (b) the rotation of the twist in the fibre.

In the next half of the period as sign of both U_x and U_y changes, the direction U_t will become clockwise. So along the axial direction is this periodic twists in clockwise and anticlockwise directions as shown in Fig. 2.19(b) where the volume remains the same.

Radial Mode

However, there is a possibility of different displacement vector combination for the S_{11} mode and one such example is shown in Fig. 2.20.

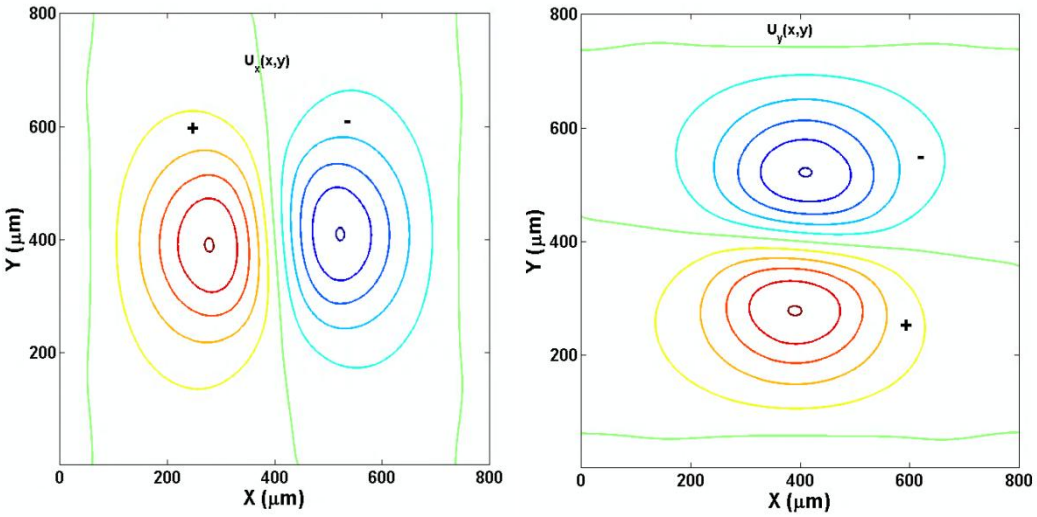

(a) (b)

Figure 2.20. S_{11} for the Radial mode (R) (a) U_x (b) U_y displacement in fibre.

The similarity of displacement between the radial mode and the torsional mode happened for the displacement in the U_x and U_y where in Fig. 2.20 shows the one positive and one negative peak with the different rotation from the *x*-axis. It is shown in Fig. 2.20(a) that the U_x displacement profile shows one positive and one negative on the left and right of the waveguide. However for the U_y displacement, the profile is placed in the upper and lower of the waveguide as shown in Fig. 2.20(b) in which it is rotated by 90 degrees. The combination of U_x and U_y shown in Fig. 2.20 can yields the vector plot of U_t as shown in Fig. 2.21.

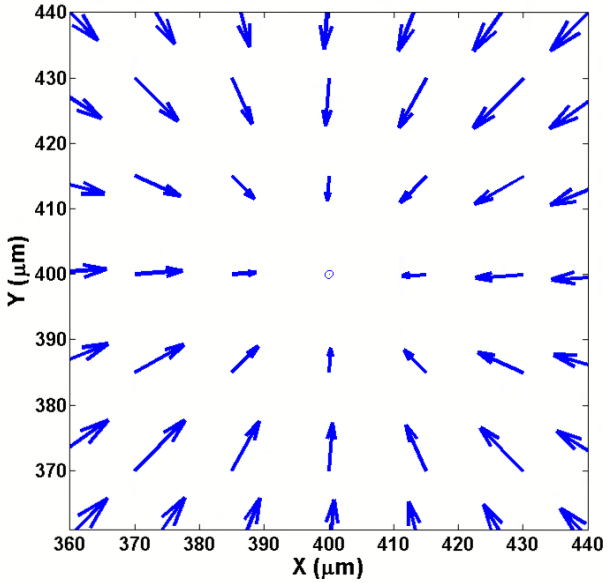

(a)

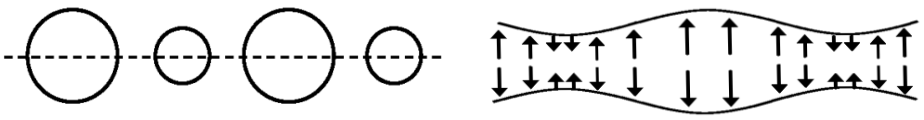

(b) (c)

Figure 2.21. S_{11} Shear mode for the Radial mode (R) of the (a) vector plot $U_t = \vec{U}_x + \vec{U}_y$,
(b) the characteristic of the Radial mode propagation,
(c) the periodic displacement of Radial mode.

Here, particles appear to move outwards, or as if its radius is increased as shown in Fig. 2.21(a). In the next half of the period, U_t will be inward radius and it will reduce therefore its periodic will increase and reduction of its radius, as if periodically 'breathing' in and out are shown in Fig. 2.21(b) and (c) as being called radial mode. In this case as the waveguide cross-sectional area changes, the density along the waveguide is also changed.

Torsional-Radial Mode

Next, another interesting shear mode (S_{11}) is shown, where this yield to a Torsional-Radial mode (TR) as shown in Fig. 2.22.

Figure 2.20 shown the shear mode of S_{11} radial mode (R) (in which, the profiles of U_x and U_y displacement vectors have shown two peaks, one positive and one negative). The displacement vector of the torsional-radial mode (TR) as shown here in Fig. 2.22 (a) that its profile is similar to that in the radial mode of the U_x and U_y profiles shown in Fig. 2.20.

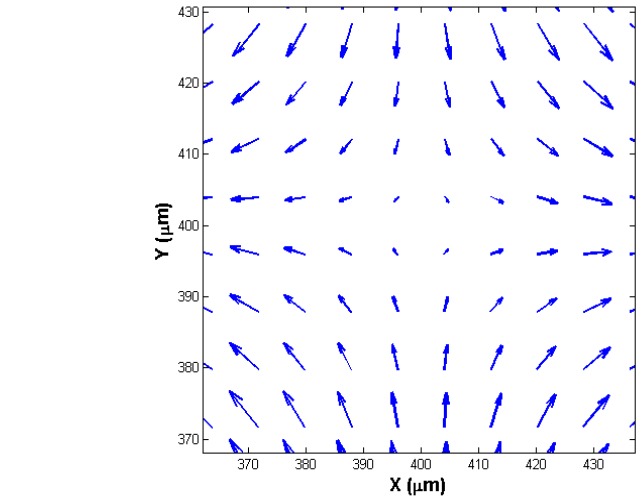

(a)

(b) (c)

Figure 2.22. The transverse S_{11} mode of the Torsional-Radial mode (TR) (a) the vector plot $U_t = \vec{U}_x + \vec{U}_y$ (b) the characteristic of the torsional-radial mode propagation (c) the periodic displacement of the TR mode.

The vector plot U_t in Fig. 2.22(a) is the combination of the U_x and U_y profile modes were similar to that of Radial mode (R) as shown in Fig. 2.20, but 90^o out of phase in time axis (and these are not shown here). It could be noticeable that the vector is spread from the inner of the core and squeeze to the side. In the next half U_t will be reduced from both sides and expand it on the other, so periodically like the

rotation of the wave with its twisted and then squeezed and expanded its shaped every half wavelength of the wave as shown in Fig. 2.22(b) and (c).

Next the higher order mode of S_{21} is shown in Fig. 2.23.

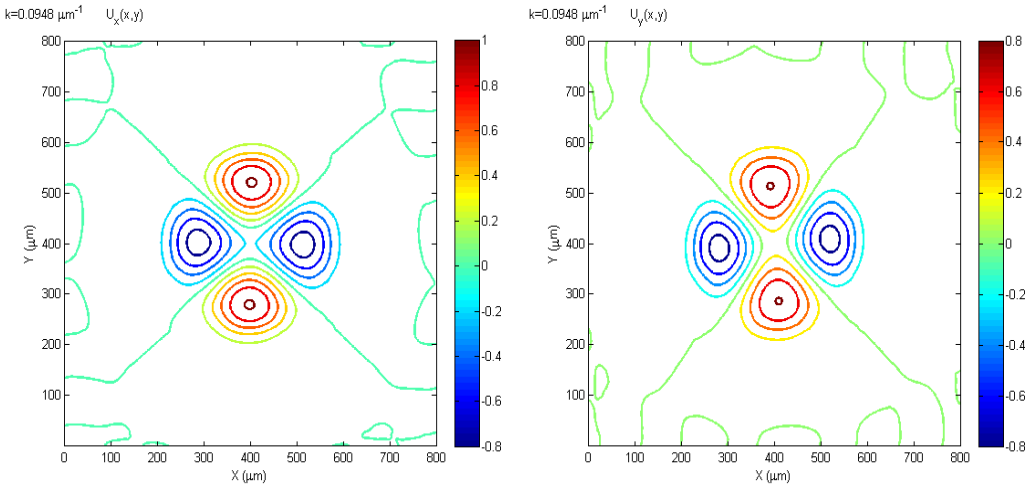

(a) (b)

Figure 2.23. Shear S_{21} for (a) U_x (b) U_y displacement in fibre.

The higher order spatial variation for two positive and two negative displacement vectors facing opposite to each other is shown in Fig. 2.23.

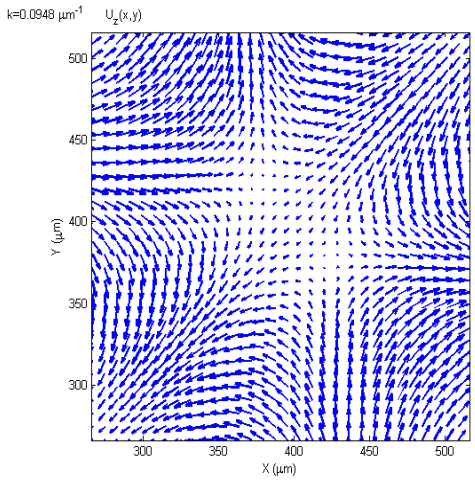

Figure 2.24. The shear S_{21} mode of $U_t = \vec{U}_x + \vec{U}_y$.

The resultant vector displacements is shown in Fig. 2.24, the different angle of the vector plot illustrates that it has been moving from one corner to another corner. Therefore the vector plot is repeatedly expanded and squeezed from one side to another and rotated to all the corners, this happened because from the combination of the U_x and U_y displacement vectors as shown in Fig. 2.23. Figure 2.24 also shows

that at the interface of positive and negative of the displacement field profile, the field is close to each other and is stretching and compressing along the direction of wave propagation.

2.10.3 Quasi-acoustic Modes

It was mentioned that modes in acoustic waveguides with sub-wavelength dimension are neither pure longitudinal nor pure transverse, but actually hybrid modes, where all the U_x, U_y and U_z components are present.

Quasi-Longitudinal

In the case if $U_z >> U_x$, U_y then this can be called quasi-longitudinal modes. In this case it has been observed that non-dominant components have higher order spatial variations than the dominant component.

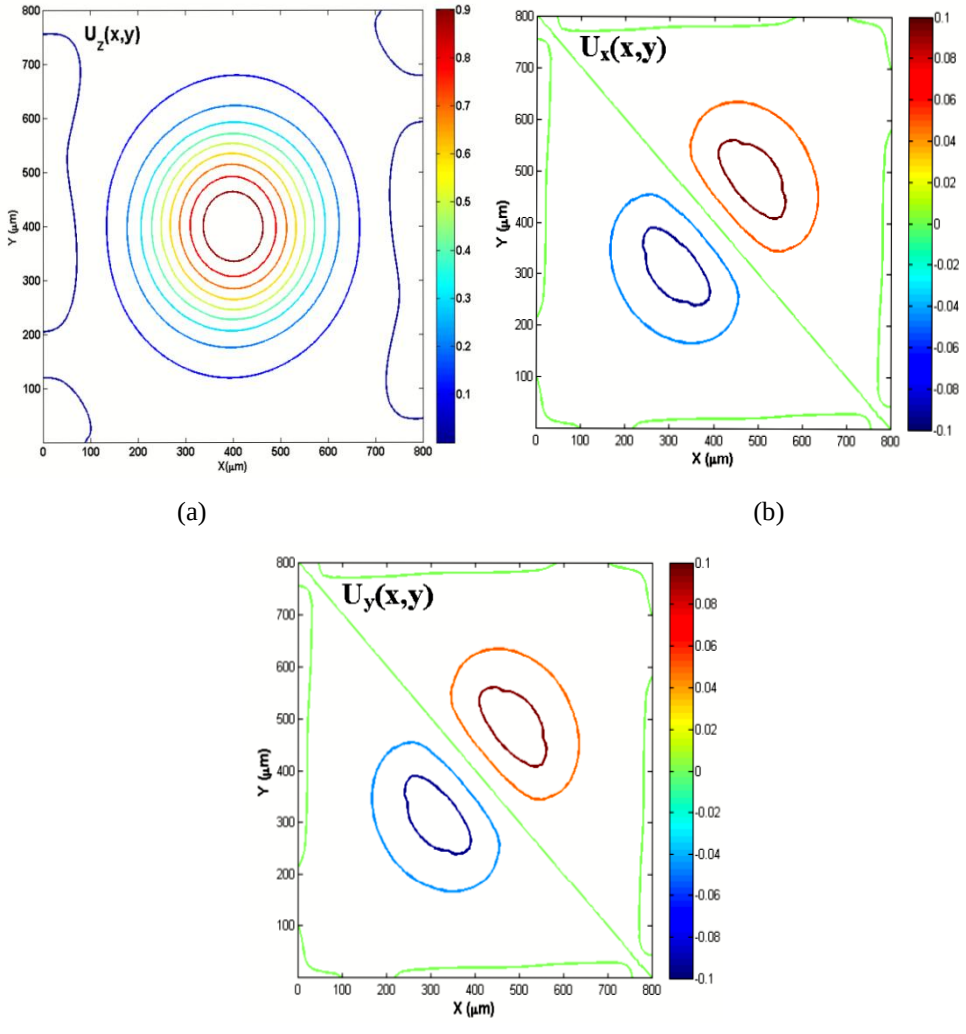

Figure 2.25. Quasi-longitudinal L_{01} mode, for the displacement vectors (a) U_z (b) U_x and (c) U_y.

The degeneration occurred for the longitudinal mode in fibre. Figure 2.25(a) shows the maximum intensity value of the fundamental U_z displacement of the L_{01} mode. It should be noted that non-dominant displacement vectors have higher order spatial variations as shown in Fig 2.25(b) and (c), in which it shows one positive and one negative peak of the U_x and U_y displacement with lower intensity value than in the dominant U_z displacement profile.

Quasi-Transverse

The hybrid transverse modes are shown in Fig. 2.26 in contrast to the quasi-longitudinal mode shown earlier. In this case for the U_y has higher intensity than U_z displacement and we can call this as a quasi-transverse mode.

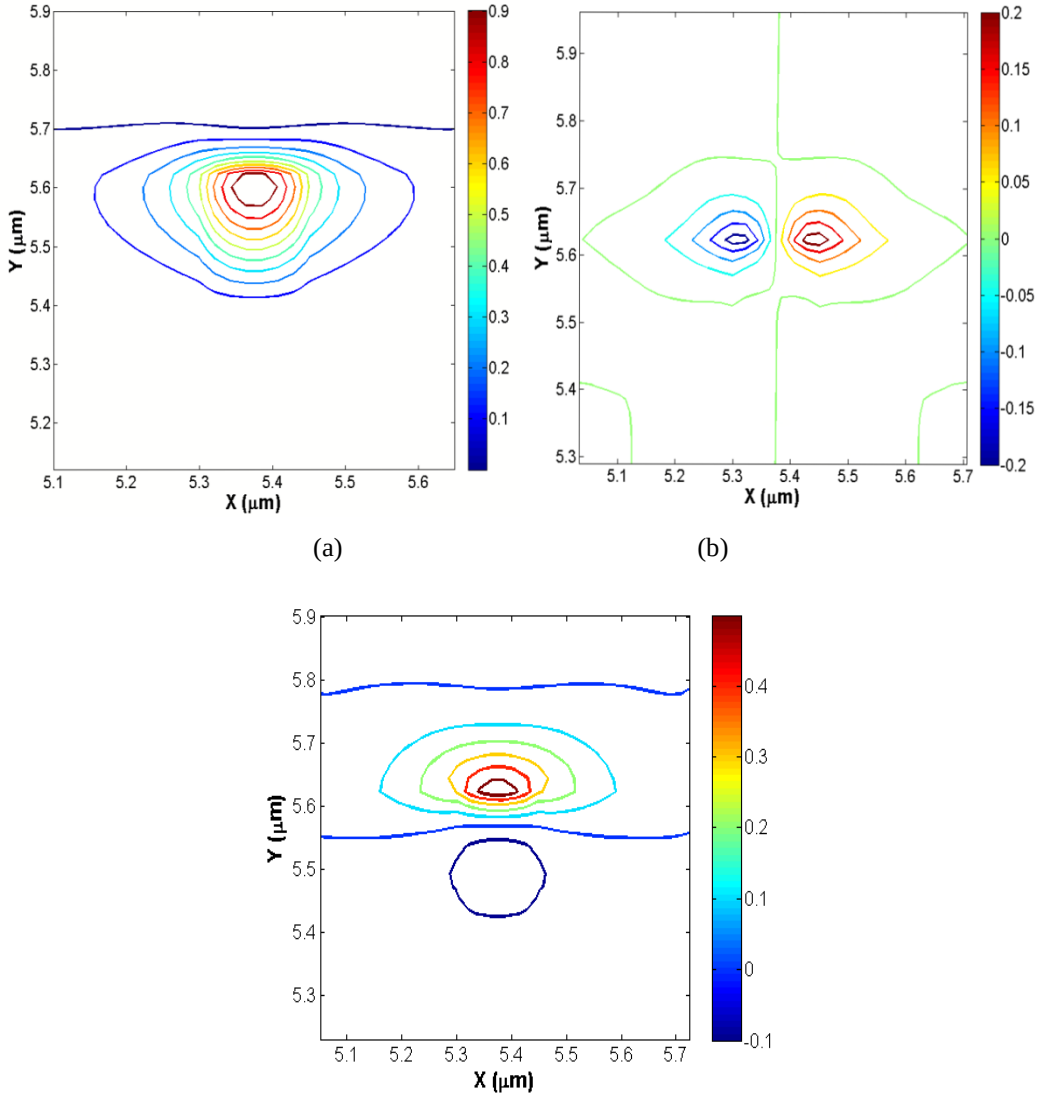

Figure 2.26. Transverse U^y mode (a) U_y (b) U_x (c) U_z displacement in Silica slot waveguide.

The fundamental U^y mode is shown in Fig. 2.26(a) with its maximum intensity and usually it will have the dominant in the U_x or U_y displacement direction. However in these cases shown, the fundamental U^y mode in the slot waveguide were studied, it will be explained in detail later in Chapter 6. The next displacement field profile mode shown one positive and one negative peak in Fig. 2.26(b) of the U_x displacement and Fig. 2.26(c) shown the U_z vector displacement of the non-dominant mode.

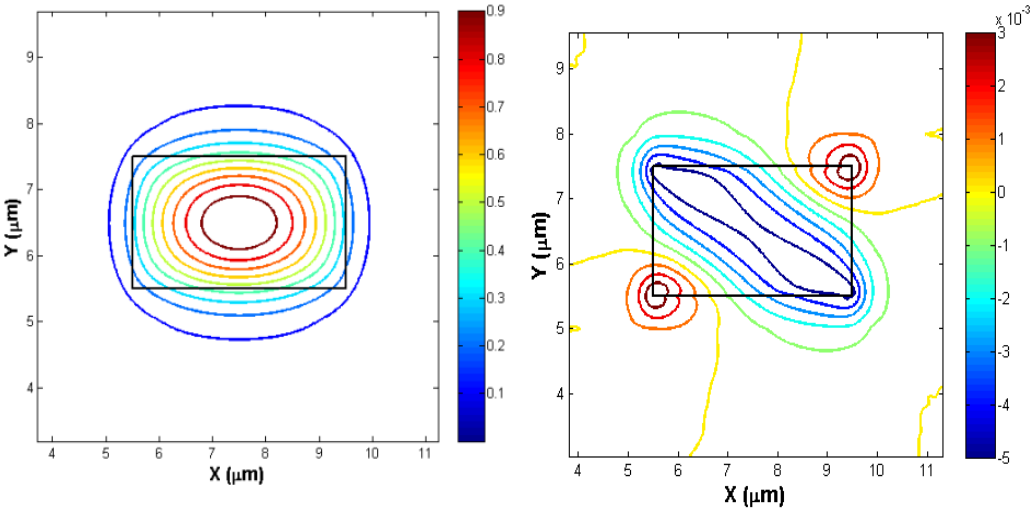

(a) (b)

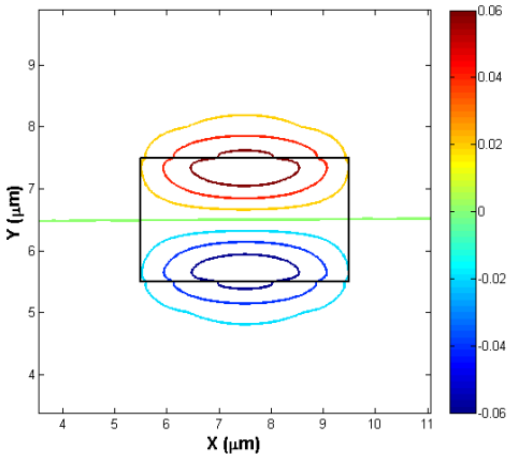

(c)

Figure 2.27. Longitudinal L_{01} for (a) U_y (b) U_x (c) U_z displacement in acoustic Ge-doped Silica core rectangular structure.

Quasi-transverse mode in Fig. 2.27(a) shows the dominant in the U_y displacement for the U^y mode with its highest intensity. The mode are non-degenerate due to the structure of the waveguide has an unequal width and height. In

Fig. 2.27(b) the mode is rotated 45 degree from the the *x*-axis with the minimum field value in the middle and Fig. 2.27(c) shows the one positive and one negative on the upper and lower of the waveguide. The U_x, U_y and U_z displacement vectors shown here are analogous to the H_y fields for optical modes in a rectangular optical waveguides.

2.11 Summary

In this Chapter, we have introduced the stress and strain notation to form the acoustic wave equation for instance the equation of motion and Hooke's law. These are the two basic fundamental acoustic wave equations in this thesis to form the acoustic 2 dimension waveguide. The longitudinal and shear wave velocity formulation have been shown with the relations between the various elastic constants for an isotropic solid. Modes of sound wave propagation has been explained in the last section of this chapter such as longitudinal, transverse, surface wave, plate wave and the 2D acoustic waveguide with mode classification of pure longitudinal, pure transverse and quasi-acoustic modes shown by using the illustration displacement field profiles and their vector plots.

Chapter 3

Finite Element Method

3.1 Introduction

The finite element method (FEM) is a versatile and powerful numerical technique for obtaining approximate solutions to a wide variety of engineering problems. The FEM first introduced in 1960, when it was used by Clough to describe the new technique for plane stress analysis [Clough, 1960]. The applied mathematicians were concerned with boundary value problems of continuum mechanics; in particular, they wanted to find approximate upper and lower bounds for eigenvalues. The effort from these different groups resulted in distinctly different viewpoints. In 1965 the FEM received an even broader interpretation when Zienkiewicz and Cheung [Zienkiewicz, 1977] reported that it is applicable to all field problems that can be cast into a variational form.

The FEM is widely used in different fields of science and technology. Many engineering problems can be defined in terms of governing equations. The finite element represents an approximate numerical solution of a boundary-value problem described by a differential equation. The finite element discretization procedures reduce the problem to one of a finite number of unknowns by dividing the solution region into *elements* and by expressing the unknown field variable in terms of

assumed approximating functions within each element. The approximating functions (sometimes called *interpolation functions*) are defined in terms of the values of the field variables at specified points called *nodes or nodal points*. Nodes usually lie on the element boundaries where adjacent elements are considered to be connected. In addition to boundary nodes, an element may also have a few interior nodes. The nodal value of the field variable and the interpolation functions for the elements completely define the behaviour of the field variable within the elements. For the finite element representation of a problem the nodal values of the field variable become the new unknowns. Once these unknowns are found, the interpolation functions define the field variable throughout the assemblage of elements.

Element properties can also be determined by the more versatile and more advanced *variational approach*. The variational approach relies on the calculus of variations and involves extremizing a *functional*. Knowledge of the variational approach is necessary to work and to extend the FEM to a wide variety of engineering problems.

The solution of a problem by the FEM always follows an orderly step-by-step process. All steps will be listed to summarize how the FEM works and it will be developed in detail later.

1. *Discretization the continuum*. The first step is to divide the continuum or solution region into elements. In this thesis, the 2-dimensional waveguide cross-section domain will be divided into an assemblage of triangular elements.

2. *Select interpolation functions*. The next step is to assign nodes to each element and then choose the type of interpolation function to represent the variation of the field variable over the element. Often, although not always, polynomials are selected as interpolation functions for the field variable because they are easy to integrate and differentiate. The degree of the polynomial chosen depends on the number of nodes assigned to the element, the nature and the unknowns at each node, and certain continuity requirements imposed at the nodes and along the element boundaries.

3. *Find the element properties*. Once the finite element model has been established (that is, once the elements and their interpolation functions have been selected), we are ready to determine the matrix equations expressing the properties of the individual elements. For this task we use the variational approach. that is often the most convenient, but for any application the approach used depends entirely on the nature of the problem.

3.2 Variational Formulations

The formulation of the FEM depends on the variational method whereas the variational approach is more advantageous as especially only one global parameter such as the propagation constant is needed to solve for the final solution. However, in this thesis's work, the variational method has been used for the implementation of acoustic waveguide with the FEM.

Once the formulation is chosen, it can be converted into a standard eigenvalue problem through the application of FEM in the form of:

$$[L]\{u\} = \omega^2 [M]\{u\} \tag{3.1}$$

where [L] is complex symmetric and [M] is real symmetric sparse matrices, and [M] is also the positive definite matrix, and the eigenvalue ω^2. Once ω is obtained for a given acoustic propagation constant, k, then acoustic wave velocity, V can be obtained from:

$$k = \frac{|\omega|}{V} \tag{3.2}$$

Here V is the velocity (m/s) of the acoustic wave. The eigenvector {u} represent the unknown values of the nodal displacement vectors. Equation 3.1 is the canonical form, as it allows for a more efficient solution and useful to solve for, by employing one of the standard subroutines to obtain different eigenvectors and eigenvalues.

3.2.1 Generalization of an Element

The basic idea of the FEM is to divide the solution domain into a finite number of subdomains (*elements*). These elements are connected only at node points in the domain and on the element boundaries. In this way the solution domain is discretized in Fig. 3.1 and represented as a patchwork of elements. Frequently the boundaries of the finite elements are straight lines or planes, so if the solution domain has curved boundaries, these are approximated by a series of straight or flat segments or even by using isoparametric elements.

In the finite element procedure once the element mesh for the solution domain has been discretized, the behaviour of the unknown field variable over each element is approximated by continuous functions expressed in terms of the nodal values of the field variable and sometimes the nodal values of its derivatives up to certain order. The function defined over each finite element are called *interpolation functions*, *shape functions*, or field variable models. The collection of interpolation functions for the whole solution domain provides a piecewise approximation to the field variable.

3.3 Discretization of the Problem

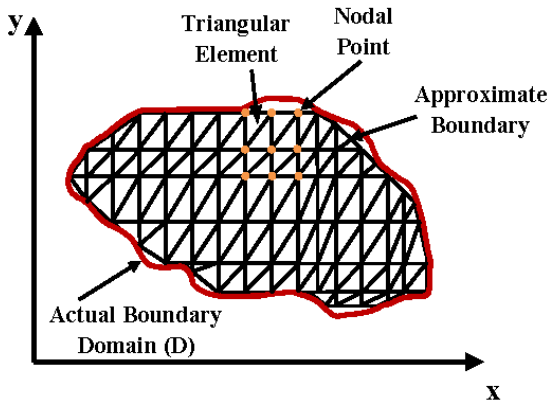

Figure 3.1. Two-dimensional domain divided into triangular elements.

To illustrate the nature of this approximation we consider the representation of a two-dimensional field variable, $\phi(x,y)$. We will show how the nodal values of ϕ can

uniquely and continuously define $\phi(x,y)$ throughout the domain of interest in the *x-y* plane, and we will introduce the notation for an interpolation function.

The domain is shown in Fig. 3.1, and can be discretized it into triangular elements with nodes at the vertices of the triangles. With this type of domain discretization can allow field variable ϕ to vary linearly over each element and the spatial domain, which is illustrated in Fig. 3.2 by green triangle. In Fig. 3.2 it is also shown a plane (with blue triangle) passing through the three nodal values of ϕ to illustrate the spatial variation of the field.

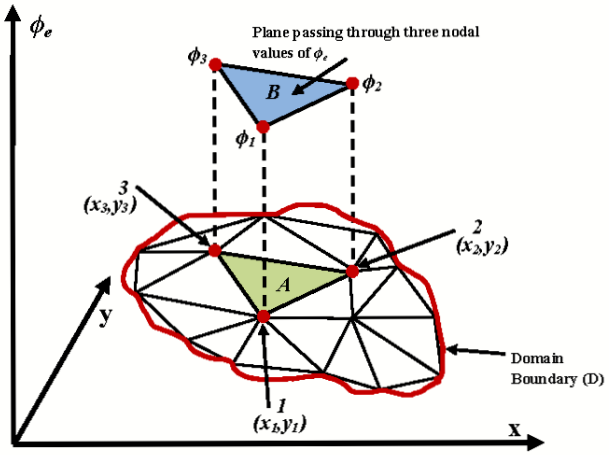

Figure 3.2. Subdivided into piecewise linear solution surface $\phi(x, y)$.

3.4 Interpolation Functions and the Shape Function

The continuous field function $\phi(x, y)$ in the domain problem may be replaced by a set of discrete values $\{\phi_e$, where e=1, 2, 3, ..., m), where m is total number of nodes. The complete representation of the field variable over the whole domain is given by,

$$\phi_e(x,y) = \sum_{i=1}^{m} \phi_e(x,y) = \sum_{i=1}^{3} N_i(x,y) \cdot \phi_i \qquad (3.3)$$

where, ϕ_i are the nodal field values.

In general, the function N_i are called *shape functions or interpolation functions*, and it is the most important in the FEM analysis. (Here the N_i are linear interpolation functions for the three-node triangular element.)

Equation 3.3 can also be expressed in the matrix from,

$$\{\phi_e\} = \begin{Bmatrix} \phi_1 \\ \phi_2 \\ \phi_3 \end{Bmatrix}, \quad [N_i] = [N_1 \quad N_2 \quad N_3] \tag{3.4}$$

$$\phi_e(x,y) = [N_e]\{\phi_e\} = [N_1 \quad N_2 \quad N_3]\begin{Bmatrix} \phi_1 \\ \phi_2 \\ \phi_3 \end{Bmatrix} = N_1\phi_1 + N_2\phi_2 + N_3\phi_3 \tag{3.5}$$

where [N] is the shape function matrix and the column vector $\{\phi_e\}$ is the vector corresponding to the element nodal field values.

The particular interpolation function (linear) and a particular element type (three-node triangle), have been shown in Eqs. 3.3 and 3.5. The complete solution of the nodal value ϕ can represent the solution surface $\phi(x,y)$ as a series of interconnected, triangular elements.

This many-faceted surface has no discontinuities or "gaps" as inter-element boundaries because the values of ϕ at any two nodes defining an element boundary uniquely determine the linear variation of ϕ along the boundary, where the shape functions can be defined as,

$$N_i = f_i(x,y) = f_i(L_1, L_2, L_3) \tag{3.6}$$

in which N_i, i=1,2,3… have to be chosen to give the coordinate and the appropriate nodal field values. The first degree polynomial can be described as $(a+bx+cy)$ and such polynomial is used for the first order triangular elements over each element.

Now we define the simplest representation, the first order polynomial is:

$$N_n = \frac{a_n + b_n x + c_n y}{2\Delta}, \quad n = 1,2,3 \tag{3.7}$$

where, Δ is the area of the triangle.

Having defined the displacement field within an element, for this linear representation these shape functions are simply the area coordinates.

$$N_i = L_i, \quad i = 1,2,3 \tag{3.8}$$

3.5 Triangle Coordinates in Two dimensions

The development of natural coordinates for triangle elements, the goal is to choose coordinates L_1, L_2, and L_3 to describe the location of any point x_p within the element or on its boundary as shown in Fig. 3.3. The original Cartesian coordinates of a point in the element should be linearly related to the new coordinates in which:

$$\begin{aligned} x &= L_1 x_1 + L_2 x_2 + L_3 x_3 \\ y &= L_1 y_1 + L_2 y_2 + L_3 y_3 \end{aligned} \tag{3.9}$$

We imposed a third condition requiring that the weighting functions sum to be unity,

$$L_1 + L_2 + L_3 = 1 \tag{3.10}$$

From Eq. 3.10 it is clear that only two of the natural coordinates can be independent, just as in the original coordinate system, where there are only two independent coordinates.

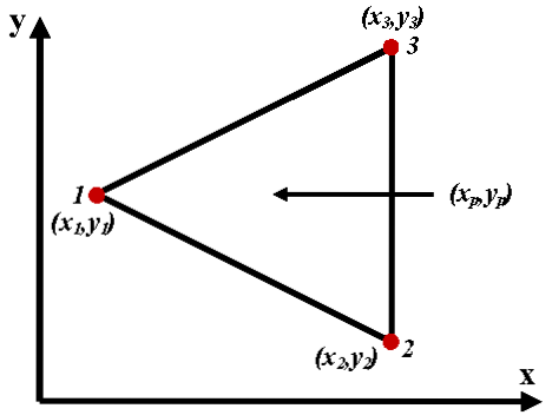

Figure 3.3. Three node triangle element with global coordinates (x_p, y_p) defining some point within the element.

Inversion of Eqs. 3.9 and 3.10 gives the natural coordinates in terms of Cartesian coordinates. Thus,

$$\begin{aligned} L_1 &= \frac{1}{2\Delta}\left(a_1 + b_1 x + c_1 y\right) \\ L_2 &= \frac{1}{2\Delta}\left(a_2 + b_2 x + c_2 y\right) \\ L_3 &= \frac{1}{2\Delta}\left(a_3 + b_3 x + c_3 y\right) \end{aligned} \tag{3.11}$$

where,

$$2\Delta = \begin{vmatrix} 1 & x_1 & y_1 \\ 1 & x_2 & y_2 \\ 1 & x_3 & y_3 \end{vmatrix} = 2(\textit{area of triangle 1 - 2 - 3}) \tag{3.12}$$

$$\begin{aligned} a_1 &= x_2 y_3 - x_3 y_2, \quad b_1 = y_2 - y_3, \quad c_1 = x_3 - x_2 \\ a_2 &= x_3 y_1 - x_1 y_3, \quad b_2 = y_3 - y_1, \quad c_2 = x_1 - x_3 \\ a_3 &= x_1 y_2 - x_2 y_1, \quad b_3 = y_1 - y_2, \quad c_3 = x_2 - x_1 \end{aligned} \tag{3.13}$$

From the linear interpolation function over triangle, that is $N_i = L_i$ for the first order linear triangle. Figure 3.4 shows the natural coordinate, often called *area coordinates*, are related to the area.

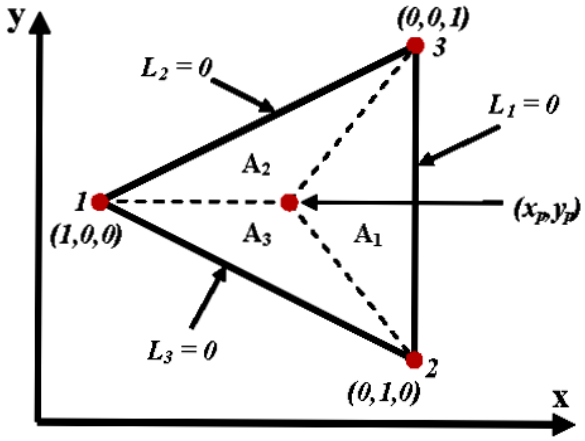

Figure 3.4. Area coordinates for triangle.

As shown in Fig. 3.4, when the point (x_p, y_p) is located on the boundary of the element, one of the area segments vanishes and hence the appropriate area coordinate

along that boundary is identically zero. As an example, if x_p and y_p is on side 1-3, then:

$$L_2 = \frac{A_2}{\Delta} = 0 \qquad \text{since } A_2 = 0$$

Interpreted the field variable ϕ as a function L_1, L_2, and L_3 instead of x, y, differentiation becomes:

$$\begin{aligned} \frac{\partial \phi}{\partial x} &= \frac{\partial \phi}{\partial L_1}\frac{\partial L_1}{\partial x} + \frac{\partial \phi}{\partial L_2}\frac{\partial L_2}{\partial x} + \frac{\partial \phi}{\partial L_3}\frac{\partial L_3}{\partial x} \\ \frac{\partial \phi}{\partial y} &= \frac{\partial \phi}{\partial L_1}\frac{\partial L_1}{\partial y} + \frac{\partial \phi}{\partial L_2}\frac{\partial L_2}{\partial y} + \frac{\partial \phi}{\partial L_3}\frac{\partial L_3}{\partial y} \end{aligned} \tag{3.14}$$

where,

$$\frac{\partial L_i}{\partial x} = \frac{b_i}{2\Delta}, \quad \frac{\partial L_i}{\partial y} = \frac{c_i}{2\Delta}, \quad i = 1,2,3 \tag{3.15}$$

The formula for integrating area coordinates over the area of a triangle element is defined as,

$$\int_{A^e} L_1^{\alpha} L_2^{\beta} L_3^{\gamma} dA^e = \frac{\alpha!\beta!\gamma!}{(\alpha+\beta+\gamma+2)!} 2\Delta \tag{3.16}$$

where ! is the factorial.

3.6 Implementation of the Acoustic Waveguide Code with FEM

The theoretical formulation for a waveguide with the incorporation of the FEM is presented in this Chapter. The problem concerned is reduced to a two-dimensional problem, where only the cross-section of the guide is meshed by using finite elements. After the validation of the method for simple cases, a steel rod is studied, and the finite element results are then compared to the numerical ones [Hennion,

1996] to demonstrate the accuracy of the model. Further, the method is extended to study a circular waveguide and slot optical waveguide.

The mathematical model for the case of a waveguide is presented here, the waveguide which is uniform and infinite in the *z*-direction, is set in the *xy* plane. An acoustic wave characterized by its propagation constant *k*, is propagating along the waveguide. The displacement field vector *u* is written as:

$$u = \begin{pmatrix} u_x(x,y) \\ u_y(x,y) \\ u_z(x,y) \end{pmatrix} e^{jkz} \tag{3.17}$$

where the time dependence $e^{-j\omega t}$ is implicit in the equation.

The problem can be solved by using FEM triangular elements and by applying a specific phase relation between the nodes of end surfaces. The acoustic wave varied in the *z*-direction but it is possible to solve the problem with the help of a bi-dimensional mesh and to reconstitute the whole solution. A unit length of the waveguide is meshed with the help of the finite element method connected by nodes. The general system of equations associated to this problem is in Eq. 3.1: $[L]\{u\} = \omega^2[M]\{u\}$ where [L] is a stiffness matrix related to the strain energy, where as [M] is the mass matrix.

In this thesis, the nodal values of the applied external forces are equal to zero (however, if needed when an external force is applied on an acoustic waveguide, this can be considered). By modal analysis, the solution of the system gives ω, the angular frequency, and U, the vector of the nodal values of the displacement field.

3.6.1 Finite Element Formulation

Classically, in the FEM for solid structure, the displacement field vector *u* can be written in the help of the interpolation function [*N*] and of the vector of the nodal values of the displacement field U where:

$$\{u\} = [N]\{u\}$$

$$\{u\} = \begin{Bmatrix} u_x \\ u_y \\ u_z \end{Bmatrix} = \left[\begin{array}{ccc|ccc|ccc} N_1 & 0 & 0 & N_2 & 0 & 0 & N_3 & 0 & 0 \\ 0 & N_1 & 0 & 0 & N_2 & 0 & 0 & N_3 & 0 \\ 0 & 0 & N_1 & 0 & 0 & N_2 & 0 & 0 & N_3 \end{array}\right] \begin{bmatrix} u_x^1 \\ u_y^1 \\ u_z^1 \\ u_x^2 \\ u_y^2 \\ u_z^2 \\ u_x^3 \\ u_y^3 \\ u_z^3 \end{bmatrix} \tag{3.18}$$

It should be noted nodes on the *x*-*y* plane can have displacement along *x*, *y* and *z* directions given by u_x, u_y and u_z and their values at 3 nodes of a triangle is given by the column vector of Eq. 3.18.

3.6.2 Generalised Coordinate and the Order of the Polynomials

The order of the polynomial use to represent the field variable within an element depends on the number of degrees of freedom we assign to the element. The number of coefficients in the polynomial should equal to the number of nodal variables available to evaluate these coefficients. The linear polynomial series given in Eq. 3.9 with the coordinate in two dimensions and the natural coordinates L_1, L_2, and L_3, which are the interpolation functions for linear interpolation over triangle (that is $N_i = L_i$ for the linear first order triangle) will be used in here.

The FEM equations for a continuum problem can be derived from variational principles to the formula as shown in Eq. 3.16.

In the case of an infinite uniform waveguide, the three components of the displacement field u of Eq. 3.17, in the x, y and z directions are expressed with the help of the interpolation functions as:

$$u = \begin{pmatrix} \left[N(x,y)\right] e^{jkz} U_x \\ \left[N(x,y)\right] e^{jkz} U_y \\ j\left[N(x,y)\right] e^{jkz} U_z \end{pmatrix} \tag{3.19}$$

where U_x, U_y, and U_z are the vectors of the nodal values of the displacement field in the x, y and z directions, respectively. Introducing the unit of imaginary number j in the expression of U_z allows one to obtain real symmetric matrices for the final system of equations.

Hooke's Law states that the strain is linearly proportional to the stress. The mathematical form of the component of stress (elastic restoring force) as a general linear function of all the strain component is:

$$T_{ij} = c_{ijkl} S_{kl} \quad (i, j, k, l = x, y, z) \tag{3.20}$$

where T is the stress matrix, S is the strain matrix and c_{ijkl} are called elastic stiffness constants (see Chapter 2 for the acoustic theory). The transformation regarding the stress and the strain field:

$$\nabla \cdot T = \nabla (c \cdot S) \tag{3.21}$$

For the stiffness matrix that needs the strain tensor, it is expressed as:

$$\begin{bmatrix} S_1 \\ S_2 \\ S_3 \\ S_4 \\ S_5 \\ S_6 \end{bmatrix} = \begin{bmatrix} \frac{\partial u_x}{\partial x} \\ \frac{\partial u_y}{\partial y} \\ \frac{\partial u_z}{\partial z} \\ \frac{\partial u_y}{\partial z} + \frac{\partial u_z}{\partial z} \\ \frac{\partial u_x}{\partial z} + \frac{\partial u_z}{\partial x} \\ \frac{\partial u_x}{\partial y} + \frac{\partial u_y}{\partial x} \end{bmatrix} = \begin{bmatrix} \frac{\partial}{\partial x} & 0 & 0 \\ 0 & \frac{\partial}{\partial y} & 0 \\ 0 & 0 & \frac{\partial}{\partial z} \\ 0 & \frac{\partial}{\partial z} & \frac{\partial}{\partial y} \\ \frac{\partial}{\partial z} & 0 & \frac{\partial}{\partial x} \\ \frac{\partial}{\partial y} & \frac{\partial}{\partial x} & 0 \end{bmatrix} \begin{bmatrix} u_x \\ u_y \\ u_z \end{bmatrix} \tag{3.22}$$

$$S_I = \nabla_{Ij}\, u_j \tag{3.23}$$

From the strain-displacement relation, $S = \nabla_S\, u$, in which the subscript *s* (for symmetric) is the gradient symbol; the symmetric gradient operator in Eq. 3.23 will be $\boldsymbol{\nabla}_{\mathrm{Ij}} = \boldsymbol{\nabla}_{\mathrm{S}}$ thus has a matrix representation.

$$\nabla_s \Rightarrow \nabla_{Ij} = \begin{bmatrix} \frac{\partial}{\partial x} & 0 & 0 \\ 0 & \frac{\partial}{\partial y} & 0 \\ 0 & 0 & \frac{\partial}{\partial z} \\ 0 & \frac{\partial}{\partial z} & \frac{\partial}{\partial y} \\ \frac{\partial}{\partial z} & 0 & \frac{\partial}{\partial x} \\ \frac{\partial}{\partial y} & \frac{\partial}{\partial x} & 0 \end{bmatrix} \tag{3.24}$$

The elastic restoring forces were defined in terms of the *stress field* $T(u_j,t)$. The relation between the inertial and elastic restoring forces (or stresses) are related through the translational equation of motion.

The translational equation of motion for a freely vibrating medium is:

$$\nabla \cdot T = \rho \frac{\partial^2 u}{\partial t^2} - F \tag{3.25}$$

and when the applied force, *F* is zero, reduces to:

$$\nabla \cdot T = \rho \frac{\partial^2 u}{\partial t^2} \tag{3.26}$$

The stress matrix is symmetric in this work, the abbreviated subscript notation introduced in strain component in Eq. 3.22 can also be used to describe the following:

$$T = \begin{bmatrix} T_{xx} & T_{xy} & T_{xz} \\ T_{yx} & T_{yy} & T_{yz} \\ T_{zx} & T_{zy} & T_{zz} \end{bmatrix} = \begin{bmatrix} T_1 & T_6 & T_5 \\ T_6 & T_2 & T_4 \\ T_5 & T_4 & T_3 \end{bmatrix} = \begin{bmatrix} T_1 \\ T_2 \\ T_3 \\ T_4 \\ T_5 \\ T_6 \end{bmatrix} \tag{3.27}$$

The spatial variance of T is given by the divergence of T for the translational equation of motion in Eq. 3.27 and can be written in terms of abbreviated subscripts as:

$$\nabla \cdot T = \begin{bmatrix} \frac{\partial}{\partial x} T_{xx} + \frac{\partial}{\partial y} T_{xy} + \frac{\partial}{\partial z} T_{xz} \\ \frac{\partial}{\partial x} T_{yx} + \frac{\partial}{\partial y} T_{yy} + \frac{\partial}{\partial z} T_{yz} \\ \frac{\partial}{\partial x} T_{zx} + \frac{\partial}{\partial y} T_{zy} + \frac{\partial}{\partial z} T_{zz} \end{bmatrix} \tag{3.28}$$

and this may be expressed as a matrix operator multiplying the stress column matrix:

$$\nabla \cdot T = \begin{bmatrix} \frac{\partial}{\partial x} & 0 & 0 & 0 & \frac{\partial}{\partial z} & \frac{\partial}{\partial y} \\ 0 & \frac{\partial}{\partial y} & 0 & \frac{\partial}{\partial z} & 0 & \frac{\partial}{\partial x} \\ 0 & 0 & \frac{\partial}{\partial z} & \frac{\partial}{\partial y} & \frac{\partial}{\partial x} & 0 \end{bmatrix} \begin{bmatrix} T_1 \\ T_2 \\ T_3 \\ T_4 \\ T_5 \\ T_6 \end{bmatrix} \tag{3.29}$$

3.6.3 Effect of Crystal Symmetry on Elastic Constants

The effect of crystal symmetry on elastic constants, valid for all solids [Royer, 2000], can be written in the matrix notation as $c_{\alpha\beta} = c_{\beta\alpha}$. The 6x6 matrix of the coefficient $c_{\alpha\beta}$ is therefore symmetric about its main diagonal, so that:

$$\left(c_{\alpha\beta}\right) = \begin{bmatrix} c_{11} & c_{12} & c_{13} & c_{14} & c_{15} & c_{16} \\ c_{12} & c_{22} & c_{23} & c_{23} & c_{25} & c_{26} \\ c_{13} & c_{23} & c_{33} & c_{34} & c_{35} & c_{36} \\ c_{14} & c_{24} & c_{34} & c_{44} & c_{45} & c_{46} \\ c_{15} & c_{25} & c_{35} & c_{45} & c_{55} & c_{56} \\ c_{16} & c_{26} & c_{36} & c_{46} & c_{56} & c_{66} \end{bmatrix} \tag{3.30}$$

The crystals system property reduces the number of independent components to 21. From the system; a centre of symmetry imposes no restriction, all these crystal systems have 21 independent elastic constants. First we consider the properties of an isotropic solid, which has the highest symmetry possible.

The properties of an isotropic solid are specified by *two independent constants*, such as the Lame constant λ and μ used here. Assigning values 1 to 6 to the pairs (*ij*) and (*kl*) gives:

$$\begin{aligned} c_{11} &= c_{22} = c_{33} = \lambda + 2\mu \\ c_{12} &= c_{23} = c_{13} = \lambda \\ c_{44} &= c_{55} = c_{66} = \frac{c_{11} - c_{12}}{2} = \mu \end{aligned} \tag{3.31}$$

The other twelve of moduli c_{ijkl} are zero since they have an odd number of distinct indices, for example $c_{25} = c_{2213}$. Expressing all the components in terms of c_{11} and c_{12} the matrix $c_{\alpha\beta}$ takes the following form:

$$\left(c_{\alpha\beta}\right) = \begin{bmatrix} c_{11} & c_{12} & c_{13} & 0 & 0 & 0 \\ c_{12} & c_{22} & c_{23} & 0 & 0 & 0 \\ c_{13} & c_{23} & c_{33} & 0 & 0 & 0 \\ 0 & 0 & 0 & c_{44} & 0 & 0 \\ 0 & 0 & 0 & 0 & c_{55} & 0 \\ 0 & 0 & 0 & 0 & 0 & c_{66} \end{bmatrix} \quad isotropic,\ c_{66} = \frac{\left(c_{11} - c_{12}\right)}{2} \tag{3.32}$$

and in the FEM, it is related to the vector of the nodal values of the displacement field *U* by the [**B**] matrix:

$$S = \left[\mathbf{B}\right]U \tag{3.33}$$

The expression for *u* in the Eq. 3.19 is incorporated in Eq. 3.22 and the strain vector *S* of the acoustic strain-displacement, in this thesis will be represented as:

$$S = \left[B_u\right]\{u\} \tag{3.34}$$

It could be noted that $[B_u] \equiv \nabla_s$ in this thesis and we can write it in the form:

$$[\mathcal{B}] = \begin{bmatrix} \frac{\partial}{\partial x} & 0 & 0 \\ 0 & \frac{\partial}{\partial y} & 0 \\ 0 & 0 & \frac{\partial}{\partial z} \\ 0 & \frac{\partial}{\partial z} & \frac{\partial}{\partial y} \\ \frac{\partial}{\partial z} & 0 & \frac{\partial}{\partial x} \\ \frac{\partial}{\partial y} & \frac{\partial}{\partial x} & 0 \end{bmatrix} \quad \textit{and} \quad [\mathcal{B}]^T = \begin{bmatrix} \frac{\partial}{\partial x} & 0 & 0 & 0 & \frac{\partial}{\partial z} & \frac{\partial}{\partial y} \\ 0 & \frac{\partial}{\partial y} & 0 & \frac{\partial}{\partial z} & 0 & \frac{\partial}{\partial x} \\ 0 & 0 & \frac{\partial}{\partial z} & \frac{\partial}{\partial y} & \frac{\partial}{\partial x} & 0 \end{bmatrix}$$

$$[\mathcal{B}]^T [c][\mathcal{B}]\{u\} = \rho (j\omega)^2 u \tag{3.35}$$

Now equation is expressed in the terms of {u} displacement field for the corresponding strain displacement.

$$\{u\}^T [\mathcal{B}]^T [c][\mathcal{B}]\{u\} = -\{u\}^T \rho\omega^2 \{u\} \tag{3.36}$$

Using the FEM procedure with the acoustic translation equation of motion in Eq. 3.28 and incorporate with Hooke's law in Eq. 3.21 of the stress and strain relation will give:

$$\{u\}^T \iint [N]^T [\mathcal{B}]^T [c][\mathcal{B}][N] dV \{u\} = -\rho\omega^2 \{u\}^T \iint [N]^T [N] dV \{u\} \tag{3.37}$$

or

$$\{u\}^T \iint [N]^T [\mathcal{B}]^T [c][\mathcal{B}][N] dV \{u\} + \rho\omega^2 \{u\}^T \iint [N]^T [N] dV \{u\} = 0 \tag{3.38}$$

The [$\mathcal{B}$] matrix, appears in the expression for the stiffness matrix [L]:

$$[L] = \iint [N]^T [\mathcal{B}]^T [c][\mathcal{B}][N] dV \tag{3.39}$$

Here [c] is the matrix of the elastic stiffness constant, *dV* is the volume of solid structure, *T* denotes transposition and where [L] is the stiffness matrix, related to strain energy and [M] is the mass matrix related to the kinetic energy. These matrices are generated for a given propagation constant, *k*. By minimising the energy

functional given in 3.38 with respect to all the nodal displacement variables {u}, it will reduce to a generalized eigenvalue equation of the system yields the eigenvalue as ω^2, where ω is the angular frequency and the eigenvector {u}, the displacement vector.

The mass matrix is classically written as:

$$[M] = \rho\omega^2 \iint [N]^T [N] dV \tag{3.40}$$

where ρ is the density of the solid with the symmetry condition of the crystal properties, the mass matrix becomes:

$$[M] = \rho\omega^2 \iint_V N(x,y)^T \, N(x,y) \begin{pmatrix} 1 & 0 & 0 \\ 0 & 1 & 0 \\ 0 & 0 & 1 \end{pmatrix} dV \tag{3.41}$$

The general system of equations associated with this problem in Eq. 3.1 can be written as:

$$[L]U - \omega^2 [M]U = F \tag{3.42}$$

where [L] is the stiffness matrix, related to strain energy and [M] is the mass matrix related to the kinetic energy. These matrices are generated for a given acoustic propagation constant, *k*. The column vectors, *F*, contain the nodal values of the applied forces, which in this case are taken to be equal to zero. Solving this generalized eigenvalue equation of the system yields the eigenvalue as ω^2, where ω is the angular frequency and the eigenvector U as the displacement vector.

From the given input *k* and output ω, phase velocity of the acoustic wave, *v*, can be calculated from Eq. 3.2. However, if it is required to calculate the propagation constant for a given frequency, a simple iterative approach can be considered.

Numerically efficient computer code has been developed by using the sparse matrix solver along with the versatile mesh generation for an arbitrary shaped

waveguide and results of an analysis are presented here for a range of acoustic and optical waveguides.

For the analysis of light guidance a full-vectorial FEM is used. The FEM, based on the vector-**H**-Field formulation, has been established as one of the most accurate and also numerically efficient approaches to obtaining the modal field profiles and propagation constants of the fundamental and higher-order quasi-TE and TM modes. The full-vectorial formulation is based on the minimization of the full **H**-field energy functional,

$$\omega^2 = \frac{\int\left[(\nabla\times \mathrm{H})^* \cdot \varepsilon^{-1}(\nabla\times \mathrm{H}) + p(\nabla\cdot \mathrm{H})^*(\nabla\cdot \mathrm{H})\right] dxdy}{\int \mathrm{H}^* \cdot \mu \mathrm{H}\, dxdy} \tag{3.43}$$

where **H** is the full vectorial magnetic field, * denotes a complex conjugate and transpose, ω^2 is the eigenvalue where ω is the optical angular frequency of the wave and ε and μ are the permittivity and permeability, respectively. In here, two-dimensional cross-section of the waveguide is meshed by using many first order triangular elements. All three components of the magnetic fields are represented by piece-wise polynomials within the elements.

3.7 Benchmarking - Steel Waveguide

Table 3.1. Material properties of steel and xenon gas used in this work [Warlimont, 2005].

Material	Velocity (m/s)		Density (kg/m^3)	Elastic Stiffness (GPa)		
	V_L	V_S	ρ	c_{11}	c_{12}	c_{44}
Steel	5797.4978	3098.8923	7850	263.8462	113.0769	75.3846
Xenon	22303.7	15472.2	5.8971	2.93	1.89	1.41

Initially to benchmark the finite element code developed, a steel waveguide of square cross-section (1cm×1cm) has been considered (originally the waveguide is in the vacuum form [Hennion, 1996], however, Xenon is considered here for benchmarking because this gas supports both the longitudinal and transverse modes). The material data of the mild steel assumed in this study are taken as follows: mass density (ρ=7850 kg/m^3) and elastic stiffness given by c_{11}=263.8462 GPa, c_{12}=113.0769 GPa,

and c_{44}=75.3846 GPa. Subsequently the shear and longitudinal velocities in bulk steel were calculated as 3098.89 m/s and 5797.49 m/s, respectively and these data are shown in Table 3.1.

3.7.1 Comparison of the FEM Numerical Results

The convergence of the solutions has also been studied by using three successive mesh divisions with the Atkin's extrapolations [Rahman, 1986] to see the accuracy of our numerical method when compared to published result [Hennion, 1996]. The study is done by increasing the mesh size in a geometrical proportional ratio and then using Atkin's extrapolation formula, which is given as:

$$f_{\infty} = f_3 - \frac{(f_{3-} f_2)^2}{f_3 - 2f_2 + f_1} \tag{3.44}$$

where f_1, f_2 and f_3 represents modal solutions using three meshes with geometric ratio and f_{∞} represents the extrapolated value. Here f_3 represents the finest mesh used.

Table 3.2. The eigenfrequency of the first two Steel waveguide modes with Atkin's extrapolation calculation and comparison with references papers.

Propagation constant (m^{-1})	Mode	Mesh			Atkin	H.Hennion
		18×18	36×36	72×72		
200	bending	68.4983	66.9905	66.7021	66.6339	64.84
	Torsional	101.5596	99.6967	98.9221	98.3708	94.66
400	bending	165.0203	163.9391	163.4915	163.1752	166.45
	torsional	192.0114	189.6773	188.6422	187.8174	189.43
600	bending	264.45	262.2535	261.2946	260.5516	269.33
	torsional	285.030	281.1514	279.3516	277.7936	285.23

Table 3.2 presents the first two eigenfrequencies obtained by the three sucessive meshes used, and for three different values of the propagation constants, *k*, 200 m^{-1}, 400 m^{-1} and 600 m^{-1}, respectively. This table also shows the Atkin's extrapolation from the three geometric variations of meshes and its comparison with the published work [H-Hennion]. From the table, each particular propagation constant have shown two frequencies where the first frequency correspond to a bending wave propagation along the waveguide whereas the second frequency corresponds to a torsional wave propagation along the waveguide. The numerical

computation is shown here in Table 3.2 that has proven our numerical calculation method is given similarly results to that of [Hennion, 1996].

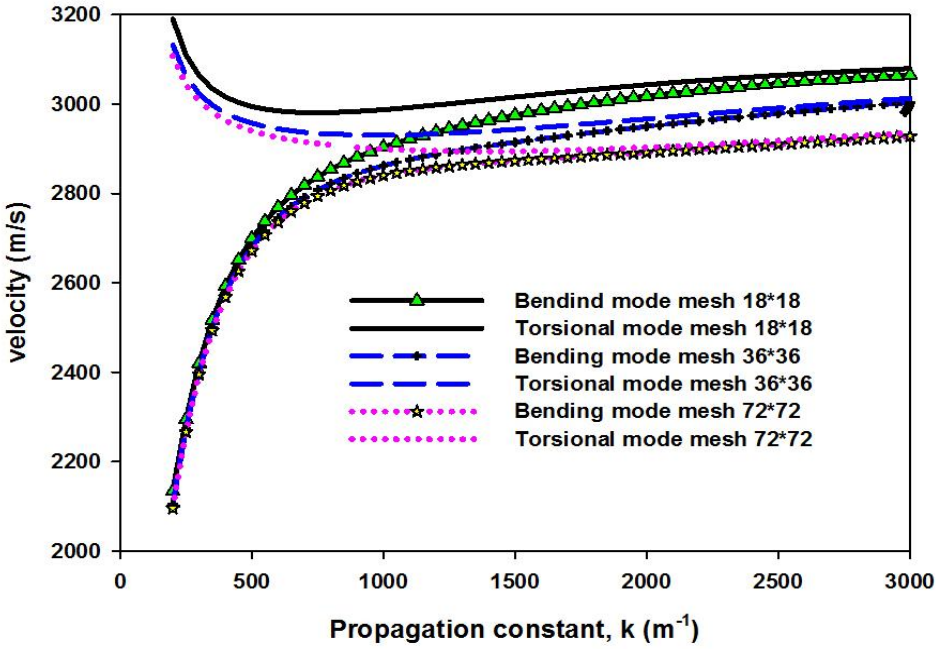

Figure 3.5. Variation of the phase velocity with the propagation constant for the bending and torsional modes with three different meshes.

The dispersion curves illustrating the variation of the phase velocity for the bending and torsional modes with of the propagation constant are shown in Fig. 3.5. This graph shows the variation for three different meshes of 18×18, 36×36 and 72×72 from the lowest propagation constant of 200 m^{-1} to 3000 m^{-1}. It can be noticed that the bending mode of the three difference mesh have the same characteristic when the propagation constant is increased the velocity is also increased. In contrast, for the torsional mode the graph shown that at the lower propagation constant the velocity is gradually increased and become stable at the propagation constant 500 m^{-1}.

In this benchmark worked, it has been decided to use around 60x60 mesh divisions, which yields 7200 first order triangles. For most of the work, 7200 first order unequal sized triangles have been used to represent the whole structure in the simulation. For this structure, at a given propagation constant, *k*, the first frequencies correspond to a degenerate bending mode and the second frequency corresponds to a torsional mode propagating along the waveguide and these are studied here. The

dispersion curves illustrating the variation of the phase velocity for the bending mode and torsional mode as a function of the propagation constant are shown in Fig. 3.6.

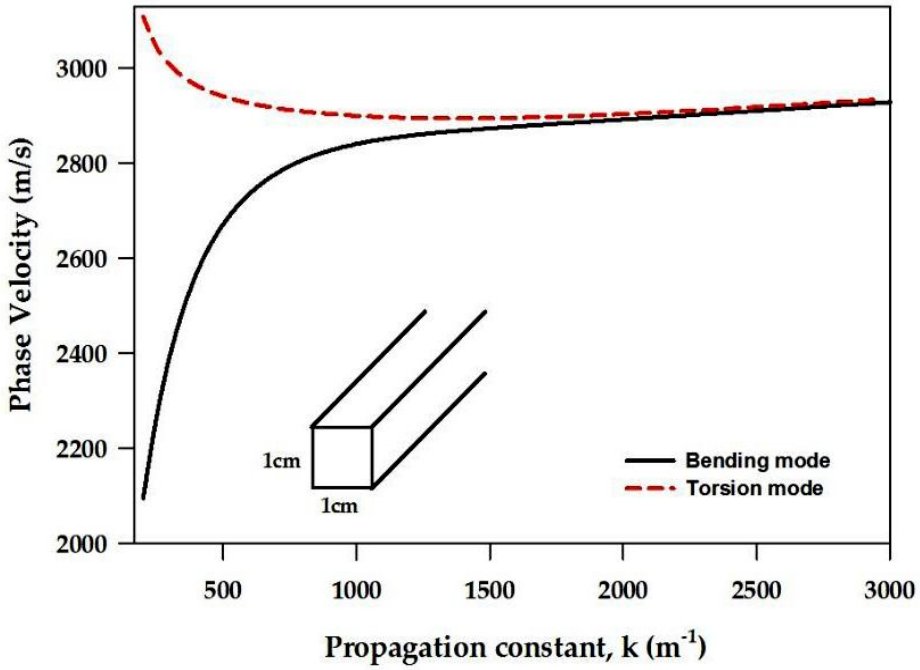

Figure 3.6. Variation of the phase velocity with the propagation constant for the bending and torsional modes (mesh 60x60).

A schematic of the steel acoustic waveguide is shown as an inset in Fig. 3.6 also. It can be observed that as *k* is increased, the velocity of the torsional mode, shown by a red dashed line, is reduced rapidly to a minimum value and then it reaches, asymptotically, the value of the Rayleigh velocity (V_R) (2894 m/s) of the steel. At lower values of *k*, the acoustic wave spreads well into the cladding and its velocity rises rapidly and the mode enters into the cut-off mode region. For the bending mode, its dispersion curve is shown by a black solid line. There are two degenerate bending modes for a square waveguide and this degeneracy is lifted when its width and height are unequal. At a lower frequency, the phase velocity is a linear function of the square root of the frequency, in a way similar to that reported earlier [Fahy and Gardonio, 2007]. At sufficiently high frequencies (or values of the propagation constant) the bending wave resembles more closely to a pure transverse shear wave and the phase velocity approaches asymptotically the Rayleigh velocity.

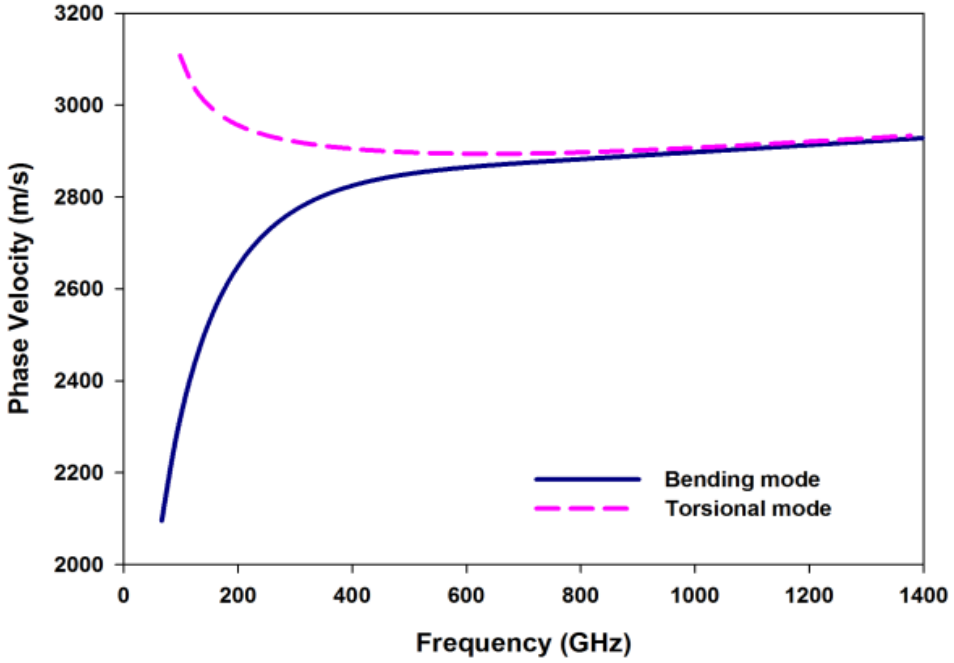

Figure 3.7. Variation of the phase velocity with the frequency for bending and torsional modes.

The variation of the phase velocity with the frequency as shown in Fig. 3.7 is of similar in nature to that shown in Fig. 3.6. The similarity between Fig. 3.6 and Fig. 3.7 concluded that the wavenumber is increased linearly and the frequency varies directly to each other. From the relation of $k = \frac{2\pi f}{v}$, the graphs shown that when frequency is increased the velocity of bending mode is increased as a function of square root of frequency. Meanwhile, the velocity of torsional mode is decreased as the frequency is increased.

3.7.2 Bending Mode

Figure 3.8 shows the dominant mode of U_x displacement vector for the bending mode U^x mode at propagation constant 200 m^{-1}. It can be observed that the displacement is maximum in the middle of the waveguide.

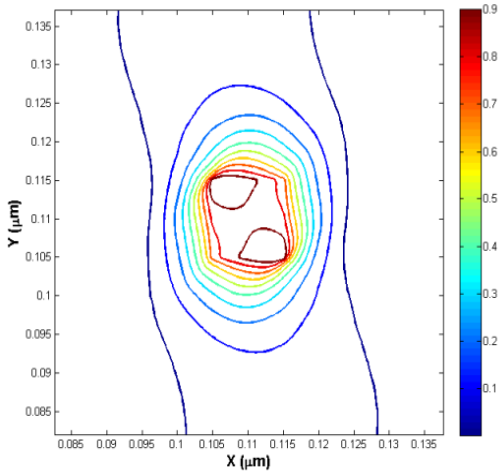

Figure 3.8. The contour plot of U_x displacement vector of the bending mode at k=200 m^{-1}.

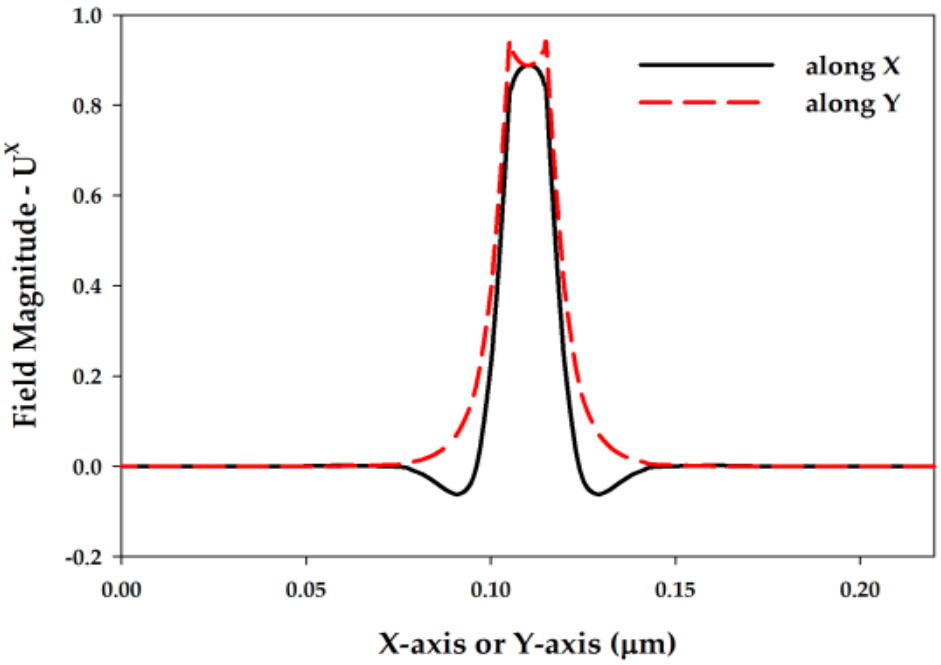

Figure 3.9. Variation of the U_x displacement vector of bending mode at k=200 m^{-1} along x and y axes.

The variations of the U_x displacement vector of the bending U^x mode along the x and y axes are shown in Fig. 3.9. It can be noticed that the mode is confined in

the middle of the core as shown by a black solid line along the *x*-axis with a small negative peak near the interface. The variation of U_x vector of the bending mode along the *y*-axis is shown by a red dashed line, which is symmetric along the waveguide. However, as the waveguide is a squared shape, its U_x and U_y mode are degenerate and their slight combination can rotate the eigenvector profile as shown in Fig. 3.8.

The lowest order bending and torsional modes corresponded to a wavenumber of 200 m^{-1} with their eigenfrequencies being 66.7021 kHz and 98.9221 kHz respectively. Two degenerate bending modes have dominant U_y or U_x displacement vector and its maximum value is inside the core. The torsional mode will be explained in detail in the later Torsional Mode section from Figs. 3.14-3.19.

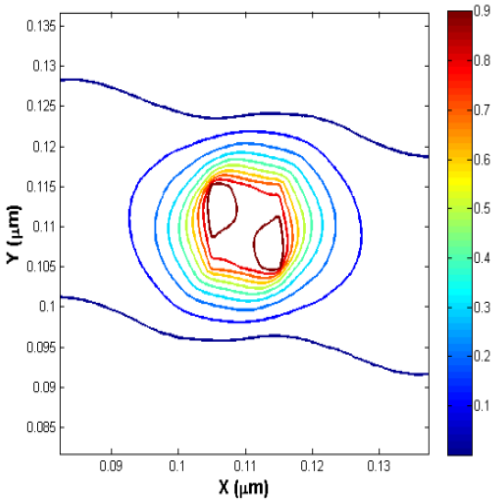

Figure 3.10. The contour plot of U_y displacement vector of bending mode at k=200 m^{-1}.

The dominant displacement vector U_y of the U^y bending mode has similar characteristic to the U_x variation of the U^x mode. The U_y displacement vector profile is rotated 90 degree from the *y*-axis as shown in Fig. 3.10 with its maximum in the middle of the core with the maximum magnitude of one.

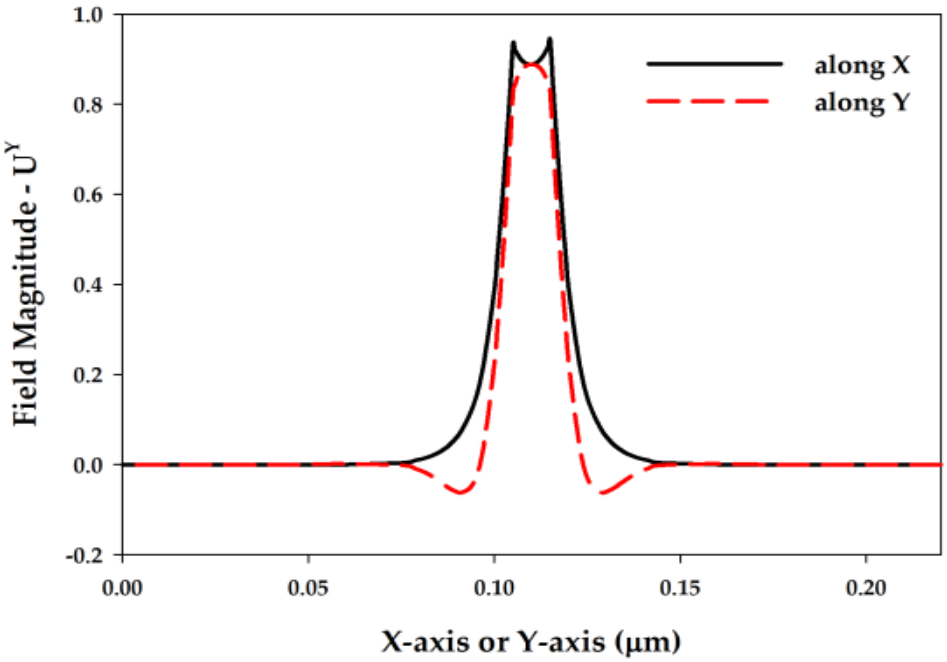

Figure 3.11. Variation of U^y bending mode at k=200 m^{-1} along x and y axes.

Figure 3.11 shows the variations of the U^y displacement vectors of the U^y bending mode at k=200 m^{-1} along x and y axes. The observation of U^y mode shows by the black solid line plot along x-axis has the dip at the centre. The U^y mode along the y-axis is shown in this figure with the red dash line. From this figure, it shows that the U^y mode along the y-axis is more confined inside the core with a negative dip outside the core become larger, and closer to the interface. It can be notice that the U^y mode along the x and y axes are symmetric and well confined in the core region.

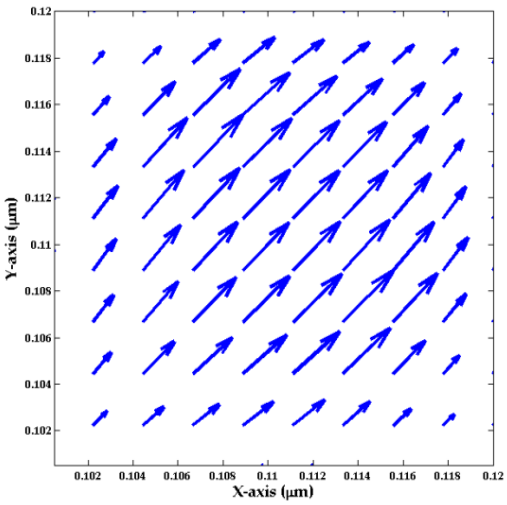

Figure 3.12. The vector displacement fields $U_t = \vec{U}_x + \vec{U}_y$ of the acoustic waveguide of the bending mode at k =200 m^{-1}.

The superposition of these two bending modes yields a transverse displacement $\mathbf{U_t}$ is oriented at 45° to the *x*-axis as shown in Fig. 3.12. As the resultant displacement vector moves in the transverse plane, it represents a microbend which periodically changes its direction along the propagation direction *z*.

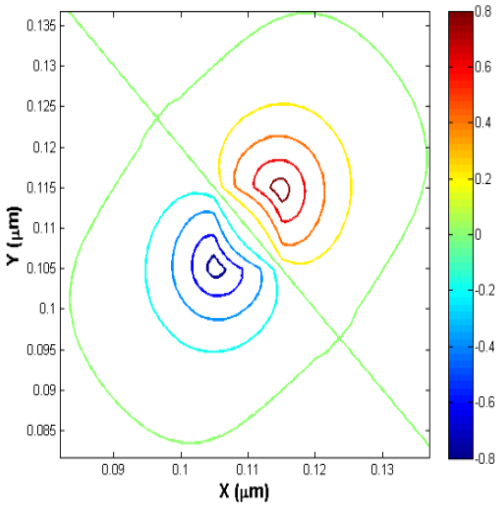

Figure 3.13. The contour plot of U_z displacement vector of the bending mode at k =200 m^{-1}.

It should be noted that this bending mode had either U_x or U_y as the dominant displacement (for a transverse mode), however, its longitudinal displacement, U_z was not zero as shown in Fig. 3.13. The U_z displacement vector shows one positive and one negative peak with the magnitude of 80% of the dominant mode.

3.7.3 Torsional Mode

Two degenerate bending modes shown previously were the fundamental transverse modes. Follow this, a higher order transverse mode is shown next. This mode represents a torsional mode which corresponding to a wavenumber of 200 m^{-1} with its eigenfrequency of 98.9221 kHz, which is shown in this section.

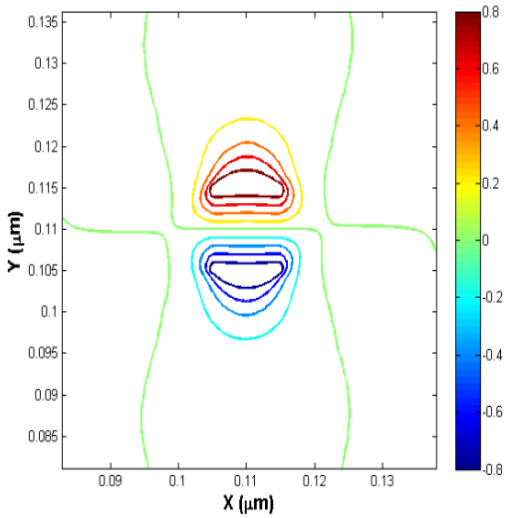

Figure 3.14. The contour plot of the U_x displacement vector of torsional mode at k=200 m^{-1}.

The U_x profile of the torsion mode at k=200 m^{-1} has one positive and one negative peaks at the upper and lower interface of the waveguide is shown in Fig. 3.14 with the magnitude of being 80%.

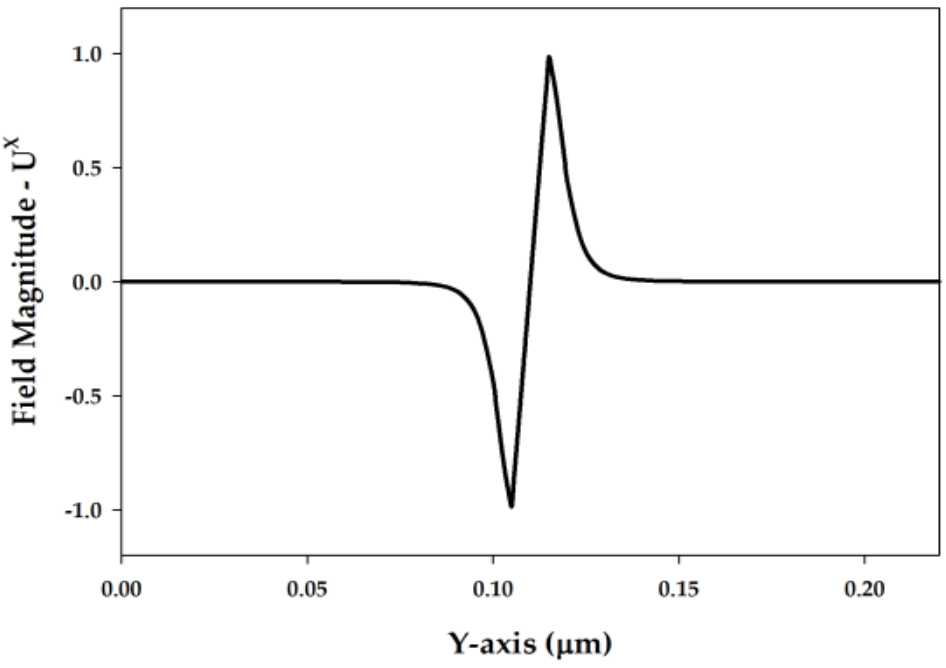

Figure 3.15. Variation of U^x torsional mode at k=200 m^{-1} along y-axis.

Variation of the U_x displacement vector of the torsional U^x mode along the *y*-axis is shown in Fig. 3.15. It can be observed that one negative and one positive peaks exist along the *y*-axis with magnitude being normalized to unity at k=200 m^{-1}.

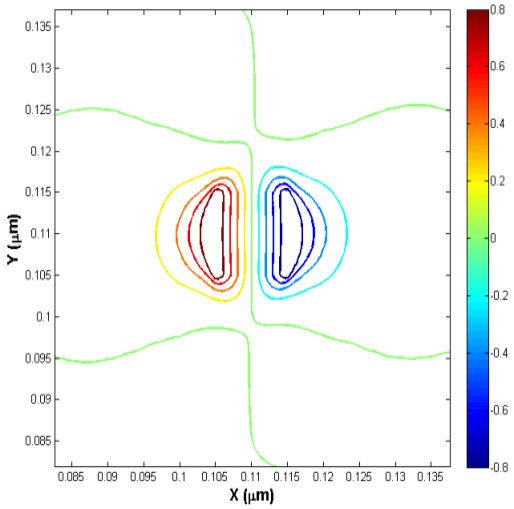

Figure 3.16. The contour plot of the U_y displacement vector of torsional mode at k=200 m^{-1}.

The U_y displacement vector profile of the torsional mode at k=200 m^{-1} is shown in Fig. 3.16. This has a similar characteristic with the U_x displacement mode, as shown in Fig. 3.14, but this has one positive and one negative peak on the left and right side of the waveguide, which is 90 degrees rotated from that shown in Fig. 3.14.

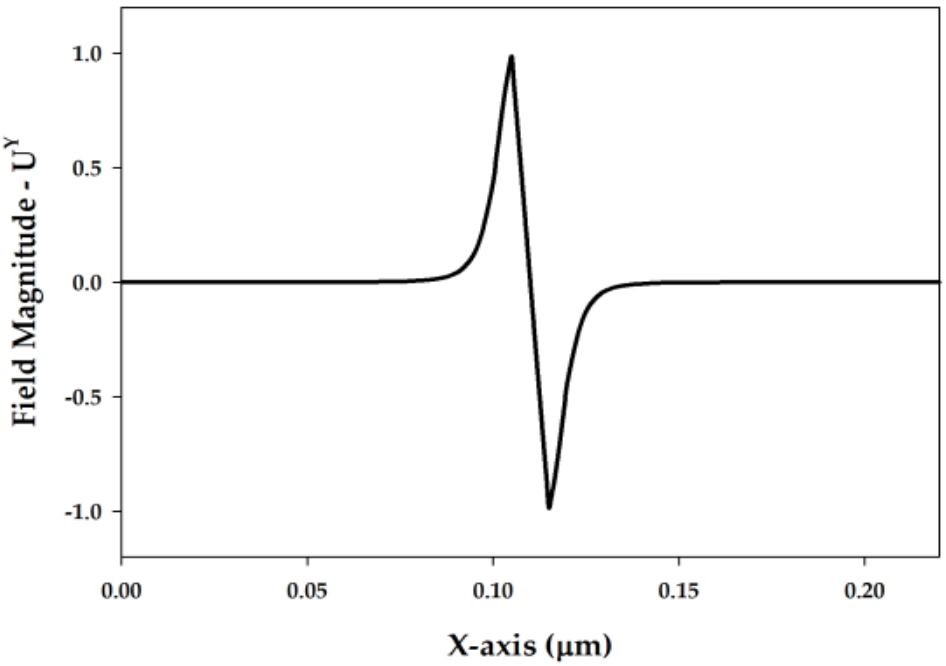

Figure 3.17. Variation of U^y torsional mode at k=200 m^{-1} along *x*-axis.

The variation of the U_y displacement of the torsional U^y mode along the *x*-axis is shown in Fig. 3.17. It can be observed here that the graph shows one positive and one negative peak which is similar to that of the torsional U^x mode. However, the contrast here is that the rotation in the U_y displacement has shown the positive peak before the negative one.

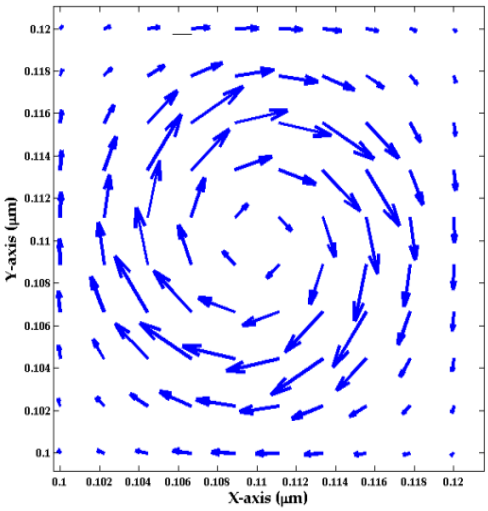

Figure 3.18. The vector fields $U_t = \vec{U}_x + \vec{U}_y$ of the torsional mode at k =200 m^{-1}.

On the other hand, in Fig. 3.18, it can be seen that the displacement parameters U_x and U_y combine to give a rotational displacement vector which results into a torsional mode, periodically twisting the fibre clockwise, then anti-clockwise as it propagates along and both the modes also have associated U_z components.

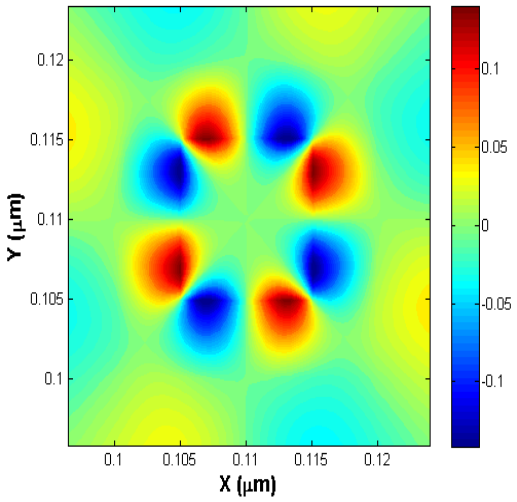

Figure 3.19. The U_z displacement fields profile of the torsional mode at k =200 m^{-1}.

As the width and height of the waveguide were equal, the torsional modes were degenerate and the magnitude of the U_x and U_y values were equal. The U_z profile of torsional mode in fig. 3.19 shown the higher order spatial variation with four pairs of positive and negative peaks paring together around the core of the waveguide.

3.7.4 Hybridness

To measure the strength of the longitudinal component, a further parameter such as the hybridness, has been evaluated. The concept of modal hybridness has been used in the optical waveguide, which is important to calculate the polarization cross-talk [Somasiri, 2003] and also in the design of the polarization rotators [Rahman, 2001].

In this work, the hybridness of a mode at a particular frequency is defined as the ratio of the maximum value of the non-dominant displacement vector to the maximum value of dominant displacement vector.

For a transverse mode with U_x as the dominant displacement vector the hybridness, Hb_x can be expressed as:

$$\mathbf{Hb}_x = \frac{\mathbf{U}_{z\_\max}}{\mathbf{U}_{x\_\max}} \tag{3.45}$$

where U_{z_max} and U_{x_max} are the maximum values of the displacement vectors along the z and *x*-directions respectively.

On the other hand, for a longitudinal mode with a dominant U_z displacement vector, the hybridness, Hb_z can be expressed as:

$$\mathbf{Hb}_z = \frac{\mathbf{U}_{x\_\max}}{\mathbf{U}_{z\_\max}} \tag{3.46}$$

where $U_{x\text{-}max}$ and $U_{z\text{-}max}$ are the maximum values of the displacement vectors along the *x* and *z*-directions respectively. It has been observed for this acoustic waveguide that at a higher propagation constant or frequency, the parameter, Hb_x, is approximately 0.5 for both the bending and torsional modes. Furthermore, it has

been noted that since the width is equal to the height of the waveguide, $Hb_x = Hb_y$ (where Hb_y is the hybridness for a U_y dominant mode). As the propagation constant decreases (k<1000 m^{-1}), the hybridness decreases for the torsional modes but increases for the bending modes. The dispersion graph shown in Fig. 3.6 agrees well with the eigenvalues reported earlier [Hennion, 1996].

We have also benchmarked our code with the acoustic modes in a multimode optical fibre, and our results agree well with the published results and these are shown in Chapter 4.2.2.

3.8 Summary

The implementation of FEM with acoustic wave theory was shown in this chapter. The combination of the full vectorial FEM with full vectorial acoustic wave was developed and studied with different acoustic modes in a high index contrast waveguide. In this Chapter, the computational results obtained shown the transverse acoustic modes of bending and torsional modes with their vector plot. Furthermore, the benchmark of the Steel waveguide shown the accuracy of the result. Finally, this Chapter also presented a detailed displacement vector profiles for the bending and torsional modes displacement vector, modal hybridness, modal displacement and 2D-line plot are also shown.

Chapter 4

Silica Fibres

4.1 Introduction

In this chapter, a numerical approach based on the versatile FEM has been applied [Koshiba, 1987], [Lagasse, 1973], [Stone 1973] for the analysis of an acoustic waveguides and subsequently both weakly and strongly guiding acoustic waveguide have been studied [Safaai-Jazi, 1986], [Jen, 1986], [Jen 1990].

In the first section, a low-index contrast silica acoustic waveguide has been analyzed using the FEM where a doped silica core, surrounded by a pure silica cladding is studied and the characteristics of the shear and longitudinal modes are determined and presented. Although similar studies have been reported previously, in those cases the shear and transverse modes were decoupled [Safaai-Jazi, 1988], [Jen, 1986], [Shibata, 1989]. In the present study, the co-existence of both the shear and the longitudinal modes has been considered and the last section guidance of acoustic waves in a strongly guiding silica (SiO_2) nanowire waveguide have been discussed, including their contribution to SBS.

4.2 Weakly Guiding Silica Fibres

In this section, initially a weakly guiding SiO_2 fibre has been analyzed by assuming (1) V_L of the TiO_2 doped silica core and pure silica cladding are equal and then, (2) V_S of the core and cladding are equal to isolate the pure longitudinal and transverse modes. Table 4.1 gives the parameters considered for the first two cases above. Subsequently, a more general situation which is more realistic, Case (3), is considered when both V_L and V_S are unequal for core and cladding regions.

Table 4.1. Material properties of a silica waveguide used in this work [Safaai-Jazi, 1986].

Doped SiO_2		Velocity (m/s)		Density (kg/m^3)	Elastic Stiffness (GPa)		
		V_L	V_S	ρ	c_{11}	c_{12}	c_{44}
Case 1	***Core***	5933	3625	2202	77.5115	28.9357	19.6401
	Clad	5933	3764	2202	77.5115	31.1973	15.1169
Case 2	***Core***	5736	3764	2202	77.4495	10.0549	31.1973
	Clad	5933	3764	2202	77.5115	15.1169	31.1973

4.2.1 Case 1: Shear Modes

Firstly, a shear mode of a weakly confined multimode optical fibre is investigated. The normalized frequency, *fa*, in this and other figures, is given in units of μm.GHz (which is the product of frequency, *f*, of the acoustic mode with radius, a=175 μm, of the fibre core). Its cladding radius was taken as 400 μm with $\Delta V_S/V_S \approx 0.036$. The material contrast is small and therefore, it becomes a weakly guiding waveguide for the shear modes. As mentioned in Section 3.7.1, a 60x60 mesh division is also used here for these simulations.

Figure 4.1 illustrates the variation of the phase velocity with the normalized frequency, *fa*, for several lower order shear modes. Here S_{nm} notation, similar to the LP_{mn} notation for optical waveguides, has been adopted for the group of shear modes. The structure is rotationally symmetric. Similar to the degenerate optical H^x_{11} and H^y_{11} modes in optical fibres, its acoustic modes are also degenerate, with both the U_x and U_y being dominant.

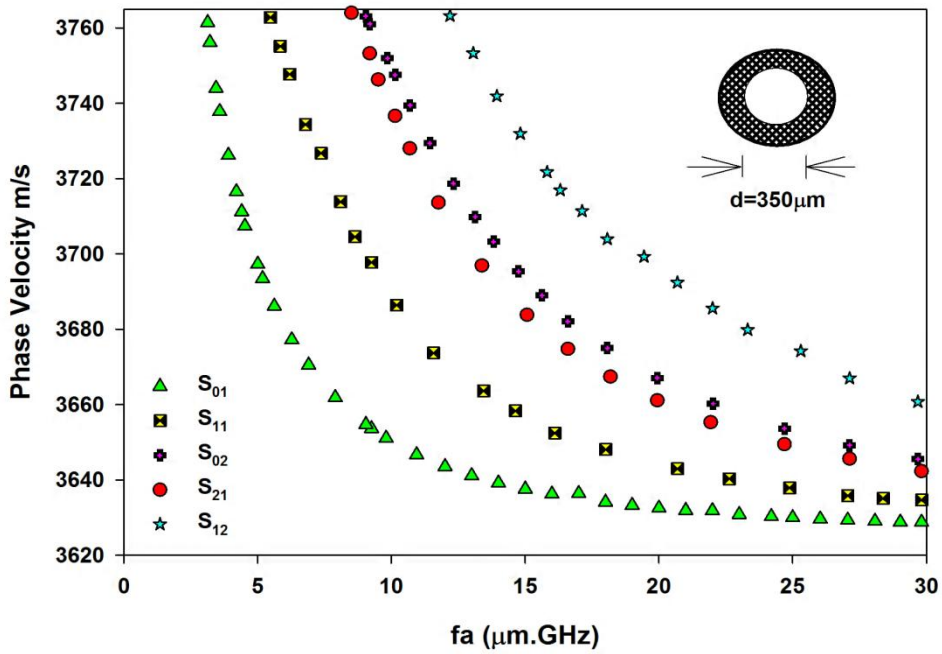

Figure 4.1. Phase velocity characteristics for lower order shear modes in a fibre acoustic waveguide.

It can be seen that as the frequency is reduced, the modal phase velocity has increased from the V_S value of the core to V_S of the cladding and approaches the cut-off. All the acoustic shear modes have non-zero cut-off frequencies. Thus for single-mode operation, the normalized frequency should be higher than 3.5 μm.GHz in order to have efficient excitation of the S_{01} (F_{11}) mode, but lower than the normalized cut-off frequency of the next higher mode, the S_{11} mode, at 7.0 μm.GHz. The corresponding cut-off frequencies for S_{01} and S_{11} are 20 MHz and 40 MHz respectively for the TiO_2 doped optical fibre with its radius, a=175 μm is considered here.

The displacement vector U_x profiles of the fundamental S_{01} mode, which is also called the Flexural F_{11} mode (equivalent to HE_{11} in the optical waveguide) for k=0.055 μ.m^{-1} and fa=5.18 μm.GHz are shown in Fig. 4.2. The S_{01} (F_{11}) mode has a dominant transverse displacement, compared to that of its longitudinal component. The 3-D contour plot of the parameter U_x, given in Fig. 4.2(a), shows the maximum U_x displacement is at the centre of the core. This value reduces monotonically as the radial distance is increased from the core, as shown in Fig.4.2(b).

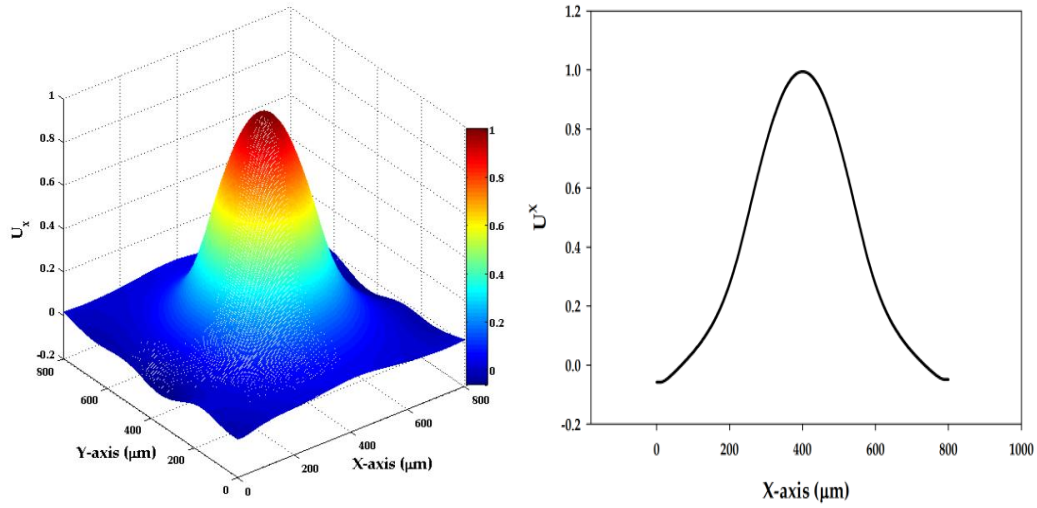

(a) (b)

Figure 4.2. The transverse S_{01} mode for (a) the 3-D plot and (b) 2-D plot of the U^x at *fa*=5.18 μm.GHz.

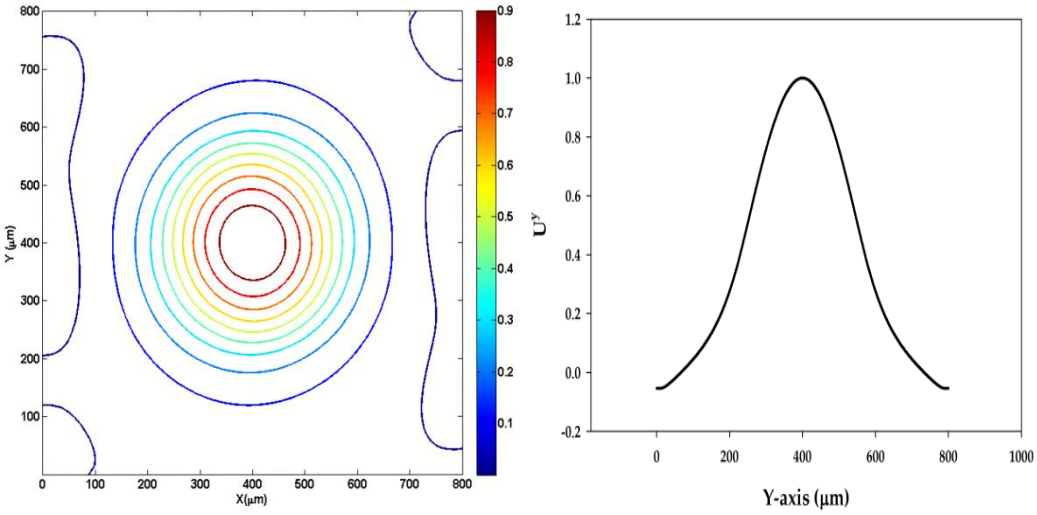

(a) (b)

Figure 4.3. The S_{01} mode (a) the U_y contour plots (b) its line plot at *fa*=5.18 μm.GHz of the transverse S_{01} mode.

The displacement vector, U_y profile and magnitude shown in Fig. 4.3 which is similar to that of the U_x profile shown in Fig. 4.2. Its contour profile is shown in Fig.4.3(a) and its variation along the *y*-axis is shown in Fig.4.3(b). This displacement is in the *y* direction, that is rotated at 90° with respect to the horizontal axis. In optical fibre, the similar fundamental L_{01} mode as shown here, consist of degenerate H^x_{11} and H^y_{11} modes.

As the magnitudes of U_x and U_y are equal, the resultant vector displacement plot, $\mathbf{U_t}$ is oriented at 45° to the horizontal axis and the combined displacement in the transverse plane, $\mathbf{U_t}$ is shown in Fig. 4.4(a). The contour profile of U_z of the S_{01} mode shown in Fig. 4.4(b) demonstrates a higher order spatial variation with positive and negative peaks on two sides of the core. Its magnitude is much smaller than that of the transverse displacements with Hb_x=0.10.

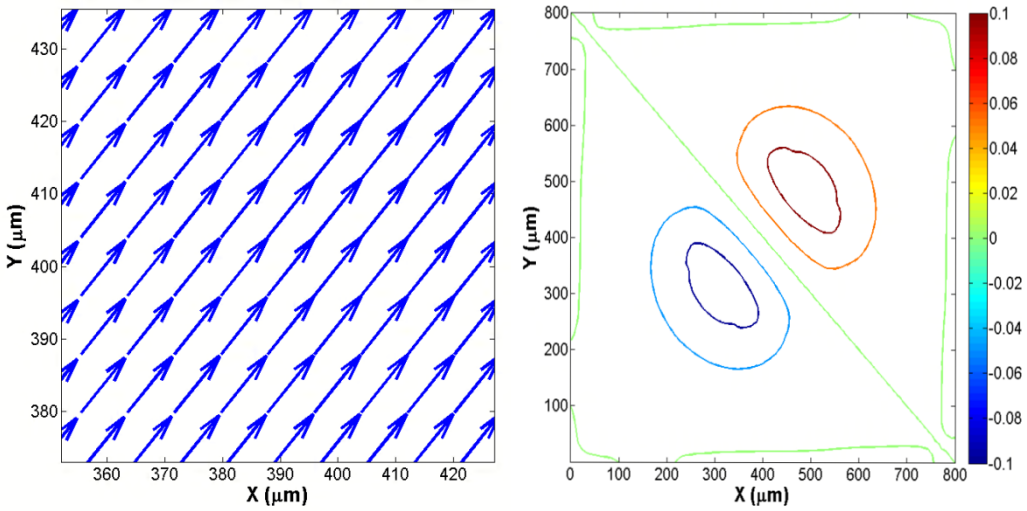

Figure 4.4. The transverse S_{01} mode of (a) $U_t = \vec{U}_x + \vec{U}_y$, (b) U_z at *fa*=5.18 μm.GHz.

The combination of both the longitudinal and transverse displacements of S_{01} (F_{11}) shown in Figs. 4.2 to Fig. 4.4 results into a bending deformation (or flexural mode). It should be noted that the fundamental optical mode of a low index contrast multimode fibre has a similar large Gaussian shaped transverse field component and a very small longitudinal component with higher order spatial variations.

The family of higher order S_{11} modes were also studied. The contour plots of both U_x and U_y have one positive and one negative peak as shown in Figs. 4.5(a) and (b). However, their vector plots fall into the following classification: Torsional mode T_{01}, Axial Radial mode R_{01}, and Torsional-Radial TR_{21} modes. The mode TR_{21} has also been referred to as the Flexural F_{21} [Shelby, 1985], [Safaai-Jazi, 1986]. The TR_{21} and R_{01} modes are of particular interest as they cause GAWBS. The vector displacement plots of the R_{01} mode is shown in Fig. 4.5(c) for *fa*=5.838 μm.GHz. It can be observed that for R_{01}, the U_x and U_y displacement vectors both act

simultaneously in a direction which is radially outwards (or inwards), resulting in a periodic expansion and contraction in the radial directions.

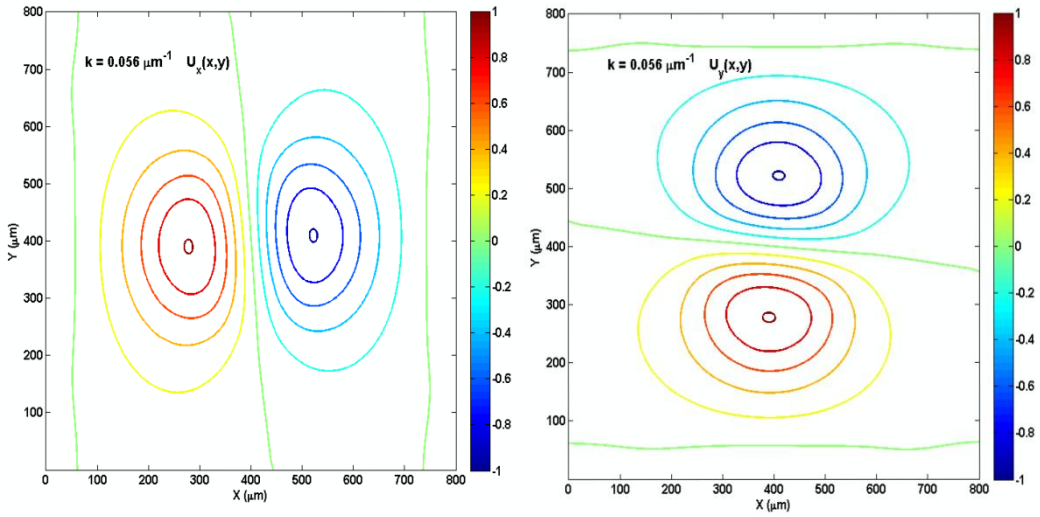

(a) (b)

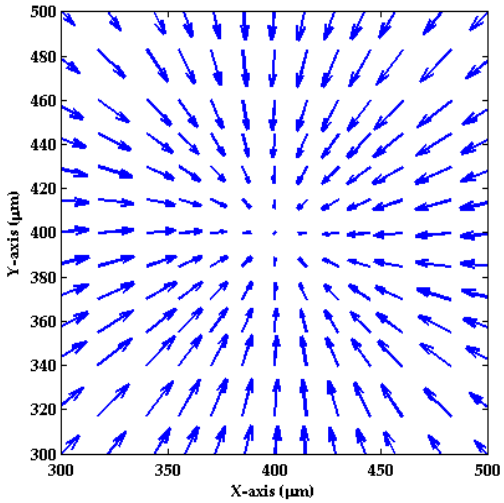

(c)

Figure 4.5. Radial mode (a) U_x (b) U_y contour plot and (c) vector U_t plot for the axial radial mode of R_{01} at fa=5.838 μm.GHz.

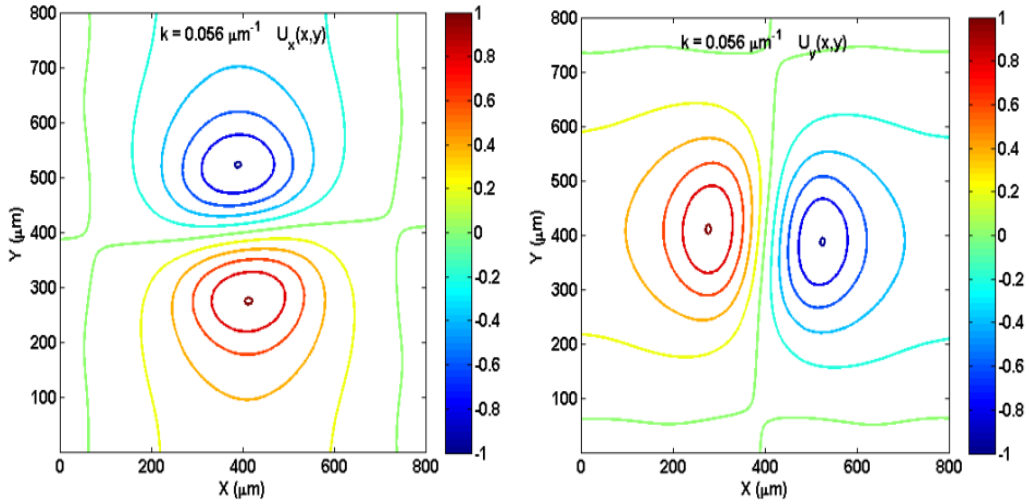

(a) (b)

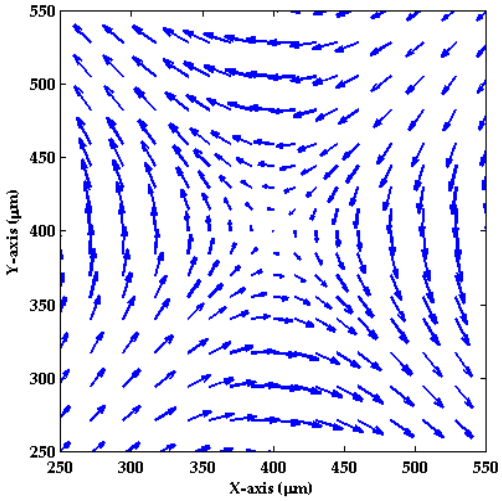

(c)

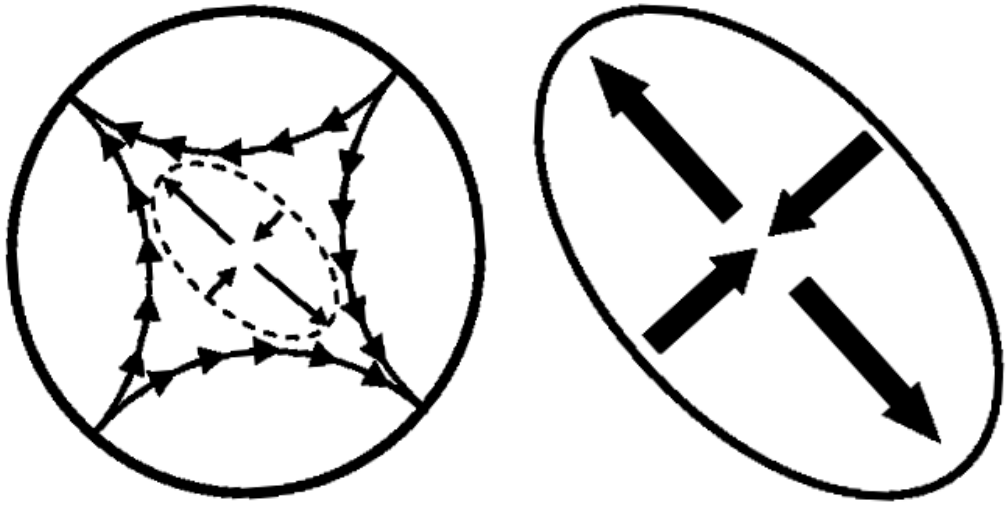

(d)

Figure 4.6. Torsional-Radial mode (a) U_x and (b) U_y displacement (c) vector U_t plot and (d) the periodic displacement of Torsional-Radial at fa=5.838 µm.GHz.

By contrast, in the case of TR_{21}, the U_x and U_y displacements are not in phase as shown in Fig. 4.6(a) and (b). Hence for TR_{21}, the unequal modal transverse displacements along the X and Y axes result in a periodic elliptical deformation of the SiO_2 fibre as shown in Fig. 4.6(c) where the periodic displacement is shown in Fig. 4.6(d) and hence this induces optical birefringence, resulting in a depolarized GAWBS. For the R_{01} mode, the displacement is in the radial direction and hence the rod expands and contracts periodically but maintaining a circular-shaped cross-section, which corresponds to the polarized GAWBS. Both of these modes have a longitudinal displacement comparable to the transverse displacement and their corresponding hybridness, Hb_x, increases with the frequency.

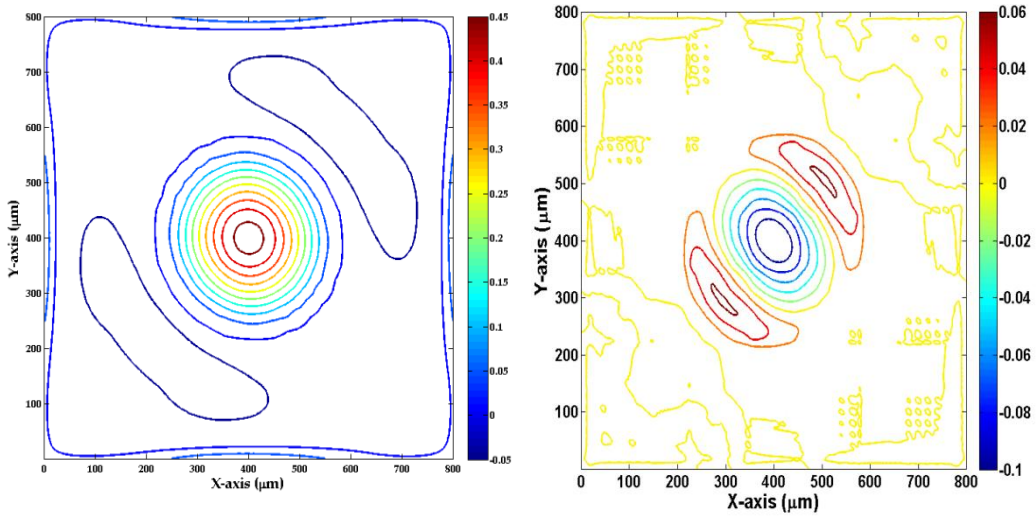

(a) (b)

Figure 4.7. U_z distribution of S_{11} at (a) *fa*=5.838 μm.GHz and (b) at *fa*=28.374 μm.GHz of the R_{01} mode.

Figure 4.7(a) shows the U_z distribution of the R_{01} mode at *fa*=5.838 μm.GHz. It can be observed that the U_z has a near Gaussian profile with its maximum value located at the centre of the core with the hybridness value, Hb_x is close to 0.5. Figure 4.7(b) shows the U_z field of the R_{01} mode at a higher frequency, *fa*=28.374 μm.GHz and it can be seen that although U_z has its maximum value at the centre, it shows a higher order spatial variation along the radiation direction. It has been noted that the hybridness reduces from 0.47 to 0.10 as the value of *fa* increases from 5.838 to 30 μm.GHz. Hence this mode may cause both GAWBS, due to its modal transverse displacement and SBS in the backward direction because of its relatively large longitudinal modal displacement, more particularly at a lower frequency. Among the higher order modes, the families of the TR_{2m} modes have been reported to cause

Forward Guided Brillouin scattering [Shelby, 1985]. However for these modes, with $m \geq 1$, the associated U_z field profiles have faster spatial variations and hence may not be suitable for the generation of SBS.

4.2.2 Case 2: Longitudinal Modes

For longitudinal modes, the longitudinal velocity of the core V_L (core) needs to be smaller than that of the cladding with V_L (core)<V_L (clad). In this case core radius was taken as 175 μm, and the cladding radius was to be very large. The variations of the phase velocity with the normalized frequency (*fa* in μm.GHz) for various longitudinal L_{nm} modes are shown in Fig. 4.8. For a larger *fa* value, all the acoustic modes are well confined in the core and their phase velocities are close to those of the bulk longitudinal velocity of the core (of doped silica glass), which is 5736 m/s. It can be observed that as *fa* is reduced, for any given mode, initially the phase velocity increases slowly and then more rapidly to reach its cut-off value of 5933 m/s, the value of the bulk longitudinal wave velocity in the cladding. It can be noted that the higher order modes approach their cut-off at higher *fa* values. These results agree well with those reported by Jen *et al*. [Jen, 1986].

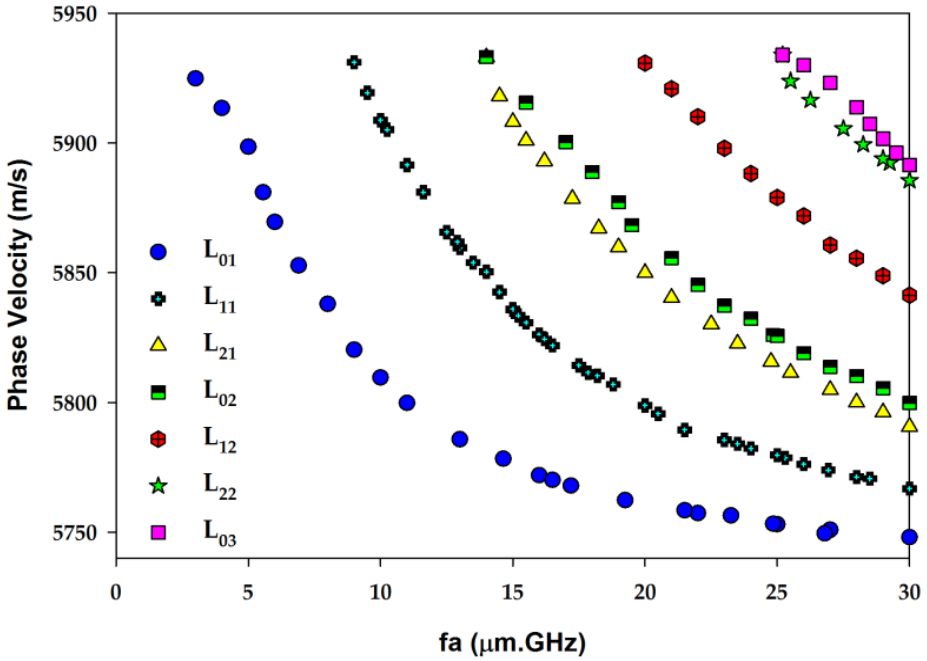

Figure 4.8. Phase velocity of the longitudinal modes in a fiber acoustic waveguide.

All modes, with the exception of the L_{01} mode shown by solid circles, have non-zero cut-off frequencies. Thus, for single-mode operation, the normalized frequency should be lower than 9 μm.GHz (or f<51.4286 MHz), the cutoff frequency

of the next higher mode, L_{11}, in order to have efficient excitation of the L_{01} mode as the only guided mode. Figure 4.9(a) shows the longitudinal displacement, U_z, contour plot of the L_{01} mode which is dominant whilst the corresponding U_x and U_y distributions have a positive and negative displacement peak but with a smaller magnitude.

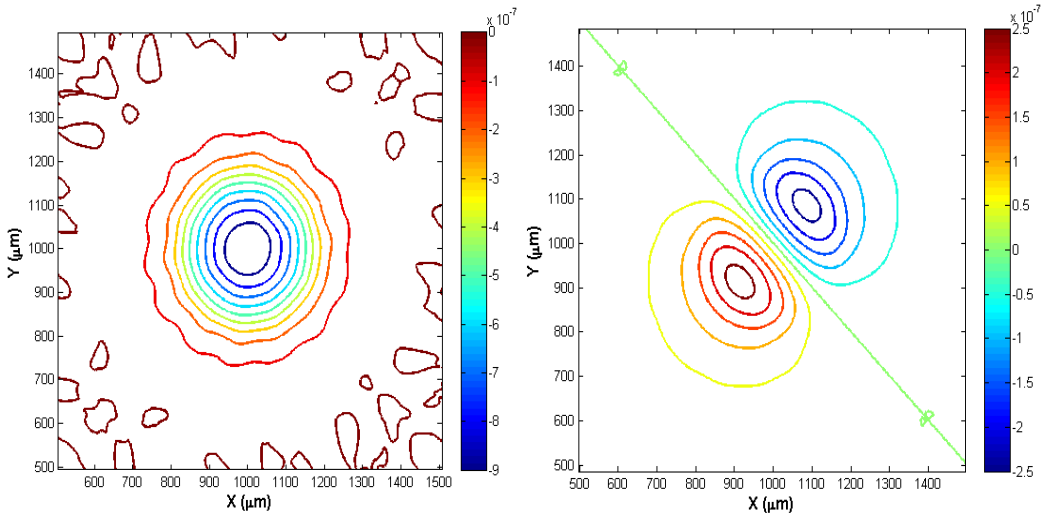

(a) (b)

Figure 4.9. U_z distribution of (a) the L_{01} Mode and (b) the L_{11} Mode at $k = 0.06$ μm^{-1}.

For longitudinal modes, U_z is dominant and the modal hybridness, Hb_z, increases from 0.16 to 1.1 as the *fa* increases from a value of 5.0 μm.GHz to 30.0 μm.GHz. This is one of the modes that introduces SBS due to the associated high magnitude of U_z with a Gaussian profile, which has a higher overlap with the optical mode [Li, 2007]. Figure 4.9(b) shows the U_z profile of the L_{11} mode and it should be noted that the longitudinal L_{mn} modes are not degenerate.

4.2.3 Case 3: $\Delta V_L/V_L \ll 1$ and $\Delta V_S/V_S \ll 1$

In the work described in the previous sections, either V_L or V_S had been considered to be identical for both the core and the cladding to isolate the longitudinal and transverse modes. However, in a real weakly guiding fibres, both the shear and longitudinal velocities for the core and cladding are unequal, i.e., $\Delta V_{L,S} \neq 0$ but their differences are small $\Delta V_L/V_L \ll 1$ and $\Delta V_S/V_S \ll 1$. In this section, the effect of different core and cladding velocities is considered. When $\Delta V_S=0$, this situation was identical to Case 2 and it was shown earlier.

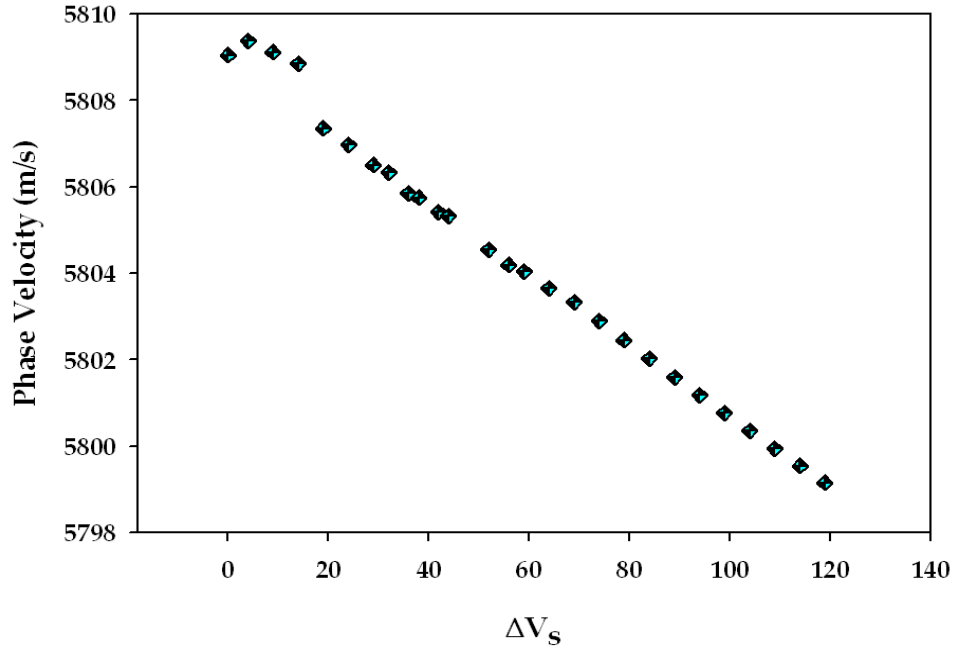

(a)

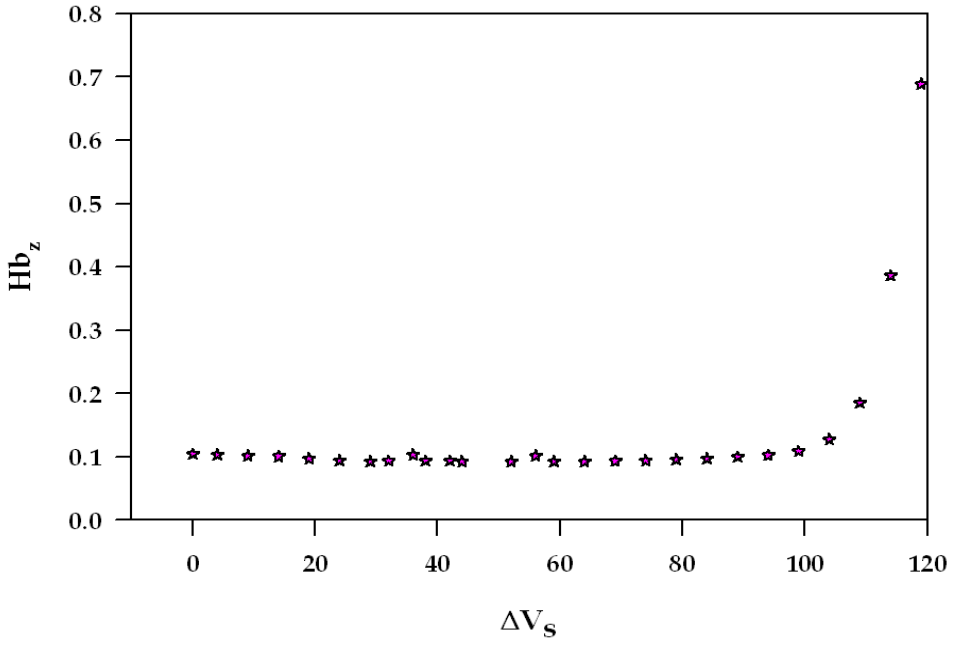

(b)

Figure 4.10. (a) Variation of phase velocity and (b) Hybridness of the L_{01} mode with the ΔV_S from Case 2.

However, in the case when $\Delta V_S \neq 0$, the variation of the phase velocity with ΔV_S is shown in Fig. 4.10(a). In this case, a fibre which is similar to that in Case 2 has been considered but additionally V_S of the core has been reduced progressively from 3764 m/s to a value of 3625 m/s, while the V_S of the cladding is kept constant

at 3764 m/s. This introduces additional shear modes into the core, as well as the longitudinal modes shown earlier in Case 2. In addition to that, as the shear velocity in the core slowly deviates more from that of the cladding, the phase velocity of the longitudinal, L_{01} is also affected progressively and starts to decrease. The reduced velocity could be due to the enhanced modal confinement, besides a fixed ΔV_L, the value of ΔV_S is also progressively increased. It can be noted that the dispersion curve appears to show some discontinuity near ΔV_S = 20 m/s. This has not been thoroughly investigated here but this may be due to the presence of some non-physical modes.

It has also been observed that V_S affects the strength of U_z as an increase in ΔV_S encourages longitudinal displacement. Figure 4.10(b) shows that the hybridness, Hb_z of L_{01} (at fa=10μm.GHz; a=175μm, f=57.1429MHz) rises rapidly when the difference, ΔV_S, exceeds 2% and encourages the propagation of longitudinal modes.

Further, the fibre mentioned in Case 1 was considered again, but additionally V_L of the core was reduced progressively from 5933 m/s to the value of 5736 m/s, while the V_L of the cladding remains at 5933m/s. The variation of the phase velocity with the additional changes in the shear velocity difference between the core and cladding, ΔV_L, for a fixed ΔV_s = 139 m/s, is shown in Fig. 4.11(a). When ΔV_L = 0, this case is identical to that of Case 1. However, it can be observed that as ΔV_L is increased, the phase velocity of the S_{01} mode reduces uniformly as the modal confinement increases. The resulting variation of the hybridness, Hb_x, with ΔV_L is shown in Fig. 4.11(b) for the S_{01} mode, which increases progressively. Hence it can be seen that the modal properties for Case 3 are different from what is seen in Cases 1 and 2, as both ΔV_L and ΔV_S are non-zero and they become more hybrid in nature with both transverse and longitudinal displacement vectors, as shown in Figs 4.10-4.11(a) and (b).

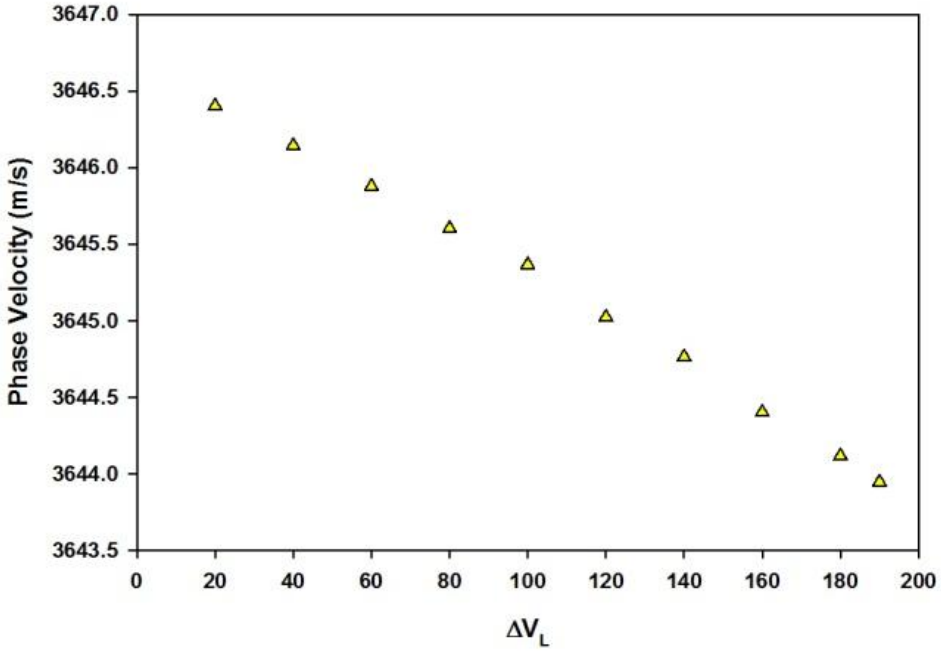

(a)

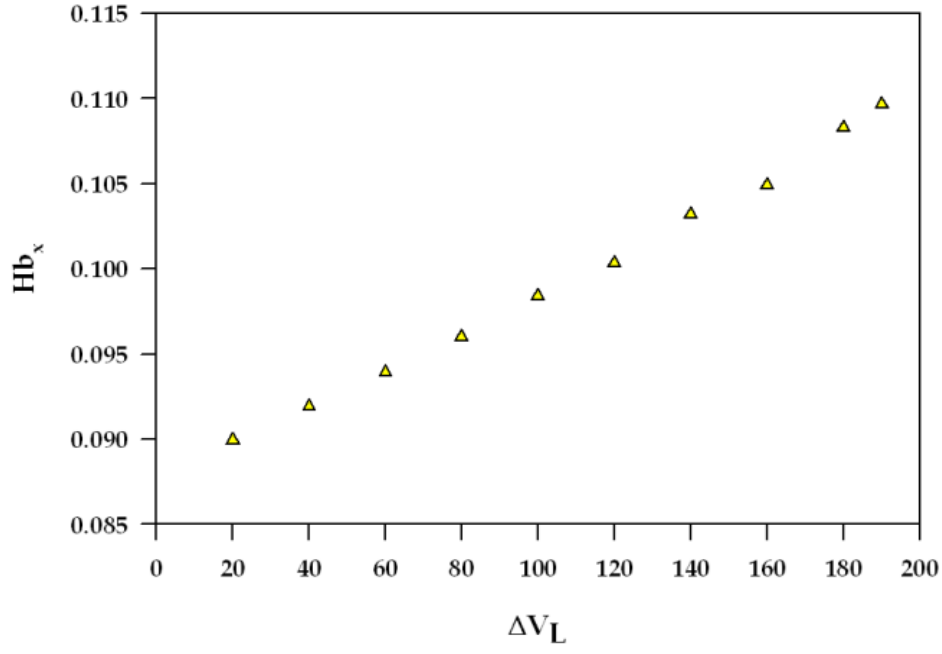

(b)

Figure 4.11. (a) Variation of phase velocity and (b) Hybridness of the S_{01} mode with the ΔV_L from Case 1.

4.3 Silica Nanowires

4.3.1 Silica Nanowire with an Acoustic Low Index Cladding

Over the last decade, sub-wavelength SiO_2 and silicon (Si) optical waveguides have been demonstrated for visible and infrared wavelengths, and these can be fabricated by using various taper-drawing techniques [Brambilla, 2004], [Chen, 2006]. Such waveguides operating in the single mode regime, have a wide range of applications in sensing and also exploit the optical nonlinearities. In these high-index contrast optical waveguides, where the light is strongly confined in the core, such optical waveguides can also confine both the shear and longitudinal acoustic modes which results in the formation of hybrid modes similar to those discussed earlier. In this study, an analysis of some of the acoustic modes in SiO_2 nanowires, surrounded by noble gases, has been carried out. The noble gas Xenon (Table 4.2) has been chosen here as the cladding material as it supports both transverse and longitudinal modes, compared to the situation experienced with air as the cladding material.

Table 4.2. Material properties of silica and xenon waveguide.

	Velocity (m/s)		Density (kg/m^3)	Elastic Stiffness (GPa)		
Material	***Longitudinal,*** V_L	***Shear,*** V_S	ρ	c_{11}	c_{12}	c_{44}
SiO2	5736	3764	2202	72.4495	31.1973	10.0549
Xenon	22303.7	15472.2	5.8971	2.93	1.89	1.41

The analysis of the SiO_2 nanowires for the acousto-optic interaction has divided into three parts. Firstly, the study of the optical waveguide to find the minimum value of the optical spot-size to achieve the strong guiding from the minimum radius at R=0.6 μm is in Section 4.3.2. Secondly, continue with the study of acoustic waveguide to find the suitable acoustic mode for the interaction between acoustic and optic is shown in Section 4.3.2 and the last part of Section 4.3.3 is to calculate the acousto-optic interaction by using phase matching and calculating the overlap integral of the SBS [Li, 2007].

4.3.2. Studied of the Optical Waveguide for the Designs of Acousto-optic Interaction

Initially, for this optical waveguide, the optical modes are analyzed by using a full-vectorial **H**-field formulation [Rahman, 1984] to determine the most suitable acoustic designs for the opto-acoustic interaction. The variations of the optical effective index and the optical spot-size area with the SiO_2 nanowire radius, R, are shown in Fig. 4.12. In this simulation, the refractive indices of the SiO_2 core and Xenon cladding are taken as 1.4651 and 1.0, respectively, for the operating wavelength, λ=1.55 μm.

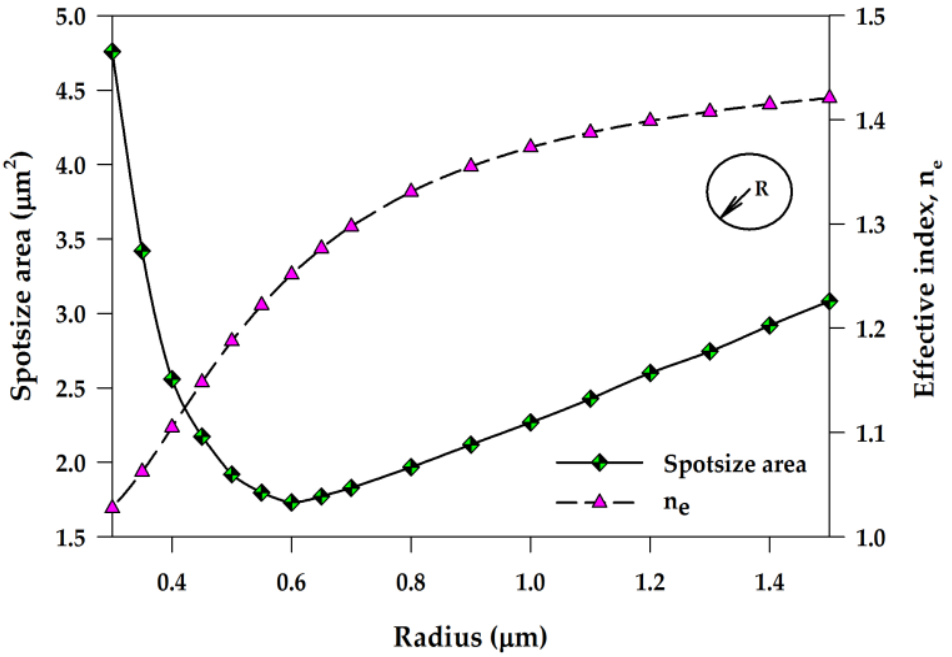

Figure 4.12. Variation of effective index and spot size area with the radius for silica nanowire at λ=1.55 μm.

In this work the spot-size area is defined as the area where the Poynting vector is more than $1/e^2$ of its maximum value for a given mode. It can be observed that the spot-size decreases with reducing radius and reaches a minimum value around R=0.6 μm. Correspondingly there is a high confinement of the optical power for this radius. A further decrease in the radius results in the rapid expansion of spot-size where a higher proportion of the optical field leaks into the air cladding as the mode approaches its cut-off condition.

4.3.3 The Analysis of the Acousto-optic Interaction with Waveguide Mode at Radius, R=0.6 μm

Subsequently, a value of the radius where R=0.6 μm has been considered for the analysis of the acoustic waves, as this corresponds to the minimum of optical spot-size to achieve possible stronger optical-acoustic wave interaction. The longitudinal and shear velocities of silica are taken as 5736 and 3625 m/s, respectively. Figure 4.13 shows three lower order acoustic modes guided at radius R=0.6 μm. The solid red line shows the bending mode, F_{11}, and at a lower propagation constant its phase velocity increases monotonically with the propagation constant until it reaches the saturation value of Rayleigh wave velocity, V_R=3565 m/s. The other two modes shown here are torsional-radial (TR_{21}) and axial radial (R_{01}) modes and their phase velocity reduces as propagation constant (or frequency) increases, which is similar to that shown for a steel waveguide in Chapter 3.7 [Hennion, 1996], [Thurston, 1987] and [Fahy, 2007].

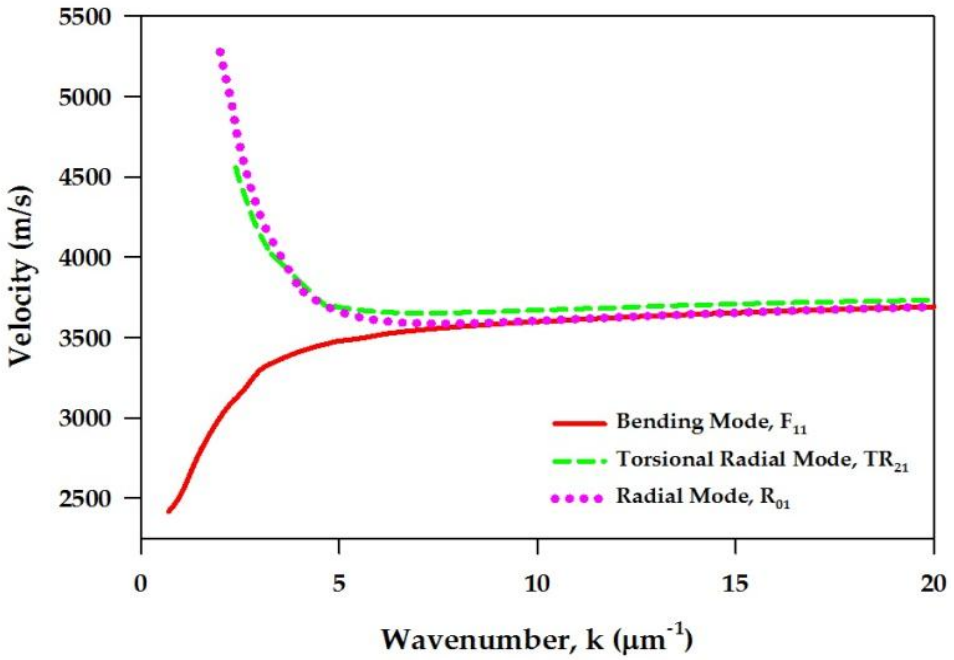

Figure 4.13. Variation of phase velocity with respect to the wavenumber for the bending, torsional-radial and radial modes in a silica nanowire.

In a way it is also similar to that seen with the optical field, the acoustic waves also spread both in the core and cladding and they can be classified as surface acoustic waves as both modes originate from the coupling of the shear and the longitudinal velocities, and appear to be concentrated near the boundary at a higher frequency as the modes transform to Rayleigh modes guided along the solid

interfaces. The TR_{21} and R_{01} are of particular interest as they cause GAWBS [Shelby, 1985]. It has also been observed that when the frequency decreases, the modal transverse field profile becomes more confined towards the centre of core for both the R_{01} and TR_{21} modes. As a results, the GAWBS can be effectively supported only at a lower value of the propagation constant (below k=10 μm^{-1}). In this regime, the effective phase velocity seems to deviate from V_S due to the coupling with V_L.

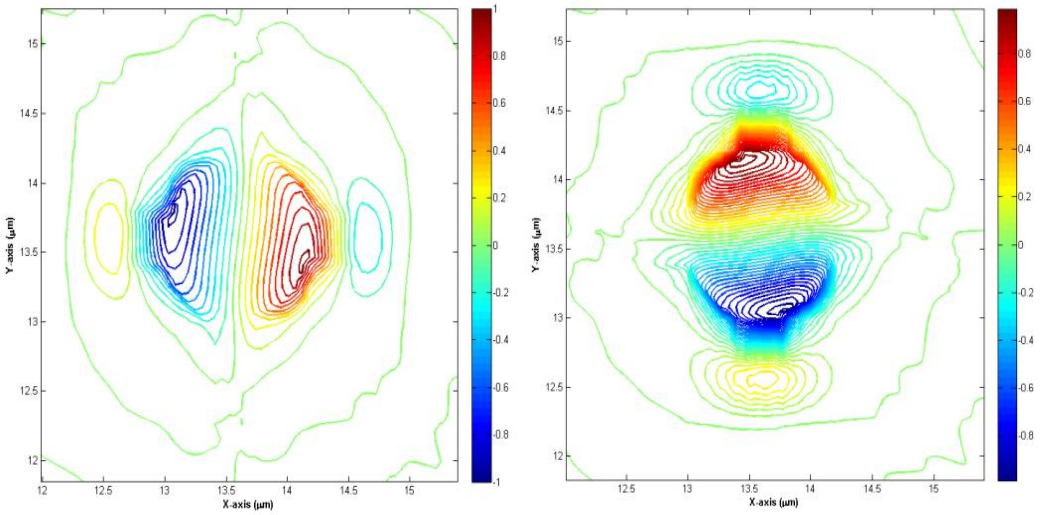

(a) (b)

Figure 4.14. Contour plot of (a) U_x and (b) U_y displacement at k = 10μm^{-1} of R_{01} mode.

In the case of the R_{01} mode, the value of U_z is large enough to cause SBS over a wide range of values of k. The hybridness ($Hb_y=U_{zmax}/U_{ymax}$) is 0.7 at k=10 μm^{-1} and it increases up to a value of 0.9 as the propagation constant reduces to a value of 2 μm^{-1}. All the three components of the displacement field plot of R_{01} mode has shown in Fig. 4.14. The displacement vector of U_x and U_y have one positive and one negative peak facing in the opposite direction and both have the similar intensity of 1.0, as shown in Fig. 4.14(a) and (b), respectively.

Figure 4.15 shows the vector plot $U_t = \overrightarrow{U_x} + \overrightarrow{U_y}$ of the Radial mode from the combination of the U_x and U_y displacement shown in Fig. 4.14(a) and (b). It can be observed that the vector plot is shown the radially outwards direction and periodically reverse its direction. It can also be noted that the maximum particle displacement is near the waveguide boundary.

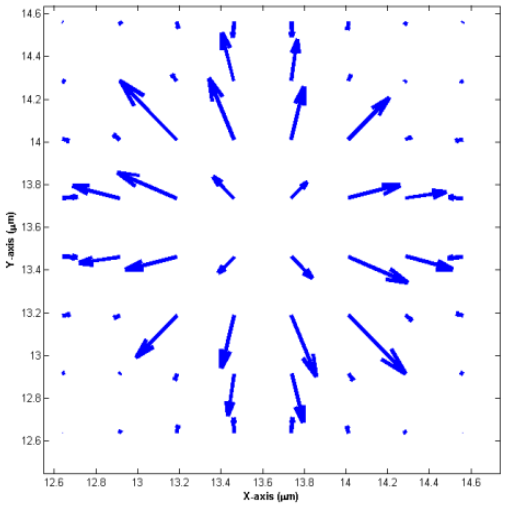

Figure 4.15. The U_t vector plot of the Radial mode (R_{01}) at k=10 μm^{-1}.

The dominant displacement U_z shown in Fig. 4.16(a) can be observed that the maximum value is outside the core region. Figure 4.16 (a) also shown the variation of U_z displacement which has the minimum value in the middle and Fig.4.16(b) the 2D U_z plot along the *x*-axis for the R_{01} mode at a propagation constant, k=10μm^{-1}, illustrates the rapid variation of U_z at the interface which changes sign and have a relatively flat displacement inside the core. Mesh divisions were limited due to the computer resources available. It appears to have some higher field near the material interface for a high index contrast guide. Similarly, localization of field (U values) at the interfaces has been observed when index contrast is higher (see Fig. 5.24).

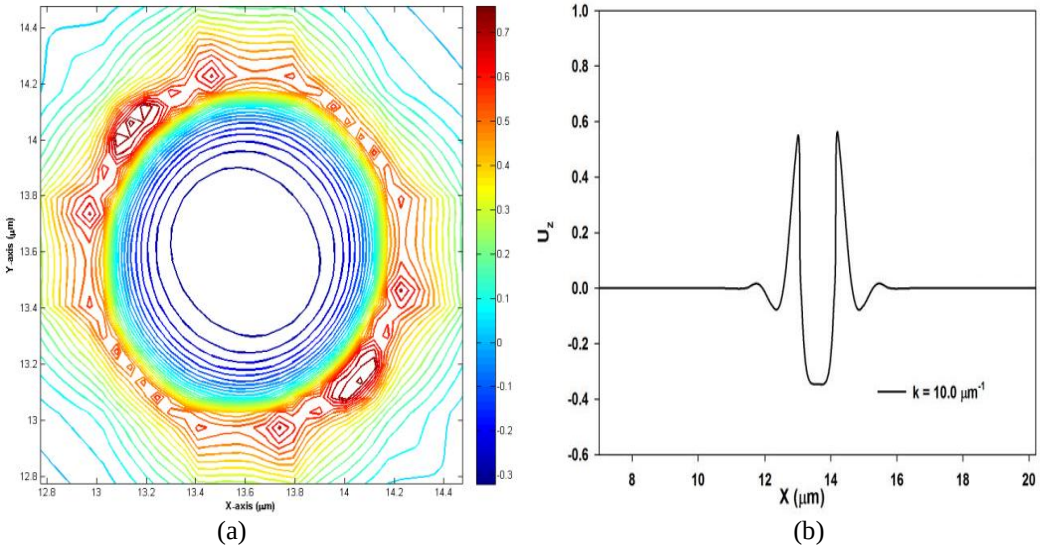

(a) (b)

Figure 4.16. U_z profiles of R_{01} mode at k=10 μm^{-1} (a) U_z displacement (b) U_z along with the contour plot of U_z.

4.3.4 Stimulated Brillouin Scattering (SBS) Generation

An intense light beam passing through an optical waveguide with a small cross-section, such as the nanowire shown here, produces an acoustic vibration due to electrostriction process resulting from the high electrical field of the optical wave.

The propagation of the generated acoustic wave is associated with the periodic distortion of the waveguide along the axial and transverse directions. This creates a periodic grating due to the material deformation and also the associated elasto-optic effects. This moving Bragg grating reflects the light – however since the acoustic wave is also travelling, the light is subject to a Doppler shift. For the R_{01} mode, its U_x and U_y profiles were although dominant, but asymmetric so, its overlap with dominant optical field were small. Its U_z profile of the R_{01} mode was very similar to the modal field profile of the fundamental optical mode, so their overlap was significant. Subsequently, the SBS frequency can be calculated using $k=2\beta'$ (the Bragg condition) [Agrawal, 2007], [Li, 2007], [Laude, 2005] where β' is the effective propagation constant of the fundamental optical mode.

Figure 4.17(a) shows the SBS frequency shift that would be obtained for the fundamental optical mode, for different radii of silica nanowires and operating at λ=1.55 μm, through the interaction of the R_{01} mode. The calculated values shown here do not correspond to those of the SBS observed in bulk SiO_2 which is closed to 11 GHz. Instead they arise due to the propagation of the surface acoustic wave (SAW) at the silica surface with phase velocity closely related to shear wave velocity over a much lower frequency range, given by 5.4-6.6 GHz. A similar frequency has been reported for photonic crystal fibres [Dainese, 2006] with small core diameters.

The existence of GAWBS and SBS *together* may cause a phenomenon defined as 'GAWBS in the backward direction stimulated by Brillouin scattering', which has previously been reported in optical fibres [Tanaka, 2004]. Here, Γ_{ij} is the normalized overlap integral between the optical and acoustic fields, where $H_i(x,y)$ is the optical field associated with the fundamental mode, and $U_j(x,y)$ is the j component displacement vector.

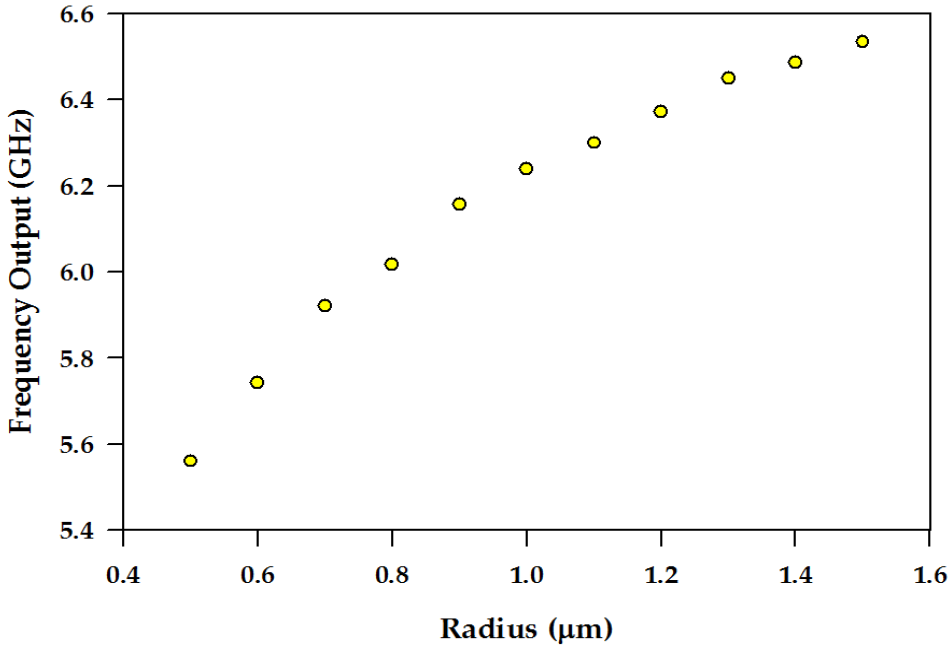

(a)

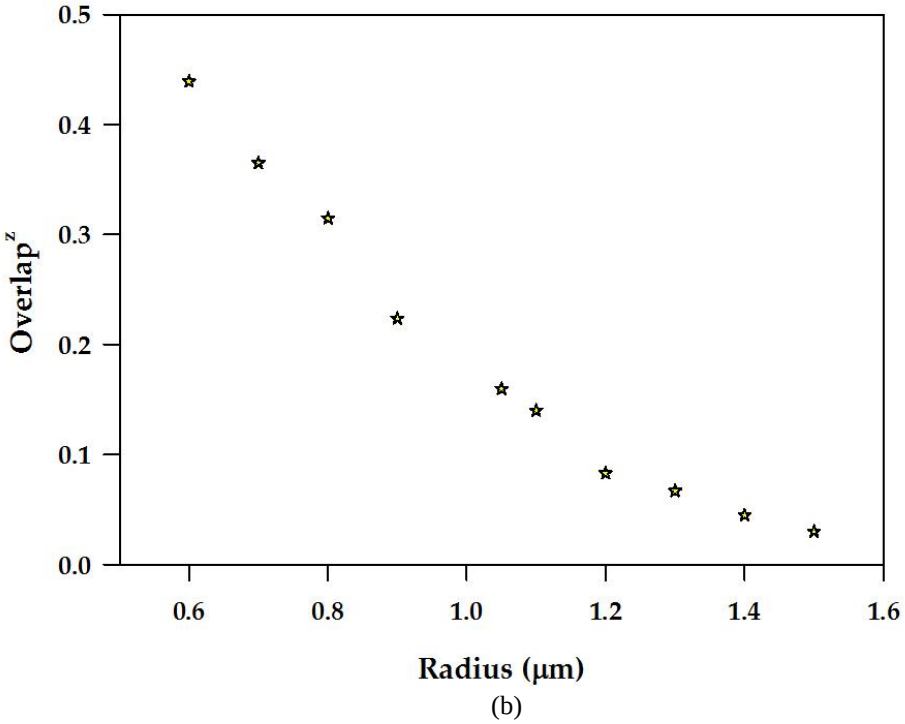

(b)

Figure 4.17. (a) The SBS frequency shift by the R_{01} mode, (b) The overlap between the acoustic and optical mode for different core radii.

The equation 4.1 shown the overlap integral equation where the overlap integral can be controlled by fibre refractive index profile design and acoustic velocity profile design.

$$\Gamma_{ij} = \frac{\int \left[\left| H_i^2(x,y) \right| \left| U_j(x,y) \right| \right]^2 dA}{\int \left| H_i(x,y) \right|^4 dA \int \left| U_j(x,y) \right|^2 dA} \tag{4.1}$$

The overlap between the optical and the acoustic modes plays a dominant role in the generation of the SBS power and this overlap in the SiO_2 nanorod has also been calculated from that reported in [Li, 2007] and this is shown in Fig. 4.17(b). It can be observed that as the radius has increased from 0.6 to 1.5 μm, the overlap ratio decreases from its highest value of 0.44 (at a radius of 0.6 μm) and this gradually reduces to 0.030 (at a radius of 1.5μm). For a higher core radius, the optical mode is more confined but the acoustic mode shows a minimum in the core and their overlap decreases.

4.4 Summary

In this Chapter, we presented numerically simulated results for the weakly and strongly guiding acoustic modes in optical waveguides. In Section 4.2, the numerically simulated results of shear and longitudinal modes are shown by dividing them into three cases. In Case 1, we have shown the purely transverse modes with the condition of the longitudinal velocity of the core is equal to that of the cladding. Case 2 showed the longitudinal mode by avoiding the mode being couple to each other. This was achieved by setting the shear velocity of the core equal to that of the cladding. In the last case studied Case 3, the effects of different core and cladding velocities were considered. When the ΔV_s and ΔV_L are not equal to '0', the result of the variation of the phase velocity of ΔV_s and ΔV_L are shown. In Section 4.3, the strong acoustic guiding silica fibre has shown the numerical results for the optical spot-size and acoustic modes such as bending, torsional, radial and torsional-radial. In this section, the acoustic and optical overlap interactions with the Radial mode (R_{01}) for U_z vector displacement are also studied. The SBS frequency shift and the overlap integral calculations are also shown.

Chapter 5

Silica Rectangular Waveguide

5.1 Introduction

Acoustic waves propagate in a medium due to the periodic displacement of the molecules inside the waveguide, and this being characterized by parameters such as the material density, elasticity, Young modulus, and Poisson ratio [Love, 1906], [Timoshenko, 1951], [Auld, 1973], [Mason, 1956], [Warlimont, 2005], [Levy, 2001] and [Ledbetter, 2001]. The particle displacement can be in the longitudinal direction or also in the transverse plane. When the core material in a waveguide is surrounded by a cladding, the propagation of the waves can be classified as being of the torsional, bending, flexural or longitudinal type [Thurston, 1978], [Bhaskah, 2003], [Engan, 1988] and [Safaari-Jazi, 1988]. The modes can be supported, provided at least one of the velocities (the shear or longitudinal velocities) of the cladding exceeds that of the core.

It is well known that the acoustic properties of optical waveguides allow for an interaction with the propagation of light through the related phenomena of

Brillouin scattering (BS), SBS and GAWBS [Agrawal, 2007], [Yu, 2003], [Shelby, 1985], [Dainese, 2006], [Li, 2007], [Liang, 2011] and [Chen, 2010]. Also. Analysis of such interactions is not trivial with the increased complexity of modern optical waveguide structures, exemplified by photonic crystal fibres and sub-wavelength waveguides, such as nanowires. In a way similar to the hybrid modes in high-index contrast optical waveguides, the acoustic modes in such optical waveguides are also complex. In these cases, a rigorous full-vectorial analysis [Koshiba, 1987], [Lagasse, 1987], [Stone, 1973] and [Vincent, 2005] is required for the accurate characterization of the acoustic wave propagation. In this chapter, the development of an approach based on the versatile FEM is reported and numerically simulated results of acoustic wave guiding in silica waveguides are also presented here.

5.2 Weakly Guiding SiO_2 Rectangular Waveguide

In this section, we have chosen a doped silica core surrounded by a pure silica cladding as a low-index contrast SiO_2 acoustic waveguide and this is studied by using the FEM to analyze the characteristics of the shear and longitudinal modes. The acousto-optic interaction has been studied and shown in the form of overlap integral calculation between acoustic and optic waves. The SBS frequency can be calculated by using $k=2\beta'$ (the Bragg condition) where β' is the effective propagation constant of the fundamental optical mode.

Table 5.1. Material properties of silica with 3% Ge doped silica.

	Velocity (m/s)		Density (kg/m^3)	Elastic Stiffness (GPa)		
Material	**Longitudinal, V_L**	**Shear, V_S**	P	c_{11}	c_{12}	c_{44}
3% Ge	5933	3677	2202	77.5115	15.117	31.1972
SiO_2	5933	3764	2202	77.5115	17.968	29.7718

The rectangular waveguides studied here would support non-degenerate modes resulted from the unequal width and height considered for these waveguides. Material data has been taken from [Jen, 1986] for pure silica cladding with its longitudinal velocity V_L is taken as 5933 m/s, shear velocity, V_S as 3764 m/s and the density, ρ, as 2202 kg/m^3 and for 3% Ge-doped core, these are taken as longitudinal velocity, V_L=5806 m/s, shear velocity, V_S=3677 m/s and density, ρ=2244 kg/m^3.

However, in this case study; it has been assumed that the longitudinal velocity of the core and cladding are equal to avoid the longitudinal modes in order to prevent coupling between the longitudinal and transverse modes. Therefore, material data has been taken from Table 5.1.

5.2.1 The Comparison of Two Different Dimensions of Waveguides

In this section, rectangular waveguides with height:width ratio of 1:2 have been considered. Two different waveguides have also been selected and the waveguide with height 1 μm and width 2 μm is identified here as H1W2 and with height 2μm and width 4 μm is identified here as H2W4.

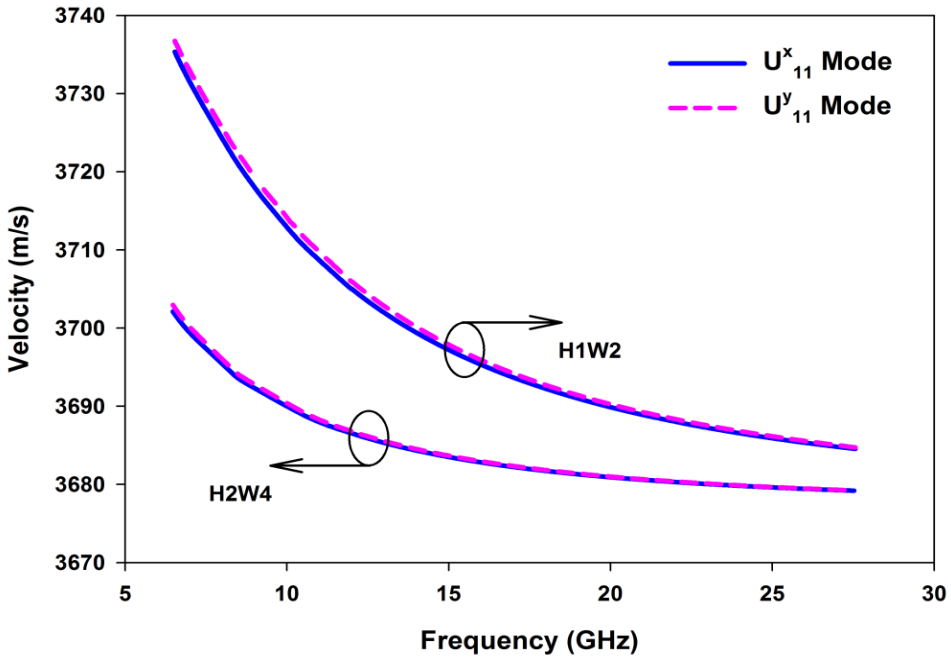

Figure 5.1. The variation of acoustic wave velocities with the acoustic frequencies for H1W2 and H2W4 waveguides.

Firstly, two dominant transverse modes have been studied here. The mode with dominant U_x displacement vector is identified as the U^x_{11} mode and similarly fundamental mode with dominant U_y displacement vector is identified as the U^y_{11} mode. It can be observed that for both waveguides (H1W2 and H2W4) and for both the modes (U^x and U^y modes) as the frequency is reduced the velocity of the acoustic waves are increased. It is also shown for the H1W2 waveguide that the velocity reduced rapidly from the cladding to the core velocity of 3677 m/s, while for the H2W4 waveguide velocity gradually reduced inside the core of the Ge-doped. It can

be noted that for both the waveguides velocity of the U^x_{11} mode is a bit lower than that of the U^y_{11} mode, as the width of the waveguide were larger than the height. For higher frequency, which most of the power is confined in the core, the wave velocity approached that of GeO_2-doped silica. On the other hand as frequency is reduced the velocity becomes more stable as shown in Fig. 5.1. For both the H1W2 and H2W4 waveguides, the velocity slowly decreased and then remains almost constant when the frequency reaches 25 GHz. At all the frequencies, H1W2 waveguide has higher shear wave velocity than the H2W4 waveguide.

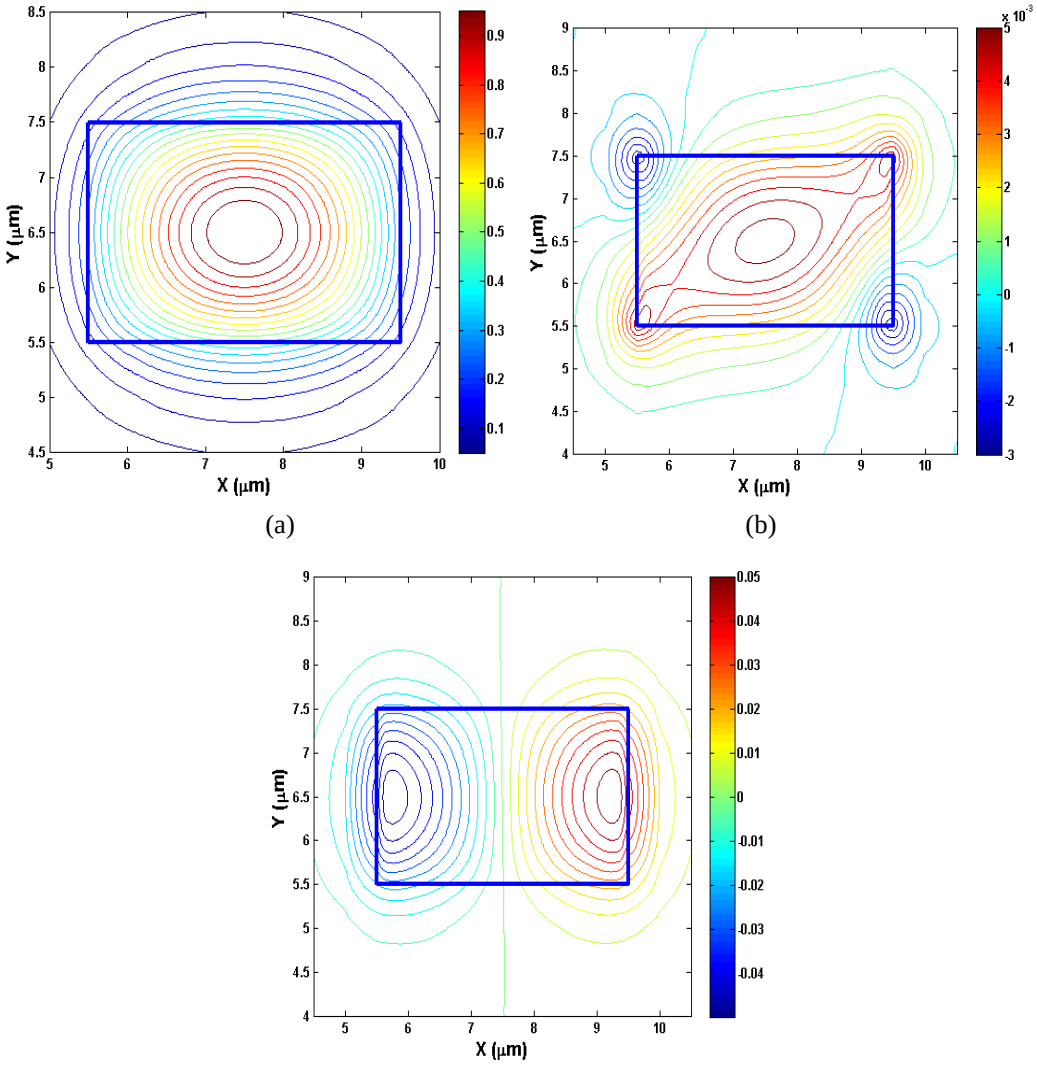

Figure 5.2. The contour plots of the displacement vectors for the U^x_{11} mode of the H2W4, (a) U_x, (b) U_y and (c) U_z displacement vector at the wavenumber k=11 μm^{-1}.

The dominant U_x displacement vector contour plot of the U^x_{11} mode for the H2W4 rectangular waveguide is shown in Fig. 5.2(a) when k=11 μm^{-1}. This mode has the maximum field value in the core and gradually decreased to the cladding. It is shown in Fig. 5.2(b) that the displacement profile of the non-dominant U_y has higher order spatial variations with four peaks at the four corners, but with a smaller intensity of 0.005. Figure 5.2(c) shows the U_z displacement vector plot which has the one positive and one negative peak at the left and right vertical interfaces. Its maximum magnitude is 0.05.

To display their spatial variation more clearly their variation along the transverse axes are shown next.

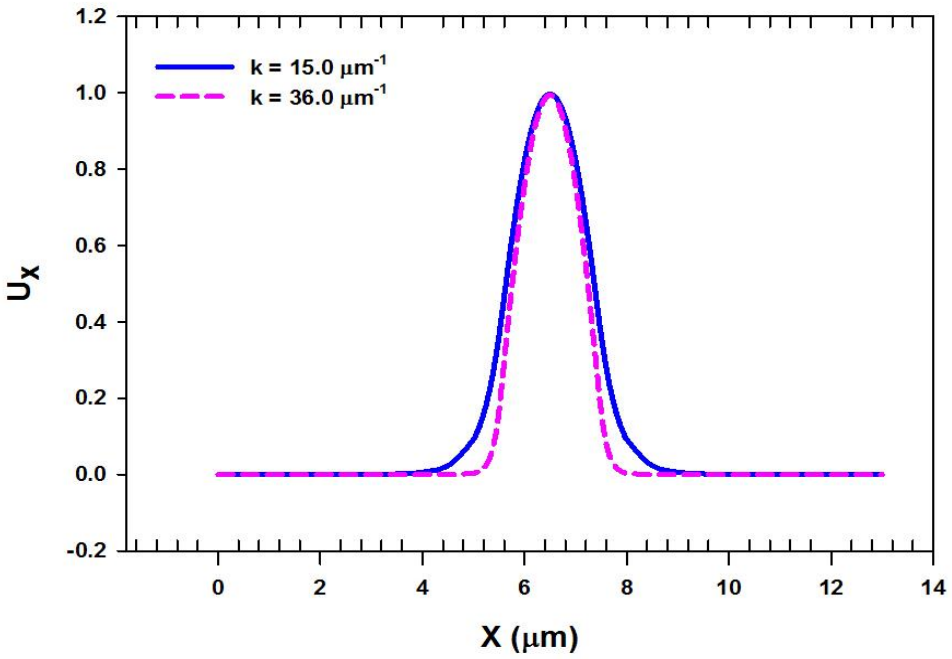

Figure 5.3. Variation of the U_x displacement vector of the U^x_{11} mode along the *x*-axis at k=15 μm^{-1} and k=36 μm^{-1}.

Figure 5.3 shows the variation of U_x displacement vector of the U^x_{11} mode along the *x*-axis for two different propagation constants. It can be observed that normalized maximum value is at the centre of the core for both the propagation constants, k=15 μm^{-1} and k=36 μm^{-1}. From the graph it can be noticed that at the lower propagation constant k=15 μm^{-1}, the U_x vector reduces slowly and spreads wider than at the higher propagation constant of k=36 μm^{-1}. The full mode width along the *x*-axis, where the field decays to *1/e* of its maximum value is 2.0067 μm

and 1.67021 μm, at the propagation constants, k=15 and 36 μm^{-1}, respectively. At a lower propagation constant, the U^x_{11} mode approaches its cut-off and the mode shape expands and as the propagation constant becomes higher, the mode is more confined inside the core of the waveguide.

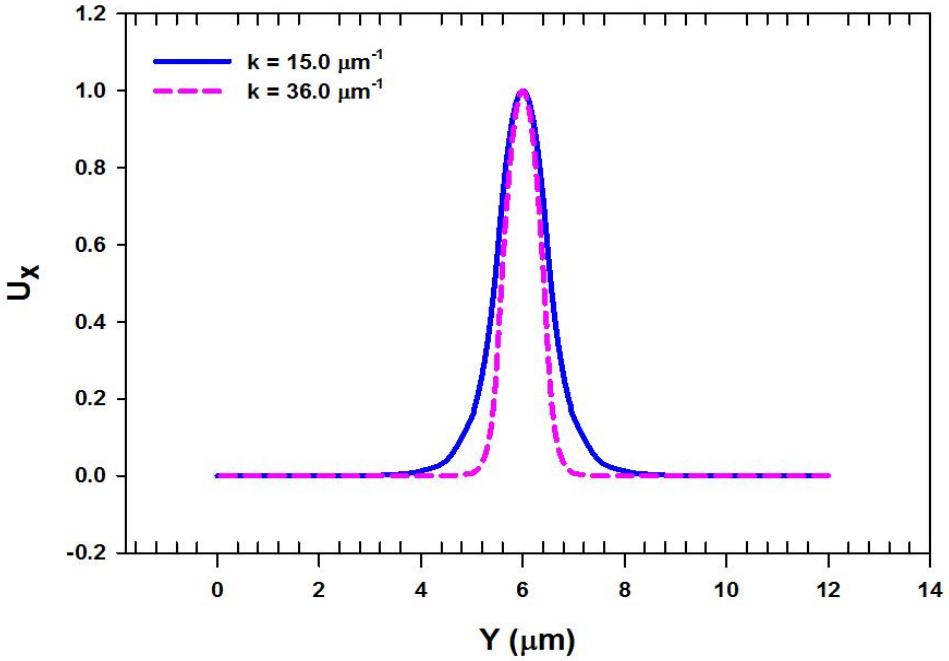

Figure 5.4. U_x displacement of the U^x_{11} mode along the y-axis at k=15 μm^{-1} and k=36 μm^{-1}.

Variation of the dominant U_x vector along the y direction is shown in Fig. 5.4 for the U^x_{11} mode. It can be observed that, for k=15 μm^{-1}, as shown by a solid line, the mode spreads more into cladding. In contrast, for a higher propagation constant, k=36 μm^{-1}, shows by a dash line the mode is more confined inside the core of the waveguide. The full mode width along the y-axis, where the field decays to *1/e* of its maximum value is 1.37098 μm and 0.96971 μm, respectively at the propagation constants, k = 15 and 36 μm^{-1}.

Contour plots of the U_x, U_y and U_z displacement vector components of the U^y_{11} mode are shown in Fig. 5.5 for the H1W2 waveguide at k=11 μm^{-1}. The displacement vector U_z of the U^y_{11} mode given in Fig. 5.5(a) shows a higher order spatial variation with one positive and one negative peak at the upper and lower horizontal interfaces. The intensity of U_z displacement is 100 times lower than that of the U^y displacement shown in Fig. 5.5(c). It is also shown that the maximum value of the U^y displacement vector is inside the core with maximum intensity of the U^y is

normalised to 1. The U_y displacement vector of the U^y_{11} mode has the highest intensity and the mode shape spreads more into the clad near the cut-off. The U_x displacement is elliptical shape with the four peaks at 4 corners of the waveguide as shown in Fig. 5.5(b). The magnitude of this U_x displacement vector is 0.006, which shows the lowest intensity of all the U^y mode at the propagation constant k=11 μm^{-1}.

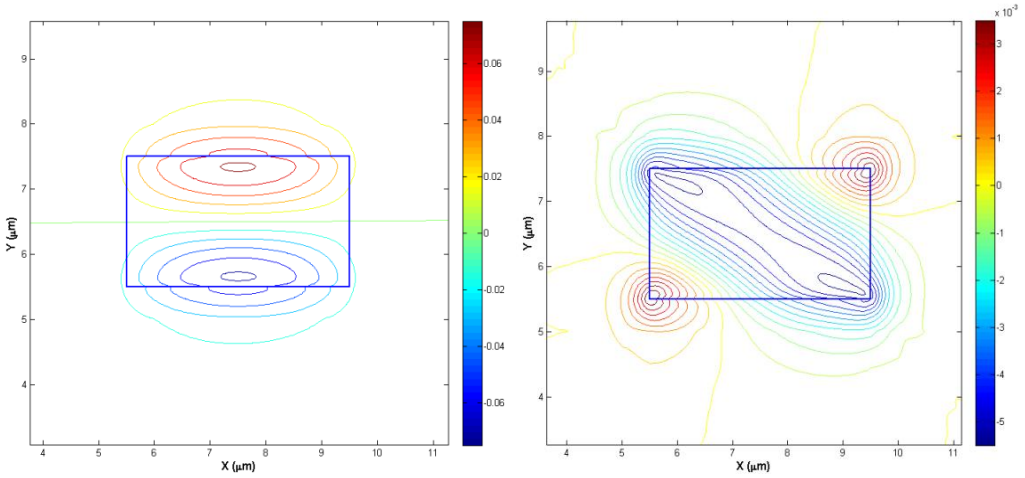

(a) (b)

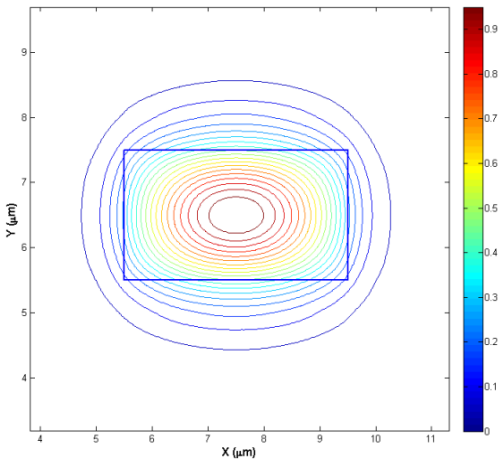

(c)

Figure 5.5. The displacement contour plot of U^y_{11} mode in H1W2 waveguide (a) U_z (b) U_x and (c) U_y displacement vectors at k=11.0μm^{-1}.

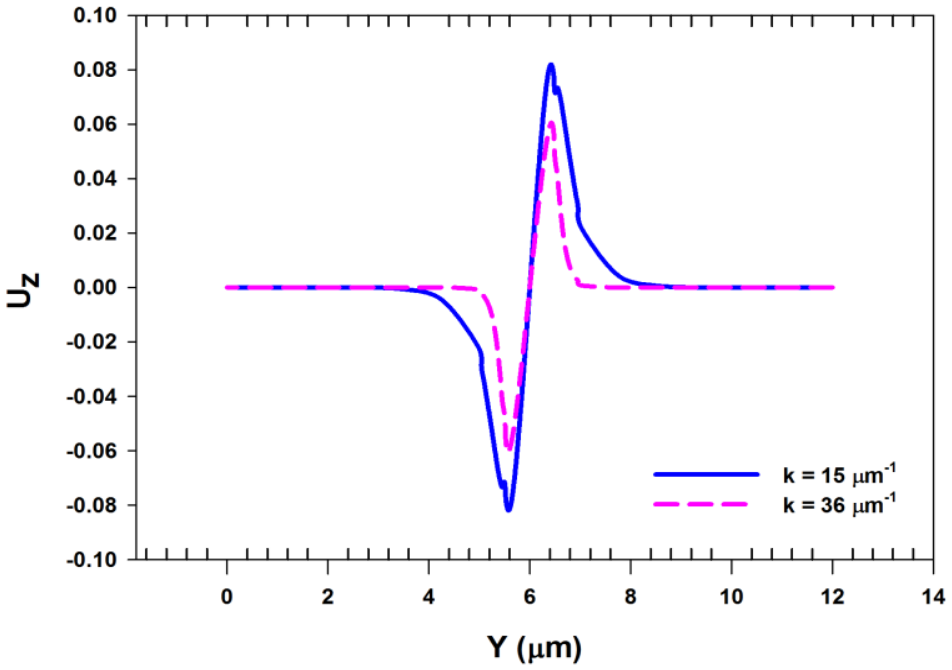

Figure 5.6. The U_z displacement vector of the U^y_{11} mode of H1W2 guide at k=15.0μm^{-1} and k=36.0μm^{-1}.

Variations of the U_z vector along the vertical direction with two different propagation constants are shown in Fig. 5.6 for the U^y_{11} mode of the H1W2 waveguide. For the lower k of 15.0 μm^{-1} the mode is expanded more in the cladding with two different polarity, one positive and one negative as shown by a solid blue line in Fig. 5.6. When the propagation constant is increased to k=36 μm^{-1}, the U_z displacement is more confined in the core of the waveguide as shown by the dashed line. Its magnitude is also reduced as the propagation constant is increased.

When the propagation constant increases the shape of non-dominant displacement vector transforms. The non-dominant U_x displacement vector of the U^y_{11} mode at propagation constants k=11, 20 and k=30 μm^{-1} of H2W4 are shown in Fig. 5.7. As the propagation constant is gradually increased the mode gets more degenerated. Mode degeneration appears when two different modes may have similar eigenvalues (here same velocity for a given k value).

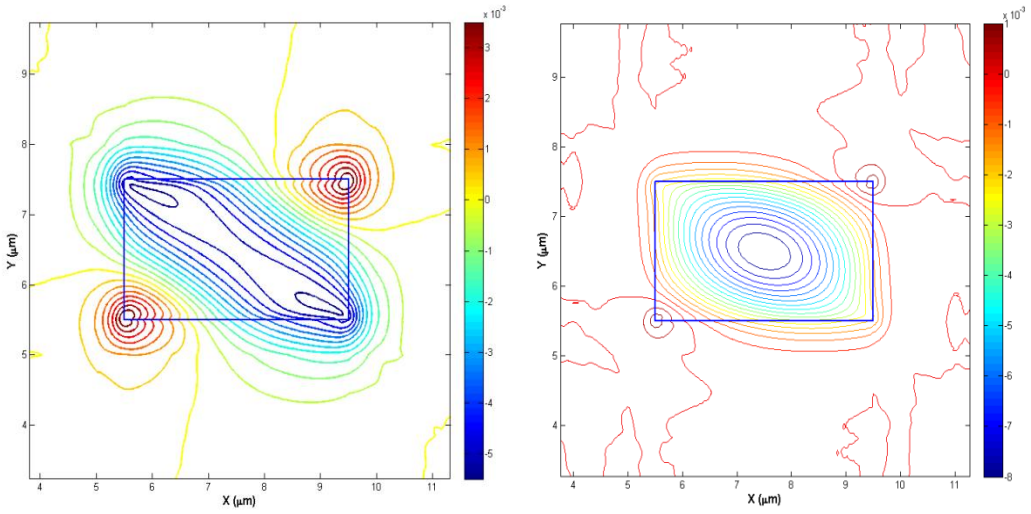

(a) (b)

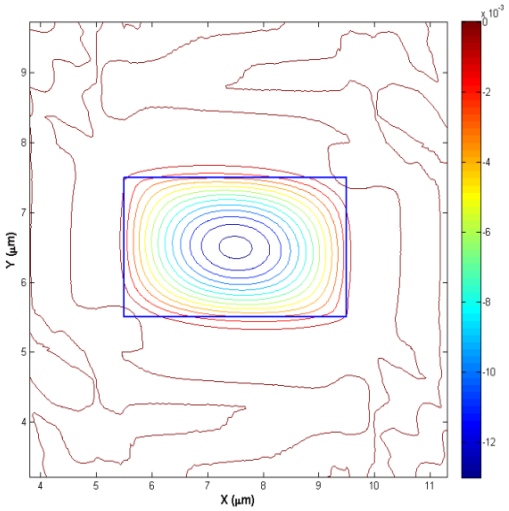

(c)

Figure 5.7. The contour plots of U_x displacement vector at (a) k=11 μm^{-1}, (b) k=20 μm^{-1} and (c) k=30 μm^{-1} of the U^y_{11} mode for the H2W4 guide.

The U_x displacement vector plot shows the higher spatial variations with four peaks at the four corners of the waveguide and as the propagation constant increases, mode starts transforming and starts merging to two peaks at two corners, as shown in Fig. 5.7(a) for k=11 μm^{-1} and in this case its maximum magnitude was 0.006. When k is increased further, the mode is gradually spread out to the corner of the waveguide at k=20.0 μm^{-1} as shown in Fig. 5.7(b) and its maximum magnitudes is increased to 0.008. At the wavenumber of k=30.0 μm^{-1}, the vector displacement is transformed further and retained its rectangular shape and the mode is confined inside the core and its maximum magnitude is increased to 0.013, as shown in Fig. 5.7(c). The

increasing of the propagation constants will also increased the magnitude of the non-dominant component.

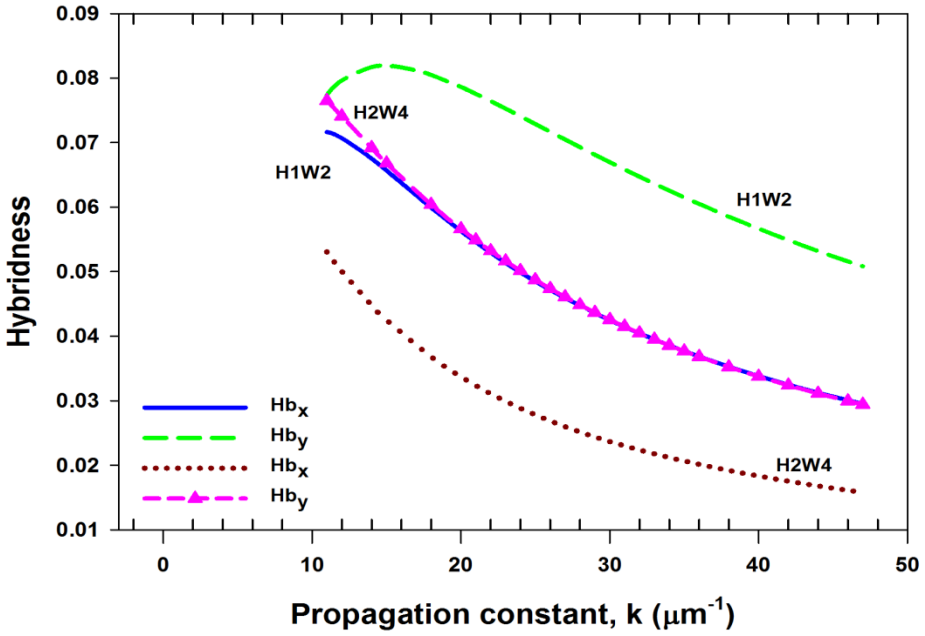

Figure 5.8. The hybridness of the rectangular acoustic waveguide with H1W2 and H2W4.

It is shown here that, for these transverse modes all the three components of its displacement vectors are present, so these are not 'pure' transverse mode. Modal hybridness is an important modal parameter, defined as the ratio of the non-dominant displacement vector (here U_z) over the dominant vector. Figure 5.8 shows the variation of different modal hybridness with the acoustic waveguide propagation constant of H1W2 and H2W4. The hybridness variation of the U^x_{11} and U^y_{11} modes of the H1W2 and H2W4 waveguides are shown here. The maximum magnitudes of the U^x and U^y eigenvectors for U^x_{11} and U^y_{11} modes are taken as 1. The hybridness of the Hb_x is identified as the maximum value of the U_z displacement vector over U^x vector for the U^x_{11} mode. It is similar for the Hb_y mode also the U_z displacement vector over U^y vector for the U^y_{11} mode. It should be noted that the Hb_y hybridness is higher than the Hb_x for the same guide and hybridness for smaller H1W2 guide is higher than that of the H2W4 guide. It can be noticed that U^x_{11} mode of H1W2 and U^y_{11} mode of H2W4 guides have similar hybridness. This could be due to the *x* side of H1W2 and *y* side of H2W4 being similar. Further investigation with a longer H4W8 guide was undertaken but in this case these two modes were degenerate (as dimension was large) and this reason could not be fully verified.

5.2.2 Effect of the Width Variation

The effect of the width of the rectangular waveguide but keeping the aspect ratio constant at 1:2 for a fixed k=25.0 μm^{-1} is studied in this section.

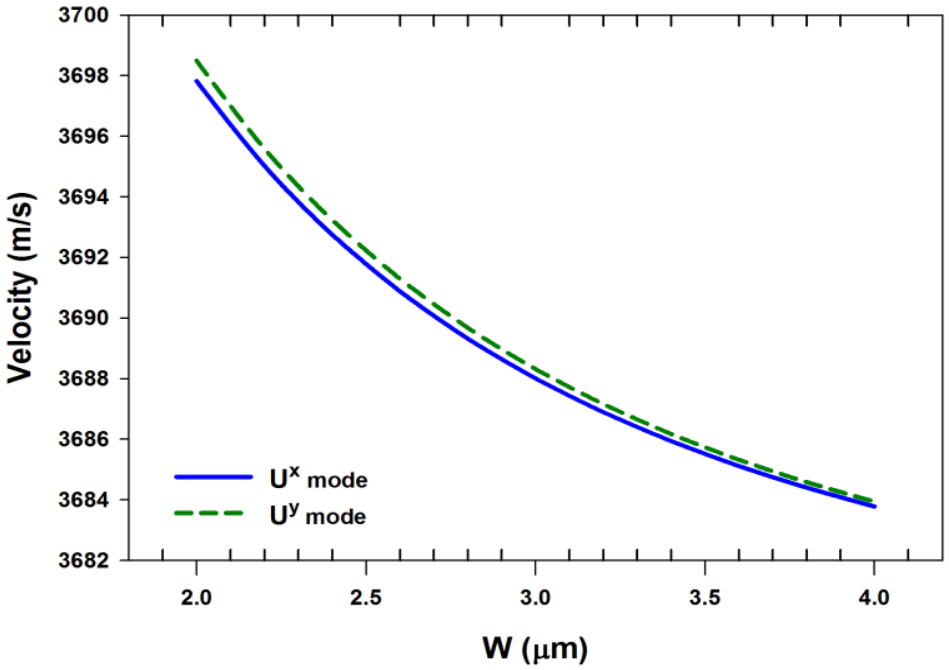

Figure 5.9. The displacement plots of U^x and U^y modes at k=25.0 μm^{-1} by varied width from 2 to 4 μm.

Variation of the phase velocities of both the U^x_{11} and U^y_{11} modes with the waveguide width are shown in Fig. 5.9. It can be observed here that as W is increased the wave velocity decreases and approaches that of 3677 m/s, the shear velocity of the core. Similarly, as width is reduced the velocity is approached that of the cladding velocity of 3700 m/s. However, as the dimension increased velocities for the U^x_{11} and U^y_{11} modes are more closer, which maybe equivalent to the reduction of birefringence of optical waveguides. Their velocity ratio of the U^x_{11} mode over U^y_{11} mode at width 2 μm and 4 μm are 99.98% and 99.996%, respectively.

5.2.3 Variation of the Waveguide Widths with Different Frequencies

The variation of wave velocities at three frequencies of *f*=10 GHz, *f*=15 GHz and *f*=20 GHz with the width have been studied for the U^x_{11} mode but with fixed aspect ratio of 1:2.

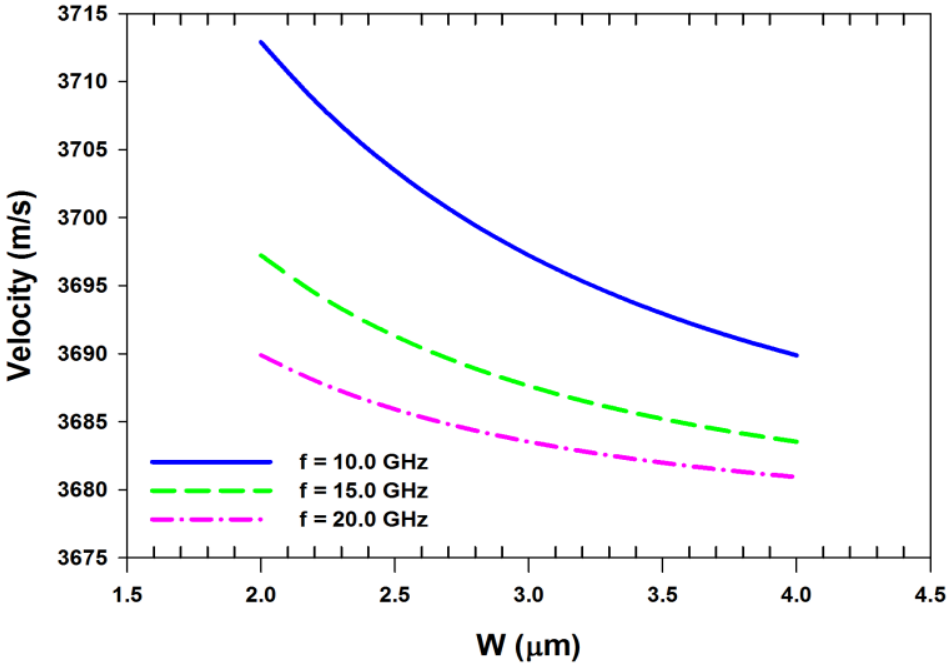

Figure 5.10. Variation of the phase velocity of the U^x_{11} mode at three frequencies of 10 GHz, 15 GHz, and 20 GHz with the width varied.

Figure 5.10 shown the variations of the phase velocity of the U^x_{11} mode at three frequencies with various widths. The width is varied from 2 μm to 4 μm, but keeping their aspect ratio fixed at 1:2. At the minimum frequency value of 10 GHz and with the minimum width of 2 μm, the velocity is 3714 m/s, as this is very close to shear velocity of the cladding and gradually decreased to the shear wave velocity of the clad 3692 m/s when width is at 4 μm. It can be noticed that when the width is increased, velocities for all the three frequencies are decreased. Similarly, at lower frequencies, velocities are increased.

Next the effect of the waveguide width on the modal hybridness is studied.

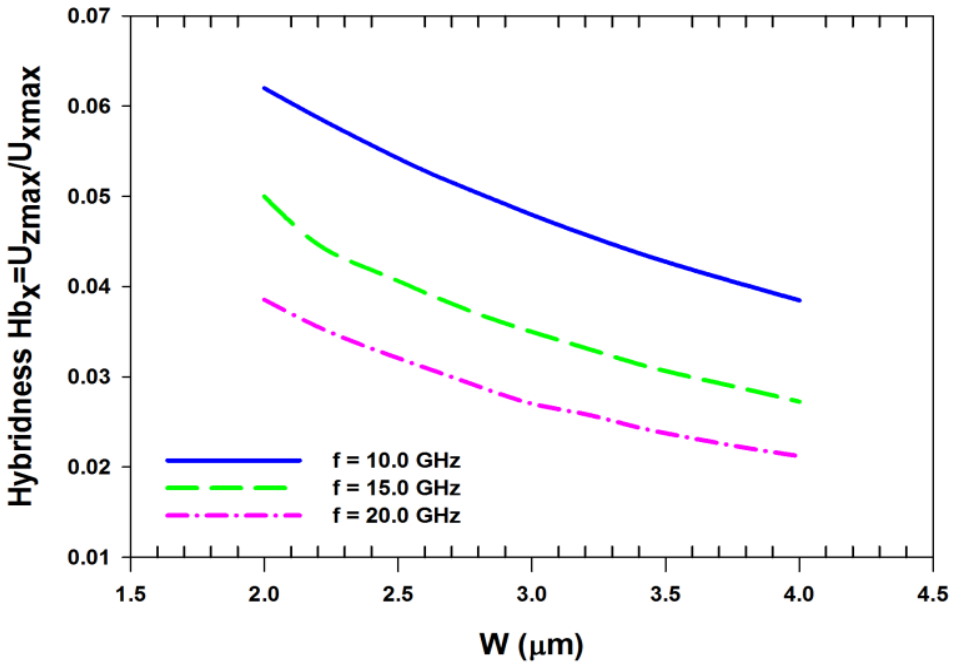

Figure 5.11. The hybridness of the three different input frequencies at *f*=10 GHz, *f*=15 GHz and *f*=20 GHz.

The hybridness of the U^x_{11} mode is shown in Fig. 5.11 for three different frequencies, 10 GHz, 15 GHz and 20 GHz. It can be observed that as the width is decreased, the modal hybridness for this U^x_{11} mode increases. It is also shown here that modal hybridness decreases when operating frequency is increased. The solid line shows the maximum hybridness is 0.062 at the acoustic *f*=10 GHz, on the other hand the dash line shows the hybridness value of 0.05 at the acoustic *f*=15 GHz and the lowest hybridness of 0.042 when the acoustic *f*=20 GHz, as shown by a pink chained line. When width of the waveguide is at its smallest at 2 μm, it shows the highest hybridness values for all frequencies and when the width of the waveguide is increased, the hybridness is reduced linearly for all three frequencies.

5.2.4 Results of the Overlap Between Optical and Acoustic Modes

Next, optical modes of these silica waveguides are studied by using the **H**-field formulation. In here, the effective area, effective index of Ge-doped optical waveguides are shown and later on the calculation of the SBS frequency shift of the acoustic mode (by using $k=2\beta$) and the acousto-optic overlap calculation between acoustic and optical modes are also presented in the last section. Firstly, refractive indices of the Ge-doped silica core and pure silica cladding are taken as 1.44836 and 1.44, respectively [Laude, 2012], for an operating wavelength, λ=1.55 μm.

Optical mode are classified as quasi-TE or quasi-TM modes as they have all the six components of the **H** and **E** fields. The **H** and **E** field components in the *x*, *y* and *z* direction for the fundamental quasi-TE (H^{y}_{11}) mode is shown next:

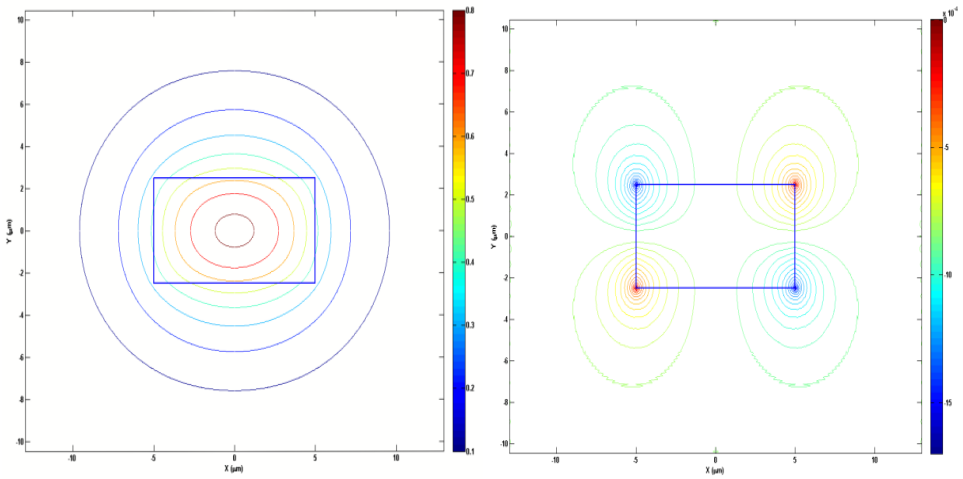

(a) (b)

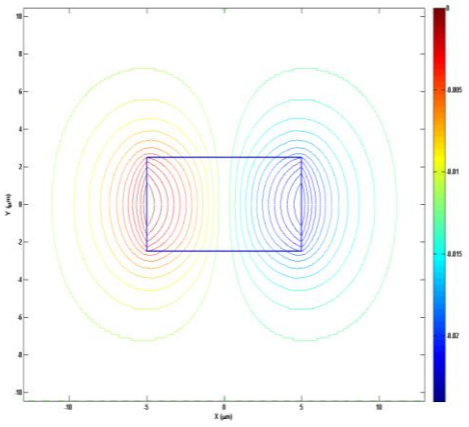

(c)

Figure 5.12. The optical mode of H5W10 (a) E_x (b) E_y and (c) E_z field plots of the H^{y11} mode.

It can be seen that the E_x electric field component is dominant for this quasi-TE (H^y_{11}) mode with its value normalized at 1 which is shown in Fig. 5.12(a), with its maximum field in the middle of the waveguide. The E_y field profile has four smaller peaks at the four corners of the rectangular waveguide as shown in Fig. 5.12(b) and with the smallest magnitude of 10^{-4}. The E_z field shown in Fig. 5.12(c) shows one positive and one negative peaks at the left and right vertical interfaces with its maximum value was 0.02.

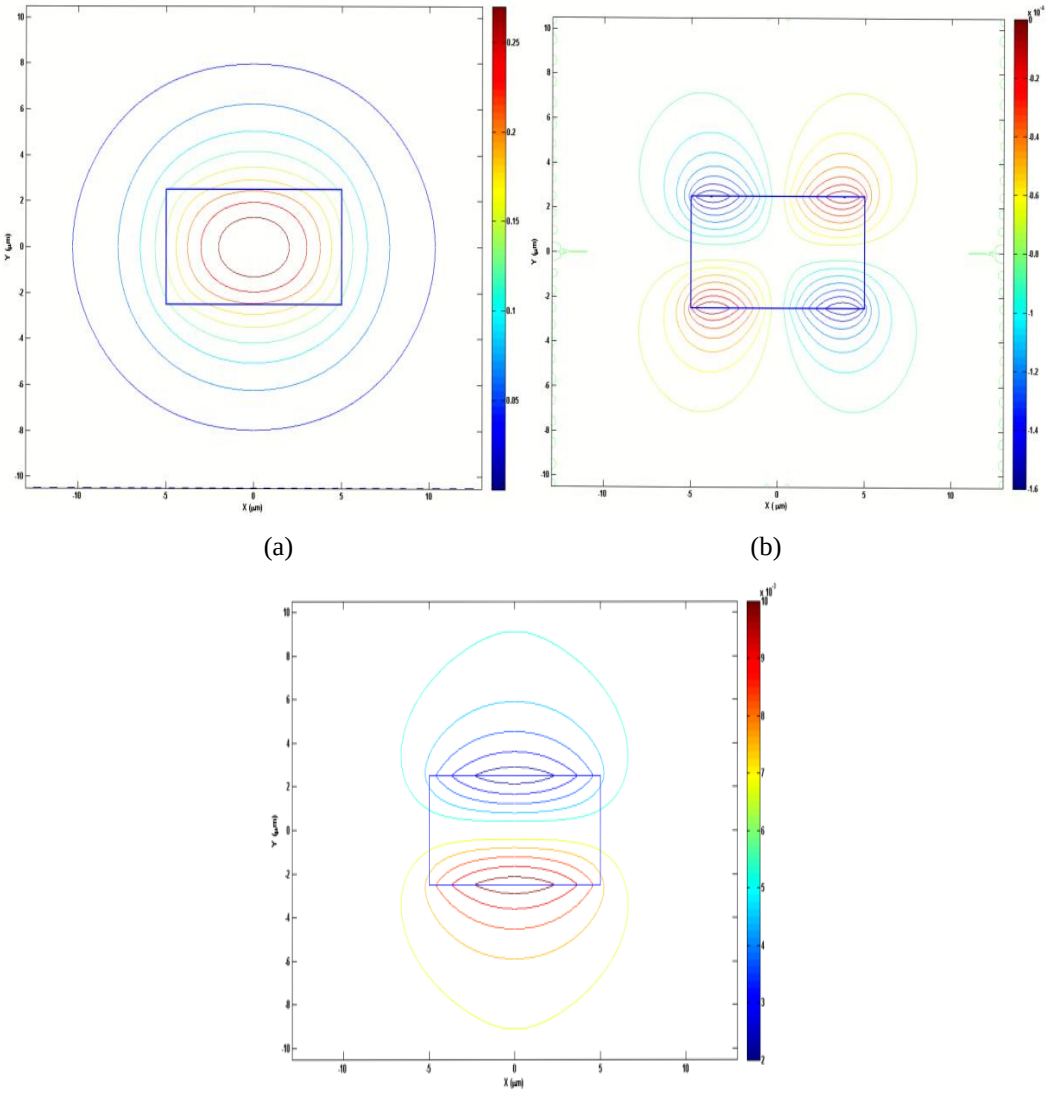

(a) (b)

(c)

Figure 5.13. The magnetic field (a) H_y (b) H_x and (c) H_z field profiles for the quasi-TE mode of H5W10.

The dominant H_y magnetic field profiles of the quasi-TE (H^y_{11}) mode shown in Fig. 5.13(a), which shows a Guassian shaped profile with maximum field in the middle of the waveguide. Figure 5.13(b) shows the spatial variation of the non-

dominant H_x field and clearly shows four peaks at the four corners of the waveguide with the smallest magnitude of 1.5×10^{-4}. The H_z profile is shown in Fig. 5.13(c) which illustrates the H_z displacement has peaks at upper and lower horizontal interfaces with the magnitude of 10^{-3} time of the dominant H_y field.

Variations of the effective index of the fundamental quasi-TE and TM modes are shown in Fig. 5.14, the effective index, n_{eff} can be defined as:

$$n_{eff} = \frac{\beta_0}{k_0} \tag{5.1}$$

where β_0 is the propagation constant of a given mode and k_0 is the free space wavenumber, defined as:

$$k_0 = \omega(\varepsilon_0\mu_0)^{1/2} = \frac{2\pi}{\lambda} \tag{5.2}$$

In this case, ε_0 is the free space permittivity, μ_0 is the free space permeability of the medium and ω is the angular (radian) frequency.

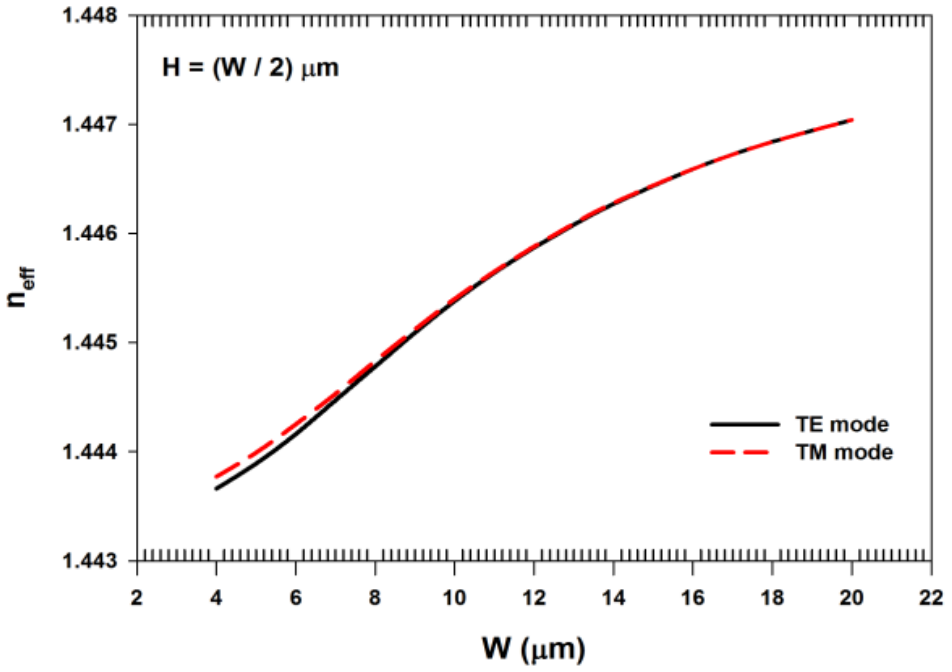

Figure 5.14. The n_{eff} variation of the quasi-TE and TM modes with the width of the waveguide.

It can be observed that as the width is increased, the effective index for both quasi-TE and TM modes are also increased as shown in Fig. 5.14. It can also be observed that the effective index of the quasi-TE mode, shown by a solid line is lower than that of the quasi-TM mode.

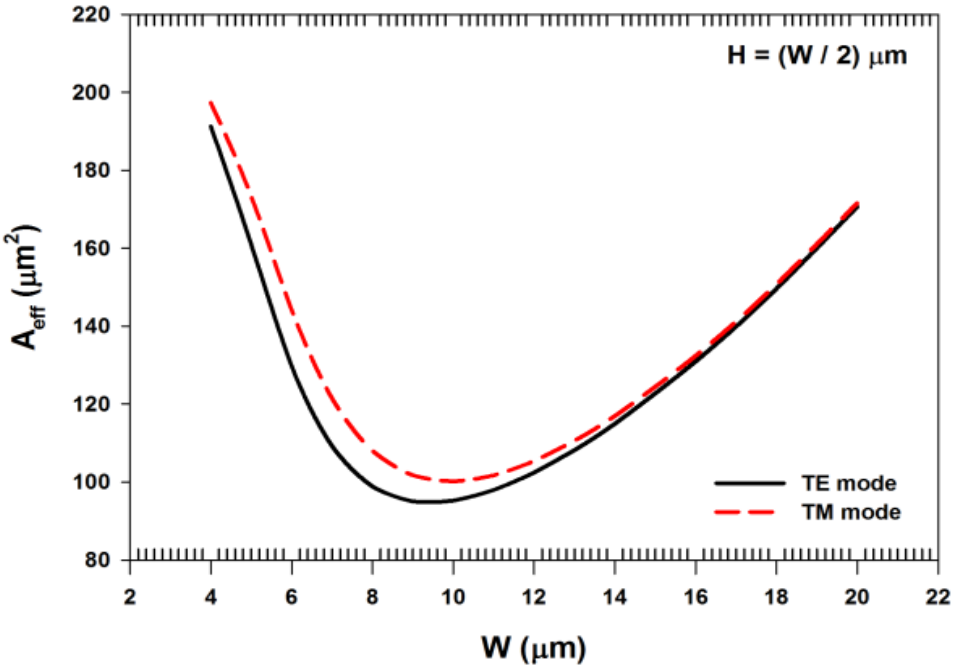

Figure 5.15. The A_{eff} variation of TE and TM modes with the width of the waveguide.

Next, the variation of the mode area, given here as effective area is studied. Mode size area or effective area is an important design parameter for various applications and Fig. 5.15 shown the variation of the effective area (A_{eff}) with the waveguide width for both quasi-TE and TM modes. Following the second moment of intensity distribution (recommended by ISO Standard 11146), the definition of A_{eff} [ISO 11146, 2005] can be given by:

$$A_{eff} = \frac{\left(\iint_{\Omega} |E_t|^2 \, dxdy\right)^2}{\iint_{\Omega} |E_t|^4 \, dxdy} \tag{5.3}$$

where E_t is the transverse electric field vector and the integration is carried out over the whole cross-section of the waveguide, Ω.

It can be observed in Fig. 5.15 that as the width is reduced, the effective area, A_{eff}, is reduced initially, however, further reduction of width resulted the effective area being increased as mode approaches its cutoff condition and spreads more into the cladding.

For the two degenerated U^x_{11} and U^y_{11} modes, their dominant U_x or U_y displacement vector profiles were very similar to the modal field profile of the fundamental optical mode, so their overlaps were significant. The SBS frequency can be calculated using k=2β' (the Bragg condition) [Agrawal, 2007 and Bhaskah, 2003] where β' is the effective propagation constant of the fundamental optical mode. Figure 5.16 shows the SBS frequency shift that would be obtained for the fundamental optical TE mode, for different width of Ge-doped SiO_2 and operating at λ=1.55 μm, through the interaction of the U^x_{11} and U^y_{11} modes.

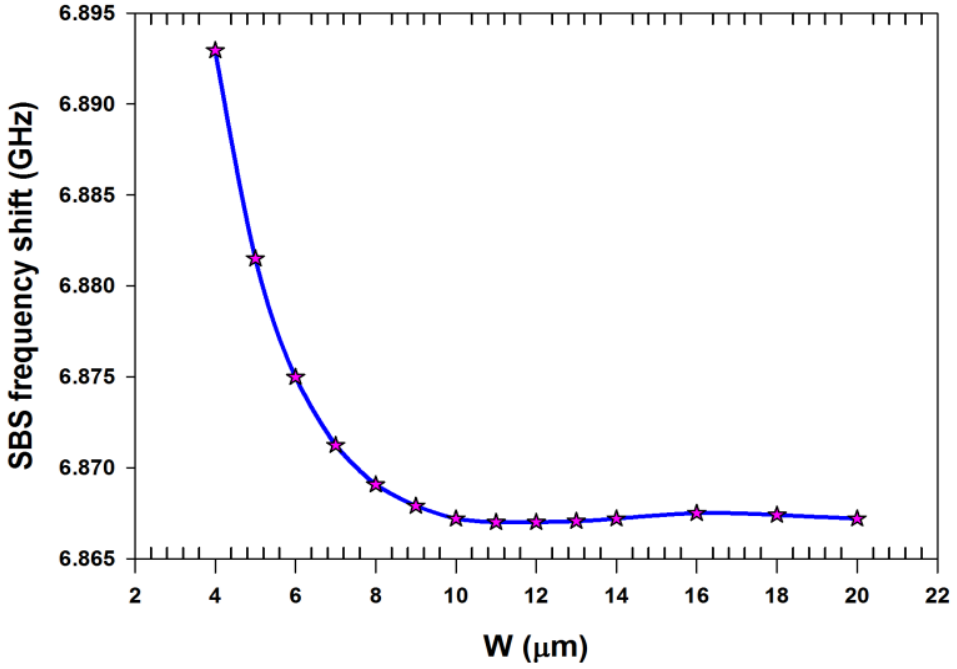

Figure 5.16. The SBS frequency of the acoustic waveguide U^x_{11} mode when k=2β of the quasi-TE optical mode.

The SBS shift has shown that the maximum value of the frequency shift is at its smallest width of the waveguide at 4 μm and frequency is rapidly decreased while the width of the waveguide is gradually increased as shown in Fig. 5.16. When the width is larger than 10 μm, the SBS frequency is nearly constant at 6.8655 GHz. It can be noticed that by increasing the waveguide width, it will increase the n_{eff}. Also the optical β_0 and phase match acoustic propagation constant (k_a) will increase which in turn will decrease the SBS frequency.

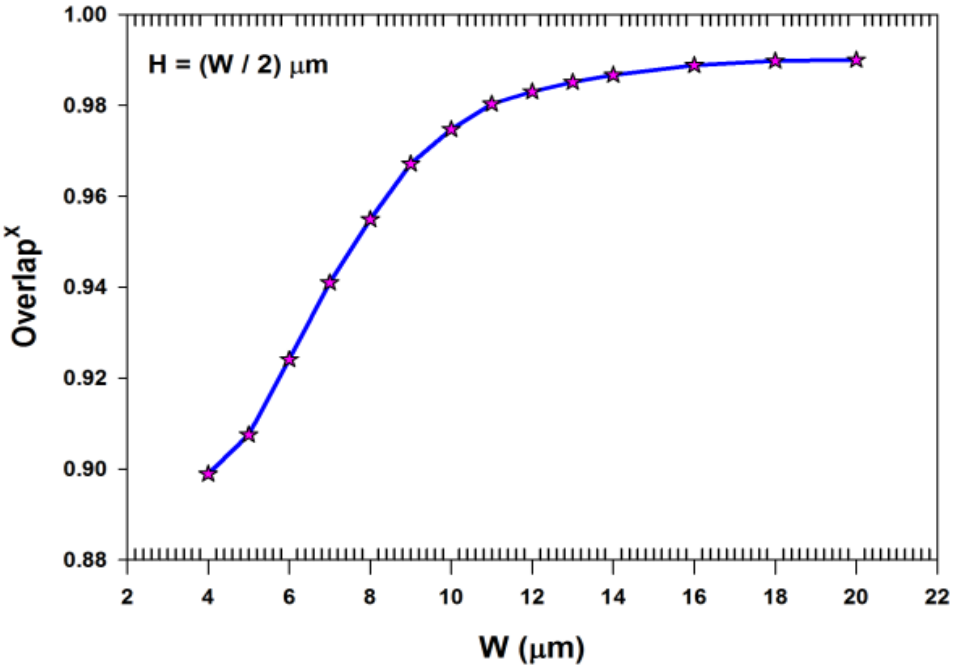

(a)

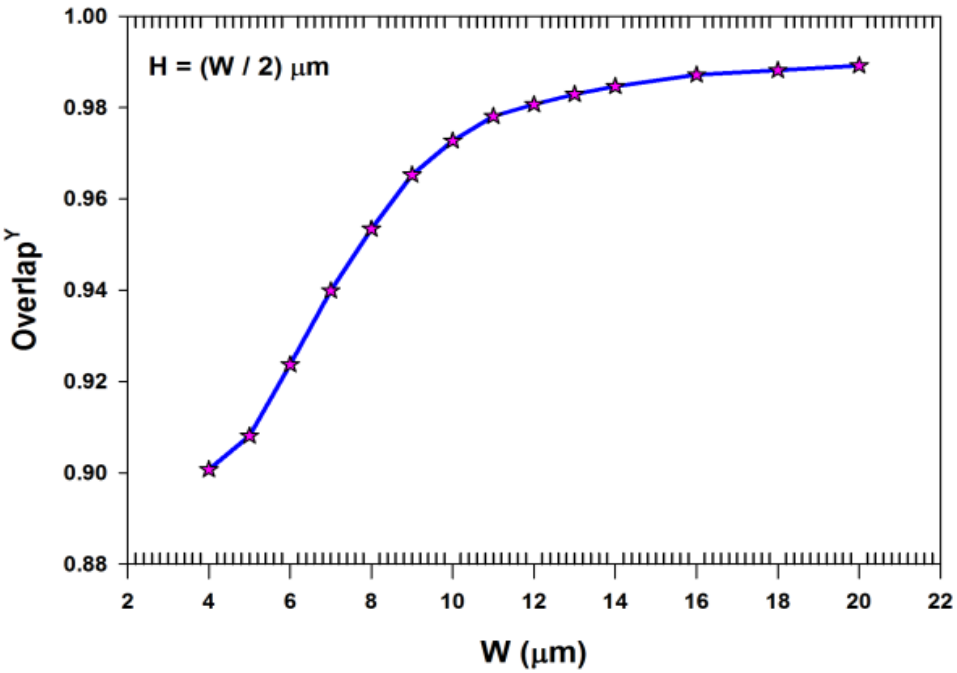

(b)

Figure 5.17. Variation of the overlap integral of the optic quasi-TE mode with the acoustic U^x_{11} and U^y_{11} modes of (a) overlap^x with acoustic U^x_{11} mode and (b) overlap^y with acoustic U^y_{11}mode of the U_x and U_y displacement vectors with width.

Although the SBS frequency will tell us the results of the optical-acoustic interaction, however, their strengths are depended on the overlap between modes. Overlap^x is the overlap of the U_x displacement vector of the U^x_{11} mode with the H_y field of the quasi-TE mode and similarly overlap^y is the overlap of U_y displacement

vector of the U^{y}_{11} mode. The overlap interaction of the transverse mode of the U^{x}_{11} of the U_x displacement vector shown here as the propagation of the shear mode is perpendicular to the *z*-axis. The overlap integral calculation of the acousto-optic interaction is shown in Fig. 5.17(a), it represents the overlap interaction of the U_x displacement vector. It can be observed that as the width of the waveguide is increased the overlap integral also increases monotonically. Figure 5.17(b) shows the overlap integral with the U_y displacement vector with the dominant optical TE mode. It can be noticed that the overlap shown in Fig. 5.17 (a) and (b) the characteristic of the graph shows the similarity between $overlap^{x}$ and $overlap^{y}$, in which when the width is increased the overlap is increased. This implied that the mismatch between acoustic and optical mode is minimum as the width is increased.

As the dominant displacement vector component of the U^{y}_{11} or U^{x}_{11} modes and that of the quasi-TE or TM modes were similar, interactions between these modes, both their overlap integral or SBS frequencies were not only higher but also similar. Therefore, the overlap integral represented the match between acoustic and optical modes. If the overlap integral approaches to a value of 1 then the match between acoustic and optical modes is at the maximum. In contrast, if the overlap integral is quite low it indicates that the mismatch between acoustic and optical modes are quite high as shown in Fig. 5.17(a) and (b).

5.3 Strongly Guiding Silica Rectangular Waveguide

The acoustic modes of strongly guided structure are studied in this section.

5.3.1 Waveguide Structure

Silica (SiO_2) is the most widely used material for optical waveguides because of its extremely low loss value and in this study a simple strongly guiding rectangular planar SiO_2 waveguide is considered and its longitudinal and shear velocities are taken as 5736 m/s and 3625 m/s, respectively. A low acoustic index material (with larger acoustic velocities) is needed as the surrounding cladding material for the guidance of both the longitudinal and shear modes. In this case, the well-studied example of xenon gas is considered, which is closed to air, but as this is known to support both the longitudinal and transverse modes. The longitudinal and shear wave velocities in xenon are taken as 22303 m/s and 15472 m/s, respectively. Any optical material with similar higher longitudinal and shear velocities is expected to give similar acoustic modes. The horizontal (Width) and vertical (Height) dimensions of the SiO_2 waveguide are taken as 1.5 μm and 1.2 μm, respectively.

The most important modal parameter, the modal dispersion properties of an acoustic waveguide show the relationship between the frequency or the angular frequency, propagation constant and phase velocities. Variations of the modal phase velocities with the frequency for the first 5 modes are shown in Fig. 5.20. These are identified as the Bending 1 (B1), Bending 2 (B2), Torsional (T1), Radial (R1) and Torsional-Radial (TR1) modes [Thomas, 1979 and Bhaskar, 2003]. Their detailed mode profiles are shown later. It can be observed that for the two bending modes as the modal frequency is increased, their phase velocities increase and approach the Rayleigh wave velocity asymptotically. Later it will be shown that as the wavenumber or the frequency is increased, the modal material displacements move closer to the interfaces. These surface waves propagating along the interface of a solid are also known as Rayleigh waves. On the other hand for the torsional, radial and torsional-radial modes, as the modal frequency is increased, their phase velocities decrease and asymptotically reach the Rayleigh wave velocity. The waveguide cross-section is also shown in Fig. 5.18 as an inset.

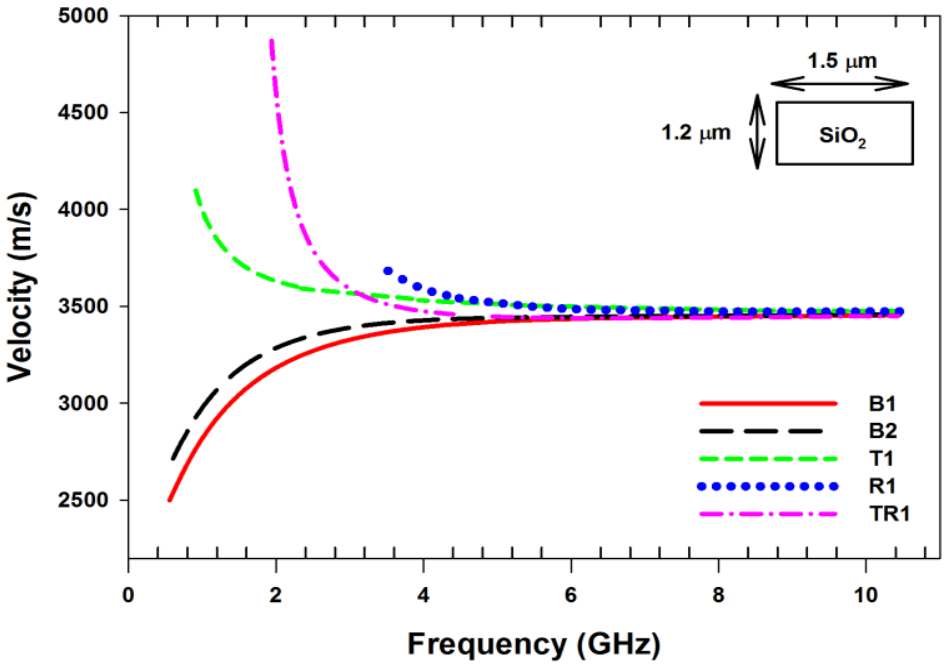

Figure 5.18 Variations of the phase velocities with the frequency for acoustic modes.

It can be observed that the phase velocity of the B1 mode is lower than that of the B2 mode for a given propagation constant, *k*. In this case, the width (W) of the waveguide was taken as being larger than its height (H) and the B1 mode with the U_y displacement vector as the dominant component: this can also be called U^y_{11} mode, whereas for the B2 mode with its U_x displacement vector as the dominant component, this can be called as the U^x_{11} mode. The '11' subscript identifies them as the fundamental modes and these numbers are related to their spatial variations, which will be shown later on. In this case, as their width and height were not equal, the U^x_{11} and U^y_{11} modes were not degenerate and it was possible to isolate them when the full structure was considered in the simulations. However, in the case when the height and the width of a waveguide are identical, these two B1 and B2 modes will be degenerate and in that case, the symmetry condition can be imposed along the vertical and horizontal axes (through the centre of the waveguide) to isolate these two degenerate modes.

For this waveguide, with W = 1.5 μm and H = 1.2 μm, and the propagation constant, k = 2.0 μm^{-1}, the frequency of the B1 or U^y_{11} mode was 0.8716 GHz and that of the B2 or U^x_{11} mode was 0.9362 GHz. However, if the waveguide height and width are identical, the U^x and U^y modes will be degenerate, so for W = H = 1.2 μm

and k = 2.0 μm^{-1}, both the frequencies have been calculated as 0.880 GHz and for the same value of k, this parameter will be 0.929 GHz when W = H= 1.5 μm. This indicates that the frequency of the fundamental U^y mode is more related to the waveguide height and that of the fundamental U^x mode is clearly related to its width.

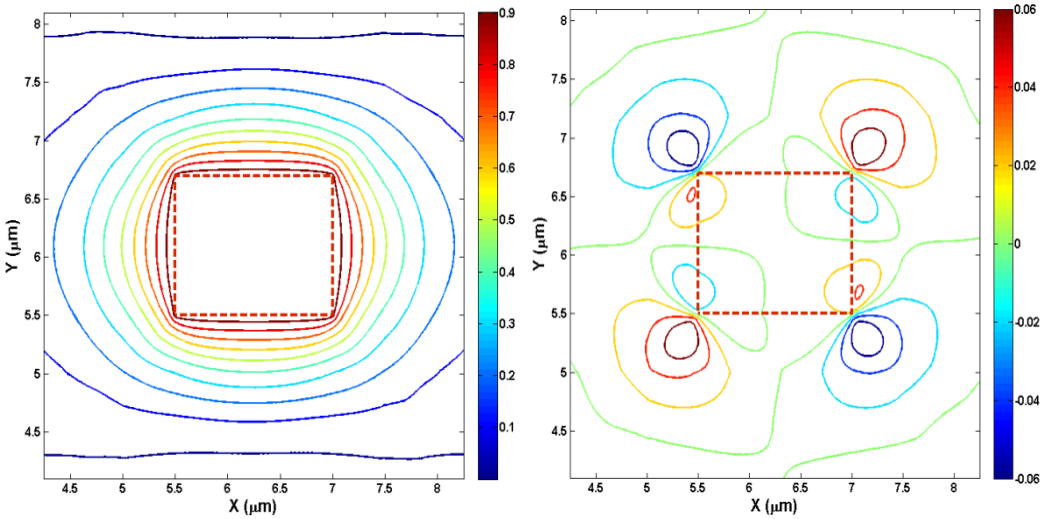

(a) (b)

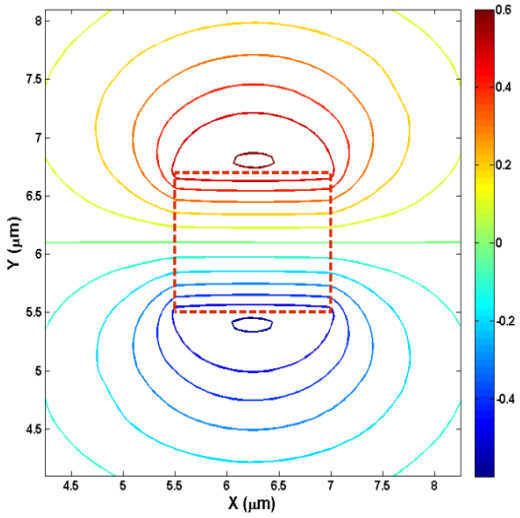

(c)

Figure 5.19. The contour plots of (a) U_y (b) U_x, and (c) U_z displacement vector components of the B1 mode (U^y_{11}) at k = 1.5 μm^{-1}.

The full-vectorial mode profile of the B1 mode is shown in Fig. 5.19, when k=1.5 μm^{-1}. For this mode the dominant displacement vector was the U_y and its spatial variation in the x-y plane is shown in Fig. 5.19(a). It can be observed that the U_y profile is strongly confined inside the waveguide with almost a constant value and this reduces monotonically in the cladding. As the spatial variation is of the lowest

order, similar as used in integrated optics '11' is used here to identify 1 half wave variation in the *x* and *x* directions. Its detailed variation along the transverse coordinates will be shown later. The variation of the non-dominant U_x profile across the waveguide cross-section is shown in Fig. 5.19(b). It can be observed that its magnitude is relatively small, at only 6% of the dominant U_y displacement vector, and clearly shows a higher order spatial variation at the four corners of the waveguide. The spatial variation of U_z vector for this mode, B1, is shown in Fig. 5.19(c), which clearly shows both positive and negative peaks along the upper and lower horizontal side walls. The waveguide outline is also shown in these figures by dashed lines. The mode profiles are similar as shown in section 5.2 for low index contrast waveguide, but the detailed spatial variation shown later will demonstrate some clear differences.

The magnitude of the U_z displacement vector is considerable at about 60% of the dominant U_y vector. It is well known that in optical waveguides with a strong refractive index contrast, all the 6 components of the electric and magnetic fields exist and a similar feature for an acoustic waveguide with a strong material contrast is also demonstrated here. It should be noted that for the quasi-TE mode of an optical waveguide [Leung, 2010], its H_y field was shown in Fig. 5.13(a), is the dominant component and is primarily confined inside the waveguide core. For the smaller non-dominant H_x field, this is mainly located around the four corners of the waveguide with higher order spatial variations as shown in Fig. 5.13(b). The parameter H_z has a relatively higher magnitude but with its peaks along the upper and lower dielectric interfaces as shown in Fig. 5.13(c), this strongly correlates with the eigenvector shown in Fig. 5.19 for the U^y_{11} mode.

The B2 mode has the U_x component as its dominant displacement vector and Fig. 5.20(a) shows its profile which is similar to that of the U_y profile for the U^y_{11} mode (or B1 mode), (which is shown in Fig. 5.19(a)). Similarly, the non-dominant U_y component of this B2 mode (with U_x dominant) shown in Fig. 5.20(b) has higher order spatial variations at the waveguide corners with only 6% of the magnitude. Its U_z profile is also similar as the U_z profile of the B1 mode (with U_y dominant), which is shown in Fig. 5.20(c), but for this profile it is rotated by 90 degrees, with its

positive and negative peaks along the left and right vertical interfaces of the waveguide. Its maximum magnitude is about 60% of that the dominant U_x component. For this U^x_{11} mode (or B2 mode) with the dominant U_x vector, strongly correlates to the eigenvector profile of the fundamental H^x_{11} (quasi-TM) mode in an optical waveguide with a strong index contrast, such as Si nanowires.

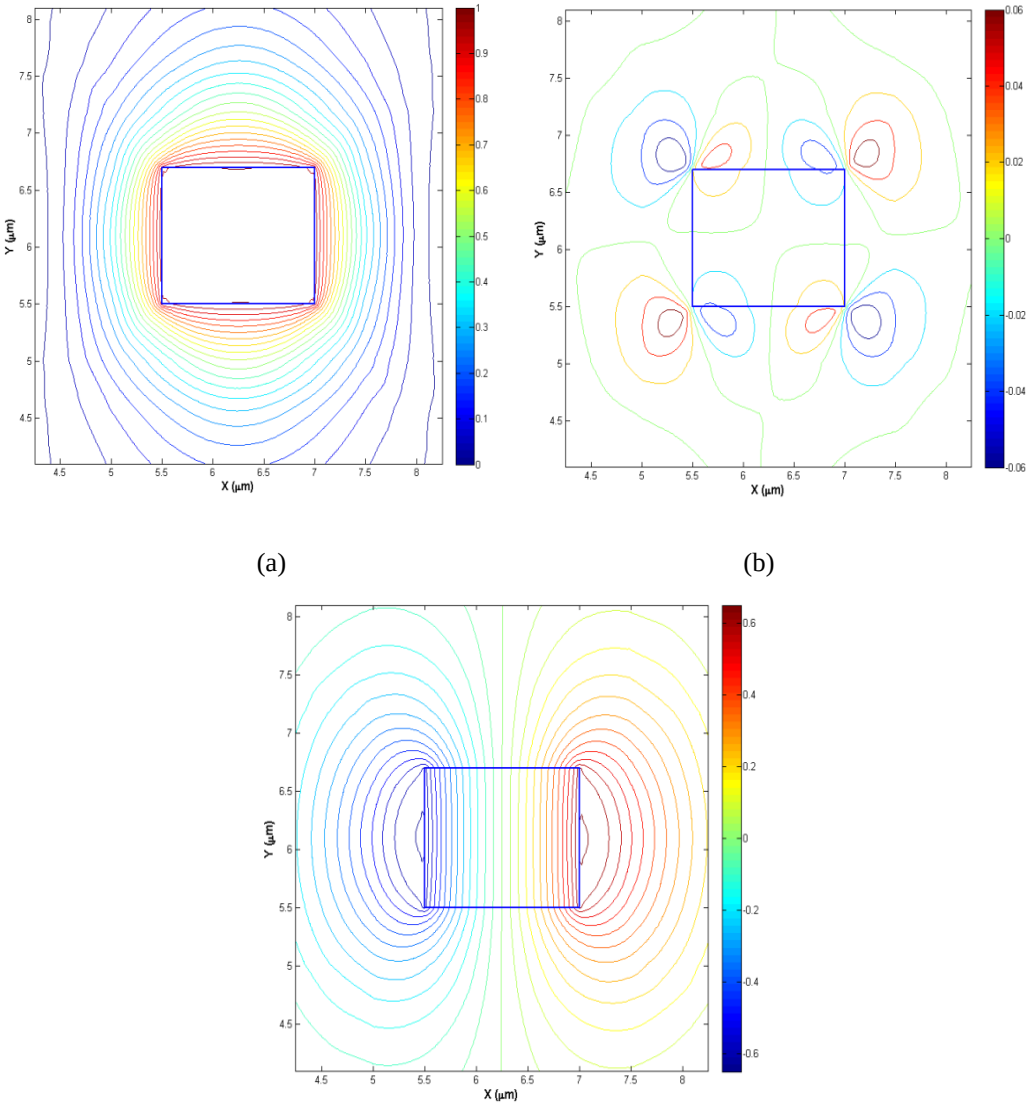

Figure 5.20 The U^x_{11} Bending mode (B2) at k_0=1.5 μm^{-1} of (a) U_x, (b) U_y and (c) U_z displacement vector.

Next, to illustrate the spatial variations of the displacement vectors, their variations along the transverse directions are also shown. Variations of the U_y displacement vector for the U^y mode (B1) and the U_x displacement vector for the U^x mode (B2) along the x-axis are shown in Fig. 5.21, when k = 1.5 μm^{-1}. The U_y profile

inside the core, shown by a dashed line, is nearly flat inside the core but with small ripples and a smaller peak at the centre (shown in the inset) and its value reduces rapidly outside the core. On the other hand, the U_x profile, shown by a solid line, is also nearly flat inside the core but with a small dip at the center (shown in the inset) and outside the core its value reduces more rapidly and is associated with the small negative values. Similar profile was also observed for a strong index contrast steel waveguide which was shown in section 3.7 in Chapter 3.

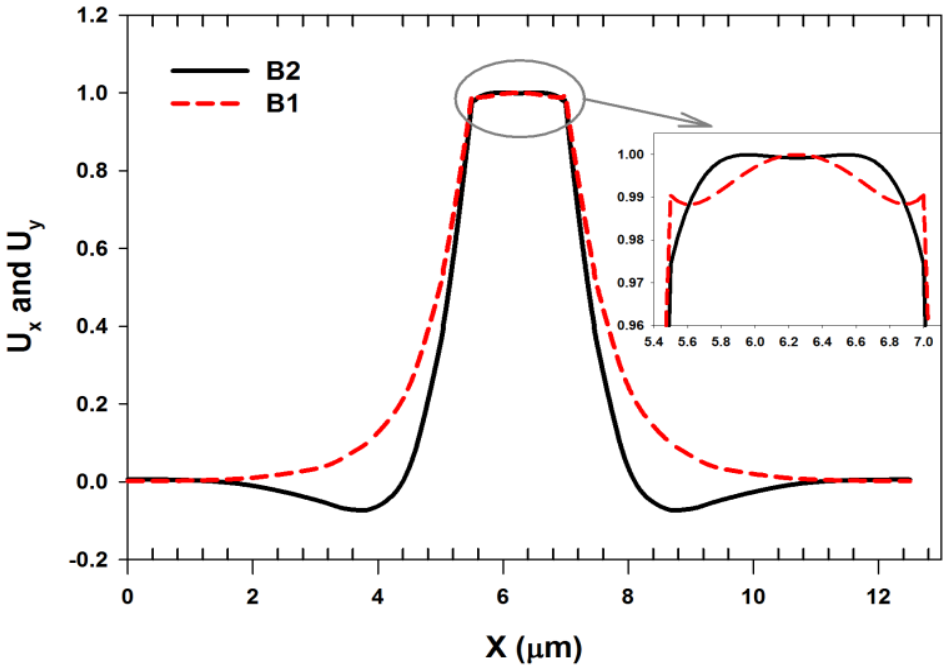

Figure 5.21. Variations of U_x and U_y displacement vectors along the *x*-axis for B1 and B2 modes, respectively at k =1.5 μm^{-1}.

For this waveguide, as the material contrast was very high, the modal eigenvectors shows strong confinement inside the core. For a smaller index contrast, such as with a Ge doped SiO_2 waveguide with SiO_2 cladding, (as shown in section 5.2) that the variations of U_x and U_y along the transverse directions are slower and can be close to a Gaussian profile in shape.

The variation of the U_y displacement vector for the U^y_{11} mode (B1) along the *y*-axis is associated with a small negative dip outside the core (similar to the U_x profile of the U^x_{11} mode (B2) along the *x*-axis as shown in Fig. 5.21). Similarly, the variation of the U_x displacement vector for the U^x mode along the y-axis is monotonic without changing its sign, in a way similar to the U_y profile along the x-

axis (as shown in Fig. 5.21) for the U^y mode. So the dominant U_y and U_x profiles of the U^y_{11} and U^x_{11} modes reverse the nature of their variations along the *x* and *y* directions. When the waveguide width and height are equal, the U^x and U^y modes are degenerate. As a result, the modes can easily exchange power between them. For two degenerate modes with the magnitudes of U_x and U_y being equal, their resultant displacement vectors would be oriented at 45 degree to the two perpendicular axes.

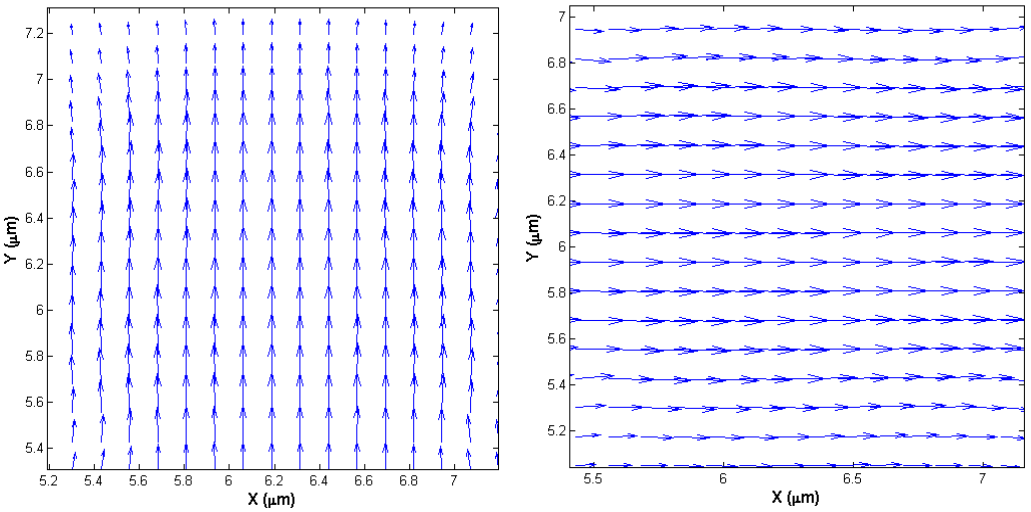

(a) (b)

Figure 5.22. The vector plot of (a) U^y B1 mode and (b) U^x B2 mode at k =1.5 μm^{-1}.

Figure 5.22 shows total transverse displacement for the non-degenerate mode. The vector plot of the U^y_{11} (B1) mode is shown in Fig. 5.22(a), a combination of the U_x and U_y displacement vector which are perpendicular to the *x*-axis. Whereas in Fig. 5.22(b) the U^x_{11} (B2) mode is horizontally directed along the *x*-axis. As the axial propagation constant, *k*, increases, these mode shapes transform slowly and get more confined and the magnitudes of the non-dominant components also increase. The U_t vectors perturb a bit near the corner of the waveguides due to the presence of stronger non-dominant components.

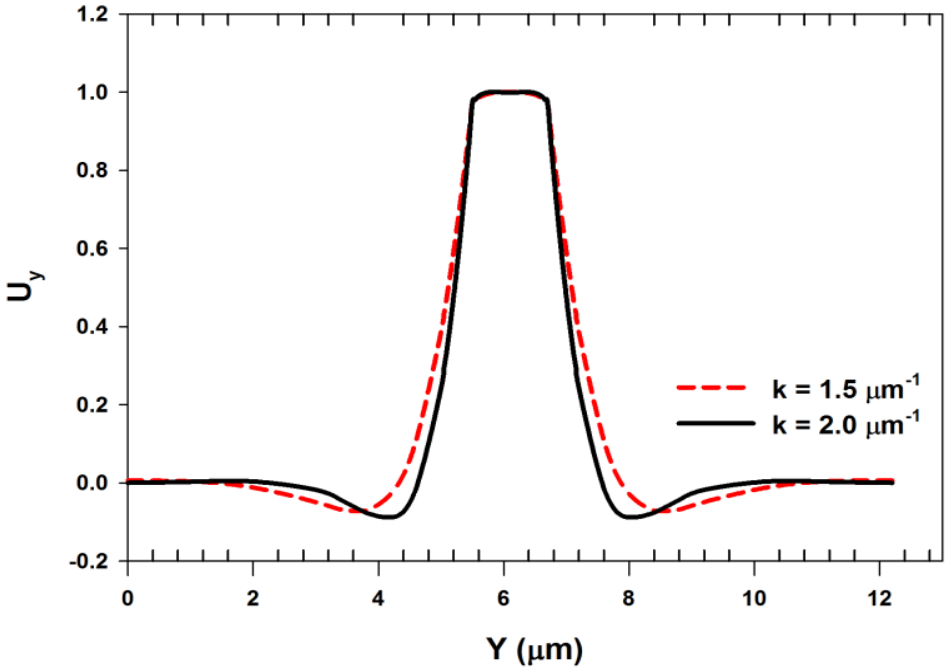

Figure 5.23. Variation of U_y of the Bending modes, B1(U^y) mode along y-axis for k = 1.5 μm^{-1} and k = 2.0 μm^{-1}.

The U_y profiles along the *y*-axis for the U^y mode (B1) are shown in Fig. 5.23, for two different *k* values. It can be observed that when the propagation constant is increased, the field outside the core reduces more rapidly, the negative peak gets slightly larger, but it moves closer to the boundary, as shown by a solid line. A larger dip at the centre of the waveguide exists (not clearly visible here) for the larger *k* value, given by k = 2 μm^{-1}. Similarly, its (U_y) variation along the *x*-axis also becomes faster outside the core when the propagation constant, *k*, is increased, but this is not shown here. As the value of *k* is increased, the non-dominant displacement vector, U_x for the B1 mode also gets more confined near the 4 corners and its magnitude is increased, as is seen for example from 6% at k = 1.5 μm^{-1} to 10% when k = 4.0 μm^{-1}.

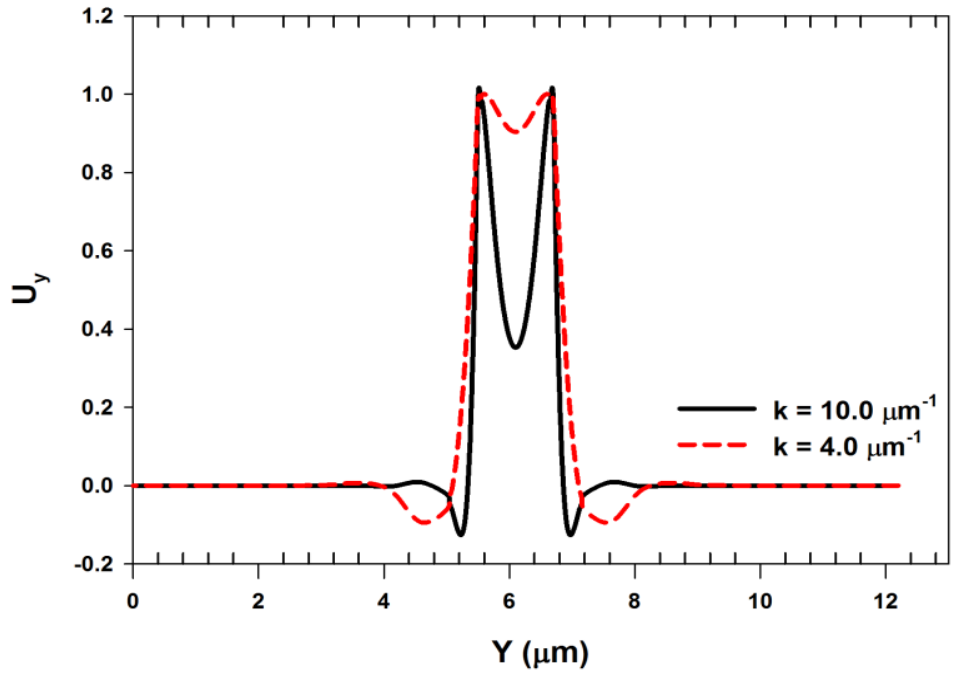

Figure 5.24. Variation of the U_y of B1 mode along y-axis at k = 4.0 μm^{-1} and k =10.0 μm^{-1}.

Variations of the U_y profile along the *y*-axis for two even higher values of the propagation constant, k = 4.0 and k= 10.0 μm^{-1} are also shown in Fig. 5.24, for the B1 mode. It can now be observed that as k value is increased, the dip at the centre is increased further and now the eigenvector is more confined along the upper and lower horizontal interfaces of the waveguide. The negative dip outside the core also becomes slightly larger, sharper and closer to the waveguide interfaces.

The transverse variation of the displacement vector, U_y, of the U^y mode (B1) across the waveguide cross-section is shown in Fig. 5.25 (a), when k = 10.0 μm^{-1}. It can be observed that the profile of U_y displacement vector for the B1 mode at k = 10.0 μm^{-1} as shown here is quite difference from the U_y profile at k = 1.5 μm^{-1}, which was shown in Fig. 5.19(a). It can be ntoiced that the displacement profile is more confined along the upper and lower interfaces and its variation along the *x*-direction is relatively flat. For this higher propagation constant, the magnitude of the non-dominant U_x displacement vector of this B1 mode as shown in Fig. 5.25(b), increases significantly to about 40%, but their displacements are mainly confined at the four corners of the waveguide.

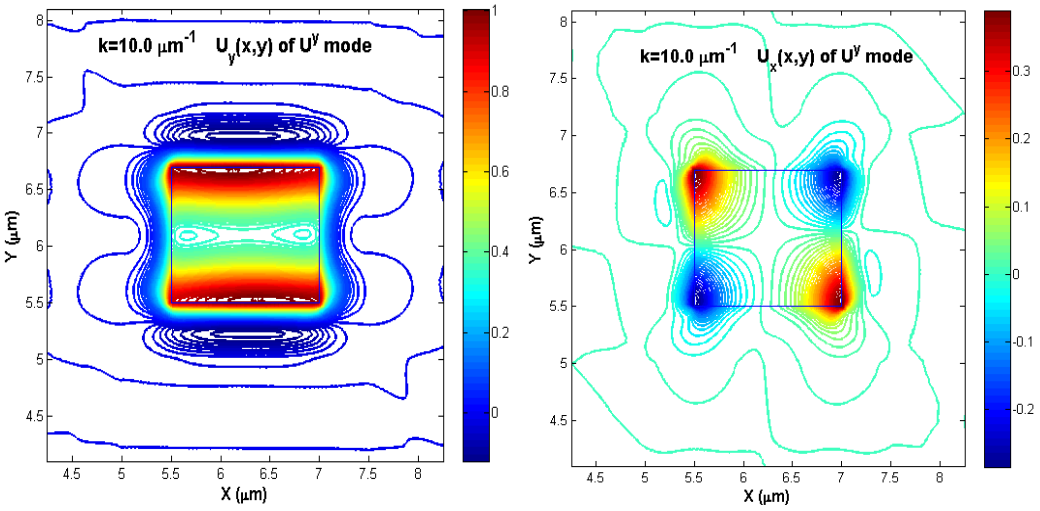

(a) (b)

Figure 5.25 U_y profile of the Bending mode (B1) (a) U_y and (b) U_x displacement at k=10.0 μm^{-1}.

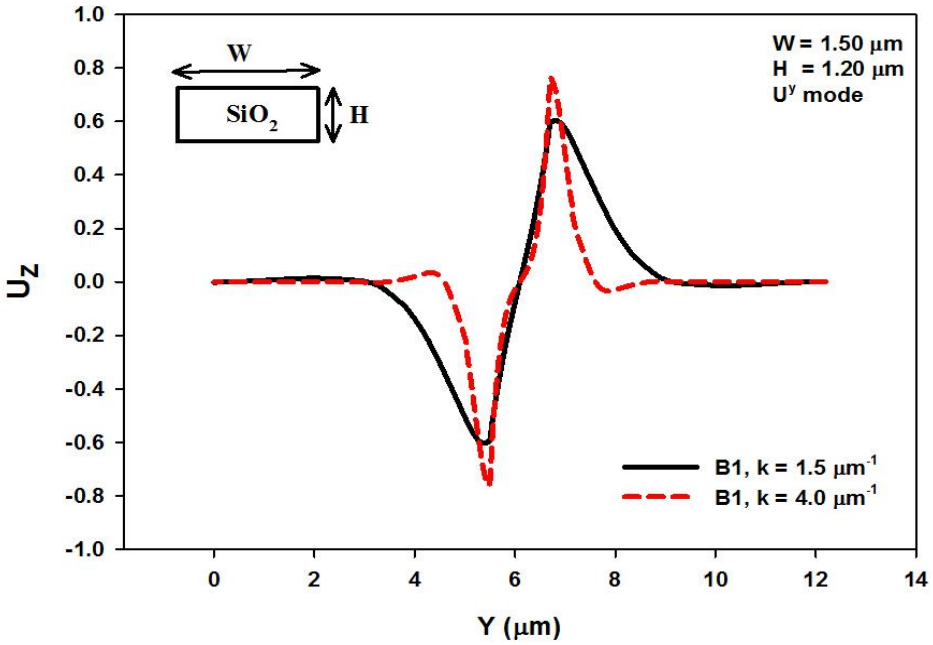

Figure 5.26. Variation of U_z along y-axis of the B1 mode(U^y) at k = 1.5 μm^{-1} and k = 4.0 μm^{-1}.

The variations of the axial displacement vector, U_z for the B1 (U^y_{11}) mode along the y-axis for k = 1.5 and 4.0 μm^{-1} are shown in Fig. 5.26. It can be observed that as the propagation constant is increased, the displacement vector U_z becomes more narrowly confined along the upper and lower horizontal interfaces and its magnitude also slightly increases.

The detailed spatial variations of all the three displacement vector components for this B1 (U^y_{11}) mode are shown in Figs. 5.19 to 5.26. For the B1 (or U^y mode), the displacement vector has the dominant U_y component and the resultant structural deformation will be in the vertical direction, particularly for lower propagation constants (or lower frequencies). However, for higher frequencies, as the magnitude of the U_x displacement also increases to nearly 40% of the U_y displacement, the profile of their combined transverse displacement vector ($\mathbf{U_t} = \mathbf{x}U_x + \mathbf{y}U_y$) will modify considerably, particularly near the four corners. The signs of the displacement vectors will change after every half-wavelength and repeat after every wavelength and this will produce a periodic structural bending along the vertical axis. Similarly, for the B2 mode, the periodic displacement along the *x*-axis will cause this mode to periodically bend the waveguide along the *x*-axis.

It should be noted that for the B1 mode although the dominant displacement is in the *y*-direction, it also has a significant U_z displacement. The variation of U_z along the transverse plane is more complicated with its positive and negative values at the upper and lower horizontal interfaces. The total displacement will vary periodically along the axial direction. As *k* increases, both the dominant U_y and the next significant component, U_z, are confined mainly along the upper and lower horizontal interfaces, and like a surface mode confined along the material interfaces, its velocity approaches that of the Rayleigh waves, which was demonstrated in Fig. 5.18.

The modal properties of other modes are of interest and are presented briefly. The torsional mode, labeled T1 (can also be called U^y_{21}) in Fig. 5.27, has nearly equal U_x and U_y displacement vectors. The U_x, U_y and U_z profiles for this mode at $k = 1.5\ \mu m^{-1}$ are shown in Fig. 5.27.

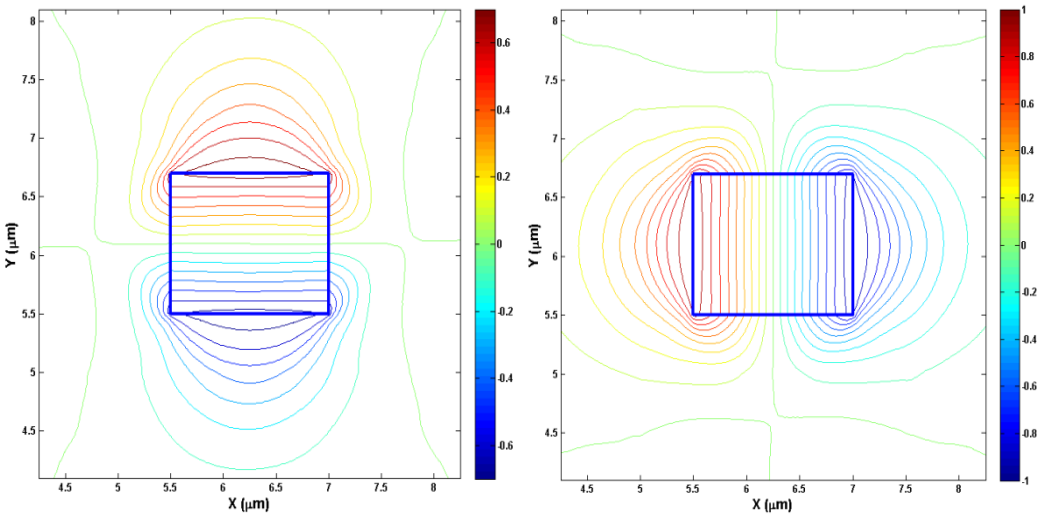

(a) (b)

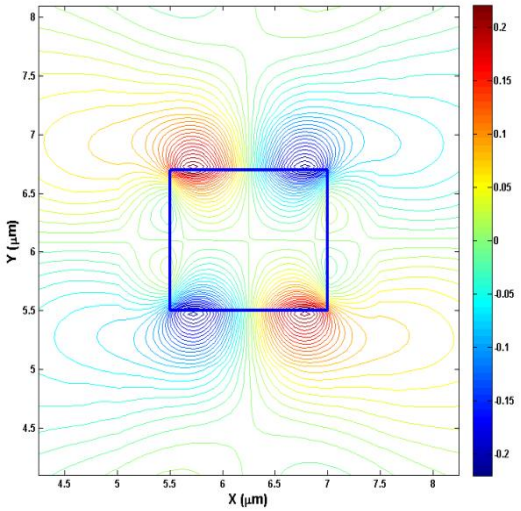

(c)

Figure 5.27. Displacement vector profiles (a) U_x (b) U_y, and (c) U_z of the T1 U^y_{21} mode at k=1.5 μm^{-1}.

It can be observed that the more dominant displacement vector, U_y shows its maximum values along the left and right vertical interfaces, as shown in Fig. 5.27(b). On the other hand the horizontal displacement vector, U_x shows its maximum value along the upper and lower horizontal interfaces, as shown in Fig. 5.27(a). As the height and width of the waveguide were not equal, the torsional modes were not degenerate and the magnitudes of the maxium U_x values was about 60% of the maximum U_y displacement. Since the spatial variation of the dominant component (U^y) mode is 2 and 1 half-wave along the horizontal and vertical directions this has also been labelled here as the U^y_{21} mode. The U_z profile of this torsional mode (T1)

is shown in Fig. 5.27(c), which exists mainly at the four corners with higher order spatial variations. For this *k* value, its magnitude was 20% of the dominant U_y components, and this shows that the relative magnitude of the longitudinal displacement vector, U_z, is lower than that of the B1 and B2 modes. This mode with asymmetric U_x and U_y displacement vectors and the U_z displacement vector with very small magnitude of 0.2 will have a smaller interaction with the more symmetric fundamental optical mode.

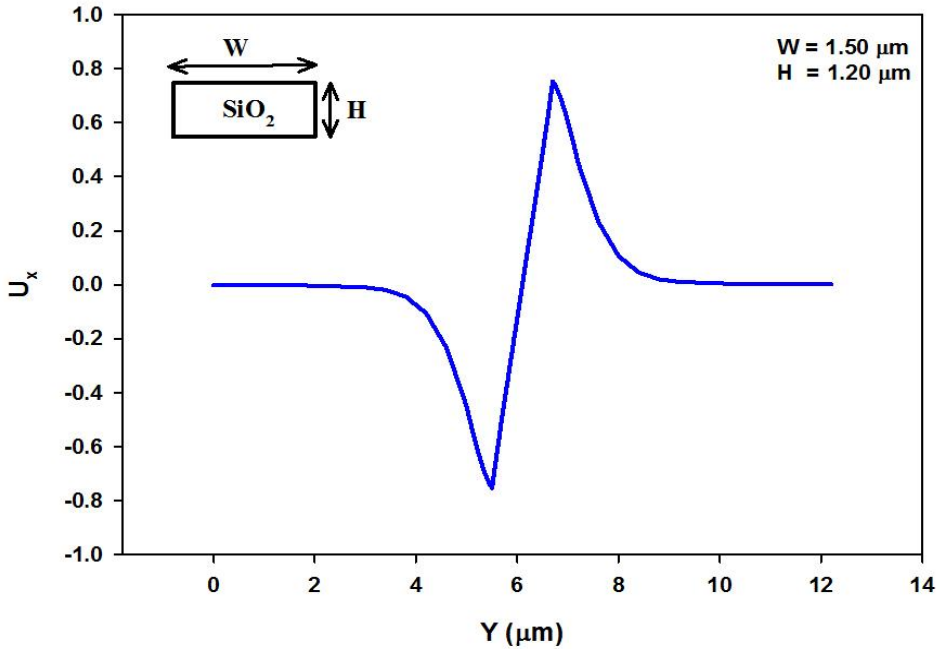

Figure 5.28. The variation of the U_x along *x*-axis of Torsional mode (T1) at $k = 1.5\ \mu m^{-1}$.

Variation of the U_x displacement vector of this Torsional mode (T1) along the *y*-direction is shown in Fig. 5.28. It can be clearly observed here that it has positive and negative peaks at the upper and lower interfaces with the magnitude of 0.8.

The combined transverse displacement vector, $\mathbf{U_t}$ in the transverse plane for this torsional mode, T1, is shown in Fig. 5.29, when $k = 1.5\ \mu m^{-1}$. This clearly shows a twist in the transverse plane due to the combination of the *x* and *y* displacement vectors, which were shown in Fig. 5.27(a) and (b), respectively. Every half-wavelength the sign of the displacement vectors (and direction of twist) will change. This will give the periodic clockwise and anticlockwise twists in the transverse plane along the waveguide.

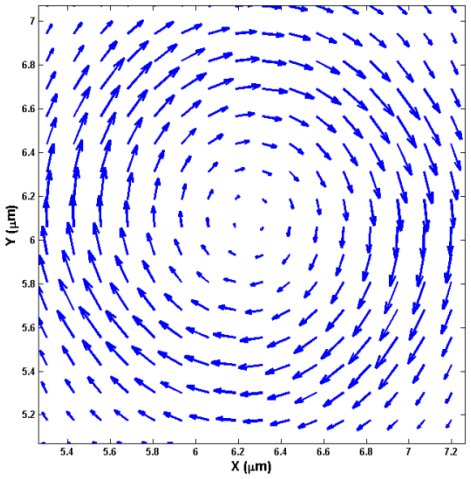

Figure 5.29. The vector displacement, U_t plot of the Torsional (T1) or U^y_{21} mode at k = 1.5 μm^{-1}.

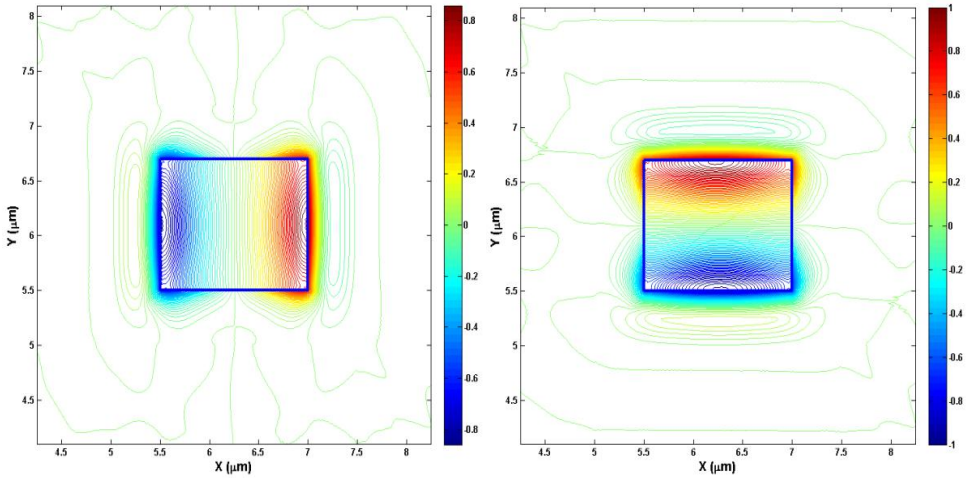

(a) (b)

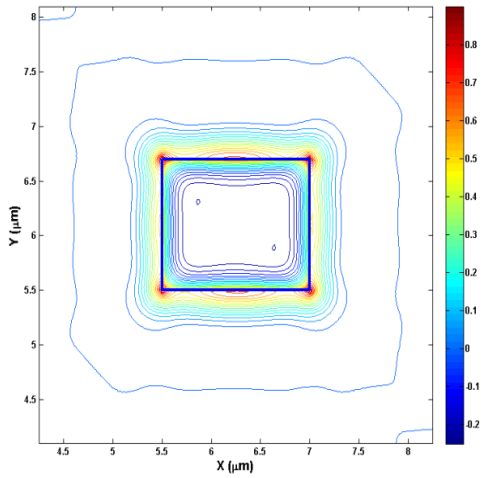

(c)

Figure 5.30. The displacement vector plots of (a) U_x (b) U_y and (c) U_z components of the R1 (U^y_{12}) mode at k = 10.0 μm^{-1}.

By contrast, the radial mode R_{01} labelled as R1, shows considerable magnitude of all the three displacement vectors. This mode is very similar as the Torsional mode but is variation along *x*-and *y*-direction are slightly different. The U_x, U_y and U_z profiles for this mode at $k = 10.0\ \mu m^{-1}$ are shown in Fig. 5.30.

It can be observed that the dominant displacement vector, the U_y profile shown in Fig. 5.30(b), is mainly confined to the upper and lower horizontal interfaces. It has 1 and 2 half wavelength variations along the *x* and *y*-directions, and can also be identified as U^y_{12} mode. On the other hand, the U_x displacement vector, shown in Fig. 5.30(a), is mainly confined along the left and right vertical interfaces with its maximum magnitude being about 80% of the maximum U_y displacement. However its U_z profile, given in Fig. 5.30(c), clearly shows its confinement along all the four interfaces with the sharp peaks at the four corners. It changes its sign at the interfaces and sustains a smaller but relatively constant magnitude inside the core. Its maximum magnitude is 80% (of that of the dominant U_y displacement vector) at the four corners, about 50% along the four interfaces and about 25% inside the core. Due to the symmetric nature of the U_z profile, this mode is expected to have a considerable overlap with the fundamental optical mode. This U_z profile of this mode (R1) is very different than that of the T1 mode.

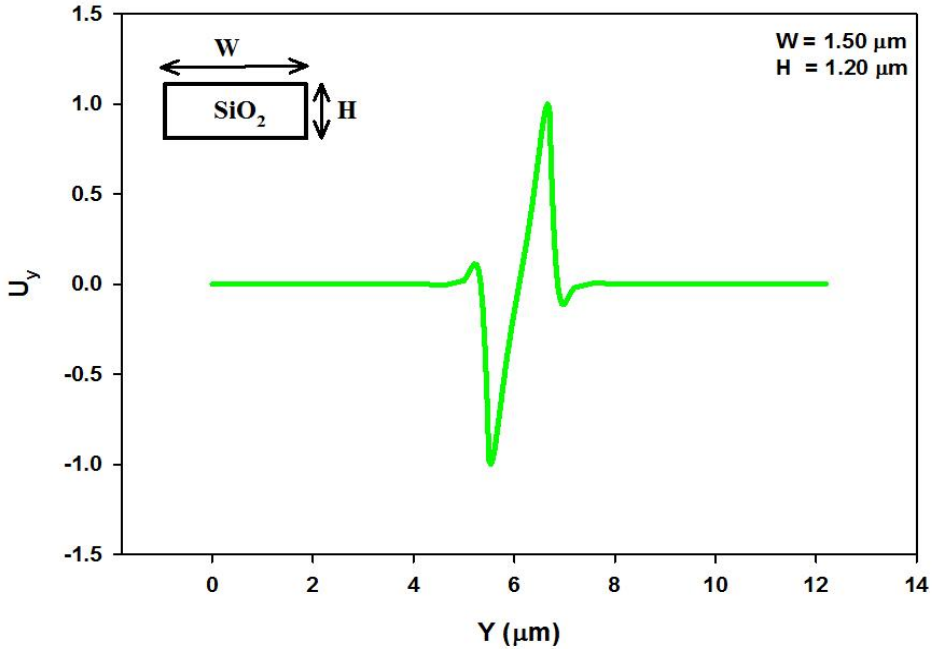

(a)

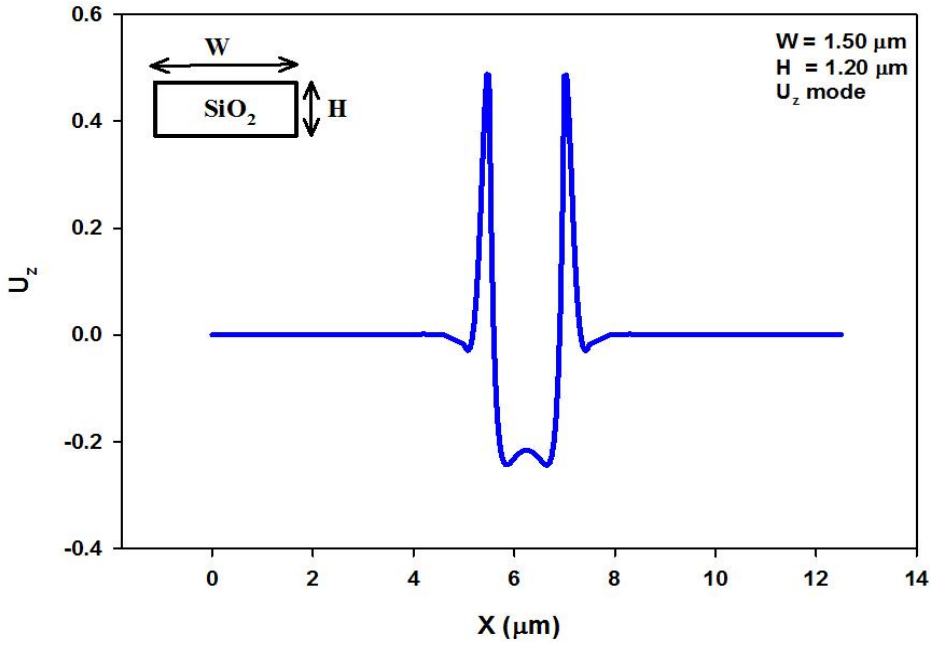

(b)

Figure 5.31. The variation of (a) U_y along *y*-axis and (b) U_z along *x*-axis of the R1 (U^y_{12}) mode at k = 10.0 µm^{-1}.

Variation of the Radial mode (U^y_{12}) of U_y displacement vector profile along the *y*-axis at k=10µm^{-1} shows in Fig. 5.31(a). The U_y displacement vector profile shows negative and positive peaks at the lower and upper interfaces with the magnitude of 1. The Radial mode in Fig. 5.31(b) shows the U_z displacement vector

profile with the negative at the centre and is increased further with the positive at both side on the upper interfaces with the maximum magnitude of 0.5.

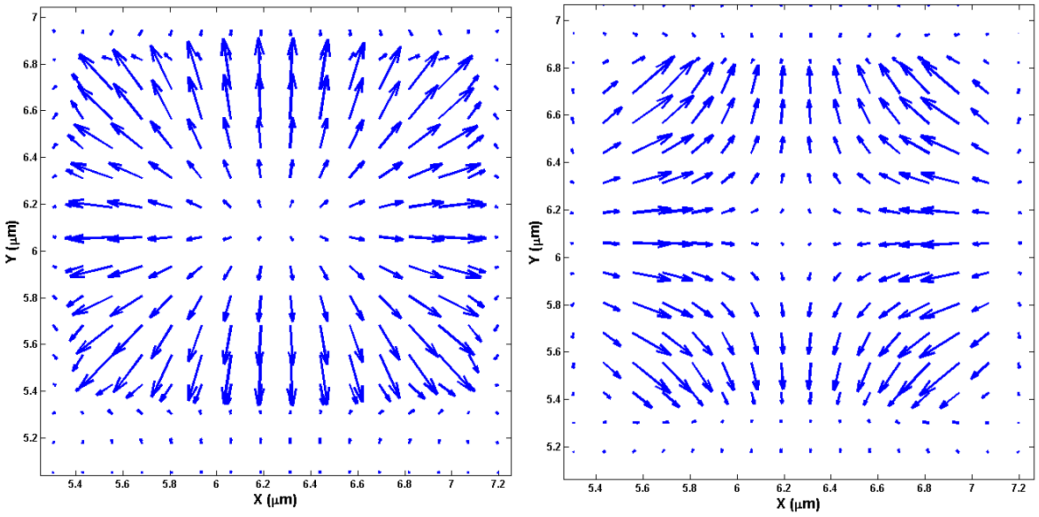

(a) (b)

Figure 5.32. Vector plot U_t of (a) Radial mode (R1) (b) Torsional-Radial more (TR1) at k = 10.0 μm^{-1}.

Figure 5.32(a) shows the resultant $\mathbf{U_t}$ vector profile in the transverse plane for the R1 mode when k =10 μm^{-1}. In this case, the dominant U_y has positive and negative peaks at the upper and lower interfaces, as shown in Fig. 5.30(b) and U_x had negative and positive peaks along the left and right interfaces as shown in Fig. 5.30(a). The resultant $\mathbf{U_t}$ vector shows a displacement which moves radially outward but is periodically reversing its direction so expanding and contracting its dimension along the propagation direction. However, its changing cross-section remains rectangular in shape. R1 would perturb the refractive index profile radially without changing the polarization of the guided wave. The combination of transverse and longitudinal displacements can give rise to nonlinear optical effects such as SBS and polarized GAWBS [Shelby, 1985 and Tanaka, 2004].

The U_x and U_y profiles of the TR_{21} mode labelled as TR1 mode were similar to that of the R1 mode as shown in Fig.5.30, but π radians out of phase in the time axis (and these are not shown here). However, their out of phase combination yields the $\mathbf{U_t}$ profile, which is shown in Fig.5.32(b). This shows the maximum displacement in the four quadrants of the core. The vector displacement shown in this figure will cause the guide to expand along the vertical axis and squeeze along the horizontal

axis. This produces a deformation of the waveguide which also reverse its shape periodically and hence induces additional optical birefringence.

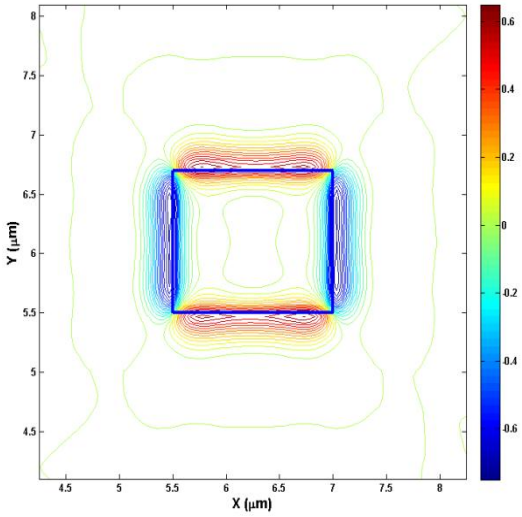

Figure 5.33. U_z profile of the Torsional-Radial mode (TR1) at k = 10.0 μm^{-1}.

The profile of the longitudinal vector, U_z, of this TR1 mode is shown in Fig. 5.33, which shows that the displacements are primarily confined along the four interfaces and their sign changes in the adjacent sides. In this case the longitudinal displacement inside the core is nearly zero. Its maximum magnitude at the interfaces was about 60% of that of the dominant U_x displacement vector. As its U_x and U_y profiles induce optical birefringence which will contribute to depolarized GAWBS [Shelby, 1985].

The acoustic modes presented here are not purely transverse or longitudinal but exist with all the three components of the displacement vectors being present. Their spatial variation are shown and their evolution with the frequency are also shown. In this work, the structural symmetry along the two transverse axes was not exploited or enforced but the full-vectorial displacement vectors clearly show their symmetry and asymmetry along these two axes for different modes.

5.4 Acousto-optic Interaction

In this section we have studied the interaction between acoustic and optical mode by using $k=2\beta$ to calculate the SBS frequency shift in the acoustic waveguide and afterwards the overlap integrals of the acousto-optic interaction are shown [Li, 2006], [Mermelstein, 2009 and Zoe, 2008].

The electric and magnetic field components in the *x*, *y* and *z* direction for the optical quasi-TE mode are shown next:

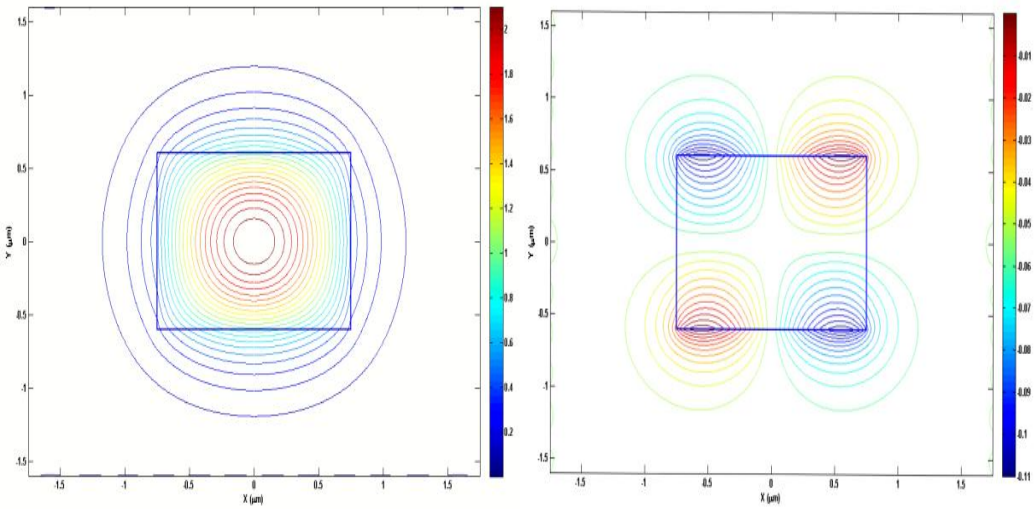

(a) (b)

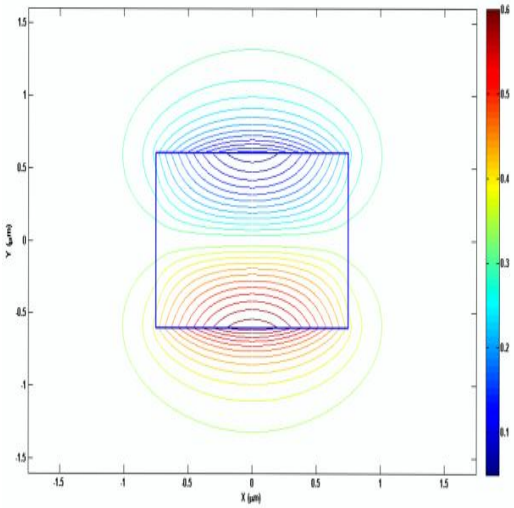

(c)

Figure 5.34. The magnetic field of (a) H_y (b) H_x and (c) H_z field plots of the quasi-TE mode.

The dominant H_y field is shown in Fig. 5.34(a) with its maximum value at the centre of the core with the maximum magnitude of 2. The spatial variation of the non-dominant H_x fields shows four peaks at the corner as shown in Fig. 5.34(b) with the lowest magnitude of 0.11 and the H_z field shows one positive and one negative peak along the upper and lower interfaces as shown in Fig. 5.34(c) with their magnitude of 0.6.

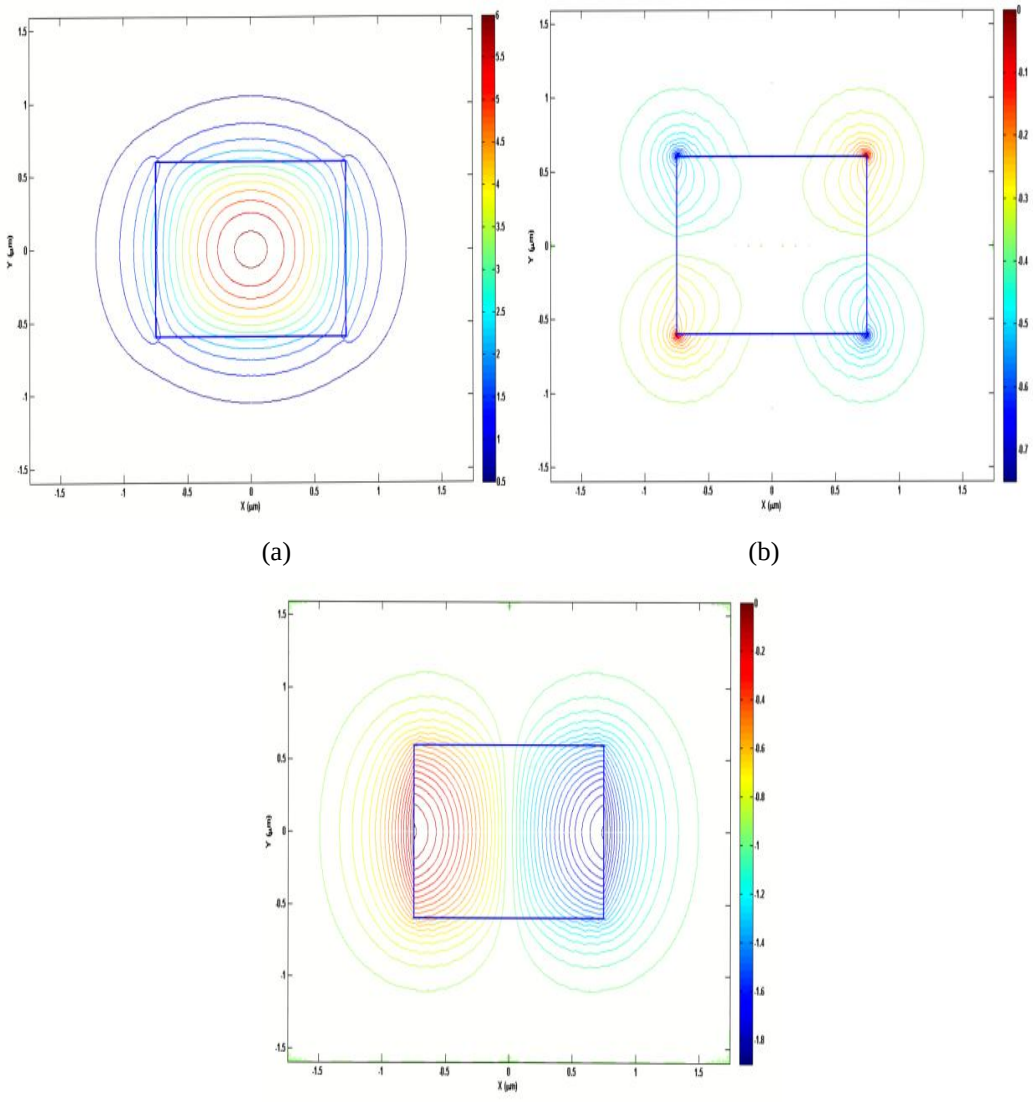

(a) (b)

(c)

Figure 5.35. The electric field variation of (a) E_x (b) E_y and (c) E_z field plots of the quasi-TE mode.

The dominant electric field E_x is shown in Fig. 5.35(a) with the maximum value at the middle of the core with its magnitude of 6. The higher spatial variation of the non-dominant E_y field shows four peaks at the four corners of the core as shown in Fig. 5.35(b) with the lowest magnitude of 0.7 and one positive and one

negative peaks along vertical interfaces for the E_z displacement in Fig. 5.35(c) with its magnitude of 1.8.

5.4.1 Study of the Waveguide when Height (H) is Varied

In this section, the effect of the waveguide height is studied to calculate the SBS frequency shift and the overlap between optical and acoustic waves. In this case the waveguide width is kept constant at 1.5 μm.

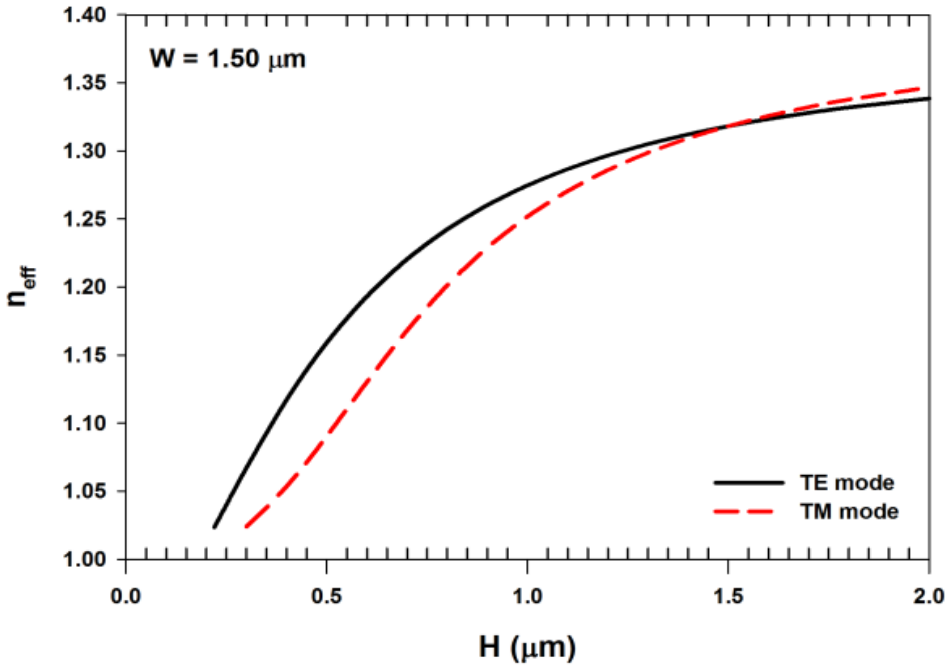

Figure 5.36. Variation of the n_{eff} by varied the height of SiO_2 waveguide.

Variation of the effective index of the SiO_2 waveguide with the waveguide height, H is shown in Fig. 5.36. It can be observed that the effective index is increased as the height of the waveguide is increased. When the waveguide height is very low, the guide is unable to support any optical mode as it approaches modal cut-off. It can also be observed that as the height is larger than the width, which is fixed at 1.5 μm, effective index of the quasi-TE mode is larger than that of the quasi-TM mode.

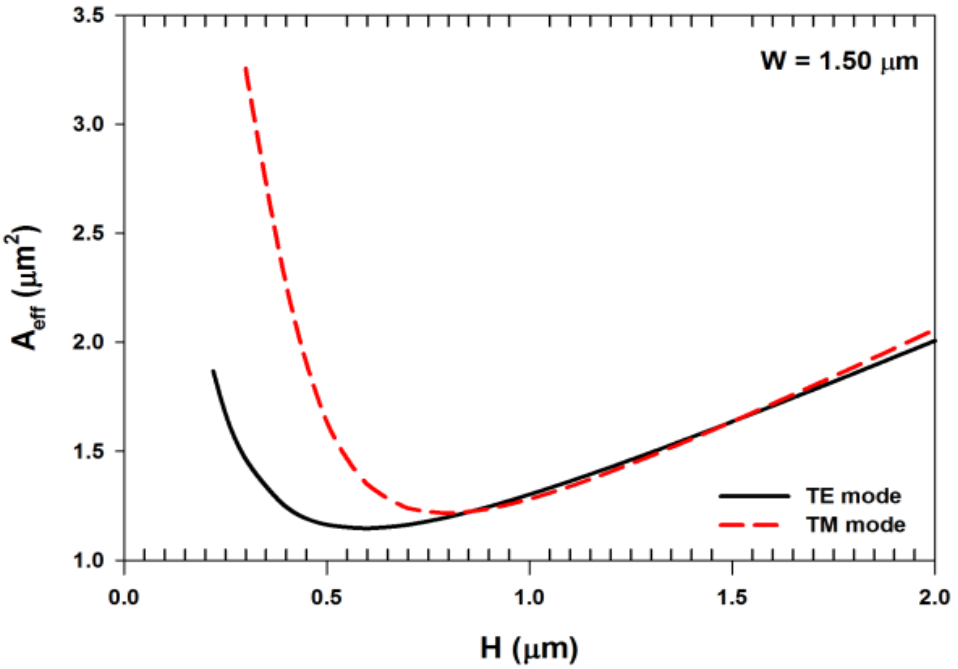

Figure 5.37. Variation of the A_{eff} with the height of SiO_2 waveguide.

Variation of the effective area, A_{eff}, with the waveguide height for both the quasi-TE and TM modes are shown in Fig. 5.37. In this case, it can be observed that as the height is reduced, initially A_{eff} reduces, then achieves a minimum value and for further reduction of the height, it increases, as the quasi-TE and TM modes approach their cut-off. It can be noticed that at the lowest height of A_{eff} the quasi-TM mode is higher than that of the quasi-TE mode as shown as 3.4 μm^2 and 1.9 μm^2, respectively.

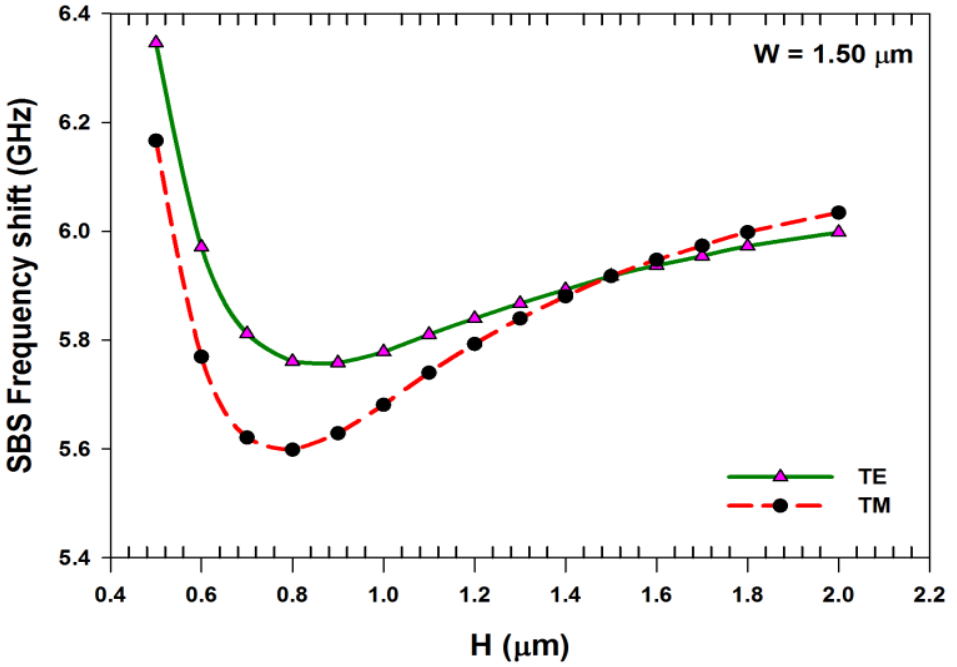

Figure 5.38. Variation of the SBS frequency shift for TE and TM modes with waveguide height.

The calculation of the SBS frequency of the acoustic mode is carried out by using $k=2\beta$. The variation of the SBS frequency shift with the waveguide height is shown in Fig. 5.38. It can be observed that as the height is reduced initially, SBS frequency is decreased and then approaching the cut-off. Further decreases of height of the waveguide results the SBS frequency being increases as shown in the figure for both quasi-TE and TM modes.

A mentioned before SBS frequency tell us the resulting frequency shift due to the optical-acoustic interaction, however, their strength depends on the overlap between these modes. The overlap interaction of the transverse Radial (R1 or U^{y}_{12}) mode with its U_z displacement vector is shown here. The variation of overlap integral values of the acousto-optic interaction is shown in Fig. 5.39. This represents the overlap interaction of the U_z displacement vector with the dominant optical field. For quasi-TE mode, overlap integral was carried out with the H^{y}_{11} field, but for quasi-TM mode, it was with the H^{x}_{11} field.

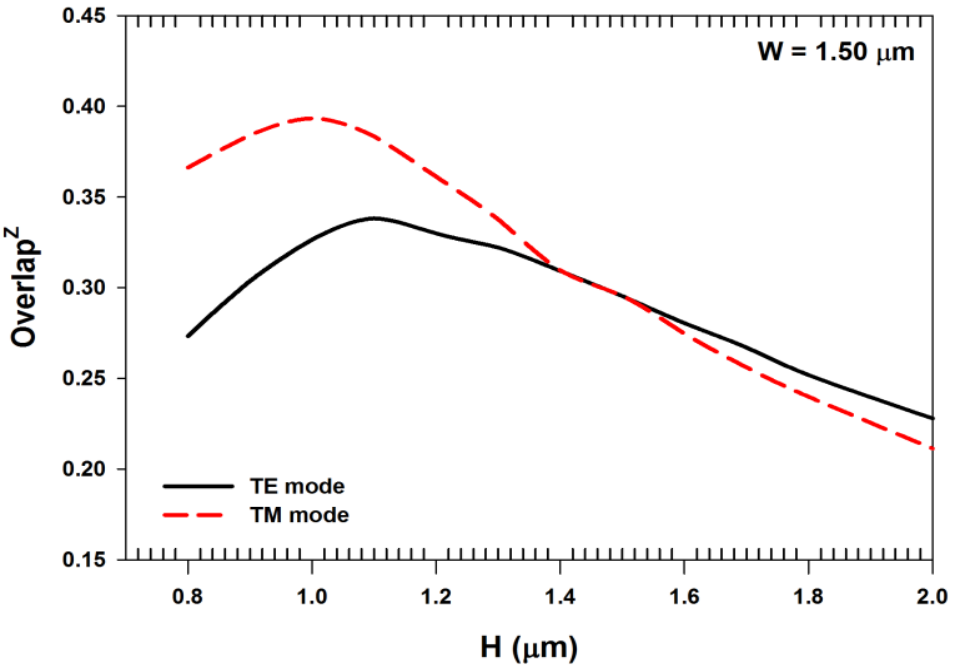

Figure 5.39. The overlap integral between acousto-optic interaction calculation.

In this figure, the overlap calculation of the U_z displacement vector profile of the radial mode will introduce GAWBS and SBS into the core of the waveguide and creates the interaction between acoustic and optical called acousto-optic interaction. The graph shows that maximum overlap is achieved when the height is 1 μm and

1.15 μm for the quasi-TE and TM mode, respectively, and further increases of height will reduce the overlap integral. Therefore, the mismatch between acoustic and optical mode is higher when height is increased.

5.4.2 Study of the Waveguide when W is Varied

In this section the effect of the width of the SiO_2 waveguide is studied on the SBS frequency shift and the overlap between the acoustic and optical waves. To achieve that, first the optical modes are studied. To obtain the SBS frequency shift, it is essential to calculate the propagation constant, which is related to the effective index of a mode.

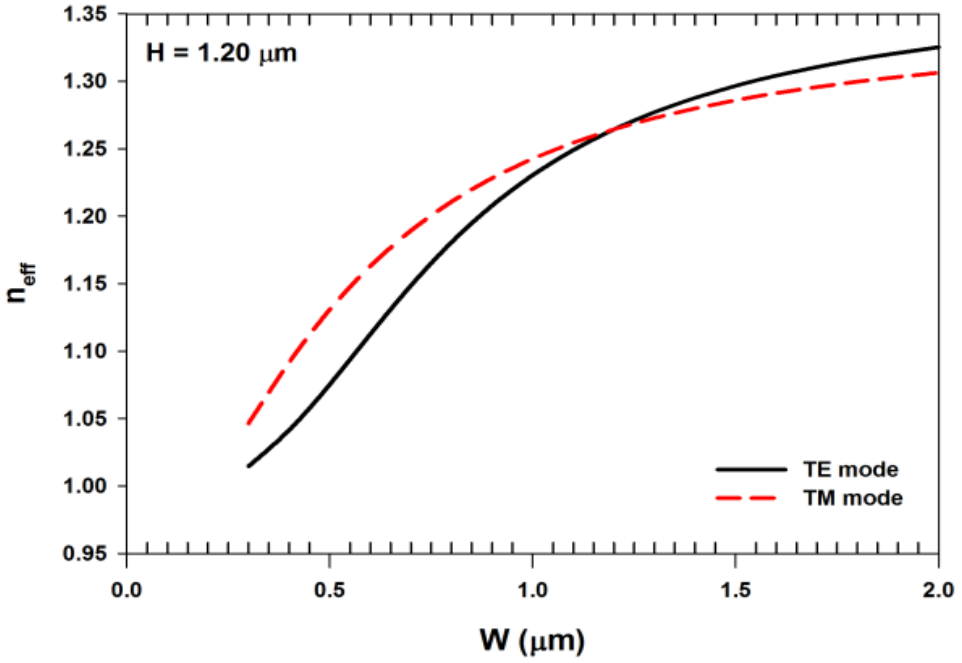

Figure 5.40. Variation of the n_{eff} of TE and TM modes with the width of the SiO_2 waveguide.

Variations of the effective index with the waveguide width are shown for both quasi-TE and TM modes in Fig. 5.40. It can be observed that as the width is reduced modal effective index is reduced, and when the width reduced to 0.3 μm, their cut-off condition approaches. It can also be observed that when the width is larger than 1.2 μm, n_{eff} of the TE mode is higher than that of the TM mode.

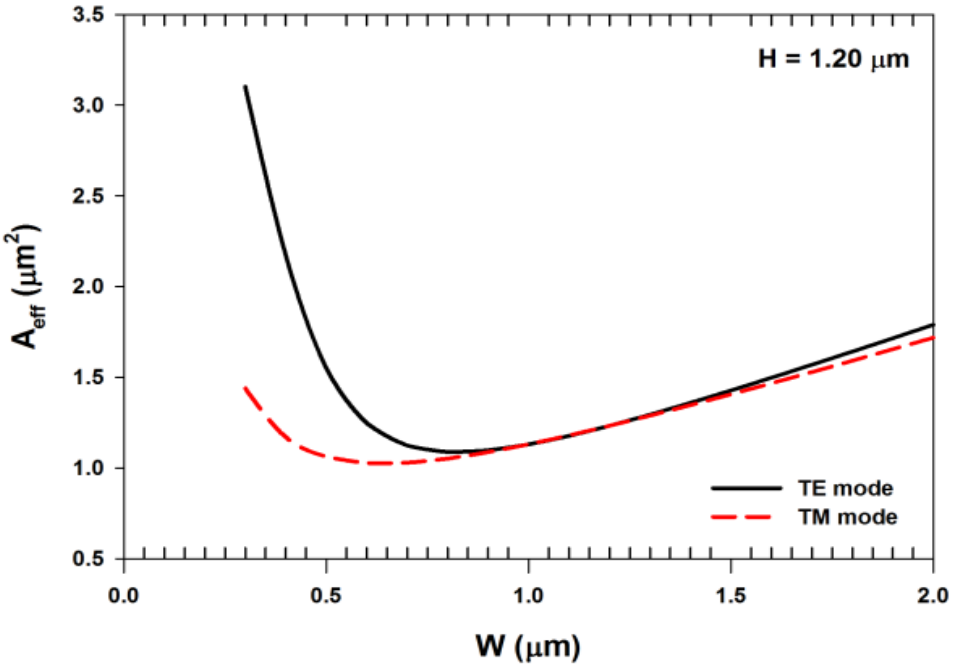

Figure 5.41. Variation of the A_{eff} of the quasi-TE and TM modes with the width of the SiO_2 waveguide.

Variation of the effective area, A_{eff}, with the waveguide width for both the quasi-TE and TM modes are shown in Fig. 5.41. In this case, it can be observed that as the width is reduced, A_{eff} reduces initially, then achieves a minimum value. Further reduction of width will increase the effective area, as the quasi-TE and TM modes approaches their cut-off.

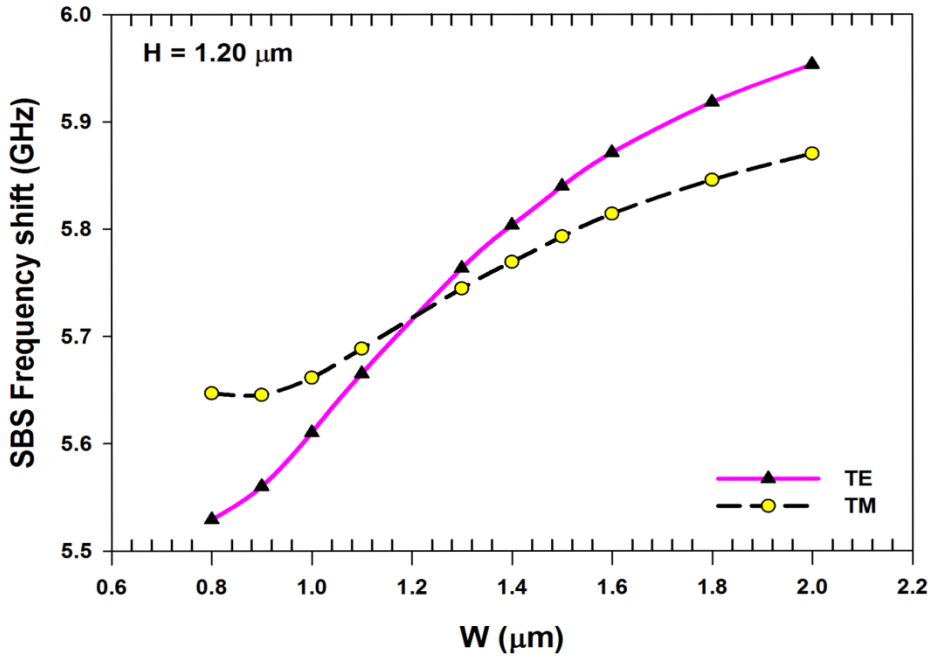

Figure 5.42. Variation of the SBS frequency shift for quasi-TE and TM modes with waveguide width.

The variation of the SBS frequency shift with the waveguide width, W, is shown in Fig. 5.42 for both quasi-TE and TM modes. It can be observed that as the width is reduced, the SBS frequency shifts for both the polarized modes are reduced. It can also be noticed that as the width is increased, the SBS frequency is increased of both quasi-TE and TM modes, as it approaches the maximum width the quasi-TE mode has higher SBS frequency than that quasi-TM mode of 5.98 GHz and 5.85 GHz, respectively.

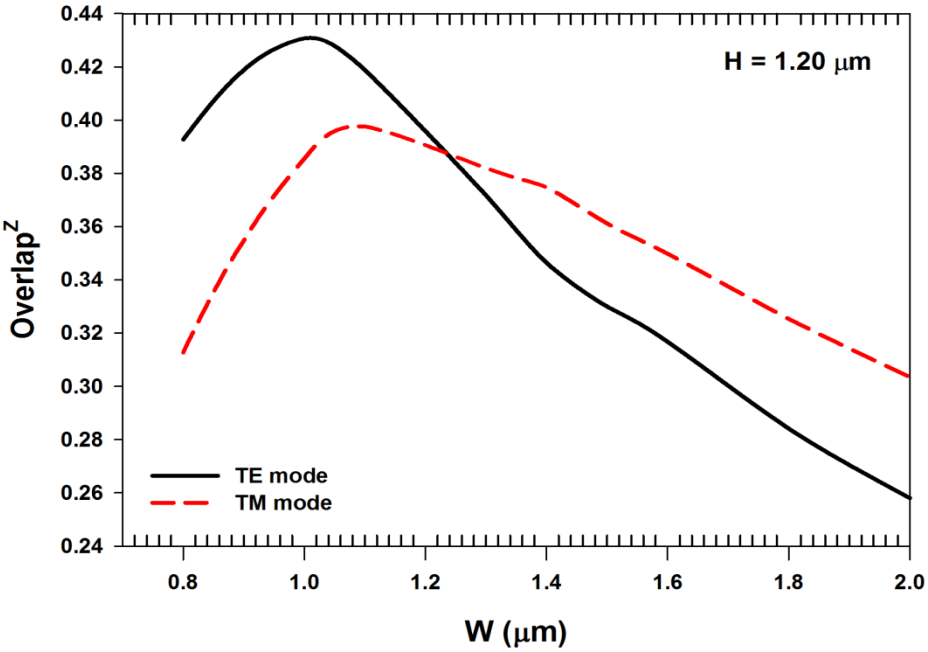

Figure 5.43. Variation of the U_z overlap integrals between acoustic and optical interaction with waveguide width.

Figure 5.43 shows the overlap integral between the acoustic radial mode (R1) of its U_z displacement vector with the fundamental quasi-TE and TM optical modes with the waveguide width. It can be observed that as the width of the guide is increased the overlap increases rapidly and reaches its maximum value, then reduces as width is increased further. When the width is at its maximum the overlap ratio between acoustic and optical modes is at its minimum. In contrast, higher overlap ratio is shown to be 0.438 and 0.40 at 1.1 μm and 1.15 μm, respectively, for the quasi-TE and TM modes. It can be observed that the mismatch between acoustic and optical waves is quite high when width is increased.

5.5 Strip waveguide

Conventionally, silica fibres are widely used in backbone and metro area networks. Although, polymer optical waveguides are being researched and developed at all over the world due to their advanced characteristics. Current semiconductor fabrication technology is thought to be complicated and expensive process, but it guarantees high accuracy. And therefore, it is still thought to be the best method for producing conventional polymer optical waveguides as well as silica optical waveguides. However, other research groups [Wright, 1971], [Fan, 2002], and [Doghmanel, 2006] have implemented a new replication process to realize both low cost and simple polymer optical waveguide. In our studies, the information provided from these research groups will be used and analysed in this section.

5.5.1 Study of Longitudinal modes in Porous Silicon Waveguide

In this section a Porous Silicon (PS) on SiO_2 buffer layer which surrounded by polymer will be studied where, the acoustic mode will be guided in the PS region that have the higher acoustic index. The strip waveguides studied here would support non-degenerate modes resulted from unequal width and height of the waveguide. Material data has been taken from [Fan, 2002], [Doghmanel, 2006] and [Jen, 1986] and for porous silicon cladding, the longitudinal velocity V_L is taken as 1675.59 m/s, shear velocity, V_S as 1170.28 m/s and with the density 460 kg/m^3. From glassy polymer core these are taken as longitudinal velocity V_L=3033 m/s, shear velocity, V_S=1388 m/s and material density ρ=1190 kg/m^3. For pure silica, the materials were taken as cladding, for the longitudinal velocity V_L is taken as 5933 m/s, shear velocity, V_S as 3764 m/s with the material density 2202 kg/m^3.

Table 5.2. Material properties and elastic stiffness constants for the strip waveguide.

	Velocity (m/s)		Density (kg/m^3)	Elastic Stiffness (GPa)			Refractive index
Material	V_L	V_S	ρ	c_{11}	c_{12}	c_{44}	n
SiO$_{2\text{-}7940}$	5933	3764	2202	77.5115	15.1169	31.1973	1.44
Porous Silicon	1675.5920	3764	2202	6.1824	56.2112	31.1973	3.43
Glassy Polymer	3033	1388	1190	10.9470	6.3618	2.2912	1.59

However, in this case; it has been assumed that the transverse velocity of the core and cladding of silica and porous silicon are equal to avoid the transverse modes in order to prevent coupling between the longitudinal and transverse modes. Here for pure silica cladding the longitudinal velocity V_L is taken as 5933 m/s, shear velocity, V_S as 3764 m/s with the material density 2202 kg/m^3. For porous silicon (PS) core these values are taken as longitudinal velocity V_L=1675.5920 m/s, but adopted its shear velocity, V_S=3764 m/s and material density ρ=2202 kg/m^3 as given in Table 5.2.

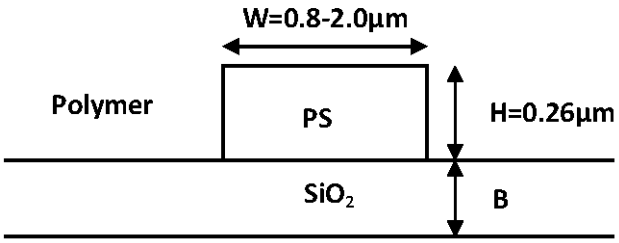

Figure 5.44. The Porous Silicon (PS) waveguide.

The PS strip waveguide is shown in Fig. 5.44 where the width of the guide has been varied from 0.8-2.0 µm with a constant height of 0.26 µm, along with the lower glass buffer layer height of 1.0 µm thick. The longitudinal acoustic mode in the acoustic waveguide is studied first. Figure 5.45 shows the variation of the acoustic velocity with the frequency for the longitudinal L_{01} U^z mode with width equals to 0.6 µm and height equals to 0.26 µm. For the longitudinal mode the dominant U_z displacement vector will play an important role for the acousto-optic interaction as shown in this section.

It can be observed that the velocity of the longitudinal L_{01} (U^z) mode decreases monotonically from the glass polymer velocity of 3033.3 m/s to the the core velocity of porous silicon (PS) at 1871 m/s. From the relation of the wavenumber ($k=\omega/V$), the frequency is increased as the phase velocity reduced as shown in Fig. 5.45. At a higher frequency, the acoustic mode is more confined in the waveguide region of the PS core, whereas at a lower frequency, the wave spreads more into the cladding and its velocity is of the cladding velocity.

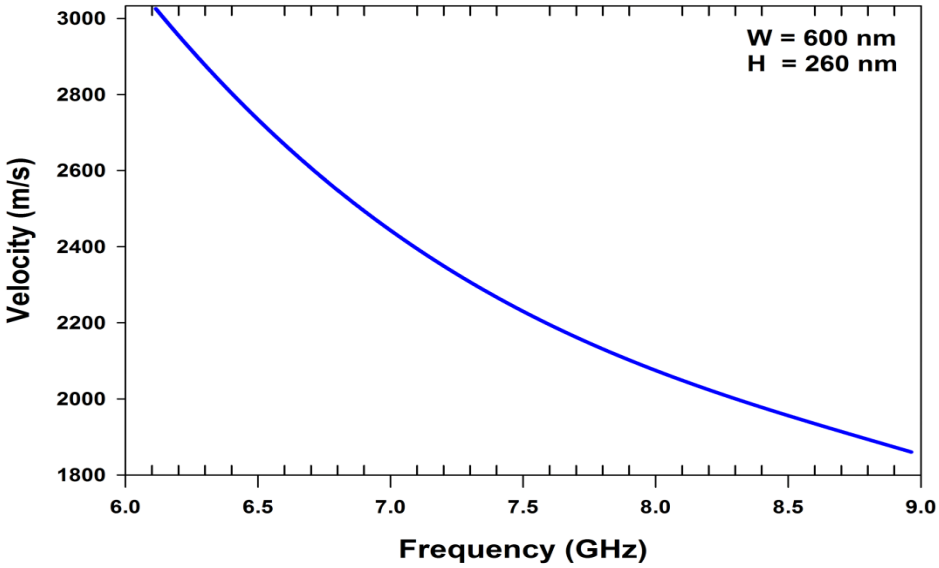

Figure 5.45. Variation of longitudinal L_{01} mode velocity with frequency of the acoustic waveguide H0.26W0.60 μm.

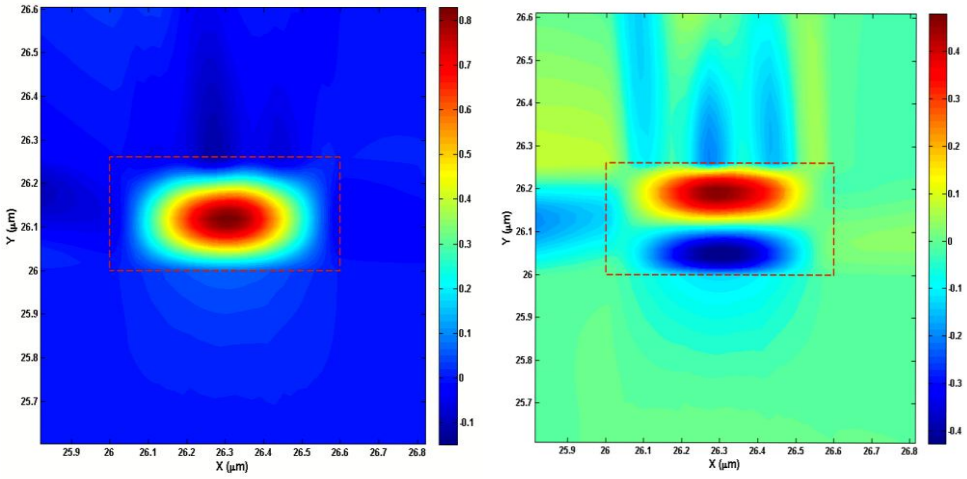

(a) (b)

Figure 5.46. The contour plots of (a) U_z and (b) U_y displacement vector of longitudinal L_{01} mode at k=17.2343 μm^{-1}.

The contour plot of the displacement vector U_z of the longitudinal L_{01} or (U^z) mode is shown in Fig. 5.46(a). This shows that the maximum displacement is at the centre of the core with the magnitude of 0.85. The U^z profile of this mode is near Gaussian in shape. However, in Fig 5.46(b) the non-dominant U_y displacement eigenvector plot of the U^z mode is shown, which has a higher order spatial variation with one positive and one negative peaks and confined in the core with the magnitude of 0.5. The U_x displacement eigenvector of this U^z mode is close to zero.

5.5.2 Study of Overlap Between Optical and Acoustic Modes

The optical modes of these PS waveguides are studied by using the **H**-field formulation. In here, the effective area, effective index of PS optical waveguides are shown and later on the calculation of the SBS frequency shift of the acoustic mode are also shown. But first we need to calculate the propagation of the optical mode to estimate the acoustic frequency by using $k=2\beta$ and then the acousto-optic overlap integral calculation will be calculated from both the acoustic and optical mode profiles. We are also showing the interaction between acoustic and optical in the last two sections of the longitudinal and transverse modes strip waveguide.

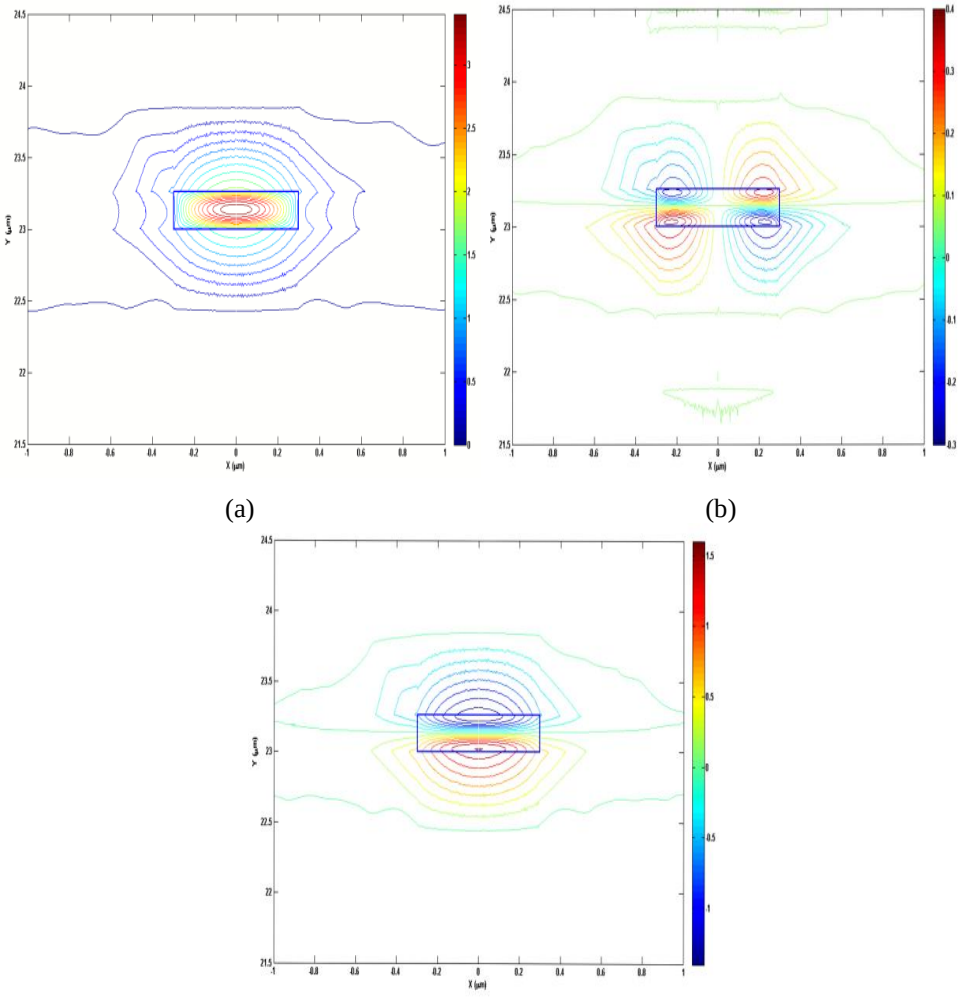

(a) (b)

(c)

Figure 5.47. The quasi-TE mode of (a) H_y (b) H_x and (c) H_z field profiles of PS waveguide H0.26W0.60μm.

Optical mode are classified as quasi-TE or quasi-TM modes as they have all the six components of the **H** and **E** fields. The electric and magnetic field

components in the *x*, *y* and *z* direction for the fundamental quasi-TE (H^y_{11}) mode are shown. All three components of the **H**-field profile of the quasi-TE (H^y_{11}) modes for the PS strip waveguide are shown in Fig. 5.47. The dominant H_y field component of H^y_{11} mode is shown in Fig. 5.47(a) illustrates that the maximum field profile is at the middle with the maximum magnitude of 4. The non-dominant H_x field profile is shown in Fig. 5.47(b) with its higher order spatial variation shows four peaks at the four corners of the waveguide with the highest magnitude of 0.4. The H_z field profile shows one positive and one negative peak along the upper and lower horizontal *x*-axis with the magnitude of 1.5. It can be noted that for this mode the maximum value of the H_z field is about 37.5% of the maximum value of H_y field and that of the H_x field is 10% of the H_y field. So the optical mode is highly hybrid in nature.

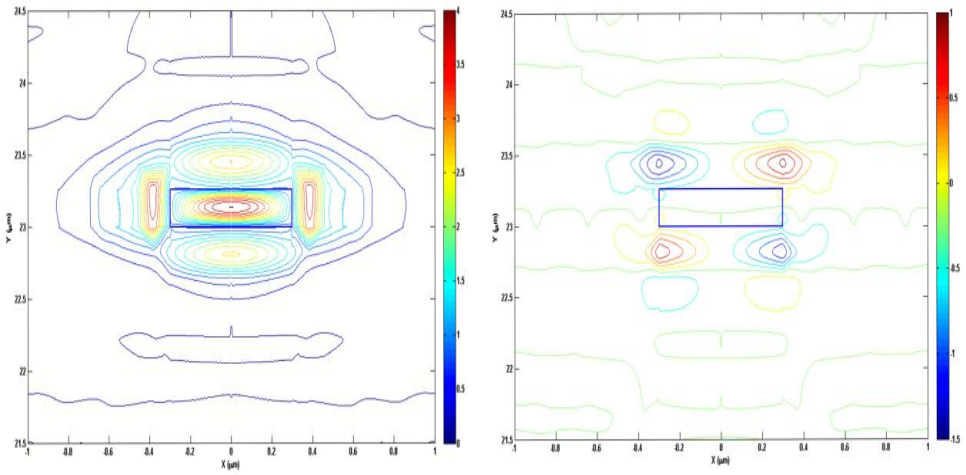

(a) (b)

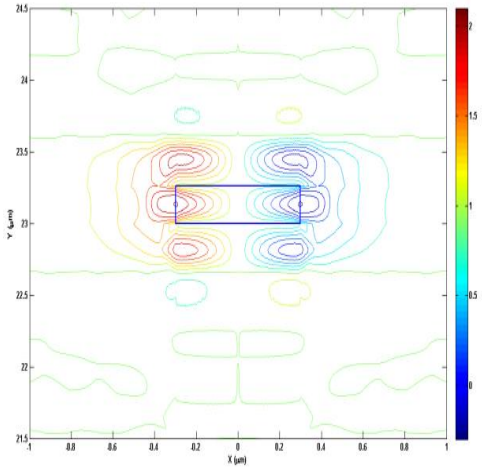

(c)

Figure 5.48. Contour plots of the quasi-TE mode of (a) E_x (b) E_y and (c) E_z profiles of PS strip waveguide.

The electric field profile of the quasi-TE modes for the PS strip waveguide is shown in Fig. 5.48. Here, the E_x component of the **E** field is dominant with the magnitude of 4.5 shown in Fig.5.48(a) at the centre of the core of PS. The higher order spatial variation of the non-dominant E_y field profile with four peaks at the four corners of PS rectangular waveguide shown in Fig.5.48(b) has the smallest magnitude of 1.5. The E_z profile shows one positive and one negative peaks in the waveguide region at the left and right interfaces. However, the mode shown in Fig. 5.48(c) has moved to the interface of the waveguide with the maximum magnitude value of 2.

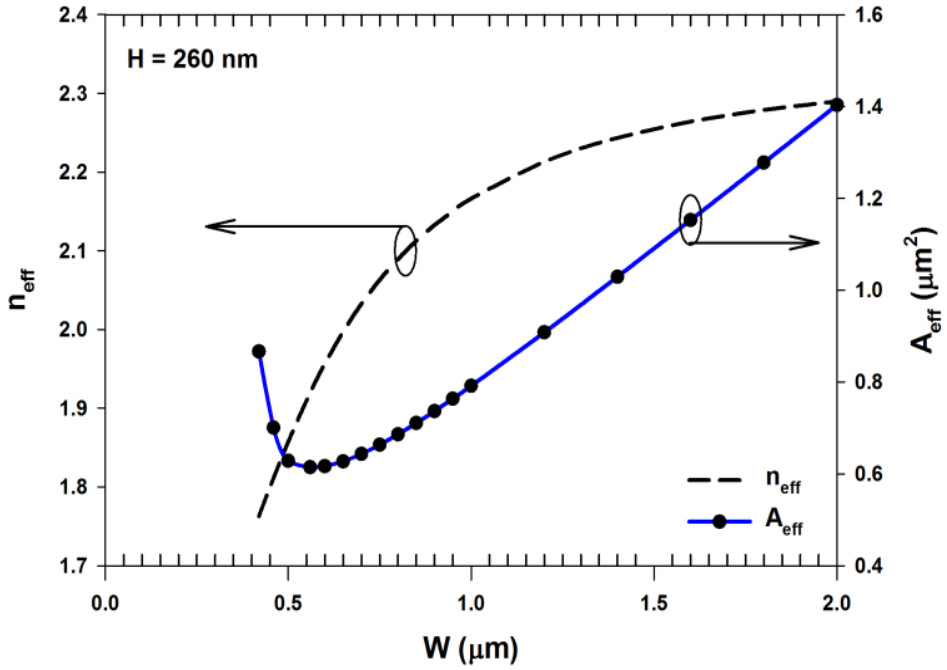

Figure 5.49. The quasi-TE variation of effective index (n_{eff}) and the area effective (A_{eff}) with width of PS waveguide.

Variation of the effective index and effective area with the waveguide width for the quasi-TE mode is shown in Fig. 5.49. The n_{eff} is increased with the width of the PS waveguide as shown in Fig. 5.49. It can be observed that at the lowest width it shows the lowest n_{eff} values and as the width is increased the n_{eff} is also increased. As the width is reduced A_{eff} reduces and reaches the smallest value at 0.5μm and afterwards the A_{eff} increased as the width of the waveguide is reduced further. At the minimum value of the A_{eff} which achieved the maximum power density intensity of the mode can be obtained as shown in Fig. 5.49. It can be noticed that when the

width is increased, it will also increase the confinement of the waveguide with the increasing of the n_{eff} and A_{eff}.

In this section we have studied the interaction between acoustic and optical mode by using $k=2\beta$ to calculate the SBS frequency shift in the acoustic waveguide and also shows the overlap integral of the acousto-optic interaction [Bhashar, 2003]. Figure 5.50 shows the variations of the SBS frequency and the overlap interaction between quasi-TE optical mode with the longitudinal $L_{01,}$ U^z mode with width of the waveguide.

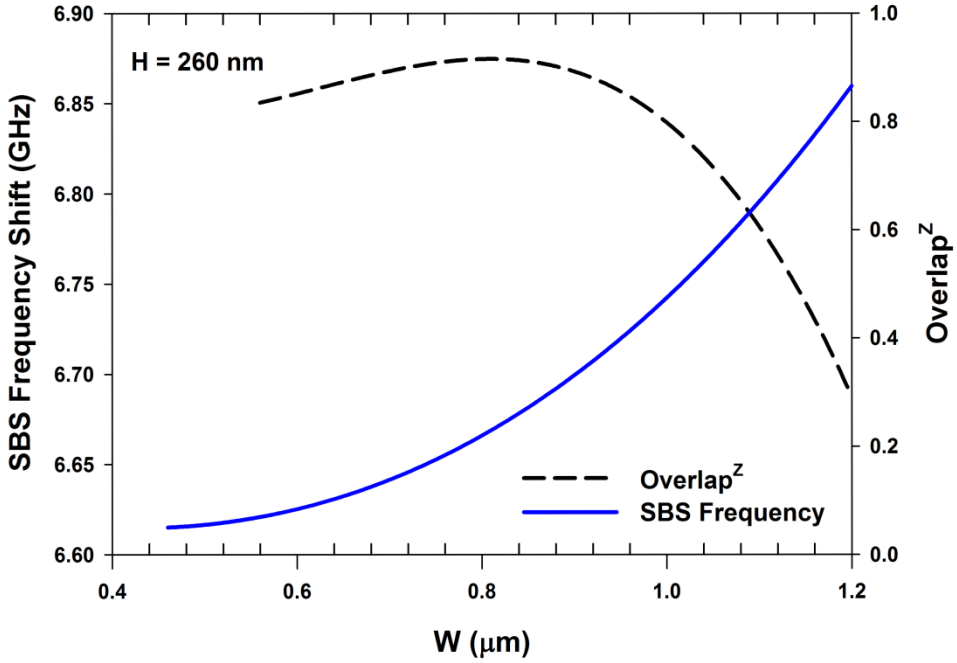

Figure 5.50. Variation of the SBS frequency shift and the overlap^z of the L_{01} or (U^z) mode between acoustic and optical modes with waveguide width.

The variation of the SBS frequency shift with width in Fig. 5.50 shows the SBS frequency is increased with width of the waveguide, its lowest SBS frequency is at width of 0.4μm. The overlap^z between quasi-TE H^y_{11} optical mode and dominant U^z longitudinal acoustic mode are calculated and shows that the overlap is decreased as width increases. As the width is increased, the overlap^z shows that its maximum values is of 0.9 at width 0.8 μm, as the width is increased further, the overlap^z is reduced to 0.3 at width 1.2 μm. In contrast, it can be noticed that SBS frequency shift is increased as the width is increased.

5.5.3 Study of Shear modes in Silicon Strip Waveguide

In this section, some of the parameters shows in Table 5.3 are different to those shown in Table 5.2, with the aim to study only shear mode. Material data has been taken from [Fan, 2002], [Doghmanel, 2006] and [Jen, 1986] for porous silicon cladding, the longitudinal velocity V_L is taken as 1675.59 m/s, shear velocity, V_S as 1170.28 m/s and the density 460 kg/m^3. From glassy polymer core these are taken as longitudinal velocity V_L=3033 m/s, shear velocity, V_S=1388 m/s and material density ρ=1190 kg/m^3. For pure silica cladding the material data were taken as, the longitudinal velocity V_L as 5933 m/s, shear velocity, V_S as 3764 m/s and the material density 2202 kg/m^3.

Table 5.3. The material properties of the waveguide.

	Velocity (m/s)		Density (kg/m^3)	Elastic Stiffness (GPa)			Refractive index
Material	V_L	V_S	ρ	c_{11}	c_{12}	c_{44}	n
SiO$_{2\text{-}7940}$	5933	3764	2202	77.5115	15.1169	31.1973	1.44
Porous Silicon	1675.5920	1170.2842	460	1.2915	0.0315	0.630	3.43
Glassy Polymer	3033	1388	1190	10.9470	6.3618	2.2912	1.59

The variation of the shear velocity of the transverse U^x mode with the propagation constant is shown in Fig. 5.51. This is shown for the acoustic porous silicon waveguide of H=0.26μm and W=0.60μm with a silica buffer layer and surrounded with polymer. The variation of the velocity with frequency of the shear U^x mode is also shown here. For this transverse modes, the component of U_x, U_y and U_z displacement vector profiles are shown in Fig. 5.52, where the dominant displacement vector is mostly confined inside the core of the PS, in which it has the highest acoustic index.

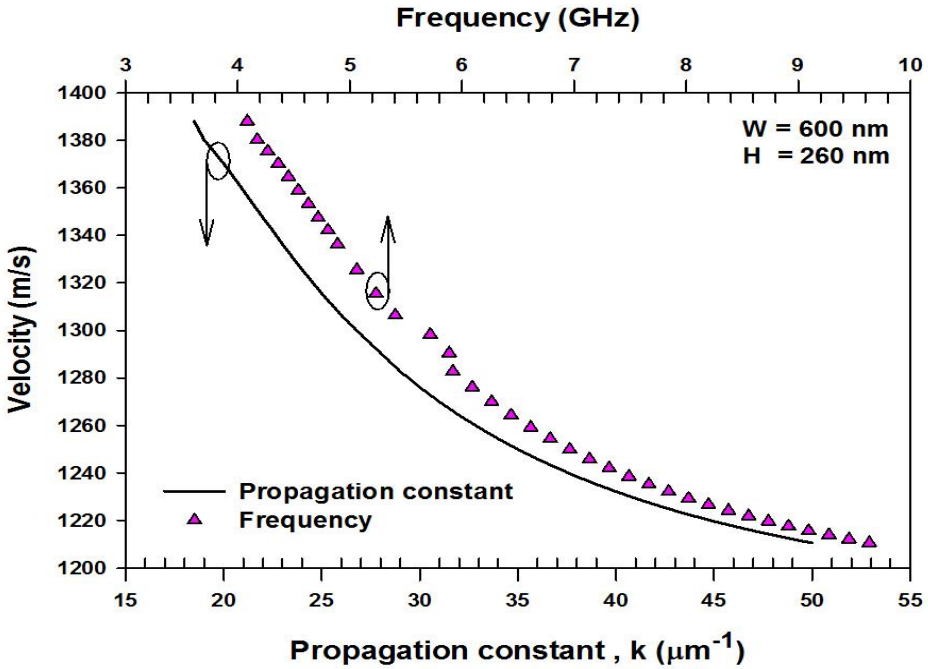

Figure 5.51. Variation of the transverse velocity of the U^x mode with propagation constant (k, μm^{-1}) and frequency (f, GHz) of the PS waveguide at H0.26W0.60um.

Variations of the velocity of the transverse U^x acoustic mode with the propagation constant (k, μm^{-1}) and frequency (f, GHz) are shown in Fig. 5.51. It can be noted that the shear velocity in the PS layer is taken as a lower value, to encourage formation of the shear modes. The width and height of the PS are taken as 0.6 μm and 0.26 μm, respectively. This figure shows the velocity is decreased as the propagation constant is increased. It can be observed that velocity of the transverse U^x profile is decreased with the frequency is increased. It is also shown in Fig. 5.51 that by increasing in frequency and propagation constant, the velocity of the mode decreases. This shows that the cladding velocity of PS decreases from 1400m/s to the core of PS velocity of 1170m/s, as an effect, this shows that the confinement in the core of the waveguide will be higher with increasing frequency and propagation constant.

In this section, the displacement vectors of the transverse U^x mode are shown in Fig. 5.52. For this waveguide, as its width and height were not equal, the fundamental U^x and U^y modes were not degenerate.

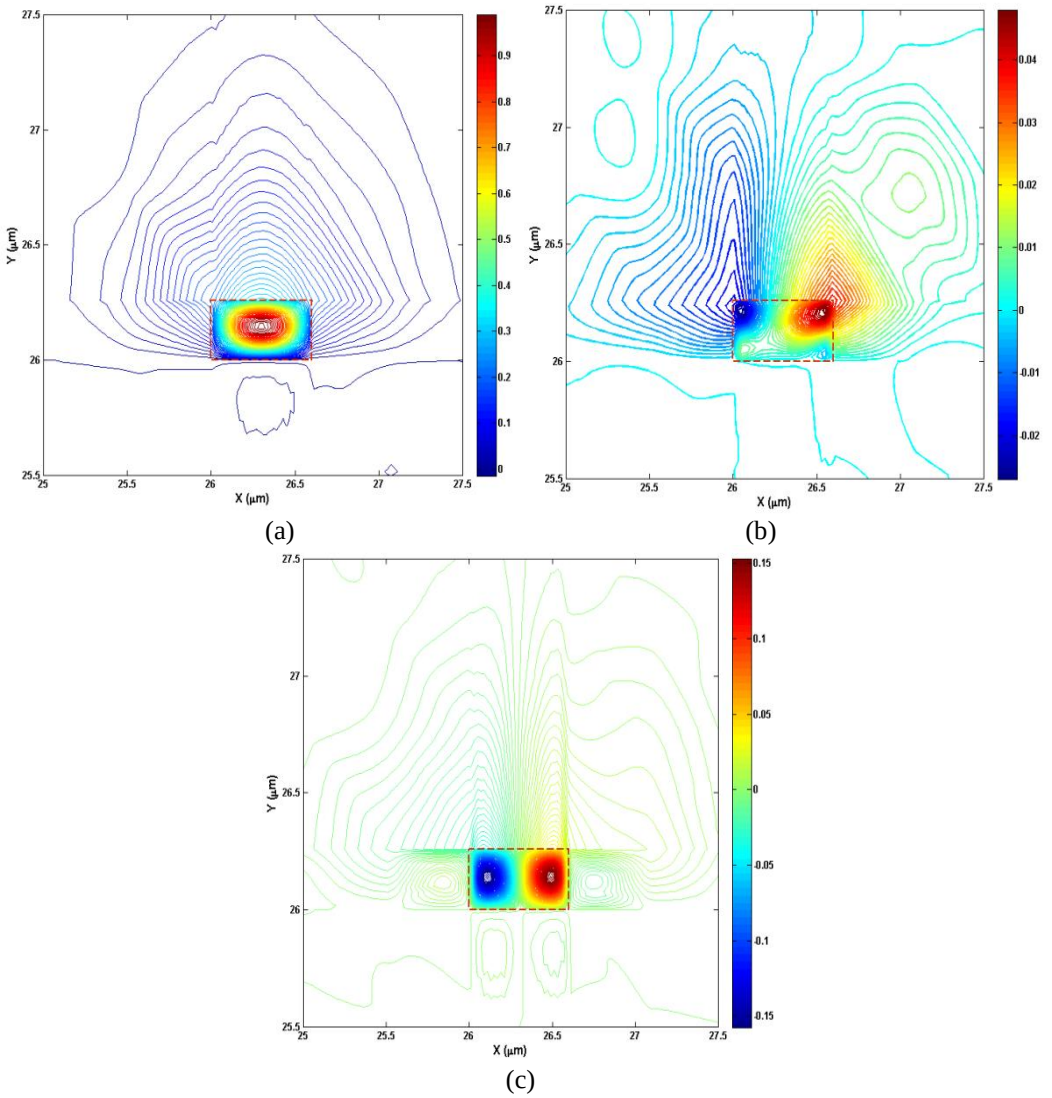

Figure 5.52. Contour profiles of the transverse U^x mode of (a) U_x, (b) U_y and (c) U_z displacement vector at k=18.50 μm^{-1} of PS waveguide H0.26W0.60μm.

The contour profile of the dominant transverse U^x displacement vector presented in Fig. 5.52(a), shows the maximum U^x profile. It also shows the maximum normalised magnitude value of unity in the core of the waveguide. The variation of the U_y displacement vector profile shows that it has one positive and one negative peaks on the left and right near the interface of the PS waveguide with the lowest magnitude of 5% of U^x profile. The displacement vector U_z profile is also shown in Fig. 5.52(c) in which there is one positive and one negative peak inside the core of the PS waveguide on the left and right side of the core with the magnitude of 25% of the dominant U^x displacement vector.

5.5.4 Study of the PS Waveguide when Width (W) is Varied

In this section, the width of the PS waveguide is varied to study the SBS frequency shift and the overlap between acoustic and optical waves. To achieve that, first the optical modes of these guides are studied. In this section part the effective area (A_{eff}), effective index (n_{eff}) of PS optical waveguides are shown and later on the calculation of the SBS frequency shift of the acoustic mode by using $k=2\beta$ and the acousto-optic overlap calculation between acoustic and optical is also presented in the last section. To obtain the SBS frequency shift, it is essential to calculate the propagation constant of the optical mode, which is related to the n_{eff} of that mode (Eq. 5.1).

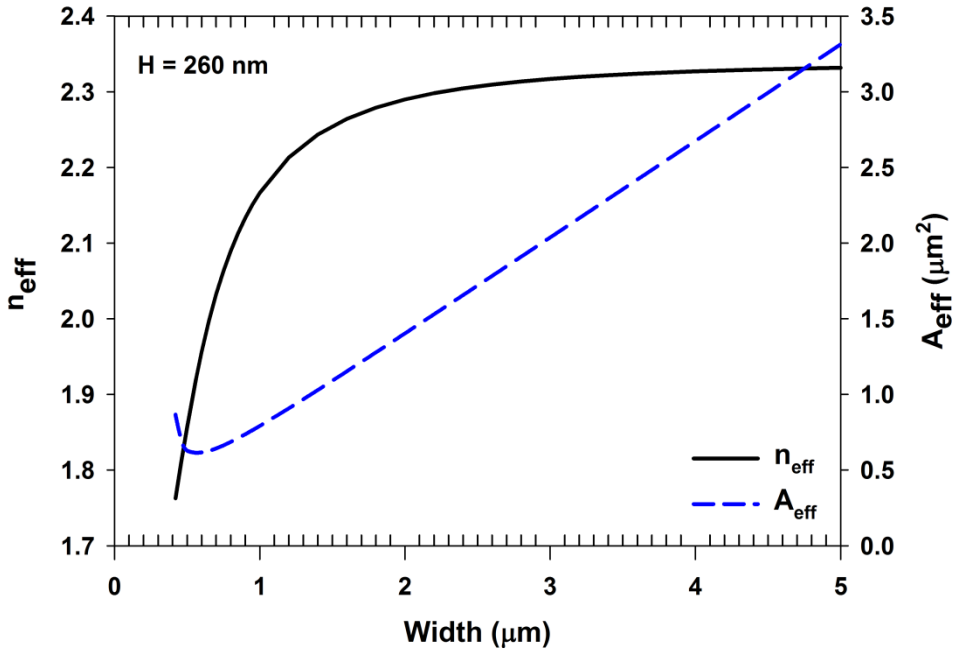

Figure 5.53. The variation of effective index (n_{eff}) and the A_{eff} of Porous Silicon with the width of the waveguide.

Variations of the n_{eff} and A_{eff} with the width of the PS waveguide are shown in Fig. 5.53. It can be noticed that n_{eff} and A_{eff} increase with the width of the waveguide. It is shown here that when the waveguide width is small, the guide is unable to support any of the optical modes as it approaches modal cut-off. At the smallest width (0.5 μm), n_{eff} is the lowest, in which case the confinement is also low. However, when the width is at its maximum, n_{eff} is high with the higher mode confinement inside the core of the waveguide. From the graph, A_{eff} also increases when the waveguide width increases.

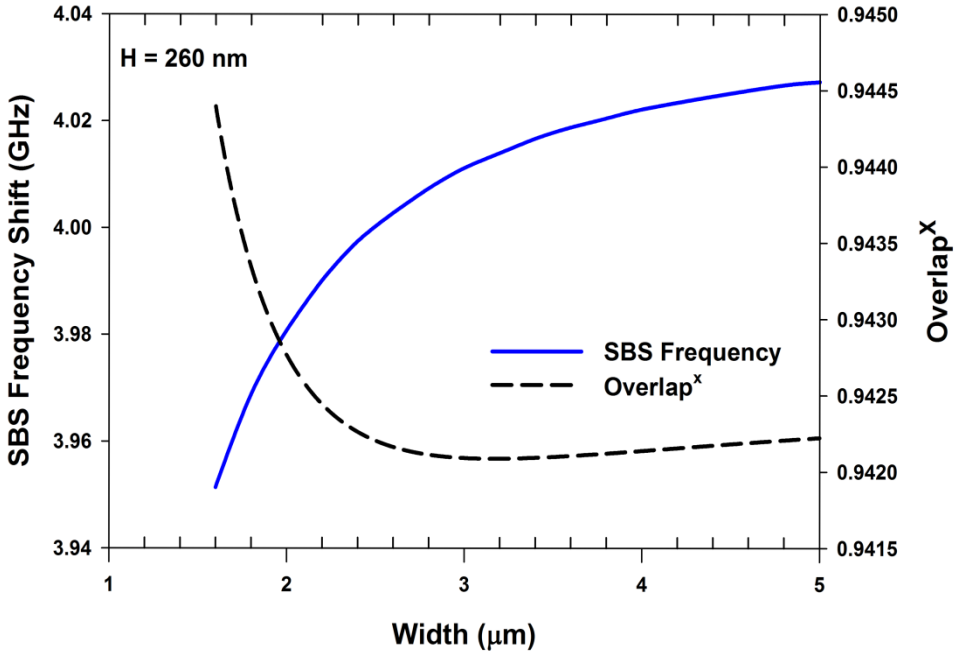

Figure 5.54. Variation of the SBS frequency and overlap^x with width of PS waveguide.

Variations of the SBS frequency and overlap with the width of PS waveguide are shown in Fig.5.54. In this figure it is shown that the SBS frequency is increased monotonically when the width of the waveguide is larger and its value is 4.02 GHz for width 5 μm. The overlap between acoustic and optical modes is reduced when the width of the waveguide is increased as shown here. It can be noticed that the overlap^x between acoustic and optical is at its maximum at the lowest width of the strip waveguide. On the contrary, the mismatch between acoustic and optical modes is high at a larger width of the waveguide than the lower width, however, their variations are small.

The overlap integral presents the matching ratio between the acoustic and optical mode profile. In Fig. 5.54, the overlap^x is calculated between H_y field of the quasi-TE H^y_{11} and the U_x displacement vector of the transverse U^x acoustic mode. The overlap^x shown the mismatch between acoustic and optical mode is quite high when the width of the waveguide is increased. In contrast, the mismatch is minimum when width of the waveguide is narrower as shown in Fig. 5.54. This figure also shown that the highest value of overlap^x is 0.945 at the lowest SBS frequency.

5.6 Summary

A group of planar rectangular waveguides have been studied in this chapter. First, a class of weakly guiding acoustic guide with Ge-doped SiO_2 core was studied as reported in Section 5.2. Next a strongly guiding acoustic guide with SiO_2 core was presented in Section 5.3 and finally acoustic mode of a strip waveguide is given in detail in Section 5.5.

Detailed displacement vectors for several fully hybrid acoustic modes with both transverse and longitudinal displacement vectors have been obtained, their profiles were shown and are discussed for a high index contrast acoustic SiO_2 waveguide. Unlike in a weakly guiding SiO_2 waveguides, the transverse and longitudinal displacements are strongly coupled in the high index contrast SiO_2 waveguide. Section 5.2, for the weakly guiding showed the transverse U^x and U^y modes with their displacement vector profiles shown Gaussian in shape. Section 5.3, the strong guiding of SiO_2 core showed the variation modes of B, T, R and TR with their spatial variation of U_x, U_y and U_z displacement vectors. In the last Section 5.5, showed the strip PS waveguide with their longitudinal U^z and transverse U^x modes. It was also shown here that their displacement vector profiles continuously evolve as the frequency or propagation constant increases and becomes increasingly confined along the waveguide interfaces. For some of these structures the interaction between acoustic and optical modes were also shown.

Chapter 6

Slot Waveguide

6.1 Introduction

The analysis of acoustic modes in slot optical waveguides and also their interactions with optical modes is reported in this chapter. Slot waveguide, is a unique structure where light is guided in a low-index region [Almeida, 2004 and Leung, 2012], which can also be air. The acoustic wave propagation of the displacement molecule inside a waveguide is depended on the properties of the material such as density, elasticity, Young modulus, and Poisson's ratio. These include acoustic shear velocity and longitudinal velocity of the core and cladding materials [Safaai-Jazi, 1988], [Lagasse, 1973] and [Stone, 1973]. These acoustic modes can be guided, provided at least one of the velocities (the shear or longitudinal velocities) of the cladding exceeds that of the core. The particle displacement can be either in the longitudinal direction or in the transverse plane and propagation of the waves can be classified as longitudinal, torsional, bending or flexural modes.

6.2 Analysis of the Slot Waveguide

The slot waveguide [Almeida, 2004] and [Leung, 2012] is a unique structure in which light is guided in a low-index region due to the continuity of the normal component of the Electric Flux Density (D) at the dielectric interfaces (which makes E_n higher in low index area), which open up new opportunities for sensor design [Wang, 2013] and [Dell'Olio, 2007] where the slot can be filled with an active or functional material to create devices such as high-speed modulators [Baher-Jones, 2008], amplifiers [Robinsor, 2008] or nonlinear devices [Wang, 2013] by accessing higher field readily accessible in the slot region. The slot waveguide is a waveguide where light can be guided in a low index region, whereas, for most of the optical waveguides light is guided in a high index region. Sound can be guided in this slot region with silica (SiO_2), as it has higher acoustic index than the surrounding silicon (Si) layer. This results in the possibility of sound-light interactions in a silica filled slot waveguide.

In this study, to isolate the acoustic wave in the slot region a low index for (both optical and acoustic) Silica Nitride (Si_3N_4) layer, a popular insulating layer in Si-based electronics, is considered here which will isolate both optical and acoustic waves.

6.2.1 Waveguide Structure

A typical slot waveguide structure is shown in Fig. 6.1. For optical guidance, a typical waveguide width, W around 200 to 300 nm, slot width, W_s, between 50 to 200 nm, and its height H around 200 to 300 nm are often used.

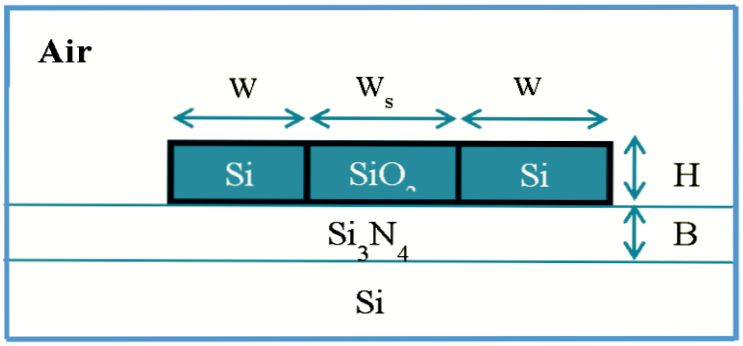

Figure 6.1. Schematic diagram of a Slot waveguide.

Initially, the slot waveguide structure considered here with the dimension of SiO_2 slot width W_s=150 nm and slot height H= 220 nm with Si width W=300 nm on the side and Si_3N_4 base B=1000 nm buffer layer at the bottom of the slot to prevent the leakage of the slot mode to the lower substrate layer, to study various acoustic modes. The material properties and elastic stiffness constants are given in Table 6.1.

Table 6.1. Material properties and elastic stiffness constants for the slot waveguide.

	Velocity (m/s)		Density (kg/m^3)	Elastic Stiffness (GPa)		
Material	V_L	V_S	ρ	c_{11}	c_{12}	c_{44}
$SiO_{2\text{-}7971}$	5736	3625	2213	72.8115	14.6511	29.0802
Silicon	8433	5845	2330	165.6	63.9	79.6
Si_3N_4	10611.6332	5956.4114	3440	387.3672	143.2728	122.0472
Xenon	22303.7	15472.2	5.8971	2.93	1.89	1.41

The relation between $v = \omega/k$ can be used for the plotting the acoustic wave phase velocity versus wavenumber or frequency, and we can also relate the parameter frequency/propagation constant (f/k) with velocity, as this parameter is also directly proportional to the velocity of the wave. In our work, some of them are considered.

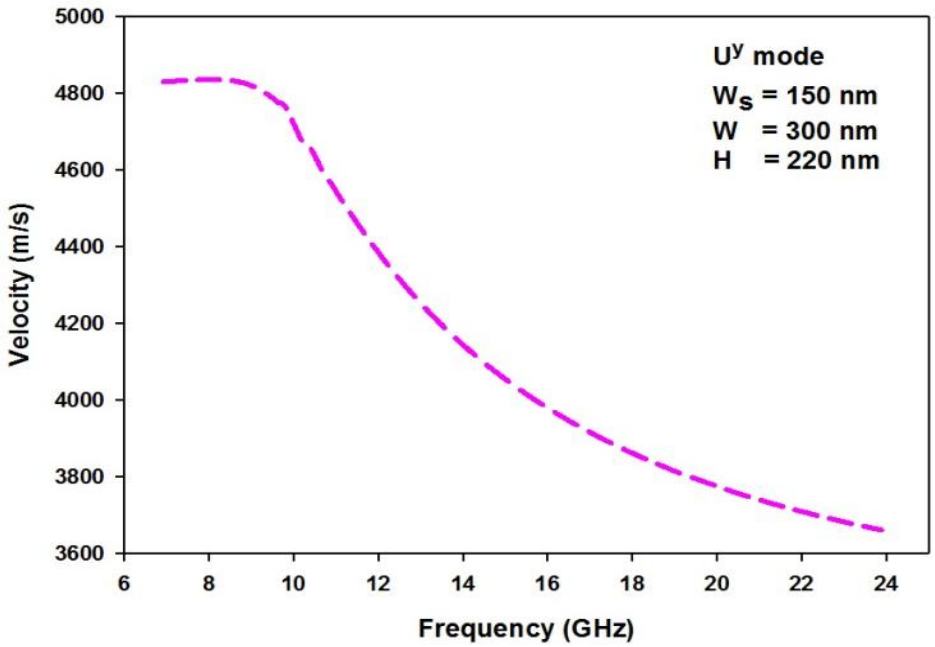

Figure 6.2. Variation of the velocity of the acoustic U^y mode with the frequency for a vertical slot waveguide.

Variation of the phase velocity with frequency is shown in Fig. 6.2 for the dominant U^y mode. It can be observed here that, as *f* increases, the velocity of the slot guide is decreased from the cladding velocity of 4800 m/s to the core velocity of 3625 m/s. The observation of this range, the f_a/k_a ratio is reduced from 0.77 to 0.55 with the operating frequency of the acoustic phase velocity is reduced to the cut-off and towards a velocity which is related to the slab acoustic mode of the Si layer. Similarly as the frequency is increased the mode asymptotically reaches a value for a very well confined mode in the SiO_2 slot region.

6.2.2 Study of Slot Waveguide Acoustic Modes

The full-vectorial displacement vector profile of this U^y mode is shown in Fig. 6.3 at propagation constant *k* equal to 20 μm^{-1}. For this mode, U_y displacement vector is dominant and this is normalised to its maximum value of 1 and its profile is shown in Fig. 6.3(a). The positions of Si waveguides and slot region are shown by red solid and dashed lines. It can be observed that U_y profile is symmetric along the horizontal direction and its peak value is located inside the slot region. Its profile along the vertical direction is not symmetric, as material properties in the upper and lower sides were different.

The non-dominant U_x profile of this U^y mode is shown in Fig. 6.3(b). It can be observed that this vector is asymmetric with a higher order spatial variation in the lateral direction, very similar to the non-dominant field of a Si waveguide [Leung, 2010]. Its maximum magnitude is about 20% of the maximum value of the dominant U_y displacement vector. It can be noted that its maximum value is along the upper interface where acoustic index contrast was higher.

Next, contour profile of another non-dominant U_z (x,y) vector is shown in Fig. 6.3(c). It can be observed that this vector also shows higher order spatial variation, but in the vertical direction. This profile is symmetric along the horizontal direction but highly non-symmetrical in the vertical direction. Its highest value is about 55% of that of the dominant U_y displacement vector and located at the upper slot interface where material contrast was higher. Later on, variation of some of these displacement vectors along the horizontal and vertical directions will be shown. It

should be noted here that, for this mode, although a transverse displacement vector (U_y) was dominant, however, magnitude of the longitudinal displacement vector (U_z) was also considerably high (50%), so this mode cannot be considered as a pure transverse mode, but a highly hybrid mode.

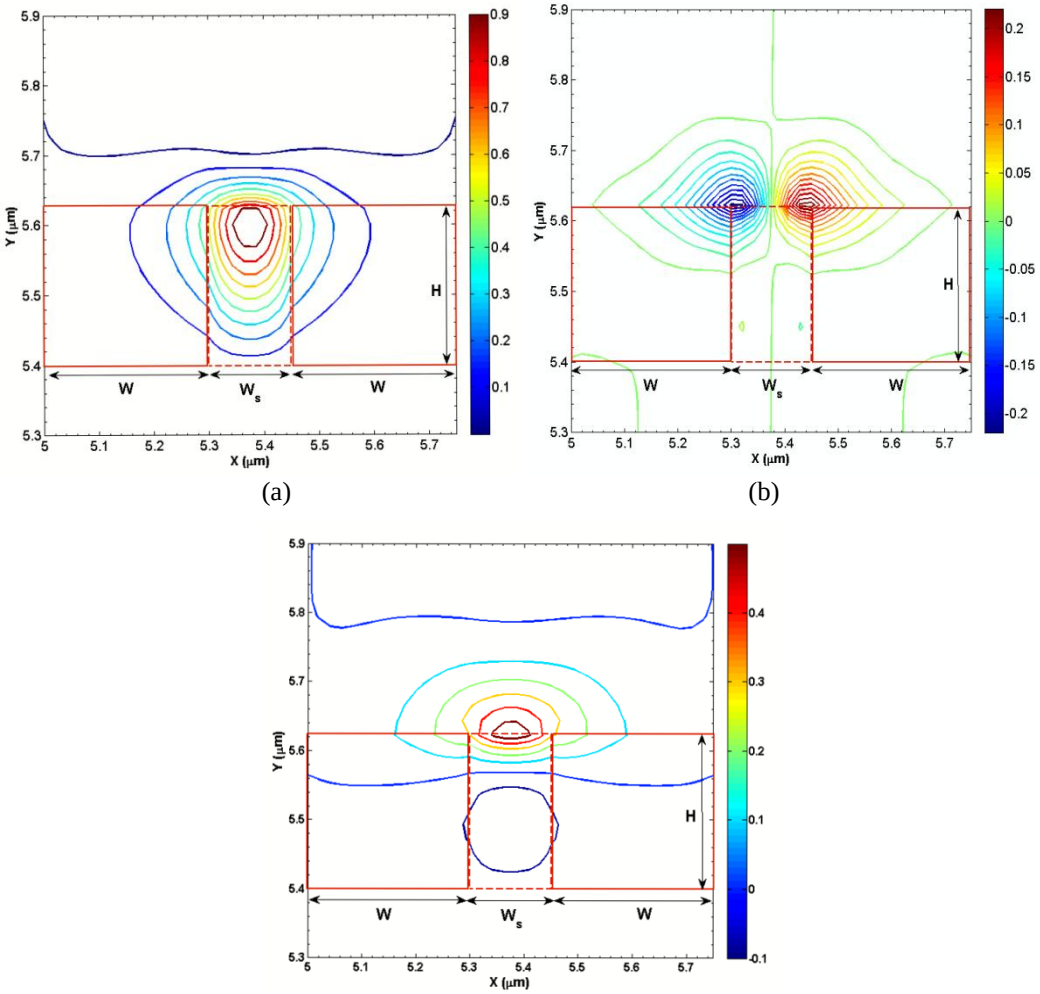

Figure 6.3. The displacement vector plots of the U^y mode in a slot waveguide (a) U_y (b) U_x and (c) U_z displacement vector profiles at k = 20 μm^{-1} for W = 300 nm, W_s= 150 nm and H = 220 nm.

In Fig. 6.2, it was shown that as the operating frequency (or correspondingly its propagation constant, k) was reduced the mode approached its cut-off. To study this, next contour plot of the dominant displacement vector U_y profile is shown in Fig. 6.4, for a lower propagation constant value, k = 11.0 μm^{-1}. The height of the waveguide and its full width (W_T = W + W_s + W) are shown by two arrows. It can be observed here that the mode has expanded well inside the two adjacent Si layers on the sides and also into the Si_3N_4 layer at the bottom. As the mode profile moves away

from the central slot region into lateral Si regions or lower Si_3N_4 layer, the contour profile of the displacement vector clearly shows distinct changes in its profile. However, it can be observed that the U_y profile penetrates more into these Si and Si_3N_4 regions compared to the upper cladding which has a much lower acoustic index.

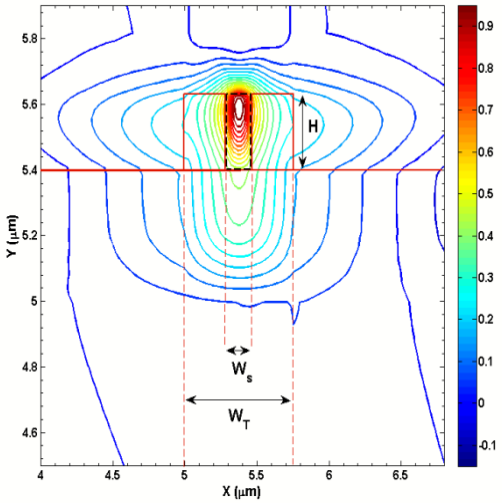

Figure 6.4. The U_y displacement vector profile of the U^y mode at k=11.0 μm^{-1} for W = 300nm, W_s= 150nm and H = 220nm.

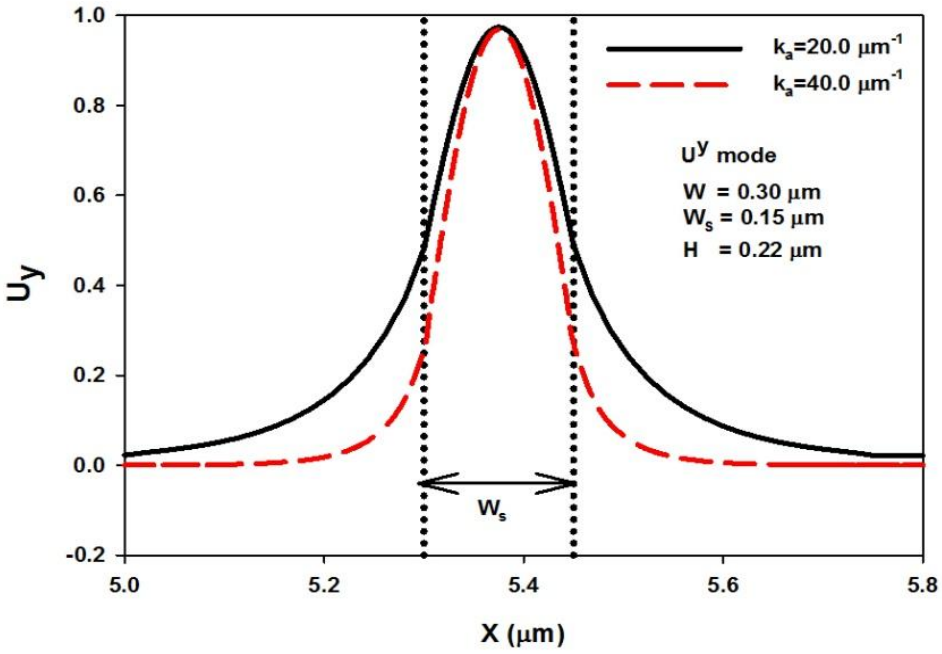

Figure 6.5. Variation of the displacement vector U_y along the x-axis for the U^y mode in a slot waveguide at k=20.0 μm^{-1} and k=40.0 μm^{-1}.

The contour profile of the dominant U_y displacement vector was shown in Fig. 6.3(a) To observe its transverse variation more clearly, next, its lateral and

vertical variations are shown. Variations of the U_y displacement vector along the horizontal direction for two different propagation constants are shown in Fig. 6.5. It can be observed that the profiles are symmetric in nature. However, it can also be observed that for a higher frequency the mode profile is more confined, as shown by a red dashed line for propagation constant, k = 40 μm^{-1}. The full mode width, where field decays to *1/e* of its maximum value is 180 nm and 132 nm respectively, at propagation constants, k = 20 and 40 μm^{-1}. The spread of the displacement vector inside the cladding (*1/e*th decay from the interface) are 100 nm and 40 nm for k = 20 and 40 μm^{-1}, respectively.

Variations of the dominant displacement vector U_y of the U^y mode along the vertical direction are shown in Fig. 6.6 for two different propagation constant, k values. It can be observed that the U_y profile is not symmetric but tilted. As this profile is non-symmetric, instead of the full-mode-width, only half-mode-width along both the lower and upper directions are calculated separately and these are of 133 nm and 20 nm, respectively at k = 20 μm^{-1}.

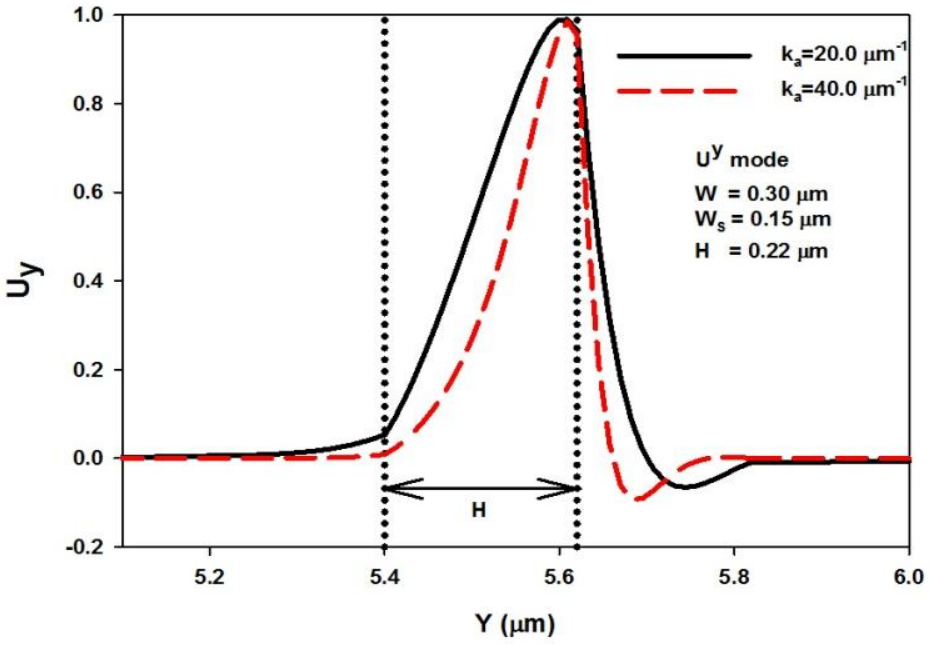

Figure 6.6. Variation of displacement vector U_y of the U^y mode along the y-axis at k=20.0 μm^{-1} and k=40.0 μm^{-1}.

It can also be observed that its peak value is closer to the upper interface where the material index difference was stronger. A small negative peak can also be

observed in the upper cladding layer. We have noticed similar negative peaks for all acoustic waveguide with a strong index contrast, where as for an acoustic waveguide with small acoustic index contrast, similar negative peak is absent. It can be noticed here, that for a higher propagation constant, $k = 40\ \mu m^{-1}$, shown by a red dashed line, the mode profile is narrow, the negative peak is sharper with a higher secondary peak value. When k is increased to $40\ \mu m^{-1}$, these half-widths in the lower and upper directions reduce to 94 nm and 10 nm, respectively, much smaller values than that for $k = 20\ \mu m^{-1}$ which were 133 nm and 20 nm for lower and upper half-mode-widths.

Similarly, it was observed that as the propagation constant increases the non-dominant displacement vectors also shrinks in its sizes. The U_x profile in Fig. 6.7(a) shows one positive and one negative with the magnitude of 0.15 and the U_z displacement vector profile for propagation constant, $k = 40\ \mu m^{-1}$ is shown in Fig. 6.7(b). If this is compared to the U_z profile shown in Fig. 6.3(c) for $k = 20\ \mu m^{-1}$, it can be clearly observed that its confinement area has substantially reduced. It can also be noticed that its peak value is now 63% of the maximum U_y displacement vector, compared to the only 55% value for $k = 20\ \mu m^{-1}$. This signifies that as propagation constant (or the frequency) increases modes are more confined but also more hybrid in nature, similar as the optical modes in high index contrast optical waveguides [Leung, 2010].

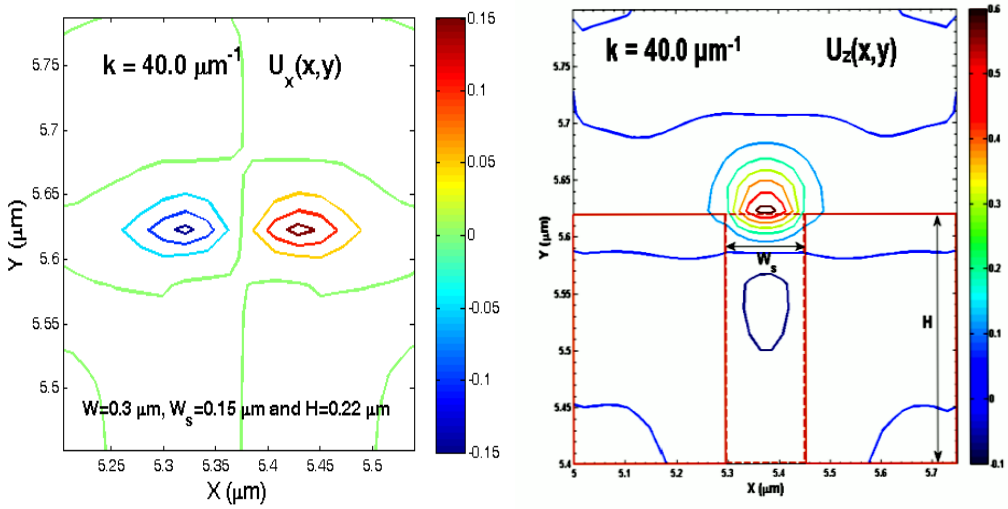

(a) (b)

Figure 6.7. U^y modes at propagation constant $k = 40\ \mu m^{-1}$ for W = 300nm, W_s= 150nm and H = 220nm of (a) U_x and (b) U_z displacement.

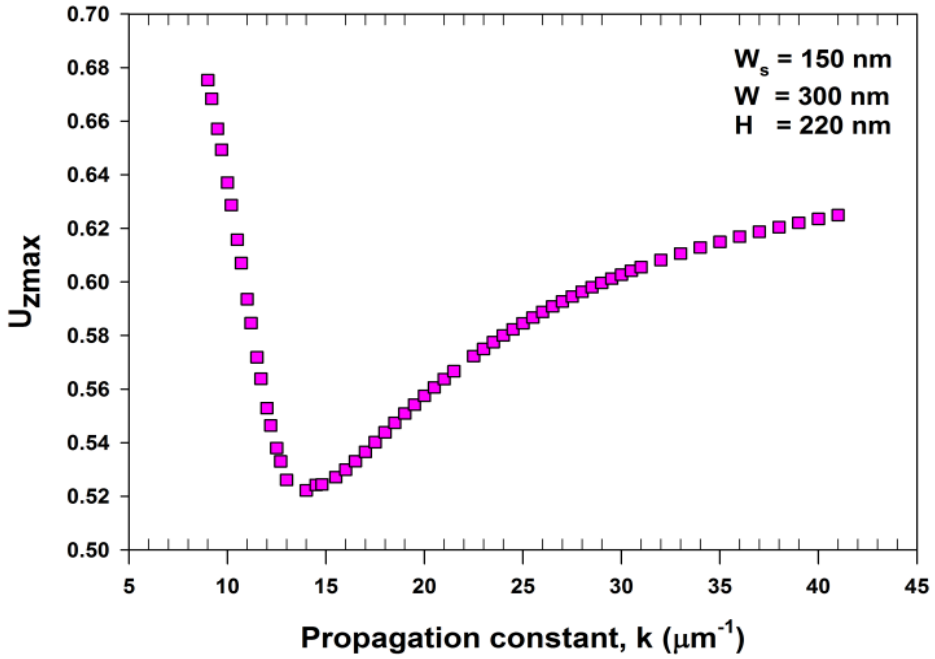

Figure 6.8. Variation of the modal hybridness of the U^y mode with the propagation constant.

Next, variation of the modal hybridness with the propagation constant is studied. The hybridness ($Hb_y=U_{zmax}/U_{ymax}$) of the acoustic modes can be defined by comparing the maximum value of the non-dominant displacement vector with the dominant displacement vector. For this U^y acoustic mode, U_y displacement vector is the dominant and U_x and U_z are non-dominants. Variation of the maximum value of the U_z displacement vector with the propagation constant, *k*, is shown in Fig. 6.8. As the propagation constant, *k* is reduced, initially modal hybridness is reduced, but when the mode approaches its cut-off at lower *k* values this modal hybridness also increases rapidly. It should be noted that the maximum value of the longitudinal displacement vector, U_z, is comparable to the maximum U_y value, and as this value is reasonably larger for this U^y mode, this mode is not purely transverse mode but a highly hybrid mode. The interaction of this highly hybrid acoustic mode with the optical modes, which are also hybrid will be quite complex in nature.

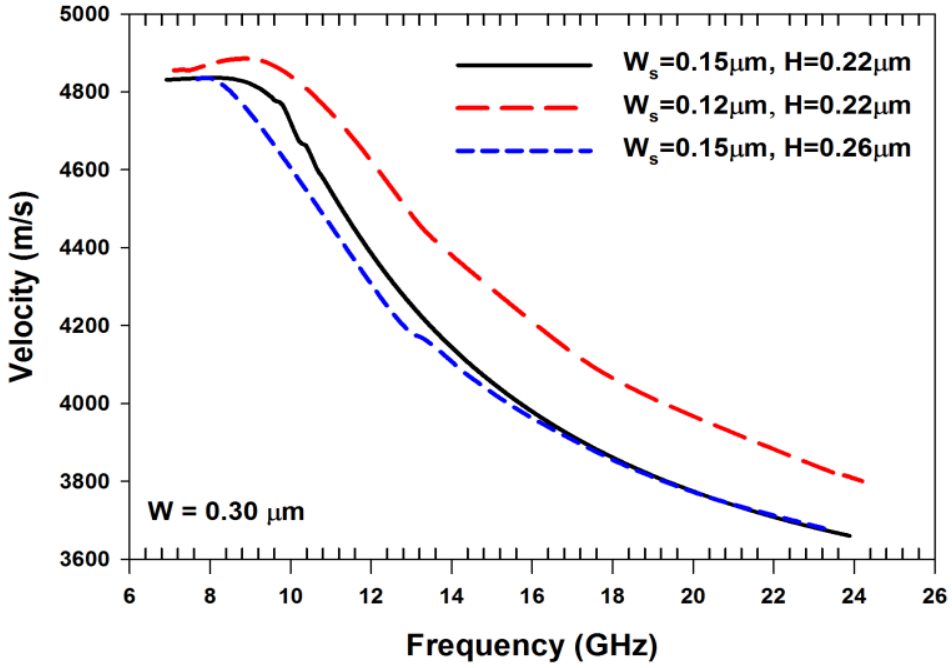

Figure 6.9. Variations of the phase velocities for the difference width and height of a slot waveguide.

Next, the effects of slot dimension on the modal properties are also studied. Variation of acoustic velocity with the acoustic frequencies for different slot heights and slot widths are shown in Fig. 6.9. When the slot width is reduced, as shown for W_s = 120 nm by a red dashed line, compared to W_s = 150 nm shown by a solid black line, it can be noted that it approaches its cutoff value at a lower acoustic frequency but with a slightly higher acoustic velocity. On the other hand, when the slot height is increased, as shown for H = 260 nm by a blue dashed line, compared to H = 220 nm shown by a solid black line, it can be noticed that its cut-off value is reached at a lower acoustic frequency but approaches the same acoustic velocity.

6.3 Acousto-optic Interaction in Slot Waveguide

Optical solutions of such Si slot waveguides are carried out by using fully vectorial **H**-field formulation [Rahman 1984]. It should be noted that, although both quasi-TE and TM modes can exist for this structure, but only quasi-TE mode will have a high power density in the slot region and for this reason only this mode is considered.

Optical mode in the slot waveguide are presented here for the electric and magnetic field of the *x*, *y* and *z* displacement variation.

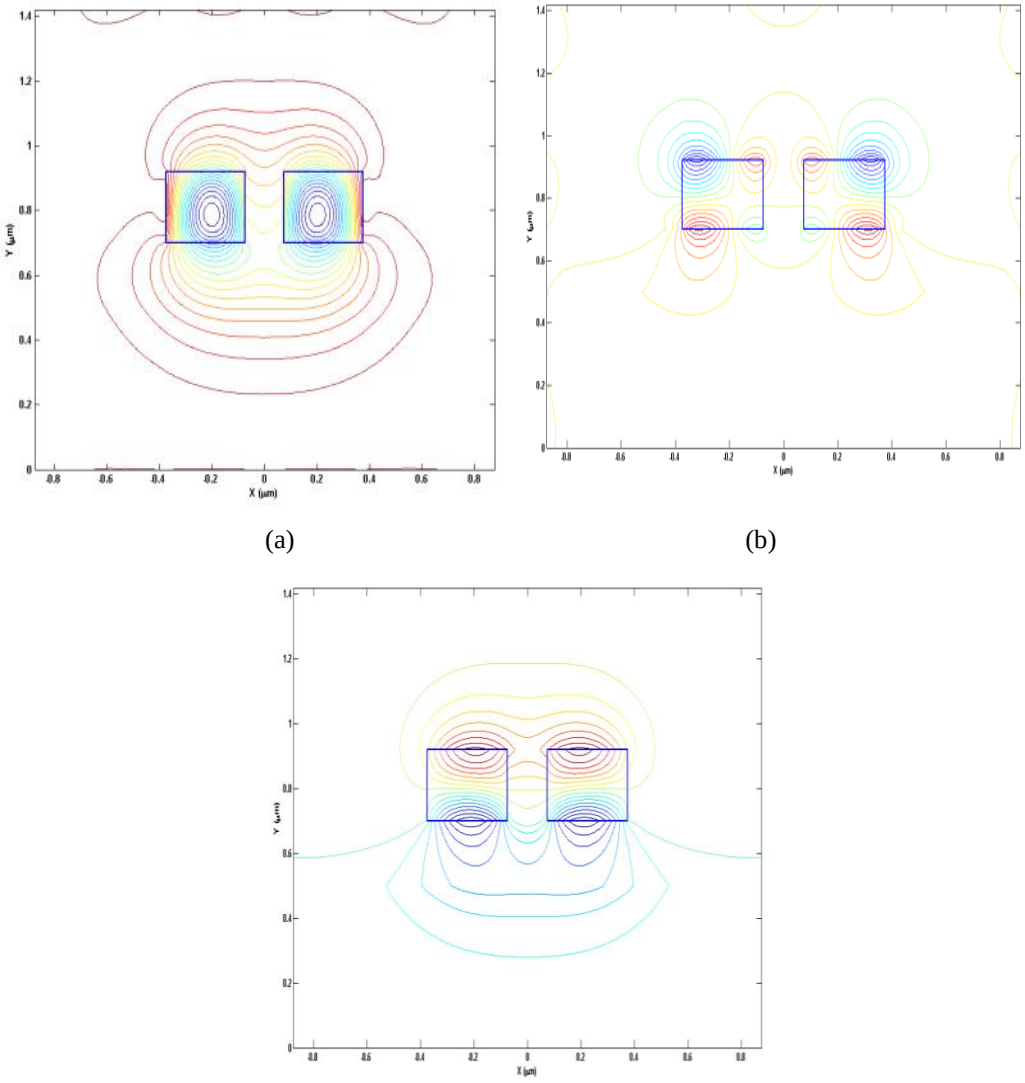

(a) (b)

(c)

Figure 6.10. The quasi-TE modes, (a) H_y, (b) H_x and (c) H_z field profiles in a slot waveguide.

The dominant H_y magnetic field profiles of the quasi-TE mode is shown in Fig. 6.10(a), which shows that the maximum field intensities are inside the Si cores. However the intensities are not in the middle of the cores but they are close to the boundary between the cores and the slot region. It can be noticed that the field extends more towards the buffer layer than the upper cladding area. Figure 6.10(b) shows the non-dominant H_x field component of the quasi-TE mode. It clearly shows four peaks at the four corners of the waveguide with alternate positive and negative signs. The non-dominant H_z field component of the quasi-TE mode is also shown in Fig. 6.10(c), which illustrates that the H_z field is zero along the x-axis in the center of

the waveguide. It can be observed that maximum intensity occurs at the horizontal interfaces between Si cores and upper cladding and Si cores and buffer layer.

6.3.1 Effect of Slot Width (W_S)

Figure 6.11 shows the variation of effective index and effective mode area with the slot widths. It can be observed that as the slot width is reduced the effective index (n_{eff}) increases. This slot mode can also be described as the even supermode of the coupled Si waveguides, where effective indices increase as the separation between the guides (similar as W_s) reduces. However, in this case, as the constituent Si waveguides are rather narrow, they cannot support a mode on their own, so the odd supermode for this structure does not exist.

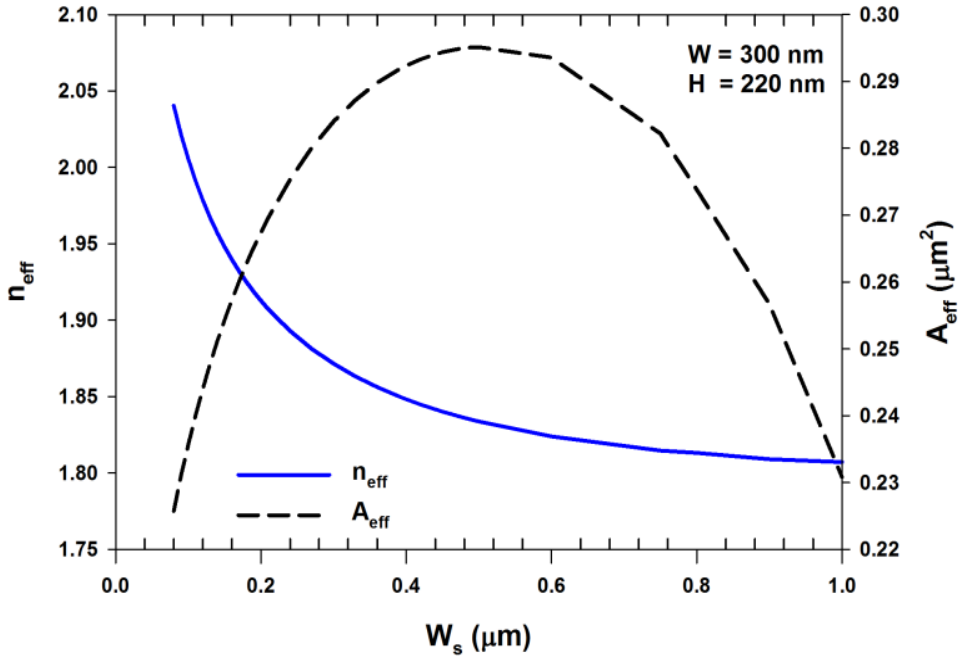

Figure 6.11. Slot waveguide varied W_s of n_{eff} and A_{eff} (μm^2).

The variation of the effective mode area, A_{eff}, is also shown in this figure, by a dashed line. The optical slot-mode only exists when slot width is not very wide, and for very smaller slot width, effective mode area is also reduced.

6.3.2 The SBS Frequency

An intense light beam passing through an optical waveguide with a small cross-section, such as the slot waveguide shown here, produces an acoustic vibration due to electrostriction process resulting from the high electrical field of the optical wave.

The propagation of the generated acoustic wave is associated with the periodic distortion of the waveguide along the axial and transverse directions. This creates a periodic grating due to the material deformation and also the associated elasto-optic effects. This moving Bragg grating reflects the light – however since the acoustic wave is also travelling, the light is subject to a Doppler shift. For the U^y mode, its U_y profile was very closer in shape with the modal field profile of the fundamental quasi-TE optical mode, so their overlap was significant.

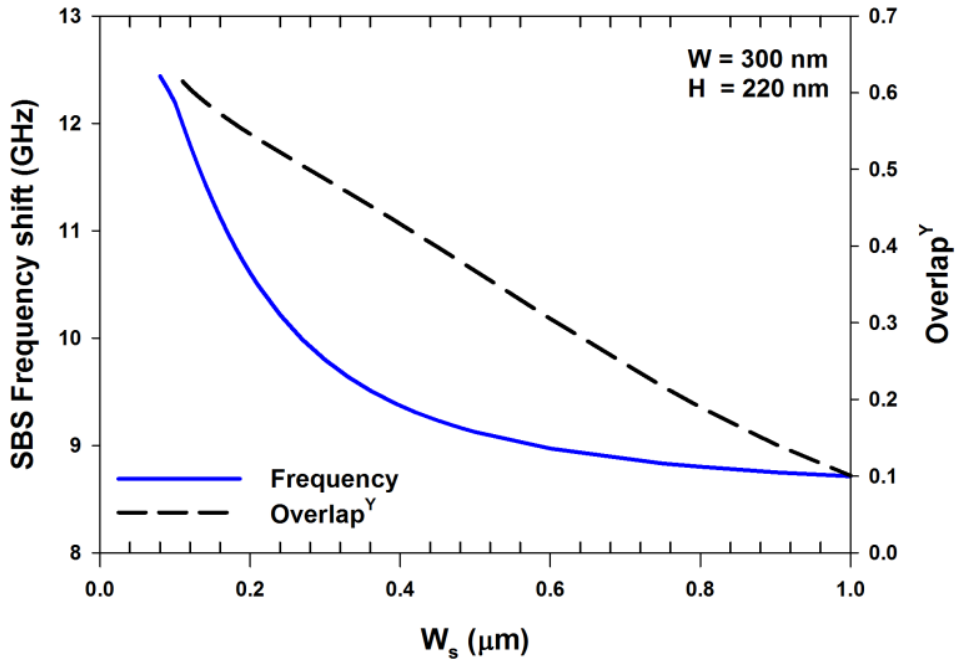

Figure 6.12. Variation of W_s with overlap integral and SBS frequency shift (GHz).

The acoustic and Stokes waves mutually reinforce each other's growth. Subsequently, the SBS frequency can be calculated using $k=2\beta'$ (the Bragg condition) [Kobyakov, 2005, Shelby, 1985 and Zou, 2008] where β' is the effective propagation constant of the fundamental quasi-TE optical mode. The backward SBS only occurs under the phase matching condition $k = 2\,\beta_o$, where $\beta_o = 2\,\pi\,n_{eff}/\lambda_o$ is the propagation constant of the optical modes. Figure 6.12 shows the SBS frequency shift that would be obtained for the fundamental optical mode, for different slot width of the slot waveguide and operating at λ=1.55 μm, through the interaction of the U^y mode. It can be observed that as the slot width is reduced the SBS frequency is increased. For this structure, as the slot width is reduced, its optical effective index is increased. This in turn increases both the optical propagation constant (β) and the phase matched acoustic propagation constant (k_a). The resultant acoustic frequency,

which in this case is the SBS frequency shift increases with increased acoustic propagation constant, as shown in this figure.

The overlap between the dominant H_y field of the quasi-TE mode with the dominant displacement vector U_y of the transverse acoustic mode is also calculated and shown in Fig. 6.12. It can be observed that the overlap with the U_y vector increases almost linearly as the slot-width is reduced, as for this structure both the optical and acoustic modes get more confined in the narrow slot region. As this mode was fully hybrid in nature, there is also considerable overlap with the longitudinal displacement vector U_z and the H_y field of the quasi-TE mode. It should be noted that U_z profiles was non-symmetric with positive and negative peaks along the vertical directions, but since these peaks were not equal, there was a reasonable overlap of this displacement vector with the optical field.

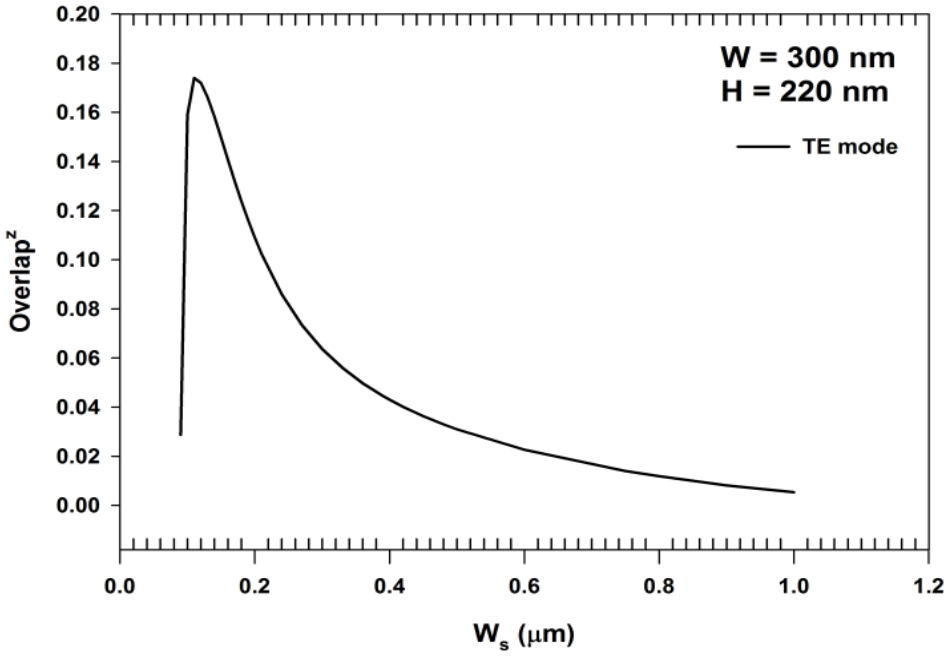

Figure 6.13. Variation of W_s with the overlap^z for a TE mode.

The overlap of H^y field of the quasi-TE mode with the U_z profile is shown in Fig. 6.13 and it can be observed that its value increases progressively as the slot width is reduced and reaches its maximum value of 0.18, when W_s = 110 nm, and then rapidly reduces as shown here. The overlap has reduced dramatically as the W_s of the slot waveguide is increased as shown in Fig. 6.13. On the other hand, overlap

of H_y field with U_x displacement vector was nearly zero as this profile was asymmetric along the horizontal directions, and this is not shown here.

6.3.3 Varied Height (H) of the Slot

Next, the effect of the slot height on the acousto-optic interaction is studied. Variations of the n_{eff} and the A_{eff} with the slot height are shown in Fig. 6.15.

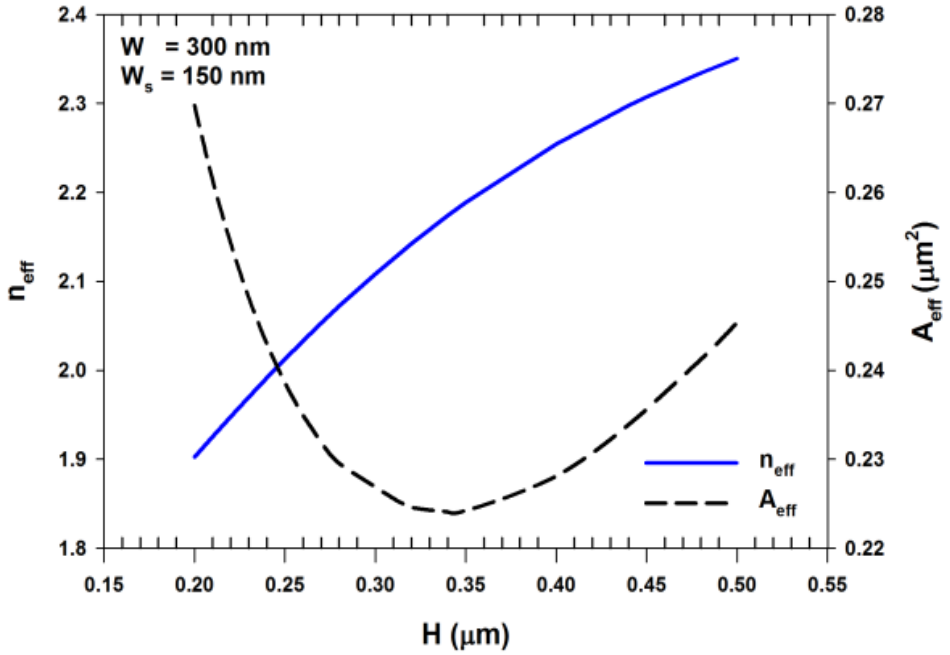

Figure 6.14. Variation of H with n_{eff} and A_{eff} (μm^2).

It can be observed that as the height is increased, the effective index for this quasi-TE mode also increases as shown in Fig. 6.14. However, as the effective index is increased with slot height, its optical propagation constant (β) and phase matched acoustic propagation constant (k_a) also increases. It can be observed that as the height is reduced, initially the effective area, is reduced however, for a further reduction of height, effective area is increased as mode approaches its cut-off and spreads more into cladding.

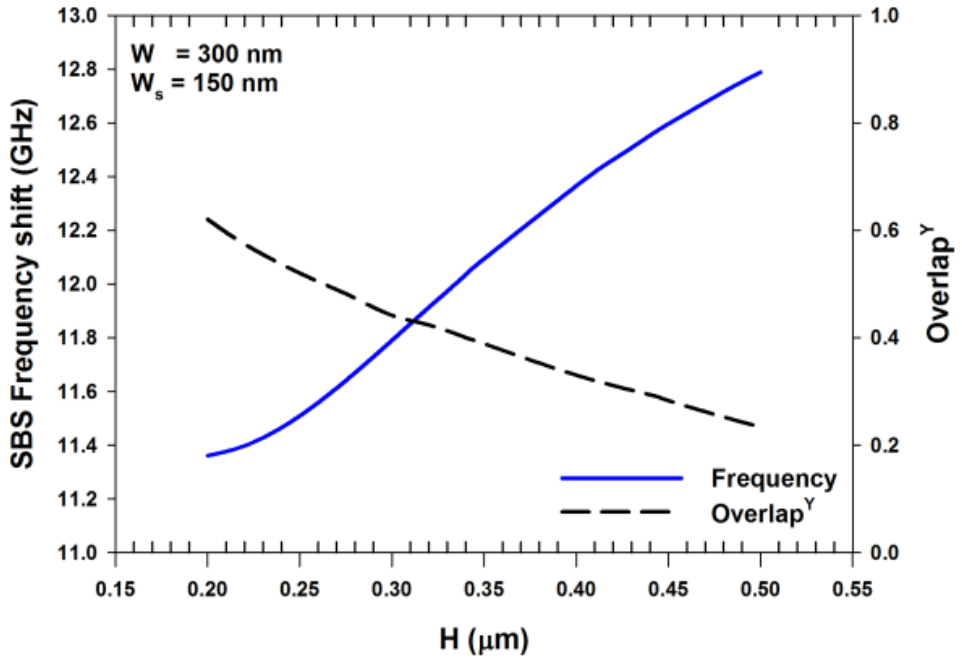

Figure 6.15. Variation of H with overlap^{y} and SBS frequency shift (GHz).

Variations of the SBS frequency shift and overlap integral with the slot height are shown in Fig. 6.15. It can be observed that as the height of the waveguide is increased the overlap integral is reduced as shown by the dashed line. However, as the height of the waveguide is increased the SBS frequency is also increased as shown by the solid line.

6.3.4 Varied Width W (Si) on the Side of Slot

Finally, the effect of slot waveguide width (W) on the generation of SBS frequency shift is also studied. The variation of the SBS frequency shift and acoustic-optical overlap integral are shown in Fig. 6.17.

It can be observed that the effective index of the quasi-TE mode, shown in Fig. 6.16, is increased as the width of the waveguide is increased as shown by a solid line. The variation of the effective mode area, with the waveguide width is also shown in this figure. In here, it can be observed that as the width is reduced, initially A_{eff} is reduces, then achieve a minimum value and for further reduction of width, it increases, as the quasi-TE mode approach their cutoff as shown by a dashed line.

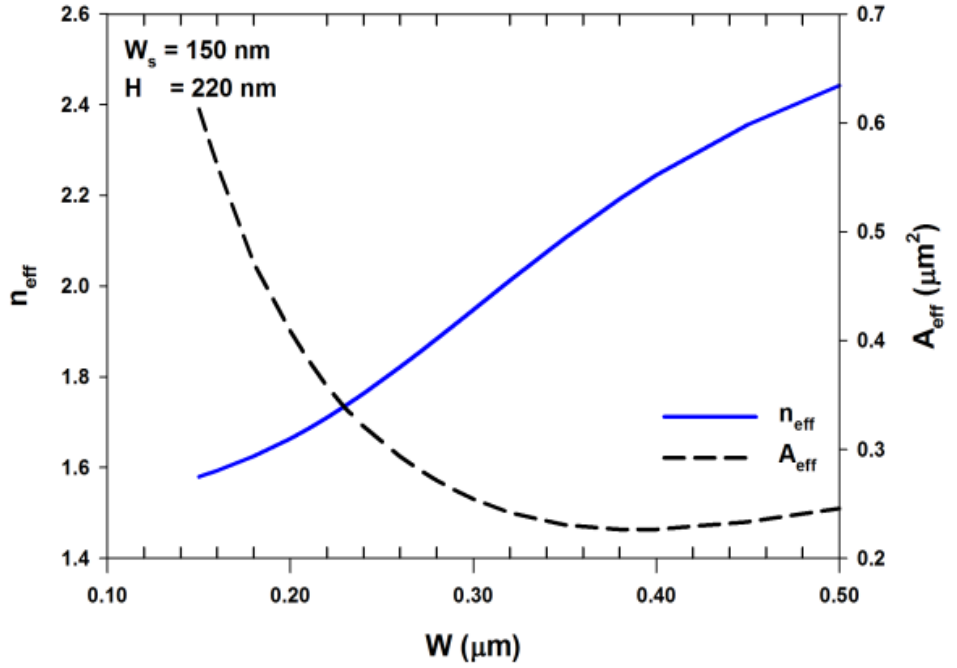

Figure 6.16. Variation of W with n_{eff} and A_{eff} (μm^2).

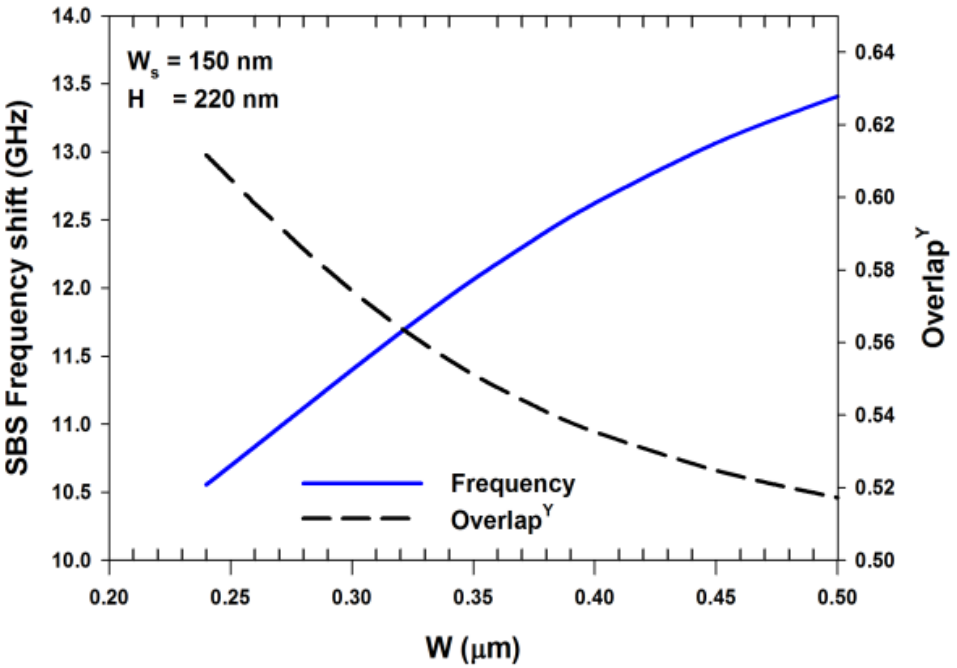

(b)

Figure 6.17. Variation of W with (a) overlap^y and SBS frequency shift (GHz).

The strength of the SBS frequency depends on the overlap between acoustic and optic modes. Therefore the overlap integral of the transverse U^y mode shown in Fig. 6.17. For this slot-waveguide as the width of the Si core is increased the effective index of the optical mode is increased. This in turn increases the phase

matched acoustic propagation constant (k_a) and also the SBS shift frequency. In this case, the acousto-optical overlap integral also reduces as the width of the waveguide is increased but only modestly, over the range shown here.

6.4 Summary

In this Chapter, it has shown that optical slot waveguide is an unique class of optical waveguides where light is guided in low refractive index region and this nature are being exploited for various functional photonic devices. For this structure, if this slot region is filled up with SiO_2, then this region can also guide acoustic waves through this high acoustic index SiO_2 slot region. The interactions of optical and acoustic modes for the slot waveguide are shown in this Chapter, by employing full vectorial approaches for both the optical and acoustic models. The identical mesh discretization has also been used for both the models and the interactions were calculated rigorously without interpolating the field variables.

The numerical result shows that the by varying the slot width and slot height of the slot waveguide, the overlap^y between acoustic and optical mode is decreased. It is also shown in this Chapter that SBS can be reduced by decreasing the overlap^y between the optical and acoustic fields.

Chapter 7

Conclusion and Further Work

7.1 Conclusion

Propagation of acoustic wave in an optical waveguide is a unique feature in which both light and sound are guided in core where both the optical and acoustic indices are higher than that of the cladding and this nature is being exploited for a various functional photonic devices. Studies of the propagation of acoustic waves in various type of waveguides has been explored in this thesis, such as the studies of acoustic fibres which may have the potential to develop devices in sensor and signal processing. A detailed analysis for the propagation of acoustic waves in circular, rectangular, square, strip and slot optical waveguides has also been presented. The results, computed with the numerical method developed for this PhD project have demonstrated the ability to predict the propagation of acoustic waves in different waveguides and a good agreement has been found with published results. Moreover, in the computer code developed, any material, either isotropic or anisotropic or with loss can be considered, when necessary.

This thesis has successfully achieved the following objectives:

1. A finite element code has been developed to study the vector acoustic modes in high and low index contrast acoustic waveguides.
2. The developed acoustic FEM code has been benchmarked against some reported results.
3. The versatile finite element approach presented in the thesis has been used to study interactions between the fully vectorial acoustic and optical modes in practical optical waveguides.
4. The study of SBS and the optimization of their interaction via acousto-optic overlap integral were also undertaken.

In achieving all these objectives, the core of this research began in Chapter 2 by looking at the fundamental and the background theory of acoustic wave. The objective of investigating different types of waveguides with acoustic wave have been presented in that Chapter and different acoustic modes in various waveguides have also been characterised, particularly longitudinal and shear acoustic waves.

In terms of how the acoustic FEM code is developed, Chapter 3 started by looking at the fundamental of the FEM theory. Following this, the incorporation of acoustic wave theory into the FEM is shown. Finally, the newly developed acoustic FEM code is benchmarked on a steel rod structure. The results obtained from the developed code along with the calculated results from the Atkin's extrapolation (in which, the mesh size is increased in geometrical proportional ratio for the bending (B) and torsional (T) modes) showed that the results obtained from the developed code matched well with the results from the published work [Hennion, 1996]. With this benchmarked results, it gave us confidence that one of the objectives is met. The importance of this benchmarked results showed that U_x, U_y and U_z displacement vector of the dominant U^x and U^y mode can be realised. The result highlighted that degeneration in the U_x and U_y displacement vector is due to the equal width and height of the waveguide structure.

In order to establish further the validity of the developed acoustic FEM code, Chapter 4 looked at the modal displacement profiles of both weakly and strongly guiding acoustic silica fibres. First, for the weakly guiding acoustic fibre waveguide, the characteristics of the longitudinal and transverse modes are presented in that chapter. In addition, three different case studies have been assumed and investigated.

- In Case I, transverse modes with the assumption that the longitudinal velocity of the core equals to that of the cladding velocity to suppress longitudinal modes, is studied first. The results showed that the fundamental and higher order shear modes exists with their spatial variation displacement of U_x, U_y and U_z modes. The combination of the U_x and U_y displacement are given as U_t (U_t=U_x+U_y) vector plot of transverse modes of S_{01} and S_{11}. Their vector combination is categorised into bending (B), torsional (T), radial (R) and torsional-radial (TR) modes. The significant mode findings are listed below:
    - The degeneration occurred in bending (B), torsional (T), radial (R) and torsional-radial (TR) modes with the U_x and U_y displacement vectors.
    - The bending mode is shown that the vector plot (U_t) is 45° rotated to the *x*-axis.
    - The U_x and U_y displacement vector profile of the torsional, radial and torsional-radial modes are similar in the characteristic of having one positive and one negative peaks that will rotated 90° to the *x*-axis in the U_y displacement vector.
    - The combination of the U_x and U_y torsional mode showed there is a periodic twisting in clockwise or anticlockwise at every half wavelength in the vector plot (U_t).
    - The radial mode vector plot (U_t) of the U_x and U_y combination shown that the mode is either in axially inwards or outwards directions.
    - The torsional-radial vector plot (U_t), as combination of the U_x and U_y displacement vector showed that there is a periodic elliptical deformation, in which, it is expanded from the inner core and squeeze to the outer core region.

- Case II showed only the longitudinal mode with the condition that the transverse velocity of the core and cladding are equal to suppress transverse modes. Again the longitudinal and higher order modes are obtained, in particular, the pure dominant longitudinal mode showed that maximum intensity of the mode occurred at the centre of the core whereas for the higher order mode, L_{11} showed there exists one positive and one negative peaks.

- Finally in Case III where all the material parameters are different. The results of ΔV_s which is similar to the case II studied is shown first. However, by decreasing the V_s of the core from 3764 m/s to the value of 3625 m/s, while the V_s of the cladding is kept constant at 3764 m/s. This introduced the shear mode into the core, in which it co-existed with the longitudinal modes. The reduction of velocity is due to the enhancing of the modal confinement as the shear velocity in the core is slowly deviates more from the cladding. Furthermore, the effect of ΔV_L is also studied in which it is similar to the scenario of case I but V_L of the core is reduced progressively from 5933 m/s to the value of 5736 m/s, while the V_L of the cladding remains at 5933 m/s. It is observed that as ΔV_L is increased, the phase velocity of the S_{01} mode reduces uniformly as the modal confinement increases.

As mentioned, Chapter 4 also looked into the study of high index contrast acoustic waveguides, in which the sub-wavelength silica nanowire is presented. Here the transverse modes of bending (B), torsional (T), radial (R) and torsional-radial (TR) modes are shown. From here, one of the objectives was to study the modal interaction between optics and acoustics. SBS frequency in acoustic waveguide was found to be one of the important parameters in order to study the interaction between optics and acoustics. An overlap integral is applied to the acoustic radial mode (R) of the U_z displacement vector and the optical modes dominant (H^y_{11}) mode to study the interaction. It is observed that the SBS frequency increased as the radius of the fibre increased, in contrast the overlap between acoustic and optical modes is reduced. In this Chapter, it has also shown that there is a different between the SBS frequency for a sub-wavelength silica waveguide and the bulk SBS frequency, in which the SBS frequency in a sub-wavelength silica

waveguide is lower due to the fact that the mode being fully hybrid and not being a pure longitudinal mode. It is important to take note that for sub-wavelength optical and acoustic waveguides, both the optical and acoustic modes are fully hybrid in nature and therefore it requires rigorous full-vectorial approaches to determine the acousto-optical interactions.

Waveguides are of different shapes and sizes, not only waveguides can be in a circular form, such as silica fibres discussed previously in Chapter 4, it can also be in rectangular shape. Therefore Chapter 5 concentrated on applying acoustic FEM code to rectangular waveguides with both low and high index contrast materials, in particular, the strip waveguide is presented at the last section of this chapter.

For the low index contrast Ge-doped SiO_2 core with the pure SiO_2 cladding, it is observed that when the hybrid transverse acoustic U_x, U_y and U_z modes overlap with the hybrid optical modes. The results showed that the SBS frequency is decreased with the width of the waveguide, in contrast their $overlap^x$ and $overlap^y$ are increased with the width.

An example of a strong index contrast SiO_2 rectangular waveguide is also studied in this chapter, the results showed fully hybrid acoustic modes with both transverse and longitudinal displacement vectors have been determined. Unlike in a weakly guiding SiO_2 waveguides, the transverse and longitudinal displacements are strongly coupled in the high index contrast SiO_2 waveguide. It is also shown here that their displacement vector profiles continuously evolve as the frequency or propagation constant increases and becomes increasingly confined along the waveguide interfaces. The overlap interaction of the transverse acoustic radial modes (R) of the U_z displacement showed that initially the $overlap^z$ is increased with height and decreased as height of the waveguide increased further. As the width of the waveguide is analysed it showed that the SBS frequency is increased with the width. The $overlap^z$ shown that when the width is reduced the $overlap^z$ is increased to its maximum, further decreased of width results into the $overlap^z$ being reduced. The increasing in width and height of the waveguide showed that it will increase the n_{eff}

and phase match acoustic propagation constant (k_a) which in turn increases the SBS frequency shift.

Finally in this Chapter, two different scenarios have been studied for the strip waveguide. In the first case, assumption is made to the transverse velocities of the core and claddings are equal to avoid the transverse mode for being coupled. The simulation results showed the U_z and U_x displacement vector profiles of the quasi-longitudinal (L_{01}) mode. The effects of the width of porous silicon (PS) on the SBS frequency shift and their acousto-optic interaction are also presented. The increased in width showed that the SBS frequency also increased, however, the overlap^z decreased with wider widths.

The second scenario assumed that all the parameters are different with only transverse acoustic modes being shown. It is shown that with the dominant in the U_x displacement vector of the U^x mode, the SBS frequency is increased with width and their overlap^x is reduced when width of the PS strip waveguide is increased. It is shown that the n_{eff} of the optical mode is increased with width this in turn increased the SBS frequency and the phase match condition.

Overall, both cases showed that the effect of variation on the width of the PS strip waveguide in the longitudinal (U^z) and transverse (U^x) modes are similar, in which the n_{eff} of both optical modes increased. This in turn increased their phase match of the SBS frequency shift and the overlap^z and overlap^x are also increased.

Lastly, acoustic and optical modes in the optical slot waveguide is presented in Chapter 6. It is found that such slot waveguide allowed light to guide in the low refractive index region and this nature are being exploited for various functional photonic devices. On the other hand, if this slot region is filled up with silica, then this region can also guide acoustic waves through this high acoustic index silica slot region, paving way for new photonic devices. The interactions of optical and acoustic modes are shown for this structure by employing full-vectorial approaches for both the optical and acoustic models. It is observed that the SBS frequency and the overlap^y are reduced with wider slot width. However for the overlap^z, it is found

that overlap^z increased with the slot width until its maximum value, further increased of width resulted in the overlap^z being reduced. It can be noticed that the reduced slot width resulted in increased of n_{eff} and phase match acoustic propagation constant (k_a) of SBS frequency.

Over the last few years several research groups have studied this important optical-acoustic interaction, often ignoring vector natures of the modes and using approximate scalar formulation. The acoustic wave not only changes refractive index to form a moving grating, but also the periodic stress variation will change the refractive index due to elasto-optic effects, which is fully anisotropic. The versatile finite element approach presented here can be used to study interactions between fully vectorial acoustic and optical modes in practical waveguides and devices. It should be noted that the optical modes are also fully hybrid with all the 6 components of the Electric and Magnetic fields being present. To evaluate and optimize the complex interactions between the hybrid optical modes and the hybrid acoustic mode, a fully-vectorial approach is necessary. A computationally-efficient finite element based approach, as presented here, is seen to be more appropriate to study and thus use to optimize such interactions. It is also well known that due to the strong index contrast and arbitrary shaped dielectric interfaces, the guided optical modes are hybrid in nature.

In this work, it is also shown that acoustic modes in the waveguides with a strong material contrast are also hybrid in nature and strongly influenced by the material interfaces. To study the complex interaction between such optical and acoustic modes a full-vectorial, yet computationally efficient and flexible, approach would be required.

7.2 Suggestions for future work

The development of this finite element code allows a more rigorous study of the vector acoustic modes in complex acoustic waveguides to be undertaken, such as guiding through exotic optical waveguides, for example via photonic crystal fibres, silicon slot waveguides and plasmonic hybrid waveguides or waveguides which may have a more complex shape. The newly developed finite element code is versatile, and therefore it can be used to study hybrid transverse and longitudinal acoustic modes in practical optical waveguides and also it can be employed to consider complex acoustic-optical wave interactions in such waveguides.

There have been significant efforts on developing high power fibre lasers with narrow line-width and good beam quality. Such high power lasers pose significant challenges on fibre designs to reduce nonlinear effects such as SBS and to achieve simultaneously single mode operation. SBS is non-desirable for high power lasers because they limit the amount of output optical power. One well known way to reduce the SBS effects is to make fibres with large mode area (LMA). However, when the core size is too large, the fibre becomes multi-moded. Modal discrimination techniques, such as bending, are then required to achieve single mode operation. But for large core size, bending deforms the mode field distribution and reduces the mode area, which puts a limit on the benefit of using large core.

Nonlinear effects can also be managed through design approaches other than increasing the effective area. It has been found that SBS can be reduced by decreasing the overlap between the optical and acoustic fields. This is achieved through fibre profiles designs to confine the optical and acoustic field in different regions in the core, in which this newly developed acoustic FEM code may be beneficial. As a further design technique for SBS suppression, an acoustic anti-guiding structure can be formed by designing an optical waveguide which does not guide acoustic wave for high power deliver. Another idea is to design an optical waveguide which also guides acoustic wave and optimises optical-acoustic interaction for sensing application.

Appendix A

Stress, Strain and Reduced Notation

Stress and strain vectors

In this appendix we derive the three-dimensional forms of the stress and strain tensors somewhat more fully and rigorously than in Secs. 2.2 and 2.3 of the text. We also describe the commonly used reduced notation based on the symmetry of the **S** and **T** tensor

Strain vectors

A point r in the material is displaced by stress to a point $r + u$, where u is the displacement vector. Suppose that we consider length l in the material between the point r and $r+\delta r$. After displacement, l changes to l' and, as illustrated in Fig. A.1, we can write:

$$l^2 = (\delta r)^2 = (\delta x_1)^2 + (\delta x_2)^2 + (\delta x_3)^2 \qquad \text{(A.1)}$$

and

$$l'^2 = (\delta r + \delta u)^2 = l^2 + 2\delta u \cdot \delta r + (\delta u)^2 \tag{A.2}$$

We shall express δu_x in the form:

$$\delta u_x = \frac{\partial u_x}{\partial x}\delta x + \frac{\partial u_x}{\partial y}\delta y + \frac{\partial u_x}{\partial z}\delta z \tag{A.3}$$

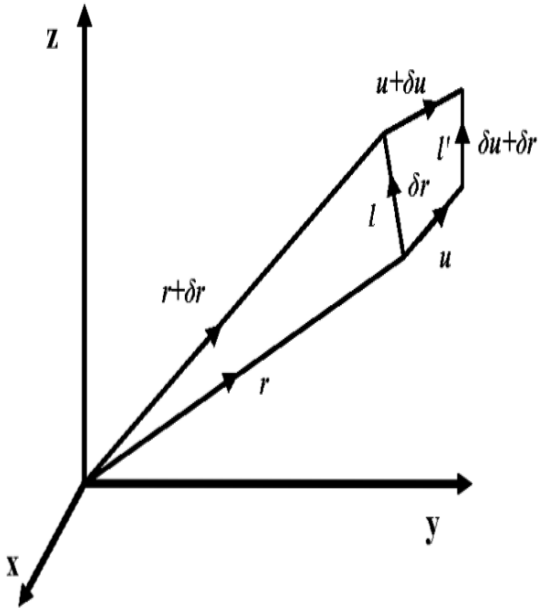

Figure A.1. Notation used in Eq. (A.1).

With similar notations for δu_y and δu_z. These relation can be summarized conveniently using tensor notation (see Sec. 2.3) and written in the form:

$$\delta u_i = \frac{\partial u_i}{\partial x_j}\delta x_j \tag{A.4}$$

This is a short and notation for:

$$\delta u_i = \sum_j \frac{\partial u_i}{\partial x_j}\delta x_j \tag{A.5}$$

where i can be x, y, z, and where for a given i, the summation over the subscript j is understood.

We may write a Taylor expansion for Eq. (A.2) and keep term to second order in δx_i. This process yields the result:

$$l'^2 = l^2 + 2\frac{\partial u_i}{\partial x_j}\delta x_i \delta x_j + \frac{\partial u_i}{\partial x_j}\frac{\partial u_i}{\partial x_k}\delta x_i \delta x_k \tag{A.6}$$

where, as discuss in Sec. 2.3, the tensor notation now implies double summations over the three independent suffixes *i*, *j*, and *k* on the right-hand side of Eq. (A.6). Note that we have replaced the vector δr by δx_i. in tensor notation. Similarly, a scalar product $A.B$ is $A_i B_i$.

The change in l^2 is the true measure of the deformation of the material. If instead, we were to use the change in δr as a criterion, this vector could be changed by a pure rotation of a rigid material without changing the length *l*; thus the change in δr would not be a measure of the deformation in this case.

We can now interchange the suffixes *i* and *k* in the third term of Eq. (A.6), and write the second term in the form:

$$\frac{\partial u_i}{\partial x_j}\delta x_i \delta x_j = \frac{1}{2}\left(\frac{\partial u_i}{\partial x_j} + \frac{\partial u_j}{\partial x_i}\right)\delta x_i \delta x_j \tag{A.7}$$

In this case, Eq. (A.6) can be written as:

$$l'^2 = l^2 + 2S_{ij}\delta x_i \delta x_j \tag{A.8}$$

where S_{ij} is known as the strain tensor and is defined as:

$$S_{ij} = \frac{1}{2}\left(\frac{\partial u_i}{\partial x_j} + \frac{\partial u_j}{\partial x_i} + \frac{\partial u_k}{\partial x_i}\frac{\partial u_k}{\partial x_j}\right) \tag{A.9}$$

We see from that definition that S_{ij} is a symmetric tensor. For small displacements, we can neglect the last term in Eq. (A.9) as being of second order. From now on we shall write

$$S_{ij} = \frac{1}{2}\left(\frac{\partial u_i}{\partial x_j} + \frac{\partial u_j}{\partial x_i} \right) \tag{A.10}$$

Alternatively, we can use a symbolic notation S, much like that for a vector, and define the strain S_{ij} in the form

$$S = \begin{bmatrix} S_{11} & S_{12} & S_{13} \\ S_{21} & S_{22} & S_{23} \\ S_{31} & S_{32} & S_{33} \end{bmatrix} = \begin{bmatrix} S_{xx} & S_{xy} & S_{xz} \\ S_{yx} & S_{yy} & S_{yz} \\ S_{zx} & S_{zy} & S_{zz} \end{bmatrix} \tag{A.11}$$

where now the subscript 1, 2, and 3 are equivalent to x, y, and z, respectively, and are used interchangeably with them in the literature. It follows that

$$\frac{\partial S_{ij}}{\partial t} = \frac{1}{2}\left(\frac{\partial u_i}{\partial x_j} + \frac{\partial u_j}{\partial x_i} \right) \tag{A.12}$$

where $v=\partial u/\partial t$ is the velocity of a particle in the material. This is equivalent to the one-dimensional equation of conversation of mass, given as $\frac{\partial}{\partial \mathbf{z}}\rho_m \mathbf{v} + \frac{\partial}{\partial \mathbf{t}}\rho_m = 0$, but it yields more information than just conservation of mass. If we take only the diagonal terms, we see that $\nabla . v = (\partial v_i)/(\partial x_i)$ and that the equation of conservation of mass is

$$\rho_{m0}\nabla \cdot \upsilon + \frac{\partial \rho_{ml}}{\partial t} = 0$$

$$\textbf{using} \quad \rho_{m0} = 0 \tag{A.13}$$

We use, from Eq. (A.12), the relation

$$\nabla \cdot \upsilon = \frac{\partial}{\partial t}\left(S_{11} + S_{22} + S_{33} \right) \tag{A.14}$$

This is directly equivalent to $\frac{\partial}{\partial \mathbf{z}}\rho_m \mathbf{v} + \frac{\partial}{\partial \mathbf{t}}\rho_m = 0$, and will be derived in another way below. The diagonal terms are associated with longitudinal strain; the off-diagonal terms are associated with the shear strain. It will be noted that the volume of a small portion δV of the material is δx_1, δx_2, δx_3. After deformation, it becomes δV', where,

$$\begin{aligned} \delta V' &= \left(\delta x_1 + \delta u_1\right)\left(\delta x_2 + \delta u_2\right)\left(\delta x_3 + \delta u_3\right) \\ &= \delta V\left(1+\frac{\partial u_1}{\partial x_1}\right)\left(1+\frac{\partial u_2}{\partial x_2}\right)\left(1+\frac{\partial u_3}{\partial x_3}\right) \\ &\approx \left(1+\frac{\partial u_1}{\partial x_1}+\frac{\partial u_2}{\partial x_2}+\frac{\partial u_3}{\partial x_3}\right) \end{aligned} \tag{A.15}$$

It follows that:

$$\delta V' - \delta V = \delta V\left(S_{11} + S_{22} + S_{33}\right) \tag{A.16}$$

We see that the sum of the diagonal components of the strain tensor is the relative volume change (δV'-δV)/δV. The shear term do not contribute to a change in volume. We can also see this result from substituting Eq. (A.14) in Eq. (A.13).

This yield result

$$\rho_{ml} = -\rho_{m0}\left(S_{11} + S_{22} + S_{33}\right) \tag{A.17}$$

which is identical to Eq. (A.15) for

$$\frac{\rho_{ml}}{\rho_{m0}} = \frac{-\left(\delta V' - \delta V\right)}{\delta V} \tag{A.18}$$

Stress Tensor

Here we shall give a different and more detailed derivation for stress than that given in Sec. 2.3. The force in the x direction on a body of a volume V is $\int F_x\, dV$, where the force F_x is a scalar quantity. We can always write a scalar quantity as the divergence of a vector.

Thus we put

$$\begin{aligned} F_x &= \nabla \cdot A \\ F_y &= \nabla \cdot B \\ F_z &= \nabla \cdot C \end{aligned} \tag{A.19}$$

Then from Gauss's theorem, we can write

$$\int_V F_x dV = \int_V \nabla \cdot A dV = \int_S A \cdot dS \quad \textbf{etc.} \tag{A.20}$$

where the surface integral is taken around the enclosing volume V.

It is apparent that we need nine components, A_x, A_y, A_z, B_x, B_y, B_z, C_x, C_y, C_z, to express $\int F_x\, dV$, $\int F_y\, dV$ and $\int F_z\, dV$ In tensor notation we write

$$F_i = \frac{\partial T_{ij}}{\partial x_j} \tag{A.21}$$

which is short and for

$$F_i = \sum_j \frac{\partial T_{ij}}{\partial x_j} \tag{A.22}$$

or

$$F_x = \frac{\partial T_{xx}}{\partial x} + \frac{\partial T_{xy}}{\partial y} + \frac{\partial T_{xz}}{\partial z} \tag{A.23}$$

and so on. The quantity T_{ij} is called the stress tensor. In our previous notation, we see that $A_x=T_{xx}=T_{11}$, $A_y=T_{xy}=T_{12}$, $A_z=T_{xz}=T_{13}$, and so on.

It follows that the average force on an element of volume dV is

$$\frac{1}{dV}\int \nabla \cdot T dV = \frac{1}{dV}\int \frac{\partial T_{ij}}{\partial x_j} dV = \frac{1}{dV}\int T_{ij} ds_j = \frac{1}{dV}\oint T \cdot n\, ds \tag{A.24}$$

where we define $\nabla.T$ as $(\partial T_{ij})/(\partial x_j)$, and where ds_j is the surface element vector directed along the outward normal. The force on a surface in the z direction therefore has three components normal to the surface that compromise the vector C in Eq. (A.19); these are T_{xz}, T_{yz} and T_{zz}. The first two terms are shear stresses that tend to distort the surface of an isotropic material, as shown in Fig. A.2(b).

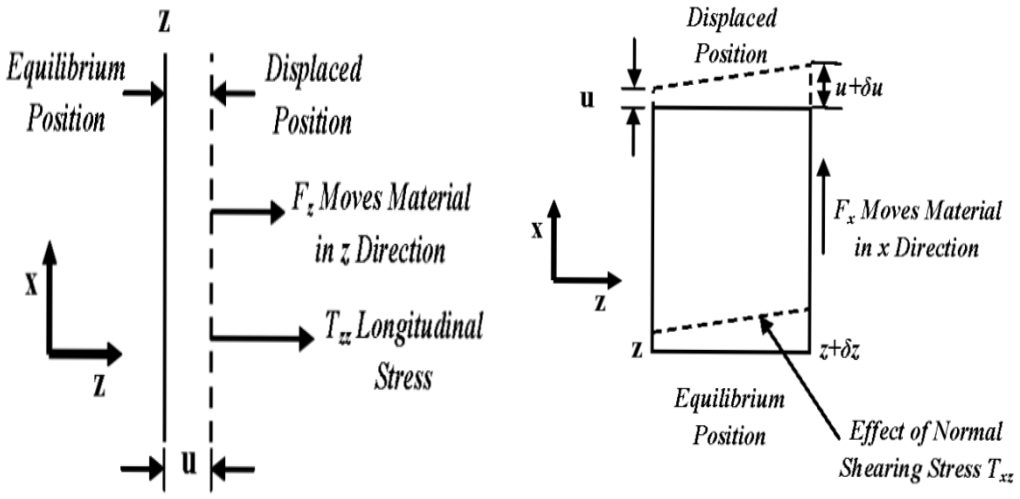

Figure A.2. Effect of normal longitudinal and shear stresses at a surface: (a) longitudinal stress; (b) shear stress.

The last term in a longitudinal stress, which acts as shown in Fig. A.2(a). All the stress components are applied to a cube, illustrated in Fig. 2.3. because $\int T_{ij} ds_j = \int T_{ji} ds_i$, it can be shown that $T_{ij}=T_{ji}$ (i.e., T is a symmetric tensor).

Equation of motion

The force on an element dV is $\int T.n\, ds_j$ due to internal stresses. Thus, if only internal stresses are applied, we can write the equation of motion for first-order displacements as

$$\rho_{m0} \frac{\partial^2 u}{\partial t^2} = \lim_{dV \to 0} \left[\frac{\int T \cdot n \, ds}{dV} \right] \tag{A.25}$$

or

$$\rho_{m0} \frac{\partial^2 u}{\partial t^2} = \nabla \cdot T \tag{A.26}$$

which is equivalent to

$$\rho_{m0} \frac{\partial^2 u}{\partial t^2} = \frac{\partial T_{ij}}{\partial x_j} \tag{A.27}$$

where ρ_{m0} is the mass density of the material

Symbolic notation and abbreviated subscripts

Strain Tensor

To reduce the complexity of the stress and strain tensors, it is helpful to use symmetry and to work with an abbreviated subscript notation. Here we shall describe this abbreviated subscript notation and show how it is used. We first consider the strain tensor S_{ij}, defined as

$$S_{ij} = \frac{1}{2}\left(\frac{\partial u_i}{\partial x_j} + \frac{\partial u_j}{\partial x_i}\right) \tag{A.28}$$

Because the strain is the symmetric tensor, we can replace S_{yx} with S_{xy}, and so on. Thus we can use a reduced notation with fewer subscripts. The standard reduced notation can be expressed in matrix form:

$$S = \begin{bmatrix} S_{11} & S_{12} & S_{13} \\ S_{21} & S_{22} & S_{23} \\ S_{31} & S_{32} & S_{33} \end{bmatrix} = \begin{bmatrix} S_1 & \frac{S_6}{2} & \frac{S_5}{2} \\ \frac{S_6}{2} & S_2 & \frac{S_4}{2} \\ \frac{S_5}{2} & \frac{S_4}{2} & S_3 \end{bmatrix} \tag{A.29}$$

Note that the notation follows a cyclic order, with the longitudinal strain terms corresponding to the subscripts 1, 2, and 3, respectively, and the shear strain terms corresponding to the subscripts 4, 5, and 6, respectively, as shown in Table A.1:

Table A.1. Reduced Tensor Notation

Normal tensor notation	*Reduced notation*	*Corresponding strain*
xx	1	Longitudinal in x direction
yy	2	Longitudinal in y direction
zz	3	Longitudinal in z direction
yz=zy	4	Shear y - z
zx=xz	5	Shear z - x
xy=yx	6	Shear x - y

Note that the off-diagonal terms are multiplied by 1/2 so that we can write the strain in the form of column matrix:

$$\begin{bmatrix} S_1 \\ S_2 \\ S_3 \\ S_4 \\ S_5 \\ S_6 \end{bmatrix} = \begin{bmatrix} \frac{\partial}{\partial x} & 0 & 0 \\ 0 & \frac{\partial}{\partial y} & 0 \\ 0 & 0 & \frac{\partial}{\partial z} \\ 0 & \frac{\partial}{\partial z} & \frac{\partial}{\partial y} \\ \frac{\partial}{\partial z} & 0 & \frac{\partial}{\partial x} \\ \frac{\partial}{\partial y} & \frac{\partial}{\partial x} & 0 \end{bmatrix} \begin{bmatrix} u_x \\ u_y \\ u_z \end{bmatrix} \tag{A.30}$$

This can be done only because the 1/2 was used in our definitions in Eq. (A.29). Following [Auld, 1973], it is convenient to define the matrix in Eq. (A.30) with symbolic notation, writing

$$S = \nabla_S u \tag{A.31}$$

where $\nabla_s u$ is defined as the symmetric part of ∇u. The symmetric operator $\nabla_s u$ is defined by the first matrix on the right-hand side of the Eq. (A.30). In the unreduced tensor notation, the symmetry of ∇_s is apparent because

$$S_{ij} = \frac{1}{2}\left(\frac{\partial u_i}{\partial x_j} + \frac{\partial u_j}{\partial x_i}\right) \tag{A.32}$$

A simple example of longitudinal motion in the x direction with propagation in the x direction is defined by the relation $S_1=\partial u_x/\partial x$; this follows from Eq. (A.30). On the other hand, a plane shear wave, in which propagation is in the z direction but particle displacement in the y direction, is defined by the relation $u_x=u_z=0$ and $S_4=\partial u_y/\partial z$. In this case, all other components of strain are on zero. The first case corresponds to a longitudinal wave passing through a flat plate; the second case corresponds to the flexural motion of a thin strip.

Stress Tensor

The stress tensor may be stated in terms of reduced subscripts just as the strain tensor was. Thus we write

$$T = \begin{bmatrix} S_{xx} & S_{xy} & S_{xz} \\ S_{yx} & S_{yy} & S_{yz} \\ S_{zx} & S_{zy} & S_{zz} \end{bmatrix} = \begin{bmatrix} S_1 & S_6 & S_5 \\ S_6 & S_2 & S_4 \\ S_5 & S_4 & S_3 \end{bmatrix} \tag{A.33}$$

Note that the 1/2 terms are not required here. The equation of motion for symbolic notation is

$$\nabla \cdot T = \rho_{m0} \frac{\partial v}{\partial t} \tag{A.34}$$

This can be put in reduced tensor form, by writing

$$\rho_{m0} \frac{\partial}{\partial t} \begin{bmatrix} \upsilon_x \\ \upsilon_y \\ \upsilon_z \end{bmatrix} = \nabla \cdot T \begin{bmatrix} \frac{\partial}{\partial x} & 0 & 0 & 0 & \frac{\partial}{\partial z} & \frac{\partial}{\partial y} \\ 0 & \frac{\partial}{\partial y} & 0 & \frac{\partial}{\partial z} & 0 & \frac{\partial}{\partial x} \\ 0 & 0 & \frac{\partial}{\partial z} & \frac{\partial}{\partial y} & \frac{\partial}{\partial x} & 0 \end{bmatrix} \begin{bmatrix} T_1 \\ T_2 \\ T_3 \\ T_4 \\ T_5 \\ T_6 \end{bmatrix} \tag{A.35}$$

For example, if the stress field has only one component, a shear stress $T_5=T_{xz}$ propagating in the z direction, then $\nabla.T$ becomes $(\partial T_5)/\partial z$ and corresponds to an acceleration in the x direction.

Elasticity

Similarly, the elasticity tensor c_{ijlk} can be expressed in reduced notation. Because $S_{ij}=S_{ji}$ and $T_{ij}=T_{ji}$, it follows that $c_{ijlk}=c_{jilk}=c_{ijkl}=c_{jilk}$, which reduces the number of independent constants required from 81 to 36. Furthermore, because of symmetry,

$c_{ijlk}=c_{klij}$. This further reduces the required number of independent constants in an arbitrary medium to 21. Thus we write

$$\begin{bmatrix} T_1 \\ T_2 \\ T_3 \\ T_4 \\ T_5 \\ T_6 \end{bmatrix} = \begin{bmatrix} c_{11} & c_{12} & c_{13} & c_{14} & c_{15} & c_{16} \\ c_{21} & c_{22} & c_{23} & c_{24} & c_{25} & c_{26} \\ c_{31} & c_{32} & c_{33} & c_{34} & c_{35} & c_{36} \\ c_{41} & c_{43} & c_{43} & c_{44} & c_{45} & c_{46} \\ c_{51} & c_{52} & c_{53} & c_{54} & c_{55} & c_{56} \\ c_{61} & c_{62} & c_{63} & c_{64} & c_{65} & c_{66} \end{bmatrix} \begin{bmatrix} S_1 \\ S_2 \\ S_3 \\ S_4 \\ S_5 \\ S_6 \end{bmatrix} \tag{A.36}$$

or

$$T = c \cdot S \tag{A.37}$$

where the general term is c_{IJ}; we use capital subscripts to denote the reduced notation and take $c_{IJ}=c_{JI}$.

Example: Cubic crystal

Most crystals have certain symmetries that reduce the required number of constants. For instance, a cubic crystal looks the same in the x,-x,y,-y,z,and-z directions. This implies that $c_{11}=c_{22}=c_{33}$, $c_{44}=c_{55}=c_{66}$ and $c_{12}=c_{13}=c_{23}$. All other diagonal terms are zero because of the mirror symmetry. Thus we find that for a cubic crystal,

$$c = \begin{bmatrix} c_{11} & c_{12} & c_{13} & 0 & 0 & 0 \\ c_{21} & c_{22} & c_{23} & 0 & 0 & 0 \\ c_{31} & c_{32} & c_{33} & 0 & 0 & 0 \\ 0 & 0 & 0 & c_{44} & 0 & 0 \\ 0 & 0 & 0 & 0 & c_{55} & 0 \\ 0 & 0 & 0 & 0 & 0 & c_{66} \end{bmatrix} \tag{A.38}$$

When there is the shear wave propagation along z axis, with motion in the x direction, it follows from Eq. (A.30) that

$$S_5 = \frac{\partial u_x}{\partial z} \tag{A.39}$$

and form Eqs. (A.36) and (A.38) that

$$T_5 = c_{44} S_5 \tag{A.40}$$

Assuming that the RF components vary as exp (jωt), then $v_x = j\omega u_x$. It follows from Eq. (A.34) or Eq. (A.35) that

$$\frac{\partial T_5}{\partial z} = j\omega \rho_{m0} \upsilon_x \tag{A.41}$$

However, from Eq. (A.39) and (A.40), we see that

$$c_{44} \frac{\partial \upsilon_x}{\partial z} = j\omega T_5 \tag{A.42}$$

Equations (A.41) and (A.42) are the transmission-line equations for the shear wave propagation. Assuming that waves propagate as exp ($\pm j\beta_s z$), we see that for shear waves in a cubic crystal,

$$\beta_s^2 = \omega^2 \left(\frac{\rho_{m0}}{c_{44}} \right) \tag{A.43}$$

If, on the other hand, we consider longitudinal motion in the z direction with only u_z or v_z finite, we find that the propagation constant β_l is given by the relation

$$\beta_l^2 = \omega^2 \left(\frac{\rho_{m0}}{c_{11}} \right) \tag{A.44}$$

Example: Isotropic material

In this case, which is very much like that of the cubic crystal, the c tensor is of the same from as that of Eq. (A.38), with the additional condition that $c_{12}=c_{11}-2c_{44}$. Note that the c_{12} term corresponds to the ratio of the longitudinal stress in the x direction to the longitudinal strain in the y direction. Such term occur because when a material is compressed in one direction, it tends to expand in a perpendicular direction. The relation given follows from the requirement that the tensor c keeps the same form; however, the axes are rotated from their original position. It follow that an isotropic

medium has only two independent elastic constants. These are usually called the Lame constants, defined as

$$\begin{aligned} \lambda &= c_{12} \\ \mu &= c_{44} \end{aligned} \tag{A.45}$$

with

$$c_{11} = c_{12} = 2c_{44} = \lambda + 2\mu \tag{A.46}$$

The c matrices of different types of crystals are tabulated in appendix A.2 of B. A. Auld's Acoustic fields and Waves in Solids [Auld, 1973]. The similar s matrices, for which $s=c^{-1}$ or

$$S = s : T \tag{A.47}$$

are also tabulated by Auld.

Appendix B

References

- Agrawal, G. P., "Stimulated Brillouin Scattering," in *Nonlinear Fiber Optics 4th edition*, Elsevier Academic Press, Amsterdam, chap. 9, pp. 329-333, 2007.
- Agrawal, G. P., *Nonlinear Fibre Optics, 3rd edition*, Academic Press, San Diego, CA, 2001.
- Alford, R. M., Kelly, K. R. and Booret, D. M., "Accuracy of finite different modelling of the acoustic wave equation," *Geophysics*, vol. **39**, no. 6, pp. 834-842, 1974.
- Almeida, V. R., Xu, Q., Barrios, C. A. and Lipson, M., "Guiding and confining light in void nanostructures," *Opt. Lett*, vol. **29**, pp. 1209-1211, 2004.
- Auld, B. A., "Application of Microwave concepts to the theory of acoustic fields and waves in solids," *IEEE Trans. Microw. Theory Techn.*, vol. **17**, pp. 800-811, 1969.
- Auld, B. A., *Acoustic Fields and Waves in Solids Vol.1*, John Wiley & Sons, Canada, chap. 1-3, 1973.
- Bao, X., Dhliwayo, J., Heron, N., Webb, D. J. and Jackson, D. A., "Experimental and theoretical studies on a distributed temperature sensor based on Brillouin scattering," *J. Lightwave Technol.*, vol. **13**, pp. 1340-1346, 1995.
- Baher-Jones, T., Penkov, B., Huang, J., Sullivan, P., Davies, J., Takayesu, J., Luo, J., Kim, T.-D., Dalton, L., Jen, A., Hochberg, M. & Scherer, A., Nonlinear polymer-clad silicon slot waveguide modulator with a half wave voltage of 0.25 V. Appl. Phys. Lett., 92, 163303 (2008).

- Bhashar, A., "Waveguide modes in elastic rods," *Proc. R. Soc. Lond. A, vol.* **459**, pp. 175-194, 2003.
- Boyd, R. W., *Nonlinear Optics*, Academic Press, San Diego, CA, 1992.
- Brambilla, G., Finazzi, V. and Richardson, D., "Ultra-low-loss optical fiber nanotapers," *Opt. Express*, vol. **12**, pp. 2258-2263, 2004.
- Brillouin, L., "Diffusion de la lumière et des rayons X par un corps transparent homogène, influence de l'agitation thermique," *A. Phys*., vol. **17**, pp. 88-122, 1922.
- Buckland, E. L. and Boyd, R. W., "Electrostrictive contribution to the intensity-dependent refractive nonlinearity in optical fibre," *Opt. Lett*., vol. **21**, pp. 1117-1119, 1996.
- Chen, L., Shakya, J. and Lipson, M., "Subwavelength confinement in an integrated metal slot waveguide on silicon," *Opt. Lett*., vol. **31**, pp. 2133-2135, 2006.
- Chen, X., Li, M. J. and Li, A., "Ge-doped laser fibre with suppressed stimulated Brilluoin Scattering," in Optical Fiber Communication Conference, OSA Technical Digest, *OSA*, 2010.
- Cherif, R., Zghal, M. and Tartara, L., "Characterisation of Stimulated Brilluoin Scattering in small core microstructured Chalcogenide fibre," *Opt Commun.*, vol. **285**, pp. 341-346, 2012.
- Clough, R. W., "The finite element method in plane stress analysis," *Proceedings of 2nd ASCE Conference on Electronic Computation*, Pittsburgh, Pa., 1960.
- Cowle, G. J., Stepanov, D. Y. and Chieng, Y. T., "Brillouin/Erbium Fibre Lasers," *J. Lightwave Technol.*, vol. **15**, pp. 1198-1204, 1997.
- Culverhouse, D., Farahi, F., Pannel, C. N. and Jackson, D. A., "Potential of stimulated Brillouin scattering as sensing mechanism for distributed temperature sensors," *Electron. Lett*., vol. **25**, pp. 913-915, 1989.
- Dainese, P., Russell, P. St. J., Joly, N., Knight, J. C., Wiederhecker, G. S., Fragnito, H. L., Laude V. and Khelif, A., "Stimulated Brillouin scattering from multi-GHz-guided acoustic phonons in nanostructured photonic crystal fibers," *Nature Phys.*, vol. **2**, pp. 388-392, 2006.
- Dell'Olio, F. & Passaro, V. M. N., Optical sensing by optimized silicon slot waveguides. Opt. Express, 15, 4977-4993 (2007).
- Doghmane, A., Hadjoub, Z., Doghmane, M. and Hadjoub, F., "Microacoustic evaluation of elastic parameters of highly porous silicon layers," *Semicond. Phys. Quantum Electron. Optoelectron.*, vol. **9**, pp. 4-11, 2006.

- Engan, H. E., Kim, B. Y., Blake, J. N. and Shaw, H. J., "Propagation and optical interaction of guided acoustic waves in Two-Mode Optical Fibres," *J. Lightwave Technol.*, vol. **6**, pp. 428-436, 1988.
- Fahy, F. and Gardonio, P., *Sound and Structural Vibration*, Elsevier/Academic, London, chap. 1, pp. 1-51, 2007.
- Fan, H. J., Kuok, M. H., Ng, S. C., Boukherroub, R., Baribeau, J.-M., Fraser, J. W. and Lockwood, D. J., "Brillouin spectroscopy of acoustic modes in porous silicon films," *Phys. Rev. B*, vol. **65**, 165330-8, 2002.
- Fong, K. L. J., *A Study of Curvature Effects on Guided Elastic Waves*, PhD thesis, Imperial College London, 2005.
- Geoffrey, O. S., "High-Order finite elements for Inhomogeneous acoustics guiding structure," *IEEE Trans. Microw. Theory Techn.*, vol. **21**, pp. 538-542, 1973.
- Gray, S., Walton, D. T., Chen, X., Wang, J., Li, M.-J., Liu, A., Ruffin, A. B., Demeritt, J.A. and Zenteno, L. A., "Optical fibers with tailored acoustic speed profiles for suppressing stimulated Brillouin scattering in highpower, single-frequency sources," *J. Lightwave Technol*., vol. **15**, pp. 37-46, 2009.
- Hladky-Hennion, A. C., "Finite element analysis of the propagation of acoustic waves in waveguides," *J. Sound Vib.*, vol. **194,** pp. 119-136, 1996.
- Huebner, K. H. and Thornton, E. A., *The Finite Element Method For Engineers 2nd*, John Wiley & Son, Unite States of America, 1982.
- Iyert, V. N. and Viswanathan, K. S., "The distribution and focusing of phonons for the rare-gas solids xenon and helium," *J. Phys. C: Solid State Phys*., vol. **20**, pp. 5261-5274, 1987.
- Jen, C. K., Safaai-Jazi, A. and Farnell, G. W., "Leaky modes in weakly guiding fiber acoustic waveguides," *IEEE Trans. Ultrason., Ferroelectr., Freq. Control*, vol. **UFFC-33**, no. 6, pp. 634-643, Nov 1986.
- Jen, C. K., Safaai-Jazi, A., Bussiere, J. F. and Farnell, G. W., "Longitudinal mode fiber acoustic waveguide with solid core and solid cladding," *J. Acoust. Soc. Am.*, vol. **87**, no. 2, pp. 921-921, 1990.
- Kee, H. H., Lees, G. P. and Newson, T. P., "All-fibre system for simultaneous interrogation of distributed strain and tempurature sensing by spontaneous Brillouin scattering," *Opt. Lett*., vol. **25**, pp. 1-3, 2000.
- Kino, G. S. and B. A. Auld, "Normal mode theory for acoustic waves and it's application to the interdigital transducer," IEEE Trans. Electron Devices, vol. **18**, pp. 898-908, 1971.
- Kino, G. S., *Acoustic Waves Devices, Imaging,& Analog Signal processing*, Prentice-Hall, Inc. Englewood Cliffs, New Jersey, 1987.

- Kobyakov, A., Kumar, S., Chowdhury, D. Q., Ruffin, A. B., Sauer, M., Bickham, S. R. and Mishra, R., "Design concept for optical fibers with enhanced SBS threshold," *Opt. Express*, vol. **13**, pp. 5338-5346, 2005.
- Koshiba, M., Mitobe, S. and Suzuki, M., "Finite-element solution of periodic waveguides for acoustic waves," *IEEE Trans. Ultrason., Ferroelectr., Freq. Control*, vol. **34**, pp. 472-477, 1987.
- Koyamada, Y., Sato, S., Nakamura, S., Sotobayashi, H. and Chujo, W., "Simulating and designing Brillouin gain spectrum in single-mode fibers," *J. Lightwave Technol.*, vol. **22**, pp. 631-639, 2004.
- Kurashima, T., Horiguchi, T. and Tateda, M., "Distributed-temperature sensing using stimulated Brillouin scattering in optical silica fibres," *Opt. Lett.*, vol. **15**, pp. 1038-1040, 1990.
- Kurashima, T., Horiguchi, T., Izumita, H., Furukawa, S. and Koyamada, Y., "Brillouin optical-fibre time domain reflectometry," *Trans. IEICE Jpn.*, **E76-B**, pp. 382-390, 1993.
- Lagasse, P. E., "Higher-order finite-element analysis of topographic guides supporting elastic surface waves," *J. Acoust. Soc. Am.*, vol. **53**, no. 4, pp. 1116-1122, 1973.
- Lagasse, P. E., Mason, I. M., and Ash, E. A., "Acoustic surface waveguide analysis and assessment," *IEEE Trans. Microw. Theory Techn.*, vol. **21**, pp. 225-236, 1973.
- Laude, L., and Beugnot, J-C., "Electrostriction and guidance of acoustic phonons in optical fibres," *Phys. Rev. B*, vol. **86**, pp. 224304-1 to 6, 2012.
- Laude, V., Khelif, A., Benchabane, S., Wilm, M., Sylvestre, Th., Kibler, B., Mussot, A., Dudley, J. M. and Maillotte, H., "Photonic bandgap guidance of acoustic modes in photonic crystal fibers," *Phys. Rev. B*, vol. **71**, pp. 045107, 2005.
- Lawrie, Proc. R., "Analytic mode-matching for acoustic scattering in three dimensional waveguides with flexible walls: application to a triangular duct," *Wave Motion*, vol. **50**, pp. 542-557, 2013.
- Ledbetter H. and Kim, S., "Monocrystal Elastic Constants and Derived Properties of the Cubic and the Hexagonal Elements," in *Handbook of Elastic Properties of Solids, Liquids, and Gases, Vol. 2*, edited by Levey, M., Bass, H. E. and Stern R. R., Academic Press, San Diego, chap. 7, pp. 97-105, 2001.
- Leung, D. M. H., Kejalakshmy, N. and Rahman, B. M. A., "Rigorous numerical analysis and characterization of silicon vertical-slot nano-waveguide," *J. Nonlinear Opt. Phys. Mater.*, vol. **21**, pp. 1250007, 2012.
- Leung, D. M. H., Kejalakshmy, N., Rahman, B. M. A. and Grattan, K. T. V., "Rigorous modal analysis of silicon strip nanoscale waveguides," *Opt. Express*, vol. **18**, pp. 8528-8539, 2010.

- Levy, M., *Handbook of Elastic Properties of Solid, Liquids, and Gases Vol. 2,* San Diego; London, Academic Press, 2001.
- Li, M. J., Chen, X., Wang, J., Gray, S., Liu, A., Demeritt, J. A., Ruffin, A. B., Crowley, A. M., Walton, D. T. and Zenteno, L. A., "Al/Ge co-doped large mode area fiber with high SBS threshold," *Opt. Express*, vol. **15**, pp. 8290-8299, 2007.
- Li, M. J., Chen, X., Wang, J., Liu, A., Gray, S., Walton, D. T., Boh-Ruffin, A., Demeritt, J., Zenteno, L., "Fibre designs for high power laser," *Optical Components and Materials IV. SPIE,* vol. **6469**, pp. 64690H-1 to 64690H-9, 2007.
- Li, M. J., Chen, X., Wang, J., Ruffin, A. B., Walton, D. T., Li, S., Nolan, D. A., Gary, S. and Zenteno, L. A., "Fibre designs for reducing stimulated Brillouin scattering," in Optical Fiber Communication Conference, 2006 and the 2006 National Fiber Optic Engineers Conference, *OFC 2006, IEEE,* pp. 3-pp., 2006.
- Liang, L. H., Wei, Z., Dong, H. Y. and De, P. J., "Acoustic longitudinal mode coupling in w-shaped Al/Ge co-doped fibre," *Chin. Phys .B,* vol. **20**, pp. 104211-1-9, 2011.
- Limpert, J., Roser, F., Klingebiel, S., Schreiber, T., Wirth, C., Peschel, T., Eberhardt, R. and Tünnermann, A., "The rising power of fiber lasers and amplifiers," *IEEE J. Sel. Top. Quant. Electron*., vol. **13**, pp. 537-545, 2007.
- Love, A. E. H., *A Treatise on the Mathematical Theory of Elasticity 2nd edition,* Cambridge University Press, Cambridge, chap. 3-6, pp. 90-162, 1906.
- Mason, W. P., "Physic acoustics and properties of solids," *J. Acoust. Soc. Am.,* vol. **28**, pp. 1197-1986, 1956.
- Matsuda, O. and Glorieux, C., "A Green's function method for surface acoustic waves in functionally graded materials," *J. Acoust. Soc. Am.,* vol. **121,** pp. 3437-3445, 2007.
- Mermelstein, M. D., "SBS Threshold measurement and acoustic beam propagation modelling in guiding and anti-guiding single mode optical fibre," *Opt. Express*, vol. **17**, pp. 16225-16237, 2009.
- Mermelstein, M. D., "SBS Threshold Measurements and Acoustic Beam Propagation Modeling in Guiding and Anti-guiding Single Mode Optical Fibre," *Opt. Express*, vol. **17**, pp. 16225-16237, 2009.
- Rahman, B. M. A. and Davies, J. B., "Finite element solution of integrated optical waveguides," *J. Lightwave Technol.,* vol. **2**, pp. 682-688, 1984.
- Rahman, B. M. A., Obayya, S. S. A., Somasiri, N., Rajarajan, M., Grattan, K. T. V. and El-Mikathi, H. A., "Design and characterization of compact single-section passive polarization rotator," *J. Lightwave Technol*., vol. **19**, pp. 512-519, 2001.
- Robinson, J. T., Preston, K., Painter, O. & Lipson, M., First-principle derivation of gain in high-index contrast waveguides. *Opt. Express*, **16**, 16659-16669 (2008).

- Royer, D., *Elastic Waves in Solids I Free and Guided Propagation*, Springer-Verlag Berlin Heidelberg, New York, 2000.
- Russell, P. St. J., "Photonic-crystal fibers," *J. Lightwave Technol.*, vol. **24**, pp. 4729-4749, 2006.
- Safaai-Jazi, A. and Claus, R. O., "Acoustic modes in optical fiber like waveguides," *IEEE Trans. Ultrason., Ferroelectr., Freq. Control*, vol. **35**, pp. 619-627, 1988.
- Safaai-Jazi, A., Jen, C. K. and Farnell, G. W., "Analysis of weakly guiding fiber acoustic waveguide," *IEEE Trans. Ultrason., Ferroelectr., Freq. Control*, vol. **33**, pp. 59-68, 1986.
- Saleh, B. E. A. and Teich. M. C., *Fundamentals of Photonics*, chap. 20, John Wiley & Sons, Inc, 1991.
- Shelby, R. M., Levenson M. D. and Bayer, P. W., "Guided acoustic wave Brillouin scattering," *Phys. Rev. B*, vol. **31**, pp. 5244-5252, 1985.
- Shibata, N., Okamoto, K. and Azuma, Y., "Longitudinal acoustic modes and Brillouin-gain spectra for GeO_2-doped-core single-mode fibers," *J. Opt. Soc. Am. B*, vol. **6**, pp. 1167-1174, 1989.
- Shimizu, K., Horiguchi, T., Koyamada, Y. and Kurashima, T., "Coherent self-heterodyne Brillouin OTDR for measurement of Brillouin frequency shift distribution in optical fibres," *J. Lightwave Technol*., vol. **12**, pp. 730-736, 1994.
- Somasiri, N. and Rahman, B. M. A., "Polarization crosstalk in high index contrast planar silica waveguides with slanted sidewalls," *J. Lightwave Technol.*, vol. **21**, pp. 54-60, 2003.
- Stenner, M. D., Neifeld, M. A., Zhu, Z., Dawes, A. M. C. and Gauthier, D. J., "Distortion management in slow-light pulse delay," *Opt. Express*, vol. **13**, pp. 9995-10002, 2005.
- Stone, G. O., "High-order finite elements for inhomogeneous acoustic guiding structures," *IEEE Trans. Microw. Theory Techn.*, vol. **21**, pp. 538-542, 1973.
- Strutz, S. J. and Williams, K. J., "Low-noise hybrid erbium/Brillouin amplifier," *Electron. Lett*., vol. **36**, pp. 1359-1360, 2000.
- Tanaka, Y., Yoshida, H. and Kurokawa, T., "Guided-acoustic-wave Brillouin scattering observed backward by stimulated Brillouin scattering," *Meas. Sci. Technol.*, vol. **15**, pp. 1458-61, 2004.
- Thévenaz, L., Facchini, M., Fellay, A., Robert, P., Inaudi, D. and Dardel, B., "Monitoring of large structures using distributed Brillouin fiber sensing," *Proc. SPIE* 3746, pp. 345-348, 1999.

- Thévenaz, L., "Slow and fast light using stimulated Brillouin scattering: a highly flexible approach," in *Slow Light—Science and Applications*, edited by Khurgin, J. B. and Tucker, R. S., CRC Press, chap. 9, 2009.
- Thomas, P. J., Rowell, N. L., Driel, H. M. V. and Stegeman, G. I., "Normal acoustic modes and Brillouin scattering in single-mode optical fibre," *Phys. Rev. B*, vol. **19**, pp. 4986-4998, 1979.
- Thurston, R. N., "Elastic waves in rods and clad rods," *J. Acoust. Soc. Am.*, vol. **64**, pp. 1-37, 1978.
- Timodhenko, S. and Goodier, J. N., *Theory of Elastic 2nd*, McGraw-Hill, New York, pp. 213-459, 1951.
- Vincent, L., Khelif, A., Benchabane, S. and Wilm, M., "Phononic band-gap guidance of acoustic modes in photonic crystal fibers," *Phys. Rev. B*, vol. **71**, pp. 045107-1-6, 2005.
- Wang, S., Hu, J., Guo, H. & Zeng, X., Optical Cherenkov radiation in an As2S3 slot waveguide with four zero-dispersion wavelengths. Opt. Express, 21, 3067-3072 (2013).
- Warlimont, M. and Warlimont Eds., H., *Springer Handbook of Condensed Matter and Materials of America*, Springer Berlin, Germany, chap. 1-3, pp. 1-153, 2005
- Wright, H., Faradayt, C. S. N., White, E. F. T. and Treloar, L. R. G., "The elastic constants of oriented glassy polymers," *J. Phys. D: Appl. Phys.*, vol. **4**, 1971.
- Yu, J. W., Park, Y. and Oh, K., "Brillouin frequency shifts in silica optical fibres with the double cladding structure," *Opt. Express*, vol. **10**, pp. 996-1002, 2002.
- Yu, J., Kwon, I1-B. and Oh, K., "Analysis of Brillouin frequency shift and longitudinal acoustic wave in a silica optical fibre with a Triple-Layered Structured," *J. Lightwave Technol.*, vol. **21**, pp. 1779-1786, 2003.
- Zienkiewicz, O. C., *The Finite Element Method*, McGraw-Hill, New York, 1977.
- Zoe, W., He, Z. and Hotate, K., "Acoustic modal analysis and control in w-shaped triple-layer optical fibres with highly-germanium-doped core and F-doped inner cladding," *Opt. Express*, vol. **16**, pp. 10006-100017, 2008.
- Zou, L., Bao, X., Ravet, F. and Chen, L., "Distributed Brillouin sensor for detecting pipeline bukling in an energy pipe under internal pressure," *Appl. Optics*, vol. **45**, pp. 3372-3377, 2006.